Karlsruher Institut für Technologie

Spectroscopic Investigations of Intermolecular Effects in the KATRIN Tritium Source Loop

Zur Erlangung des akademischen Grades eines

DOKTORS DER NATURWISSENSCHAFTEN (Dr. rer. nat.)

von der KIT-Fakultät für Physik
des Karlsruher Instituts für Technologie (KIT)

genehmigte

DISSERTATION

von

M. Sc. Bennet Krasch

aus der Hansestadt Lübeck

Referent:	Prof. Dr. Guido Drexlin Institut für Astroteilchenphysik Karlsruher Institut für Technologie
Korreferent:	Prof. Dr. Ralph Engel Institut für Astroteilchenphysik Karlsruher Institut für Technologie
Tag der mündlichen Prüfung:	17.02.2023

Declaration of Authorship

Herewith I affirm that I wrote the current thesis on my own and without the usage of any other sources or tools than the cited ones and that this thesis has not been handed neither in this nor in equal form at any other official commission.

Erklärung der Selbstständigkeit

Hiermit versichere ich, die vorliegende Arbeit selbstständig angefertigt zu haben und keine Hilfsmittel jenseits der kenntlich gemachten verwendet zu haben. Weiterhin habe ich weder diese noch eine äquivalente Version dieser Arbeit bei einer anderen Prüfungskommission vorgelegt.

Karlsruhe, den 11. Januar 2023

Bennet Krasch

Contents

List of Figures

List of Tables

List of Abbreviations

BGA binary gas analyser

BIXS Beta Induced X-ray Spectrometry

BOSS Baryon Oscillation Spectroscopic Survey

CCD charge coupled device

CKM Cabibbo-Kobayashi-Maskawa

CMB cosmic microwave background

CNO carbon–nitrogen–oxygen

CPS cryogenic pumping section

cw continuous wave

DPS differential pumping section

FPD focal plane detector

FSD final-state distribution

HAZOP hazard and operability study

HST Hubble Space Telescope

HYDE HYdrogen DEuterium

IR infrared

ISS isotope separation system

KATRIN Karlsruhe Tritium Neutrino

LARA laser Raman

MAC-E magnetic adiabatic collimation with electrostatic retardation

MSW Mikheyev–Smirnov–Wolfenstein

NIST American National Institute of Standards & Technology

op ortho-para

p-p proton-proton

PMNS Pontecorvo-Maki-Nakagawa-Sakata

RaCoon Raman catalytic ortho-para normlaizer

RS rear section

SM Standard Model of Elementary Particle Physics

SNO Sudbury Neutrino Observatory

SSM Standard Solar Model

TApIR Tritium Absorption Infrared Spectroscopy

T_2ApIR Tritium Absorption Infrared Spectroscopy 2

TLK Tritium Laboratory Karlsruhe

TTS tritium transfer system

WDS water detriation system

WGTS windowless gaseous tritium source

ZTS central tritium retention system

1 Introduction

Since the postulation of the neutrino by Wolfgang Pauli in 1930 [Pau30], the scientific research field of neutrino physics has repeatedly provided groundbreaking discoveries that have had an impact on other areas of physics [Shu11; Kis13; Raj16; Ere17]. Thus, the discovery of neutrino oscillation - neutrinos changing their flavour (ν_e, ν_ν, μ_τ) as they travel - led to the realisation in 2001 [Ahm01; Ahm02] that neutrinos have a finite, non-zero mass. This directly contradicts the assumption of massless neutrinos in the Standard Model of Elementary Particle Physics (SM) [Oer06]. This discovery earned its discoverers, Takaaki Kajita and Arthur B. McDonald, the 2015 Nobel Prize [The15] in Physics. Since then, several research institutions have been trying to determine the absolute mass scale of neutrinos [Zub20] using various experimental methods and theoretical calculations. So far, however, only different upper limits for the neutrino masses have been determined [Lor02; Rie11; Dvo11; Par12; Rie14; Gas17; Shi17; Nuc18; Ago19; Alv19; Ant19; Arn19; Upa19; Ake22]. In the broad field of neutrino research, there are two different approaches to determining the absolute mass: model-dependent, indirect methods and model-independent, direct methods. In the first approach, observations of cosmological and astrophysical phenomena (supernova explosions or dark energy) form the basis for model-dependent calculations [Lor02; Par12; Rie14]. The other approach involves the spectroscopic study of the energy spectrum of the electrons e^- released during radioactive decay [Kra05; Ase11; Dvo11; Gas17; Nuc18; Ake22]. A non-vanishing neutrino mass has a direct influence on the shape of the spectrum, especially visible at the kinematic endpoint. The current mass limit is held by the Karlsruhe Tritium Neutrino (KATRIN) experiment with $0.8\,\mathrm{eV}/c^2$ (90 % C.L.) [Ake22]. KATRIN's design sensitivity is $0.2\,\mathrm{eV}/c^2$ (90 % C.L.) [Ang05], which is a factor of 10 better than the previous experiments in Mainz and Troitsk [Kra05; Ase11].

KATRIN investigates the shape of the energy spectrum of electrons e^- released during the β-decay of molecular tritium T_2

$$T_2 \rightarrow {}^3HeT^+ + e^- + \bar{\nu}_e + 18.6\,\mathrm{keV} \tag{1.1}$$

near the kinematic endpoint E_0 of approximately 18.6 keV [Ang05; Dre13; Are18b; Alt19; Ake19; Ake20a; Ake21; Ake22]. These β-electrons are adiabatically guided to a magnetic adiabatic collimation with electrostatic retardation (MAC-E) filter based spectrometer for analysis. To determine sub-eV neutrino masses in this way requires a high luminosity source, the windowless gaseous tritium source (WGTS), with an activity of 100 GBq stabilised at the per mil level [Hei17], and a high voltage system with a ppm stability at the spectrometer, which has an ultra-high vacuum inside [Are16; Are18a]. Only by meeting these high technical requirements will KATRIN be able to experimentally investigate small distortions in the shape at the end point, where the neutrino mass manifests itself. In order to be able to unambiguously assign these small deviations to a neutrino mass, it is indispensable to know and quantify all the systematic effects that have an influence on the shape of the spectrum. The work of Seitz-Moskaliuk [Sei19] provides the current state of the systematic uncertainty budget with all effects and their contributions. Much of these

systematic effects reside in the 30 K cold KATRIN source (WGTS). A central, systematic effect is the final-state distribution (FSD) [Dos06], whose calculations are based, among other things, on the gas composition, i.e. the rotational states of the tritiated molecules ($^3HeT^+$, $^3HeD^+$, $^3HeH^+$), in the WGTS.

The molecular gas composition of the six hydrogen isotopologues (Q_2) is characterised mainly by the following contributions:

- chemical: H_2, HD, HT, D_2, DT, T_2,
- ortho(o)-para(p): o-H_2, p-H_2, o-D_2, p-D_2, o-T_2, p-T_2 and
- dimers $(Q_2)_2$: (T_2-T_2, $DT-T_2$, $HT-T_2$, ...).

For KATRIN, it is mainly the tritiated species that are present in the WGTS and are important for the calculation of the FSD. Predicting the gas composition inside the WGTS is difficult because the only spectroscopic measurement of the chemical composition takes place far outside the WGTS at room temperature using laser Raman (LARA) spectroscopy, and there is no other direct experimental access. Thus, simulations and calculations are used to determine the actual gas composition in the WGTS [Dos06; Bod15b], and assumptions are made about how and how fast the gas state changes towards the WGTS at the time of the measurement. The main process for changing the chemical and ortho-para (op)[1] gas composition are exchange reactions, both within the gas by isotope exchange (conversion) and outside the gas with external partners, such as carbon atoms from the stainless steel surfaces, i.e. the pipes, pumps, buffer vessels. While the conversion rates and equilibrium states depend on temperature, pressure and composition, the gas composition of KATRIN is only measured at one point in the warm state by laser Raman spectroscopy [Ang05]. However, as it passes through the tritium source loop, the temperature changes several times in ranges between 30 K, 300 K and ≈ 600 K [Stu21]. The op fractions are not measured at all, but are assumed not to change significantly based on literature values. In addition, the presence of tritium in particular creates many complex reaction channels. For this reason, the literature contains a large number of experimental and theoretical studies of **chemical** conversion of the Q_2 [Dor54; Gen70; McC83b; McC83a; McC85; Sou86; Gen70; Uda92b; Uda92a; Gan99; Saz11]. The investigations described therein mainly refer to observations in the gas phase. Occasionally, the exchange reaction with external partners, such as carbon, has also been studied by [Tho58; Aqu65; Uda92a]. There are also studies of **op** conversion, both natural [Sou86; Mil72; Mil97] and catalytically driven [Tay33; Emm35; Wei55; Wil57; Cha57; Wei58b; Hut67; Hut70; Sou86; Ili92; Fuk13; Boe17]. For catalytic conversion, various materials, such as iron oxide or chromium oxide, have been studied mainly for hydrogen in the context of liquefaction [Ber09; Car17; Yin19]. As a result, there is little data available for the catalytic op conversion of tritium. Clusters are a van-der-Waals bond between molecules, the simplest case between two molecules is called a **dimer**. The investigation of the energy levels of such van-der-Waals clusters for the inactive isotopologues (H_2, HD, D_2) in the gas phase has been sufficiently accomplished with infrared (IR) absorption studies [Wat65; McK74; McK90; McK91]. Studies in the liquid phase, on the other hand, are less common [McK94; Grö15b; Grö17; Grö20; Mir20] and studies on the tritiated isotopologues are not yet available. Furthermore, the KATRIN design report [Ang05] states that dimers only exist below 30 K (WGTS temperature), but the results of Mirz [Mir20], who examined H_2 and D_2 dimers under KATRIN-like conditions, indicate that clusters exist

[1] Due to the coupling of the nuclear spin of the two molecules, the homonuclear hydrogen isotopologues H_2, D_2, and T_2 gain an additional degree of freedom, the ortho and para states.

under these conditions. This suggests that tritiated dimers also form. In general, it can be said that there are either no data or little or incomplete and contradictory data on the study of the different processes with tritium.

Nevertheless, it is of utmost importance to investigate these molecular effects (exchange reactions, conversion processes, dimer formation) in order to quantify their influence on the systematic effects (e.g. FSD) and thus ultimately on the shape of the energy spectrum. In order to obtain this necessary information, the present work pursues the goal:

T_2ApIR: Design, construction and set-up of a tritium-compatible experiment for the systematic investigation of the molecular and intermolecular effects of all six hydrogen isotopologues under KATRIN-like conditions.

T_2ApIR stands for Tritium Absorption Infrared Spectroscopy and is the evolution of TApIR, which only studied hydrogen and deuterium. Chapter 2 describes the scientific environment in the field of neutrino physics and the working principle of the KATRIN experiment. The theoretical basis of the exchange reactions and conversion processes as well as the systematic effects in the thermal cycle of the KATRIN tritium source loop are part of chapter 3. In order to be able to study all these diverse molecular and intermolecular effects, adequate measurement technologies have to be developed and evaluated in advance in appropriate pre-investigations, see chapter 4. In turn, the results obtained are directly shaping the design of the new Tritium Absorption Infrared Spectroscopy 2 (T_2ApIR) experiment. With regard to the thermal cycle of KATRIN, it is indispensable to understand how fast the gas composition changes as it passes from the warm region (measurement LARA) to the cold region (WGTS) due to internal and external reactions, which is why a warm and a cold measurement cell are desired for spectroscopic investigations. To determine the influence of the β-decay on the natural isotope exchange reaction, the two reactions of $H_2 + T_2 \rightleftharpoons 2\,HT$ and of $H_2 + D_2 \rightleftharpoons 2\,HD$ are studied in the warm region. The results are presented in section 4.2, considering the possible influence of exchange reactions with metal surfaces on the reaction are part of the investigations. Since the natural op and chemical conversion is too slow, suitable catalyst materials are needed to selectively force the gases into different compositions and thus trigger exchange reactions. The simultaneous measurement of the op and chemical conversion with LARA spectroscopy enables systematic conversion studies with the new Raman catalytic ortho-para normlaizer (RaCoon) experiment developed in this thesis. The measurement technique developed for this purpose and the proof of principle of this method are presented in sections 4.3.2 and 4.3.4. In order to investigate the influence of small amounts of gas admixtures on the conversion process, targeted measurements were conducted, see section 4.3.4. For the spectroscopic investigation of conversion times and equilibrium states with LARA and dimer formation with IR, a combined spectroscopic setup with a cryogenic measurement cell has to be developed. For this purpose, certain optical components are either suitable for both types of spectroscopy or can be automatically moved out of the optical path. The results of the relevant pre-investigations concerning coatings and moving linear stages are presented in section 4.4. All of these results will be directly incorporated into the design of T_2ApIR. The creation of the T_2ApIR experiment, starting from the definition of the scientific and technical objectives (see section 5.1) and requirements (see section 5.2), through the realisation of the resulting process design (see section 5.3), finally to the technical realisation and construction (see section 5.4), is presented in detail in chapter 5. Chapter 6 concludes with a general summary of the results achieved in this thesis and gives an outlook on the upcoming research with T_2ApIR for KATRIN.

2 The KATRIN experiment in the field of direct neutrino mass experiments

With the beginning of the last century, neutrinos have played an increasingly important role in the discovery of physics beyond the SM and in the research fields of cosmology and astroparticle physics [Shu11; Kis13; Ere17; Dep19; Ath22]. The number of Nobel Prizes in Physics awarded to neutrino-related research shows the importance of the research and its significant discoveries: the detection of the neutrino [The95], the detection of cosmic neutrinos [The02] and the oscillation of neutrinos [The15]. Therefore, in the first part of this chapter, section 2.1 presents a brief history of the discovery of the neutrinos and their typical properties, see section 2.1.1, and the status of recent experiments to determine the neutrino mass using different approaches, see section 2.1.2. The second part of this chapter introduces the Karlsruhe Tritium Neutrino Experiment (KATRIN). After an explanation of the general measuring principle in section 2.2.1, the tritium source of KATRIN is described in more detail in section 2.2.2, since it is crucial for this work. The latest results and the current status of the KATRIN experiment conclude this chapter, see section 2.2.3.

2.1 Neutrinos, from postulation to the measurement of their masses

Neutrinos are the fundamental particles of the SM. Their properties, being electrically neutral and only weakly interacting, have made their discovery and detection quite challenging, but they also work well as messenger particles of distant galactic events. Therefore, this section will give an overview of the discovery of the three neutrinos, followed by neutrinos in the context of the SM, neutrino oscillation in the context of the solar neutrino problem, and finally the mass generation process.

2.1.1 Neutrinos in the Standard Model of Elementary Particle Physics

At the end of the 19th century, the success story of the neutrino began hand in hand with the intensive observation and study of the radioactive decay. From 1896 on, H. Becquerel and P. and M. Curie systematically studied the radioactive decay of materials [Bec96; Cur10]. The classification into the three groups of alpha (α), beta (β) and gamma (γ) decay was made by E. Rutherford [Rut99]. In 1914, J. Chadwick observed the decay spectrum of radium. Contrary to his expectation of a discrete spectrum with two single lines, one for the daughter nucleus and one for the remaining electron, as investigated in the two-body alpha decay [Bra04], he measured a continuous β-decay spectrum [Cha14]. Ellis and Wooster proved the continuous β-spectrum with their experiments in 1927 [Ell27]. This observation contradicted the conservation of energy and angular momentum, two cornerstones of the physical understanding of the last centuries. Therefore, in his famous letter "Liebe Radioaktive Freunde" in 1930 [Pau30], W. Pauli postulated

that there must be an additional particle with a tiny mass and spin 1/2. At first, it was called the neutron. In 1934, E. Fermi developed a theoretical approach to explain this three-body decay by

$$\begin{aligned} \mathrm{n} &\rightarrow \mathrm{p} + \mathrm{e}^- + \bar{\nu}_\mathrm{e}, \\ \mathrm{M}(A, Z) &\rightarrow \mathrm{D}(A, Z+1) + \mathrm{e}^- + \bar{\nu}_\mathrm{e}, \end{aligned} \tag{2.1}$$

with n as neutron, p as proton, e^- as electron and $\bar{\nu}_\mathrm{e}$ as the electron antineutrino, and M as mother nucleus, D as daughter nucleus, A as mass number and Z as proton number. Fermi used the name neutrino because in the meantime the neutron had been discovered as a heavy particle [Cha32] and therefore, the neutron could not be the missing particle. Regarding the equation 2.1, Fermi assumed that a neutron n decays into a proton p, an electron e^- and an electron antineutrino $\bar{\nu}_\mathrm{e}$. The latter has a vanishing mass or even no mass according to the data Fermi had. The β-decay thus became a three-body decay. It took almost 20 years of research before the neutrino was first discovered. In 1953, F. Reines and C. Cowan detected the neutrino in their famous "Poltergeist" experiment [Cow56]. "Poltergeist" is placed next to the commercial Handford Plant Reactor, where a large flux of electron neutrinos can be expected. Two tanks filled with a total of 300 l of cadmium-loaded scintillator material and 100 photomultiplier tubes surrounding each tank form the experimental setup. The measurement principle follows the inverse β-decay

$$\nu_\mathrm{e} + \mathrm{p} \rightarrow \mathrm{n} + \mathrm{e}^+, \tag{2.2}$$

where e^+ is the positron, the anti-particle of the electron. By measuring the two photon signals, one from the annihilation of the positron with an electron, emitting two γ at 180° with 511 keV each, and the second photon from the neutron capture in cadmium, with a time difference of a few μs. This clear signature allowed F. Reines and C. Cowan to measure the electron antineutrino flux with a signal-to-background ratio of 1/17. After the discovery of the muon μ, a muon neutrino ν_μ was predicted and measured at the Brokhaven AGS in 1962 [Dan62]. In this experiment, muons μ and muons neutrinos ν_μ were produced by the decay of charged pions π^{+-}

$$\begin{aligned} \pi^- &\rightarrow \mu^- + \bar{\nu}_\mu \\ \pi^+ &\rightarrow \mu^+ + \nu_\mu. \end{aligned} \tag{2.3}$$

These produced neutrinos interact with matter to create muons μ^{+-}. By investigating the ratio of the electron to muon neutrinos, it was shown that there are two different types of neutrinos, with a ratio of 29 to 6. The last neutrino, the tau neutrino ν_τ, was discovered in the Donut experiment at Fermilab in 2001 [Kod01]. The D_s mesons decay into a tau τ and a tau antineutrino $\bar{\nu}_\tau$. Again, the interaction of the neutrino with matter was observed in a charged-current reaction. The produced tauon τ typically decays within the next 2 mm and produces a typical kink [Pat01]. A high resolution for particle tracks allowed the detection of four tauon kinks [Kod01]. It took almost 90 years from Chadwick's observation of a continuous β-spectrum to the experimental determination of the third neutrino. All these discoveries completed the leptonic sector of the SM, which will be discussed in the next paragraph.

Standard Model of Elementary Particle Physics

The Standard Model of Elementary Particle Physics (SM) has been developed and confirmed by various experiments over the last century [Oer06]. This model describes the three fundamental

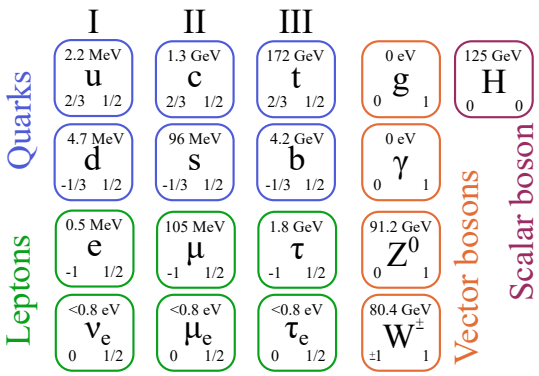

Figure 2.1: Standard Model of Elementary Particle Physics (SM). The fermions, spin 1/2-particles, are grouped on the left according to their three generations by mass: quarks (blue) at the top and leptons (green) at the bottom. The vector (or gauge) bosons (orange) are on the right, mediating the strong (g), electromagnetic (γ) and the weak (Z^0, $W^{\pm}$) forces. The scalar Higgs boson (violet) is the excitation of the Higgs field. For each particle, the mass is shown at the top, the charge at the bottom left and the spin at the bottom right. All the properties are based on the reference [Zyl20].

forces (electromagnetic, weak, and strong), their interactions and includes all fundamental particles. The fourth force, the gravity, is not part of the SM, since there is no unified theory that includes gravity and the other three forces up to now. The fundamental particles are divided into **fermions** and **bosons**, see figure 2.1. The group of the twelve fermions is subdivided into the six quarks u, d, c, s, t, b and into the six leptons e^-, μ^-, τ^- with the corresponding neutrinos ν_e, ν_μ, ν_τ. There are three generations with respect to the rising mass. Each generation forms a weak isospin doublet. The six quarks have an additional colour charge, so they only interact via the strong force. Fermions are spin 1/2 particles and also exist as antiparticles. Antiparticles have the same mass, but opposite electric charge, colour charge and an opposite third component of the weak isospin [Pov15].

The group of bosons consists of the vector bosons (also called gauge bosons), the gluon g, W^+, W^-, Z^0 and the photon γ with spin 1 and the scalar Higgs boson H with spin 0. The gluon g is the exchange particle for the strong interaction and it is described by eight colour combinations . The electromagnetic force is mediated by the photon γ. The weak interaction is described by the W and Z bosons, where the W boson is a doublet of the charged variants W^+ and W^-. The Z^0 boson is electrically neutral. The unification of the two fundamental forces, the electromagnetic and the weak, forms the electroweak interaction. The Higgs boson H was the last particle to be experimentally discovered and added to the SM [Hig64]. It is the quantum excitation of the Higgs field and is responsible for the mass generation of the elementary particles.

The chargeless leptons do not interact via the strong force, but only via the weak force. A key feature of the weak interaction is the violation of parity. Parity describes the transformation of the mirroring $x \rightarrow -x$. In 1957, Madam Wu et al. [Wu57] showed the violation of parity within the weak interaction. This is directly related to the helicity $\vec{H}$

$$\vec{H} = \frac{\vec{S}\vec{p}}{Sp}, \tag{2.4}$$

with $\vec{S}$ is the spin vector and $\vec{p}$ is the momentum vector. Helicity is the projection of the spin vector $\vec{S}$ onto the direction of the momentum vector $\vec{p}$. In the context of neutrinos, it is also called

chirality. In the SM, there are only **left-handed ($H = 1$) neutrinos** and right-handed ($H = -1$) antineutrinos.

Initially, neutrinos were assumed to be massless and were integrated as such in the SM. One phenomenon, neutrino oscillation, indicates that neutrinos have a mass. This oscillation process and its detection are the subject of the next two paragraphs.

Neutrino flavour oscillation

In 1962, Maki, Nakagawa and Sakata proposed a theory of flavour mixing of two generations of neutrinos [Mak62]. This theory was based on Pontecorvo's thoughts on the theoretical possibility of neutrino-antineutrino oscillation [Pon57; Pon58; Pon68]. As a direct consequence, the proposed flavour mixing implies neutrino flavour oscillation. According to their theory, the neutrino flavour oscillation is only possible if the neutrino weak interaction eigenstates are a superposition of the neutrino mass eigenstates, but they do not coincide [Zub11]. This proposal was quite promising since previous observations in the quark sector showed that the weak and the mass eigenstates are connected via the Cabibbo-Kobayashi-Maskawa (CKM) matrix [Zub11]. All the following description of the theory of neutrino flavour oscillation is based on [Zub11; Pov15].

The starting point of the theory is that the mass eigenstates $|\nu_i\rangle$ $(i = 1, 2, 3)$ do not coincide with the eigenstates of the weak interaction $|\nu_\alpha\rangle$ $(\alpha = \mathrm{e}, \mu, \tau)$. Instead, the weak interaction eigenstates can be written as a linear combination of the mass states

$$\begin{pmatrix} |\nu_\mathrm{e}\rangle \\ |\nu_\mu\rangle \\ |\nu_\tau\rangle \end{pmatrix} = \begin{pmatrix} U_{\mathrm{e}1} & U_{\mathrm{e}2} & U_{\mathrm{e}3} \\ U_{\mu 1} & U_{\mu 2} & U_{\mu 3} \\ U_{\tau 1} & U_{\tau 2} & U_{\tau 3} \end{pmatrix} \cdot \begin{pmatrix} |\nu_1\rangle \\ |\nu_2\rangle \\ |\nu_3\rangle \end{pmatrix}, \tag{2.5}$$

with U as the Pontecorvo-Maki-Nakagawa-Sakata (PMNS) matrix [Mak62]. This matrix is often parameterised as

$$U = \begin{pmatrix} 1 & 0 & 0 \\ 0 & \cos(\theta_{23}) & \sin(\theta_{23}) \\ 0 & -\sin(\theta_{23}) & \cos(\theta_{23}) \end{pmatrix} \cdot \begin{pmatrix} \cos(\theta_{13}) & 0 & \sin(\theta_{13})e^{-\mathrm{i}\sigma} \\ 0 & 1 & 0 \\ -\sin(\theta_{13})e^{-\mathrm{i}\sigma} & 0 & \cos(\theta_{13}) \end{pmatrix} \cdot \begin{pmatrix} \cos(\theta_{12}) & \sin(\theta_{12}) & 0 \\ -\sin(\theta_{12}) & \cos(\theta_{12}) & 0 \\ 0 & 0 & 1 \end{pmatrix} \tag{2.6}$$

with θ_{ij} as the mixing angles and σ as the CP-violating phase [Bil10; Zub20]. If neutrinos are their own antiparticles, so-called Majorana particles, the above PMNS matrix must be extended by two Majorana phases α_1 and α_2 to

$$U_{\mathrm{Majorana}} = \begin{pmatrix} 1 & 0 & 0 \\ 0 & e^{\mathrm{i}\alpha_1/2} & 0 \\ 0 & 0 & e^{\mathrm{i}\alpha_2/2} \end{pmatrix}. \tag{2.7}$$

For experiments that determine a specific flavour state $|\alpha\rangle$, which is a superposition of the mass eigenstates $|\nu_i\rangle$, the distance between the production and the detection point is crucial. As the

neutrino propagates, the mass eigenstates evolve at different velocities, leading to oscillation. The time evolution of a neutrino with a particular flavour α at the time $t = 0$ and at the position $\vec{x}$ can be expressed as

$$|\nu_\alpha(t, \vec{x})\rangle = \sum_i U_{\alpha i} e^{-\mathrm{i}\left(E_i t - \vec{p}_i \vec{x}\right)} |\nu_i\rangle \,, \tag{2.8}$$

where $E_i = \sqrt{\vec{p}_i{}^2 + m_i^2}$ is the energy, m_i is the mass of the eigenstate $|\nu_i\rangle$ and $\vec{p}_i$ is the angular momentum. Further assumptions, calculations and simplifications lead to the expression for the transition probability P

$$P(\alpha \to \beta) = \sum_{ij} U^*_{\alpha i} U_{\beta i} U_{\alpha j} U^*_{\beta j} \cdot \exp\left(-\mathrm{i}\frac{\Delta m^2_{ij} L}{2E}\right), \tag{2.9}$$

where $\Delta m^2_{ij} = \Delta^2_i - \Delta^2_j$ is the difference between the squared masses and L is the oscillation length. This equation 2.9 shows that

- measurements of the neutrino oscillation are not sensitive to the absolute mass scale, but only to the squared differences and
- neutrino oscillations are possible as long as at least one neutrino mass eigenvalue is not zero and if the weak eigenstates do not coincide with the mass eigenstates.

With regard to the measurement campaigns carried out in the past, which assumed only two neutrino states, this simplification is valid for the targeted sensitivity. Then, equation 2.9 is simplified to

$$P(\alpha \to \beta) = \sin^2 2\theta \cdot \sin^2\left(\frac{\Delta m^2 L}{4E}\right), \tag{2.10}$$

where θ describes the mixing angle between two flavour states and Δm^2 the difference of the squared masses. There are many experiments that study and determine the oscillation parameters with accelerator, atmospheric, and reactor neutrinos [Dre13; Ada14; Abe16; An16; Abe18; Ade18; Ace19; Abi20; Shi20]. In the following, only the difference of the squared masses Δm^2_{12} and Δm^2_{23} is discussed. Experiments have so far only been able to determine a value for the difference of the squared masses. The open questions are the absolute mass scale and the mass hierarchy. Experimental results for the absolute mass scale of the mass eigenstates $|\nu_i\rangle$ are only available from direct neutrino measurements, as described in section 2.1.2. Regarding the order of the three mass eigenstates $|\nu_i\rangle$, three scenarios are still possible and discussed. Only the sign of the Δm^2_{12} is known (positive) due to the Mikheyev–Smirnov–Wolfenstein (MSW) effect [Wol78]. This effect describes how the oscillation conditions for neutrinos change as they travel through dense matter, as is the case for solar neutrinos in the core of the sun.

If the sign of Δm^2_{23} is positive, the neutrino mass eigenstate ν_1 would be the lightest one and the mass states would be arranged in ascending order. If the sign of Δm^2_{23} is negative, the mass eigenstate ν_3 would be the lightest one and the hierarchy would be inverted. If the mass scale turns out to be much larger than Δm^2_{23}, the individual differences would be negligible and the three mass eigenstates would have approximately the same mass. The three possible mass hierarchies are:

- normal: $m_1 < m_2 \ll m_3$,
- inverted: $m_3 \ll m_1 < m_2$ and

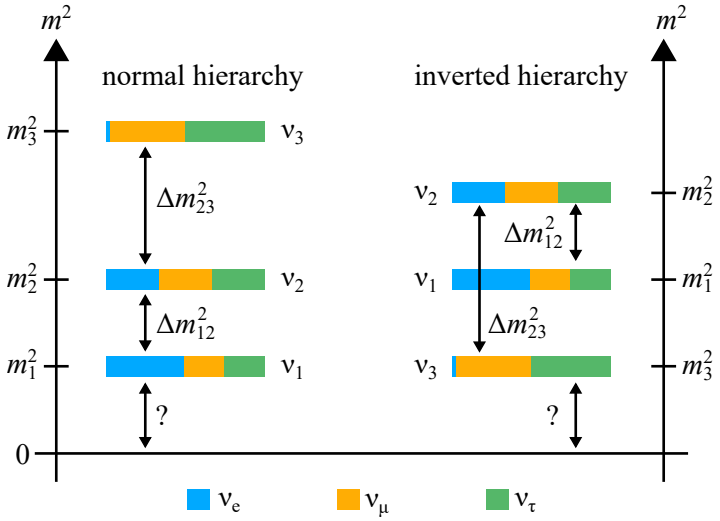

Figure 2.2: Neutrino mass hierarchy. The two hierarchy scenarios are displayed: normal and inverted. In the normal scenario, the masses increase starting with ν_1. The inverted scenario foresees ν_3 as the lightest neutrino. For both scenarios, the absolute scale is unknown. The colours blue, orange and green are the three flavours electron, muon and tauon for the single mass eigenstates. Figure after [Zub20].

- quasi-degenerate: $m_1 \approx m_2 \approx m_3$.

Figure 2.2 shows the normal and inverted mass hierarchy. The two experiments JUNO [An16] and DUNE [Abi20] target to measure the exact mass hierarchy. The global NuFit group [Est20] favours a normal mass ordering.

In the next paragraph, the theoretical concept of flavour oscillation is supported by the discovery of neutrino oscillation by solving the solar neutrino problem.

Solar neutrino problem

Due to the small cross section of the weak interaction, neutrinos are predestined as messenger particles in the context of exploring the universe [Spu15; Bra16; Aar18; Reu22]. As explained above, neutrinos are electrically neutral particles and therefore cannot be deflected by magnetic fields in the galaxy, thus pointing back to their source. In addition, due to the weak interaction, neutrinos can travel long distances without being absorbed by matter. For this reason, neutrinos are called astroparticle messengers, carrying information from their source for a long travel time.

At the end of the 19th century, the absolute flux of the solar electron neutrinos as a test of J. Bahcall's theory of the sun [Bah63; Bah64; Bah01]. Inside the sun, several fusion processes take place simultaneously, producing neutrinos. The two main cycles are the proton-proton (p-p) cycle and the carbon–nitrogen–oxygen (CNO) cycle. The latter contains much heavier elements such as carbon. The neutrino energy spectrum of the p-p solar neutrinos is shown in 2.3. The

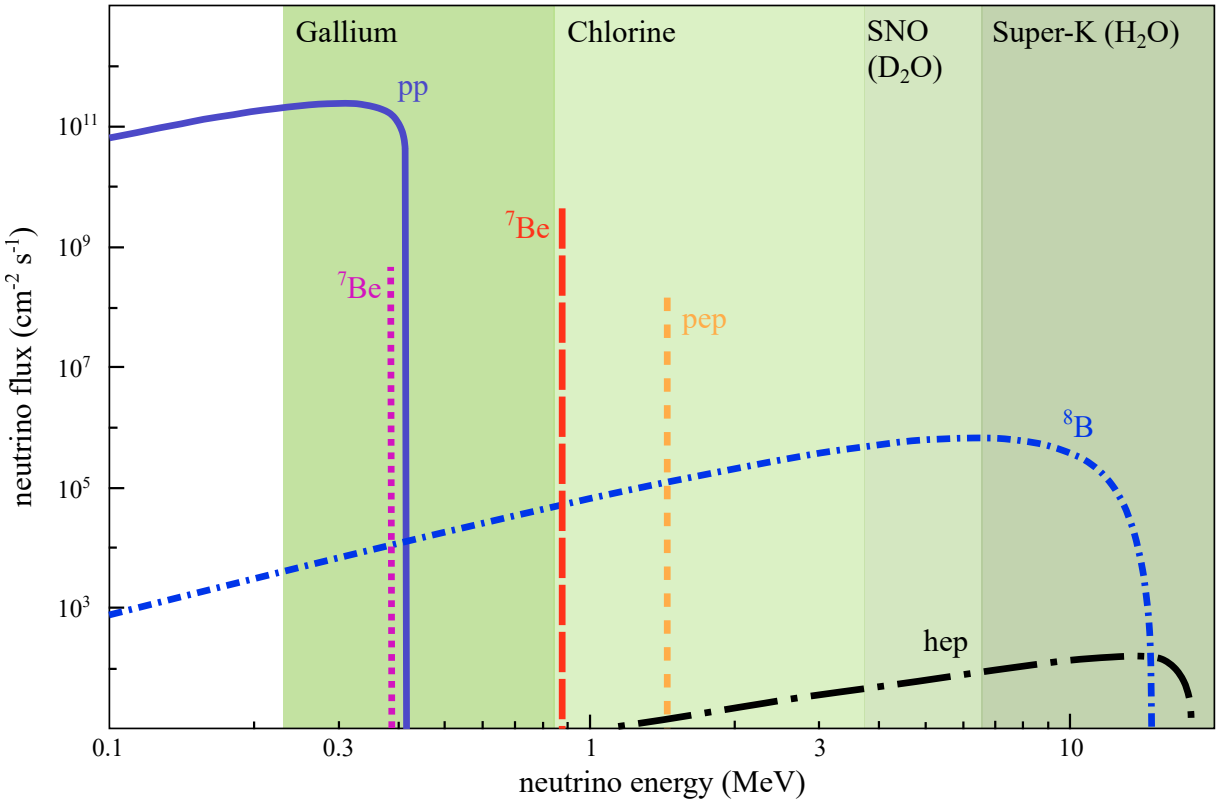

Figure 2.3: Energy spectrum of solar neutrinos from the p-p cycle. The solar neutrino flux for the p-p cycle is plotted as a function of neutrino energy, as predicted by the Standard Solar Model (SSM). The underlying processes are summarised in equation 2.11. In addition, the sensitivity range of the individual detection methods are indicated in different shades of green. According to [Bah96].

underlying processes are

$$\begin{aligned}
\text{pp}: &\quad \mathrm{p} + \mathrm{p} \rightarrow \mathrm{D} + \mathrm{e}^{+} + \nu_{\mathrm{e}} \\
\text{pep}: &\quad \mathrm{p} + \mathrm{e}^{-} + \mathrm{p} \rightarrow \mathrm{D} + \nu_{\mathrm{e}} \\
^{7}\text{Be}: &\quad {}^{7}\mathrm{Be} + \mathrm{e}^{-} \rightarrow {}^{7}\mathrm{Li} + \nu_{\mathrm{e}} \\
^{8}\text{B}: &\quad {}^{8}\mathrm{B} \rightarrow {}^{8}\mathrm{Be}^{*} + \mathrm{e}^{+} + \nu_{\mathrm{e}} \\
\text{hep}: &\quad {}^{3}\mathrm{He} + \mathrm{p} \rightarrow {}^{4}\mathrm{He} + \mathrm{e}^{+} + \nu_{\mathrm{e}}.
\end{aligned} \tag{2.11}$$

The first solar neutrino experiments measured a lower than expected absolute electron neutrino flux from the sun through the p-p and CNO cycles. The Homestake experiment was the first experiment to observe this phenomenon [Dav94]. The results of the Kamiokande-II experiment were also in agreement with the Homestake results [Hir91]. Over the years, newer and more sensitive experiments such as Super-Kamiokande [Hos06] or the Sudbury Neutrino Observatory (SNO) [Ahm01; Ahm02] confirmed the very first results. Meanwhile, the Super-K experiment observed a deficit of atmospheric muon neutrinos ν_{μ}, which was seen as a first indication of the oscillation [Fuk98]. The SNO and Super-K experiments use the same measuring principle, detecting the Cherenkov light, which is emitted when high-energy particles (neutrinos and leptons they produce) travel faster than the speed of light in matter. The Super-K facility uses a huge water tank, surrounded by photomultipliers to detect the Cherenkov light. The SNO uses

instead heavy water D_2O as a moderator. The benefit of heavy water is that it provides more verification possibilities. The three reaction channels [Zub20] are

$$\begin{aligned} \text{CC}: &\ \nu_e + D \rightarrow e^- + p + p - 1.44\,\text{MeV} \\ \text{NC}: &\ \nu_l + D \rightarrow \nu_l + p + n - 2.23\,\text{MeV} \\ \text{ES}: &\ \nu_l + e^- \rightarrow \nu_l + e^-. \end{aligned} \tag{2.12}$$

l indicates any flavour $l = e, \nu, \tau$. At Super-K only the elastic scattering (ES) processes were measured and observed. Due to the smaller effective cross section for ν_μ and ν_τ, mainly the electron neutrino flux was measured. In contrast, the SNO was able to measure all three channels thanks to the heavy water. Therefore, all flavours were measured in their entirety and additionally the electron flux alone. As a result, the total flux of all solar neutrinos matched the expected total rate, and additionally the absence of the electron neutrino was also confirmed. The combination of both SNO and Super-K results [Ahm01; Ahm02] is seen as the proof of neutrino oscillations. This is the evidence that neutrinos are not massless, as originally assumed in the SM. This is a first step towards Physics beyond the SM was made.

The theoretical principle behind the mass generation is explained in the next paragraph.

Neutrino mass generation

With regard to the previous explanations, the discovery of the neutrino flavour oscillation confirms that neutrinos have mass, in contrast to the SM, which originally included massless neutrinos. Originally, only left-handed neutrinos and right-handed antineutrinos were thought to exist. Now, there are three ways to introduce right-handed neutrinos and left-handed antineutrinos in the SM. All following explanations are based on [Pov15; Zub20].

Dirac approach In the SM, all Dirac particles derive their mass from the mass term of the Lagrangian

$$\mathcal{L} = m_D \bar{\psi} \psi, \tag{2.13}$$

with m_D is the Dirac mass of a particle and ψ is the four component Dirac spinor. In the next step, the four-component spinors can be replaced by the two-component Weryl spinors ψ_L and ψ_R to

$$\mathcal{L} = m_D \left(\bar{\psi}_L \psi_R + \bar{\psi}_R \psi_L \right). \tag{2.14}$$

L and R indicate the chirality. The coupling of particles to the Higgs field is the process by which particle mass is produced. For leptons, the Yukawa coupling describes the coupling to the Higgs field through

$$\mathcal{L}_{\text{Yuk}} = -c_l \bar{l}_R \phi^\dagger \begin{pmatrix} \nu_{l,L} \\ l_L \end{pmatrix} + \text{h.c.}, \tag{2.15}$$

with $l = e, \nu, \tau$, ϕ as the Higgs field and c_l as the coupling constant. Implementing the vacuum state of the Higgs field

$$\phi_0 = \frac{1}{\sqrt{2}} \begin{pmatrix} 0 \\ v \end{pmatrix}, \tag{2.16}$$

with v as the vacuum expectation value, the Yukawa term becomes

$$\mathcal{L}_{\text{Yuk}} = -c_l \frac{v}{\sqrt{2}} \left(\bar{l}_{\text{R}} l_{\text{l}} + \bar{l}_{\text{L}} l_{\text{R}} \right), \tag{2.17}$$

where $c_l \frac{v}{\sqrt{2}}$ can be identified with the Dirac mass term m_{D}. The free coupling constant c_l has to be measured. Since there are no right-handed neutrino singlets ν_{R} in the SM, neutrinos are considered to be massless particles. And in this train of thought, a first approach would be to implement an existing ν_{R} singlet as for other fermions, which leads to

$$\mathcal{L}_{\text{Yuk}} = -c_l \bar{l}_{\text{R}} \phi_0^\dagger \begin{pmatrix} \nu_{l,\text{L}} \\ l_{\text{L}} \end{pmatrix} - c_{\nu_l} \bar{\nu}_{l,\text{R}} \tilde{\phi}_0^\dagger \begin{pmatrix} \nu_{l,\text{L}} \\ l_{\text{L}} \end{pmatrix} + \text{h.c.} \tag{2.18}$$

The transformed vacuum state is given by

$$\tilde{\phi}_0 = \frac{1}{\sqrt{2}} \begin{pmatrix} v \\ 0 \end{pmatrix}. \tag{2.19}$$

This derivation leads to a neutrino mass term similar to that for charged leptons, since the mass is proportional to the Higgs vacuum expectation value. In view of the fact that neutrino masses are orders of magnitudes smaller than lepton masses, the coupling constant $\tilde{c}_{\nu_l}$ must be correspondingly different from that for leptons. The main drawback of this derivation is that there is no explanation for the large difference in the coupling constants.

Majorana approach The second approach holds that neutrinos are Majorana particles, i.e. their own antiparticles. The Lagrangian changes to

$$\mathcal{L}_{\text{m}} = \frac{1}{2} m_{\text{M}} \bar{\phi} \phi^c + \text{h.c.}, \tag{2.20}$$

with ϕ^c as the charge-conjugated spinor. The next step is to separate the spinors in their chiral projections

$$\begin{aligned} \mathcal{L}_{\text{M}}^{\text{L}} &= \frac{1}{2} m_{\text{L}} \left(\bar{\phi}_{\text{L}} \phi_{\text{R}}^{\text{c}} + \bar{\phi}_{\text{R}}^{\text{c}} \phi_{\text{L}} \right) \\ \mathcal{L}_{\text{M}}^{\text{R}} &= \frac{1}{2} m_{\text{R}} \left(\bar{\phi}_{\text{L}}^{\text{c}} \phi_{\text{R}} + \bar{\phi}_{\text{R}} \phi_{\text{L}}^{\text{c}} \right). \end{aligned} \tag{2.21}$$

This allows one to identify a right-handed and a left-handed mass term. The advantages of this approach are the restriction that only left-handed neutrinos exist in the SM and the necessity that neutrinos are massive particles by obtaining the Majorana mass m_{L}.

Combination of Dirac and Majorana In the last approach, the Dirac mass term is combined with the Majorana mass term to

$$\mathcal{L} = \frac{1}{2} m_{\text{D}} \left(\bar{\phi}_{\text{L}} \phi_{\text{R}} + \bar{\phi}_{\text{L}}^{\text{c}} \phi_{\text{R}}^{\text{c}} \right) + \frac{1}{2} \left(m_{\text{L}} \bar{\phi}_{\text{L}} \phi_{\text{R}}^{\text{c}} + m_{\text{R}} \bar{\phi}_{\text{L}}^{\text{c}} \phi_{\text{R}} \right) + \text{h.c.} \tag{2.22}$$

and simplified to

$$\mathcal{L}_{\mathrm{m}} = \frac{1}{2}\left(\bar{\phi}_{\mathrm{L}}, \bar{\phi}_{\mathrm{L}}^{\mathrm{c}}\right)\begin{pmatrix} m_{\mathrm{L}} & m_{\mathrm{D}} \\ m_{\mathrm{D}} & m_{\mathrm{R}} \end{pmatrix}\begin{pmatrix} \phi_{\mathrm{R}}^{\mathrm{c}} \\ \phi_{\mathrm{r}} \end{pmatrix}. \tag{2.23}$$

A popular model says, that the left-handed Majorana mass m_{L} is negligible and m_{D} is much smaller than m_{R}. This results in the following equation

$$M = \begin{pmatrix} 0 & m_{\mathrm{D}} \\ m_{\mathrm{D}} & m_{\mathrm{R}} \end{pmatrix}. \tag{2.24}$$

The mass eigenvalues of this matrix are

$$\begin{aligned} m_1 &= \frac{m_{\mathrm{D}}^2}{m_{\mathrm{R}}} \\ m_2 &= m_{\mathrm{R}}\left(1 + \frac{m_{\mathrm{D}}^2}{m_{\mathrm{R}}^2}\right) \approx m_{\mathrm{R}}. \end{aligned} \tag{2.25}$$

In this case, m_1 is recognised as the mass of the light (active) neutrino with masses in the sub-eV region and m_2 is the mass of the heavy right-handed (sterile) neutrino with energies above GeV. This assumption is the basis for the seesaw mechanism [Zyl20].

2.1.2 Overview and recent results of neutrino mass experiments

The discovery of the neutrino oscillation in 1998 confirmed that neutrinos have a non-vanishing mass. This was in contradiction to the SM, which foresees massless neutrinos. This clear evidence for a non-vanishing mass gave rise to a new field of experiments to determine the absolute scale of the mass eigenstates of the neutrinos, although experiments in 1947 [Kon47] and in 1988 [Rob88] had already attempted to measure the neutrino mass. Since neutrinos are only weakly interacting particles, it is a scientific and technical challenge not only to detect them but also to determine their masses.

There are two main strategies to obtain the neutrino mass: the indirect or model-dependent approach and the direct or model-independent approach. Model-dependent approaches include cosmological studies, supernova observations and the neutrinoless double beta decay. The direct methods focus on the shape of the energetic spectrum of the β-electrons. To date, the world's leading limit on the effective mass of the electron (anti)neutrino has been established by the KATRIN experiment [Ake22] with

$$m(\nu_{\mathrm{e}}) < 0.8\,\mathrm{eV} \qquad (90\%\ \mathrm{C.L.}). \tag{2.26}$$

In the following subsections, the different approaches as well as the experimental results are presented.

Indirect, model-dependent approaches

There are several ways to determine the neutrino mass, depending on the model. Currently, only upper bounds are available. A model-dependent approach means that either the assumptions for

the measurement, or for the underlying physics, or for the analysis of the measured data, depend on one or more models. There are three model-dependent approaches, such as cosmological investigations, supernova neutrino observations, and the neutrinoless double beta decay. These three approaches are described in detail and their results are briefly discussed.

Cosmological observations The universe consists of dark energy, cold dark matter and (baryonic) matter. Neutrinos are the most abundant massive particles in the universe [Fuk00] and these massive neutrinos are part of the matter section and are considered to be hot dark matter. They are hot because they travel at the speed of light. They are also thought to be invisible due to their weak interactions. Neutrinos have an impact on the structure formation of the early universe on small scales. According to the SM, the Standard Model of Cosmology ΛCDM describes the evolution of the universe and predicts small neutrino masses.

By studying the cosmic microwave background (CMB), which is a ubiquitous photon signal throughout the universe, or weakly interacting neutrino streams coming out of gravitational potential walls to damp matter fluctuations on small scales [Les12], the combination of the measured and analysed data from the Planck satellite and the Baryon Oscillation Spectroscopic Survey (BOSS) leads to an upper limit for the total neutrino mass

$$\begin{aligned} M_{\text{tot}} &< 0.18\,\text{eV}/\text{c}^2 \qquad \text{(NO)}, \\ M_{\text{tot}} &< 0.21\,\text{eV}/\text{c}^2 \qquad \text{(IO)}, \end{aligned} \tag{2.27}$$

at 95 % C.L. [Upa19]. (NO) indicates normal ordering and (IO) inverted ordering of the mass hierarchy, see also figure 2.2. Other experiments such as the Hubble Space Telescope (HST) [Rie11] or the WiggleZ Dark Energy Survey [Par12] lie in the same region of 200 meV/c^2 [Rie14].

Supernova neutrino observations During the collapse of a core, a massive amount of neutrinos is emitted, with almost 99% of the energy being carried away. By using the time-of-flight method to detect neutrinos coming from the well-known supernova SN1987A from several underground laboratories, such as Kamiokande-II [Hir88], an upper limit of

$$m_\nu < 5.7\,\text{eV}/\text{c}^2 \tag{2.28}$$

was determined [Lor02]. Lamb and Loredo used a Bayesian analysis to derive this value, however many model assumptions have to be made for supernova processes.

Neutrinoless double beta decay Double beta ($2\nu\beta\beta$) decay is a second order process and is therefore suppressed by single beta decay. Double beta decay is the simultaneous decay of two single beta decays according to the reactions

$$\begin{aligned} 2\nu\beta^+\beta^+ &: {}^{A}_{Z}\text{X} \rightarrow {}^{A}_{Z-2}\text{Y} + 2\text{e}^+ + 2\nu_\text{e}, \\ 2\nu\beta^-\beta^- &: {}^{A}_{Z}\text{X} \rightarrow {}^{A}_{Z+2}\text{Y} + 2\text{e}^- + 2\bar{\nu}_\text{e} \end{aligned} \tag{2.29}$$

with Z is the proton number, A is the nucleon number and X and Y are the mother and daughter elements. In 1987 a double beta decay was first observed for the element ^{82}Se as a $2\nu\beta^-\beta^-$ emitter [Ell87]. To date, 35 natural isotopes [Tre02] are known, of which eleven [Zyl20] have been studied experimentally. A special case is the neutrinoless double beta decay, where the neutrino is not

emitted but exchanged (emitted and absorbed) within the nucleus. In this context, the neutrino is described as a mediator particle. This process is only possible if the neutrinos are their own antiparticles, i.e. Majorana particles. The exchange of the neutrino between the two nuclei forces a helicity flip of the neutrino, which means that the neutrino has a mass. The decay energy Q is completely transferred to the two electrons (positrons), since the neutrino does not carry any energy. In the resulting spectrum, a single peak with an energy higher than the endpoint energy E_0 is located above the continuous $2\nu\beta\beta$-spectrum. The effective Majorana neutrino mass is given by

$$|m_{\beta\beta}| = \frac{m_e^2}{G^{0\nu\beta\beta}|\mathcal{M}^{\nu\beta\beta}|T_{1/2}^{0\nu\beta\beta}} = \left|\sum_{i=1}^{3} U_{ei}^2 m_i\right|, \tag{2.30}$$

where $G^{0\nu\beta\beta}$ is the phase factor and $\mathcal{M}^{\nu\beta\beta}$ is the element of the nuclear transition matrix as a function of the half-life time $T_{1/2}^{0\nu\beta\beta}$ of the decay. It represents the sum of the coherent mass eigenstates.

The search for neutrinoless double beta decays has led to a new field of experimental research. There are many possible elements, but for experimental reasons, only those elements are used in which the single beta decay is energetically forbidden, in order to reduce possible background fluctuations. The most promising results have been obtained with ^{76}Ge (GERDA [Ago19], MAJORANA [Alv19]) and ^{136}Xe (EXO [Ant19], KamLAND-Zen [Shi17]) and ^{100}Mo (SuperNEMO [Arn19]). The best results for the upper limits are achieved by combining the data from GERDA [Ago19] and KamLAND-Zen [Shi17]

$$\begin{aligned} \text{GERDA} &: |m_{\beta\beta}| < 70\,\text{meV/c}^2\text{to}160\,\text{meV/c}^2\ \left(^{76}\text{Ge}\right), \\ \text{KamLAND}-\text{zen} &: |m_{\beta\beta}| < 61\,\text{meV/c}^2\text{to}165\,\text{meV/c}^2\ \left(^{136}\text{Xe}\right). \end{aligned} \tag{2.31}$$

As mentioned in the previous sections, due to CP-violation and the two additional phases of the mixing matrix U for Majorana neutrinos, the contributions from the mass eigenstates can cancel out. This leads to a possible vanishing of the $|m_{\beta\beta}|$. Inevitably, this leads to the conclusion that only direct measurements of the neutrino mass are useful for determining the neutrino mass eigenstates $|\nu_i\rangle$.

Direct, model-independent approaches

Model-independent approaches focus on the kinematic spectrum of the β-electrons and its calculations, since the shape of the spectrum is mass dependent. For the calculations, it is important to remember that the endpoint energy E_0 is the maximum energy an emitted electron can receive. The endpoint energy E_0 is directly related to the decay energy Q, which is the difference in mass between the mother and the daughter atoms. For massive neutrinos, $E_0 < Q$ means that the rest mass of the neutrino cannot be transferred to the kinetic energy of the beta electron. Based on Fermi's golden rule, the shape of the differential β-spectrum is

$$\frac{\mathrm{d}\Gamma}{\mathrm{d}E} = \frac{G_F^2 \cdot \cos^2\theta_C}{2\pi^3}|\mathcal{M}|^2 \cdot F(Z,E)p(E+m_e)\sum_{i=1}^{3}|U_{ei}|^2\epsilon\sqrt{\epsilon^2-m_i^2}\cdot\Theta(\epsilon-m_i), \tag{2.32}$$

with G_F is the Fermi coupling constant, θ_C is the Cabbibo angle, $\mathcal{M}$ is the nuclear transition matrix element, and $\epsilon = E_0 - E$ is the energy difference with respect to the endpoint energy

E_0. The Heaviside step function Θ guarantees the energy conservation. Assuming the quasi-degenerated neutrino mass hierarchy (see subsection 2.1.1), the measuring observable is the incoherent sum of the mass eigenstates

$$m_\nu^2 = \sum_{i=1}^{3} |U_{ei}|^2 m_i^2, \tag{2.33}$$

which is the effective squared electron neutrino mass [Kle19].

Not every β-electron emitter is suitable for direct neutrino mass research. On the one hand, the energy endpoint E_0 should not be high, since the count rate is even lower in this region. On the other hand, too low endpoint energies produce spectroscopically unmeasurable electrons. A short lifetime and a high activity are also required to obtain a sufficiently high count rate. The three most promising candidates are tritium, rhenium, and holmium. Holmium ^{163}Ho is used in the ECHo [Gas17] and Holmes [Nuc18] experiments, which have not yet achievd an upper limit. Rhenium ^{187}Re is used in the MIBETA experiment [Dvo11], which determined an upper limit of

$$m_\nu < 15\,\mathrm{eV/c^2} \tag{2.34}$$

by using cryogenic microcalorimeters [Sis04]. The major advantages of using tritium (T or ^{3}H) are

- its short lifetime of 12.32 y [Bas09],
- its low endpoint energy of $E_0 = 18.57\,\mathrm{keV}$ [Ake22],
- only one outer electron, so that there is no Coulomb interaction within the atomic shell,
- its β-decay is a super-allowed transition from $J = 1/2 \rightarrow J = 1/2$, hence the nuclear matrix transition element $\mathcal{M}$ is energy-independent, and
- its gaseous state, as it eliminates losses due to solid-state effects.

Therefore, the current best limit is held by KATRIN using a gaseous high luminosity molecular tritium source

$$m_\nu < 0.8\,\mathrm{eV/c^2} \qquad (90\%\ \mathrm{C.L.}). \tag{2.35}$$

A drawback is that tritium exists in its natural molecular state, which introduces systematic effects on the final states as electronic or rotational excitations in the eV-range. Project8 aims to use atomic tritium in cold traps and measure the electron energy released using the new technique of cyclotron radiation emission spectroscopy [Ash22].

In the next section, the KATRIN experiment, in particular the measuring principle, is presented in detail.

2.2 The Karlsruhe Tritium Neutrino (KATRIN) experiment

In the previous section, an overview was given of the fundamentals of neutrino physics and its importance for the SM as well as for the understanding of the universe (cosmology). The focus was on experiments to determine the absolute mass scale of neutrinos. The KATRIN experiment is one of these experiments and currently holds the world's leading neutrino mass limit of $0.8\,\mathrm{eV/c^2}$ (90 % C.L.). Therefore, the second part of this chapter deals with the KATRIN

experiment in detail. First, in section 2.2.1, the general working principle of how KATRIN determines the mass of the electron antineutrino is explained. This is followed by a more detailed description of the source of the experiment, including the 30 K cold beam tube, where the tritium decays take place, and the inner loop system for the tritium infrastructure. The last part of this chapter 2.2.3 concludes with the current status and results on the upper limit of the neutrino mass measured with KATRIN.

2.2.1 Measuring principle and overview of the experimental setup

The predecessor neutrino mass experiments at Troitsk [Ase11], Mainz [Kra05] and Los Alamos [Rob91] set an upper limit of $2\,\mathrm{eV/c^2}$ for the electron neutrino mass. Based on the results and the knowledge from these experiments, KATRIN was designed to improve the sensitivity by an order of magnitude to $0.2\,\mathrm{eV/c^2}$ with 90 % C.L. within a total net measurement time of three years. Starting in the early years of the 21st century with the design and construction phase [Ang05], it took more than 15 years until the first tritium campaigns were performed with KATRIN in 2018 [Ake20a].

As explained in section 2.1.2, there are different ways to determine the absolute scale of the effective neutrino mass m_{ν_e}. The KATRIN experiment uses a direct, model-independent approach by measuring the shape of the β-energy spectrum of molecular tritium T_2[1]. The decay of molecular tritium T_2 follows the equation

$$T_2 \longrightarrow \left({}^3\mathrm{HeT}^+\right) + e^- + \bar{\nu}_e, \tag{2.36}$$

with

- $\left({}^3\mathrm{HeT}^+\right)$ as the meta-stable, molecular state of a helium-tritium ion,
- e^- as the beta electron and
- $\bar{\nu}_e$ as the corresponding electron antineutrino.

The derivation of the function of the differential tritium energy spectrum (see equation 2.32) and its interpretation is discussed at length in the previous section 2.1.2. To recapitulate the result, the effect of a non-zero neutrino mass on the β-spectrum is significant only close to the endpoint where $E \approx E_0$ and hence the observable of the neutrino mass squared $m(\nu_e)^2$ becomes clear. This means that the desired improvement in sensitivity by one order of magnitude results in an improvement by a factor 100. To achieve this goal, three requirements are essential:

- A high-luminosity tritium β-source with an activity of about $1.7 \cdot 10^{11}$ Bq to reach a sufficiently high count rate in the endpoint region of $E_0 - 30\,\mathrm{eV}$ and $E_0 + 5\,\mathrm{eV}$.
- An electrostatic high-pass filter as spectrometer with sub-eV energy resolution at 18.6 eV.
- Systematic effects need be fully characterised and finally taken into account in the data analysis.

To meet these requirements and to fulfil the design sensitivity, the two main components of KATRIN are a high-luminosity windowless gaseous tritium source (WGTS) and a MAC-E type tandem spectrometer setup for energy analysis. These two components as well as the remaining experimental setup are briefly presented. All explanations and descriptions of the experimental

[1] The benefits of tritium as an electron source are presented in section 2.1.2.

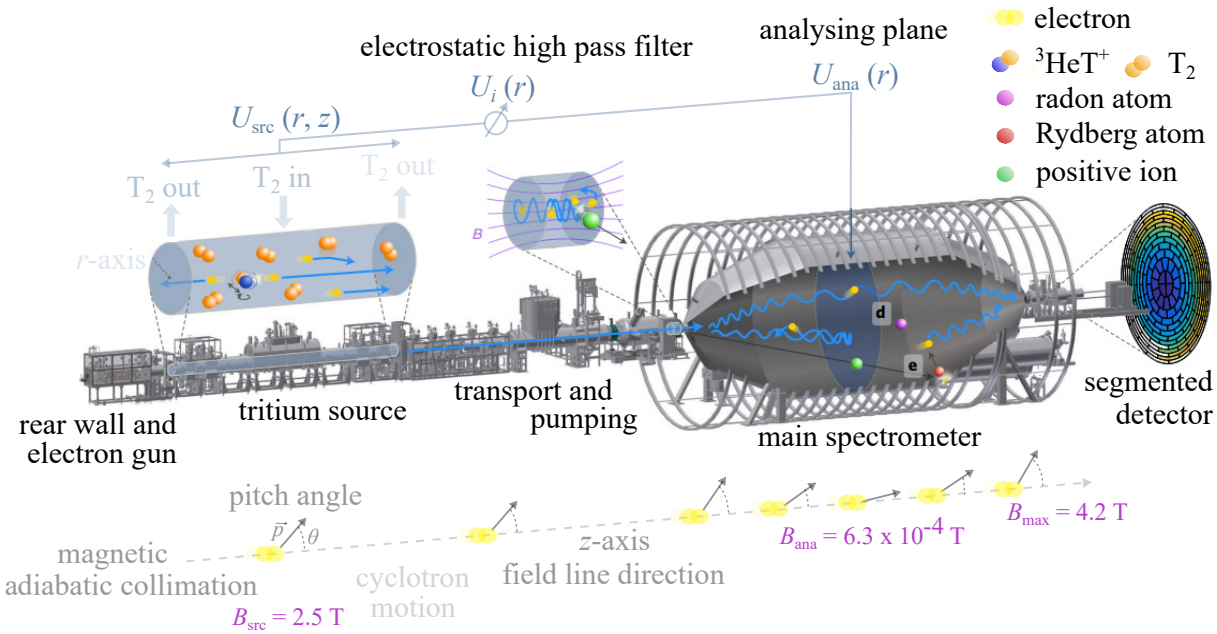

Figure 2.4: The Karlsruhe Tritium Neutrino (KATRIN) beamline. The figure shows the 70 m long KATRIN beamline and its main components. Starting on the left with the **rear section** with the rear wall and the electron gun, followed by the **windowless gaseous tritium source (WGTS)** as the tritium source, the **differential pumping section** and **cryogenic pumping section**, both forming the transport section, entering the **pre-spectrometer** and then the **main spectrometer**, the beamline ends with the segmented **detector** on the right. A detailed description of the individual components is given in the text. In addition, the principle of the magnetic adiabatic collimation is shown at the bottom, illustrating the movement of the electron and the transformation of the transversal into the longitudinal component of the kinetic energy. At the top of the figure, the basics of the electrostatic high-pass filter are visualised.

setup and the underlying physics are based on the KATRIN design report [Ang05] and the updated version [Ake21]. Figure 2.4 shows the entire KATRIN setup with the 70 m long beamline. The main components are the WGTS, followed by the transport and pumping sections with a differential pumping section (DPS) and a cryogenic pumping section (CPS). This is followed by the pre- and main spectrometer with the MAC-E filter and finally the segmented focal plane detector (FPD). At the other end of the beam tube is the rear section (RS) for monitoring and calibration purposes. As mentioned above, KATRIN measures the count rate of the β-electrons produced by the decay of molecular tritium.

The following paragraphs describe the path an electron would take along the KATRIN beamline.

Windowless gaseous tritium source Molecular tritium T_2 is injected through a capillary at a constant flow of 1.8 mbar l s^{-1} into the centre of the WGTS cryostat, so that a linear first-order pressure profile is obtained. Most of the injected tritium is directly pumped out at the pump ports at both ends of the WGTS. The pumped away tritium is returned to the inner tritium loop system, which is a closed tritium cycle. See the next section 2.2.2 for more information. The generated β-electrons leave the WGTS adiabatically on both sides due to the seven magnet modules surrounding the beam tube. For more detailed information on the cryogenic design see [Gro08] and for the operating principle of the WGTS see [Hei17].

Transport and pumping section Towards the detector, the electrons enter the transport section, which has two functions. The first is to guide the β-electrons adiabatically from the source to the spectrometer and the second is to prevent any other molecules, especially tritiated molecules and ions, from entering the spectrometer section. The reason for this is that tritium decaying inside the spectrometer vessel at the same potential as the vessel, would cause a false signal and increase the background. Two different transport sections were therefore designed. The main tasks of the differential pump section **(DPS)** can be summarised as follows [Luk12]:

1. to reduce the tritium flow by five orders of magnitude,
2. to transport adiabatically the electrons to the spectrometer section and
3. to block all kinds of ions as T_3^+.

The special feature of the DPS is its curved beamline, so that there is no direct path from the source to the detector. The DPS consists five 1 m long elements inclined at 20° to each other, with a molecular turbo pump between them. Each segment contains a superconducting magnet of 5.5 T. In this arrangement, neutral molecules and atoms are blocked directly by hitting the wall of the first segment. Charged electrons are guided along the magnetic field to the next transport section. The remaining (tritiated) ions must not only be blocked, but also analysed to quantify the ion blocking methods. Three methods are briefly mentioned here [Kle17; Kle18; Mar21]:

1. Ring electrodes with +100 V counter voltage are installed in beam tube five and pump port five (located between DPS and CPS).
2. One dipole electrode per element one to four is installed to remove reflected ions from the flux tube due to an $\vec{E} \times \vec{B}$ drift. The ions hit the stainless steel walls and are neutralised.
3. A Fourier transform ion cyclotron resonance (FT-ICR) is installed downstream of beam tube element five to analyse the remaining amount of different ion species.

However, not all neutral and ionised molecules are blocked or trapped and then pumped away.

As a final barrier, the cryogenic transport section **(CPS)** [Gil10; Röt17] is 7 m long and consists of seven single beam tube elements equipped with seven superconducting magnets of about 5.6 T [Gil17] to guide the β-electrons adiabatically to the spectrometer. There is only one inclination of 15° between elements two and four. The walls of the CPS elements two to five are cooled down to 3 K and covered with an argon frost layer. This prevents neutral tritium molecules from following the magnetic field lines and hitting the walls, where they are cold-trapped, instead. Every 60 days the argon frost has to be renewed by increasing the temperature of the beam tube. During these 60 days, approximately 1 Ci of tritium will accumulate on the frost layer under nominal KATRIN conditions. As an aside, this is the reason why a typical KATRIN measurement campaign cannot last longer than these 60 days. The β-electrons leaving the CPS can now enter the spectrometer section. In addition to this way of leaving the WGTS, the β-electrons also have the possibility to leave the WGTS on the opposite side towards the rear section.

Rear section The β-electrons from the WGTS hit the gold-coated rear wall. The rear section is used to terminate the beam tube and for monitoring and calibration purposes. The rear section contains an electron gun (e-gun) that produces electrons with a well defined energy and angle [Bab12; Bab14; Sch16]. The maximum rate is $1 \cdot 10^4\,e^-\,s^{-1}$ by illuminating a cathode with UV

light. These electrons are used to measure the energy-loss function due to electron scattering, to monitor the column density and to measure the transmission function of the spectrometers pixel by pixel. The β-electrons hitting the gold coated rear wall produce bremsstrahlung, which is analysed by Beta Induced X-ray Spectrometry (BIXS) system [Röl13]. This allows the WGTS activity to be measured to a 0.1 % level within 70 s.

Spectrometer section The pre- and the main spectrometers are based on the MAC-E principle and are arranged in a tandem configuration. This type of spectrometer was first introduced by [Kru83] and also implemented in the neutrino mass experiments in Mainz and Troitsk [Lob03; Kra05; Ase11]. The reason for using such a MAC-E filter is its high energy resolution combined with a large acceptance angle for the β-electrons. For KATRIN, this is important due to the isotropic emission of the β-electrons created in the source beam tube. A typical MAC-E filter requires a vacuum vessel and two strong magnets, one at the entrance and one at the exit. The β-electrons coming from the source perform spiral trajectories around the magnetic field lines due to their cyclotron motion. The total kinetic energy of the β-electrons is divided into a longitudinal and in a transverse component. By entering the main spectrometer with a high magnetic field, the transversal component of the kinetic energy is transferred to the longitudinal component. This is because the magnetic field decreases from the entrance to the centre of the spectrometer and at the same time the magnetic moment

$$\vec{\mu} = \frac{e}{2 \cdot m_\mathrm{e}} \cdot \vec{L} \tag{2.37}$$

is conserved, where e is the electric charge, m_e is the mass of the electron and $\vec{L}$ is the angular momentum. The magnetic field strength is therefore lowest in the centre of the spectrometer, the analysing plane, and the electrostatic retarding potential is highest. In the ideal case, the magnetic field strength in the centre of the vessel drops to zero, so that a complete conversion of the transversal component into the longitudinal component of the kinetic energy is possible, see also the lower part of figure 2.4. β-electrons with a longitudinal kinetic energy higher than the retarding voltage can pass the analysing plane and are re-accelerated to their previous energy at the exit of the spectrometer.

According to the following equation

$$\frac{\Delta E}{E} = \frac{B_\mathrm{A}}{b_\mathrm{max}} \tag{2.38}$$

where

- $B_\mathrm{A} = 3 \cdot 10^{-4}\,\mathrm{T}$ is the magnetic field strength in the analysing plane,
- $B_\mathrm{max} = 6\,\mathrm{T}$ is the maximum magnetic field at the entrance and exit of the spectrometer vessel and
- $E = 18.6\,\mathrm{K}$ is the retarding voltage

the energy resolution for KATRIN is $\Delta E = 0.93\,\mathrm{eV}$.

Detector section The FPD counts the β-electrons that have sufficient kinetic energy in the longitudinal component to exceed the retarding potential. The detector is a silicon waver consisting of 148 pixels with a total diameter of 0.09 m. Its energy resolution is (1.52 ± 0.01) keV

with a detection efficiency of (95 ± 1.8 ± 2.2) %. The maximum count rate is limited to 100 kcps during a standard 1 cps tritium campaign [Ams15; Mer19].

All the described components have been successfully commissioned, so that first tritium measurements were possible [Ake21]. In order for KATRIN to be able to measure the neutrino mass with a sensitivity of 0.2 eV/c^2, the entire system must work as designed. In the next section, the source of the KATRIN experiment is presented in more detail, in particular the tritium supply, the closed tritium cycle of the Tritium Laboratory Karlsruhe (TLK).

2.2.2 The KATRIN tritium source loop

After the general overview of the working principle and the main components of the KATRIN experiments, a detailed description of the tritium source system is part of this section. This additional focus on the tritium source system is necessary because the present work deals specifically with this part of the experiment.

There are only a handful of civilian tritium laboratories in the world. The Tritium Laboratory Karlsruhe (TLK) is a semi-technical scale facility and the only one with the necessary scientific and technical expertise to handle large quantities of tritium on the one hand and with the technical infrastructure to store, process, analyse and recycle tritium[2]. This is the reason why KATRIN is located next to the TLK, as it requires a tritium throughput of 40 g d^{-1}.

Figure 2.5 shows a simplified flow chart of the KATRIN tritium loop system, which is described in detail in [Kaz08; Pri15; Stu21]. The whole tritium loop system can be divided into three sub loops: the circulation loop, the feed loop and the exhaust loop. The circulation loop includes parts of the KATRIN experiment and is the starting point for describing a complete cycle of tritium within this loop system. Starting from the 2 l buffer vessel, a gas mixture containing mainly molecular tritium T_2 flows through an adjustable flow controller. In the next step, the gas passes through an optical cell, the so called LARA cell. In this cell, the concentration of the gas composition is measured by inelastic light scattering based on Raman spectroscopy[3]. The gas mixture then enters a pressure and temperature controlled and stabilised vessel with a volume of 15 l. After leaving the vessel, the gas mixture flows through the transfer line and the ≈ 5 m long capillary and is injected into the centre of the WGTS source tube in the injection chamber, see figure 2.6. The injection chamber has 415 orifices, through which the gas stream diffuses into the beam tube, to achieve uniformity. The capillary and the injection chamber are thermally coupled to the beam tube, which is operated at 30 K. The WGTS beam tube is 10 m long and 90 mm in diameter. The injected gas distributes to both sides and forms an almost rectangular density profile along the WGTS source tube at a column density of $5 \cdot 10^{17}$ molecules /cm^2, see lower part of figure 2.6. Most of the injected gas is directly pumped away by fourteen turbomolecular pumps (TMPs) of the type Leybold MAG W2800 located at each end of the WGTS. The unpumped gas flows to the DPS or to the RS. The vented gas is transferred to a permeator by a HiPace300 and a combination of Normetex and a metal bellows. The permeator is a palladium membrane filter that allows only hydrogen isotopologues to pass. To prevent clogging of the permeator by impurities, such as tritiated methane from the walls or helium from the decay, a constant amount of gas "bleed", including tritium, is processed to a 106 l

[2] The TLK has a license of 40 g tritium to process.

[3] The Raman effect describes a wavelength shift due to inelastic scattering of light by molecules. Each molecule has characteristic lines in the detected spectrum [Lon02].

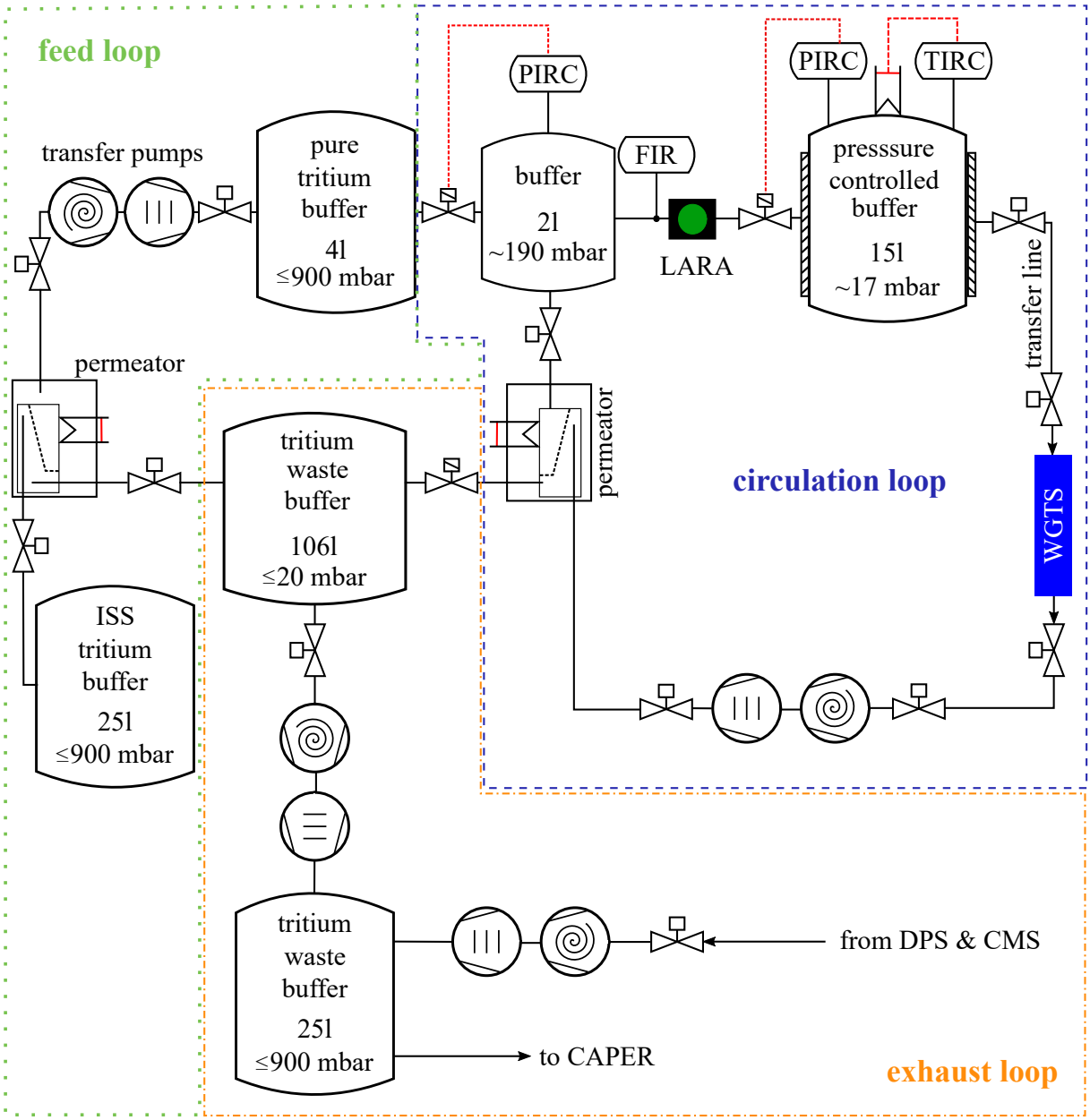

Figure 2.5: Flow chart of the KATRIN tritium loop system. The tritium loop system consists of three individual loop systems. The circulation loop (dashed line) as the main part, the feed loop (dotted line) for fresh tritium supply and the exhaust loop (dashed-dotted line) for waste gas collection. The abbreviation PIRC stands for a **p**ressure sensor with **i**ndication whose data is **r**ecorded and which **c**ontrols a valve. For TIRC, it is a temperature sensor controlling a heater. Figure according to [Stu21].

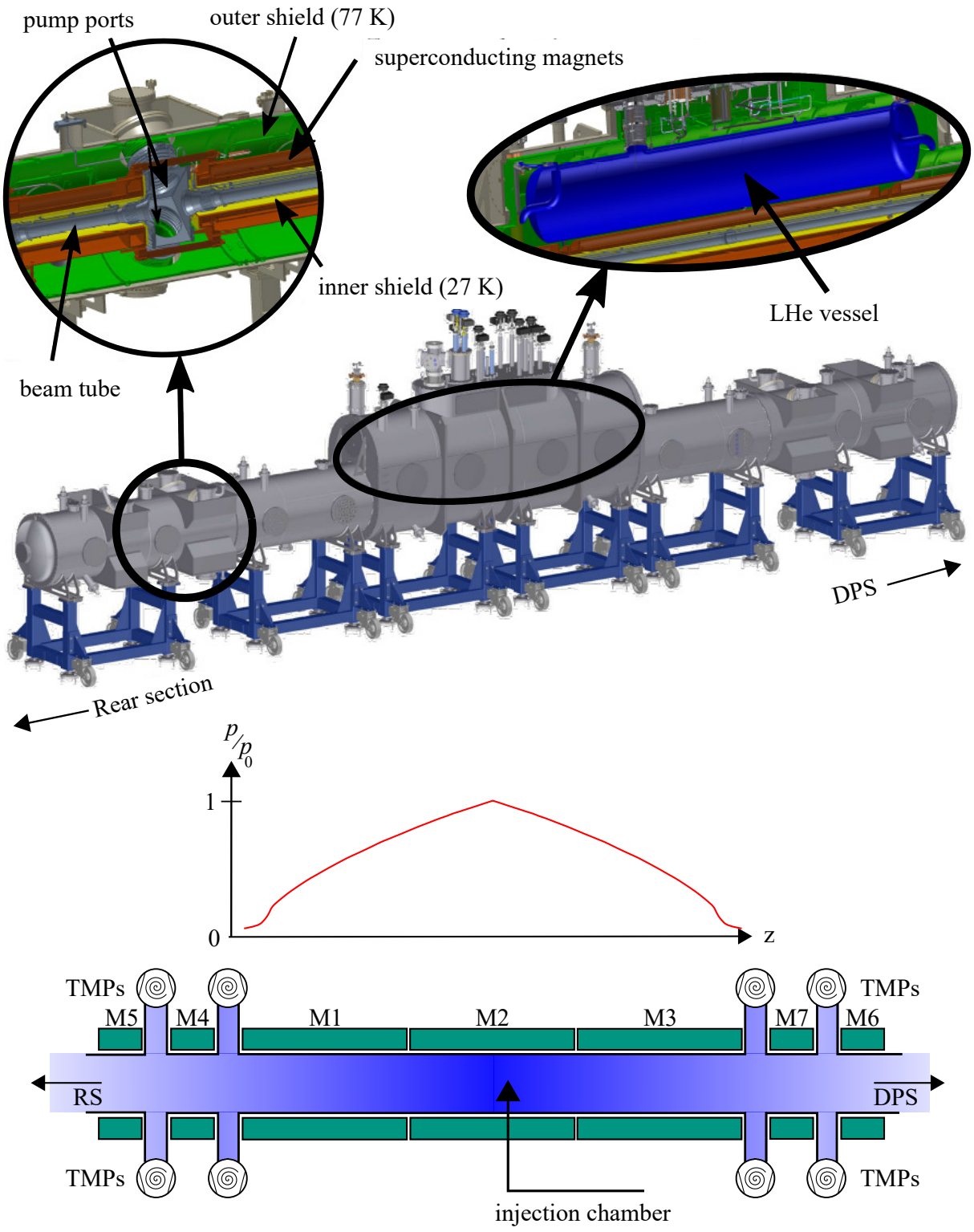

Figure 2.6: Windowless gaseous tritium source (WGTS): drawing and pressure profile. The upper part shows the 16 m long, 4 m high and 1.5 m wide cryostat, which is in fact the WGTS [Gro08]. The two smaller extracts show the different cooling shields of the cryostat. The outer shield (highlighted in green) is cooled down with liquid nitrogen from a 10^6 l big reservoir, shown on the right side, to 77 K. The superconducting magnets (shown in red) are surrounded by the outer shield and cooled down to 4 K. The next layer, the inner shield (shown in yellow), is cooled down to 27 K. This inner shield ensures a beam tube temperature of 30 K with a stability of 0.1 %. The stabilisation of the beam tube is achieved by two copper tubes brazed to the source beam tube, which directly couple it to a two-phase neon thermosyphon [Gro09]. In the lower part, molecular tritium T_2 is injected into the centre of the beam tube and pumped out through eight pump ports (blue colour gradient). this results in an almost rectangular molecular density profile is reached (red curve). The beam tube is surrounded by seven superconducting magnet modules of 3.6 T and 5.6 T.

tritium waste buffer vessel. This constant bleed is replenished with fresh tritium gas from the pure tritium buffer vessel. This is how a typical tritium circulation through the WGTS beam tube looks like.

In the exhaust loop, the waste gas is collected together with the exhaust gases from the other components (DPS & CPS) in an additional buffer vessel and sent to the TLK internal recycling facility CAPER[4].

In the feed loop, fresh and pure tritium is prepared within the TLK internal isotope separation system (ISS) and sent via a palladium membrane filter (permeator) to a 4 l pure tritium buffer vessel.

In summary, the entire loop system consists of 33 TMPs, 4 Normetex/metal bellows, ≈ 220 sensors and ≈ 230 valves. This description of the tritium loop system of KATRIN shows why an additional tritium laboratory with the appropriate infrastructure is essential.

The KATRIN experiment determines the effective mass of the electron antineutrino with a sensitivity of 0.2 eV/c^2 at 90 % C.L. The effect of a non-vanishing neutrino mass has its maximum near the kinetic endpoint of the β-spectrum. Since only a fraction of $2 \cdot 10^{-13}$ decay electrons is in the last 1 eV region, a strong and long term stable (on a 0.1 % level for the whole WGTS setup) tritium source is required. This results in the following requirements for the WGTS resultant.

- To achieve the desired column density of $5 \cdot 10^{17}$ molecules /cm^2 on the 0.1 % level, a constant injection rate of 1.8 mbar l s^{-1} (equivalent to $1.7 \cdot 10^{11}$ Bq or 40 g d^{-1} tritium) is required.
- The temperature set point of the soure beam tube is 30 K.
- A high isotopic purity with ≥ 95 % of tritium due to possible influences of different hydrogen isotopologues.
- Constant pumping and recycling of the tritium gas to ensure a stable injection rate.

The tritium source is more than just the WGTS with its beam tube. It is a complex system of three closed tritium cycles to allow the circulation of pure tritium at a specific flow rate through the WGTS source tube, through the pumps and the permeator. The requirement for long term stability at the 0.1 % level makes it even more challenging. Connection to the TLK infrastructure is necessary to provide the required amount of pure tritium and the ability to recycle it.

2.2.3 Current status and first measurement results

In summer 2017, the KATRIN beamline was successfully commissioned [Are18b]. In the mid-2018, the first operation with deuterium D_2 and small amounts of tritium $(5 \cdot 10^8$ Bq) was performed [Ake20a]. It was shown that KATRIN, in particular the ion blocking systems, work as designed, and first spectra were taken. The first KATRIN neutrino mass (KNM1) measurement campaign started in 2019 with a reduced activity of $2.5 \cdot 10^{10}$ Bq. The aim of this campaign was to "train"materials by exposing them to large amounts of tritium. For the first time, a new upper limit for the absolute neutrino mass was set at 1.1 eV. The KNM2 measurement campaign was the first run with a nominal activity of $9.5 \cdot 10^{10}$ Bq. Due to major technical achievements, such

[4] CAPER is the abbreviation for **CA**PRICE **PER**MCAT at the TLK and is evolved from the experiment CAPRICE (**Ca**talytic **P**u**r**i**f**ic**a**tion **E**xperiment). CAPER demonstrated the feasibility of a two step clean-up process for fusion reactor exhaust gases [Bor05].

as improved vacuum conditions in the main spectrometer [Are16], a new upper limit of 0.7 eV at 90 % C.L. was achieved Combining the results of KNM1 and KNM2, KATRIN sets the upper limit for the absolute electron antineutrino mass to

$$m_\nu < 0.8\,\mathrm{eV/c^2} \qquad (90\%\ \mathrm{C.L.}). \tag{2.39}$$

It is estimated, that KATRIN will reach its design sensitivity of $0.2\,\mathrm{eV/c^2}$ by 2025. By that time, the tritium loop systems and all associated TLK infrastructure will have processed $\approx 50\,\mathrm{kg}$ of pure tritium T_2 [Pri20].

3 Intermolecular effects in the tritium source loop and their influence on the neutrino mass determination

The KATRIN experiment aims to measure the mass of the electron antineutrino $m_{\bar{\nu}_e}$ with a projected sensitivity of $0.2\,\mathrm{eV/c^2}$ (C.L. 90 %) which corresponds to a 5σ discovery potential of $0.35\,\mathrm{eV/c^2}$. This targeted sensitivity value of $0.2\,\mathrm{eV/c^2}$ is a factor of 10 improvement over previous direct neutrino mass experiments in Troitsk [Ase11] and Mainz [Kra05]. To achieve this sensitivity, it was clear from the very beginning of KATRIN that, among other things, it is only possible if all systematic uncertainties are known, understood and quantified. For this reason, the KATRIN design report of 2004 [Ang05] devotes a large part of the report to the systematic effects, in addition to the design, the working principle and the foreseen measurement campaigns.

The chapter is structured as follows. In section 3.1, the current status of the systematic uncertainty budget with the individual effects and their contribution is presented. The final-state distribution as a major systematic effect is discussed in detail in section 3.2, followed by the thermal cycle in the KATRIN tritium source loop in section 3.3. Regarding the molecular effects, the temperature dependence of the chemical and op equilibrium is described in section 3.4. How the gas composition changes towards the equilibrium states is presented in section 3.5 for internal reactions and in section 3.6 for external reactions. Finally, based on the previous explanations and the results, the scientific goal of this thesis is explained in section 3.7.

3.1 Overview of the systematic effects in the KATRIN experiment

According to the design report [Ang05], the projected sensitivity and the 5σ discovery potential are derived from the following two assumptions: First, there are five major systematic uncertainties of at most

$$\Delta m_\nu^2 = 7.5 \cdot 10^{-3}\,\mathrm{eV^2/c^4}, \tag{3.1}$$

each of them contributing to the total systematic uncertainty budget. Adding them quadratically as independent systematic effects without correlation leads to the total systematic uncertainty

$$\sigma_{\mathrm{sys}} = 0.017\,\mathrm{eV^2/c^4}. \tag{3.2}$$

Secondly, the statistical uncertainty is calculated for a three year measurement period with a background signal of 10 mcps in a measurement interval of $[E_0 - 30\,\mathrm{eV}, E_0 + 5\,\mathrm{eV}]$ to

$$\sigma_{\mathrm{sta}} = 0.018\,\mathrm{eV^2/c^4}, \tag{3.3}$$

balancing the systematic uncertainty. This gives a total uncertainty of

$$\sigma_{\mathrm{tot}} = \sqrt{\sigma_{\mathrm{sta}}^2 + \sigma_{\mathrm{sys}}^2} = 0.025\,\mathrm{eV^2/c^4}. \tag{3.4}$$

The KATRIN sensitivity is therefore calculated as

$$L(90\,\%\,\text{C.L.}) = \sqrt{1,64 \cdot \sigma_{\text{tot}}} \approx 0.2\,\text{eV/c}^2 \tag{3.5}$$

and the discovery potential as

$$L(5\sigma) = \sqrt{5 \cdot \sigma_{\text{tot}}} \approx 0.35\,\text{eV/c}^2. \tag{3.6}$$

Within the design report, the systematic effects are treated in different ways and can thus be assigned to three groups. The first group includes most of the effects mentioned, which are already known from previous experiments, e.g. the Doppler effect, and therefore, dedicated simulations or measurements under KATRIN-like conditions are proposed to determine their contribution. Other systematic effects are considered to be negligible based on experience from previous experiments or the literature knowledge at the time, e.g. the absence of tritiated molecular clusters in the WGTS below 30 K, forming the second group. A third group is concerned with new systematic effects, which have become apparent for the first time due to the measuring principle of KATRIN and the improved sensitivity, e.g. synchrotron radiation [Sei19]. For these effects, simulation studies and/or dedicated measurements are proposed. The condensed knowledge from 17 years of research to improve the understanding of the original design report [Ang05] can be found in the work of Seitz-Moskaliuk [Sei19] and is recapitulated in table 3.1. This table represents the state of knowledge at the beginning of this work. As can be seen, several of these systematic effects (marked with the * symbol), such as the source magnetic field, the trapped electrons in the WGTS, the gas dynamics in WGTS, and the monitoring of column density, are directly related to the tritium source of KATRIN. Within this work, the focus is uniquely on source systematic effects caused by the hydrogen molecules and especially by their intermolecular reactions within the tritium source loop (WGTS and closed tritium loop, see section 2.2.2) of the KATRIN experiment. Therefore, the influence of the molecular effects is shown using the example of the final-state distribution.

3.2 Final-state distribution in the context of molecular effects

In the previous section, it was shown that the systematic effects are numerous, diverse and located along the entire KATRIN beamline. The source-related systematic effects and especially those influenced by molecular effects are an essential part of this work. In the following, this relationship will be illustrated using the example of the final-state distribution, as this is an important systematic effect which, according to table 3.1, is still in progress.

Since KATRIN determines the mass of the electron antineutrino $m_{\bar{\nu}_e}$ by studying the shape of the β-spectrum near to its energetic endpoint, and since the shape depends on the distribution of the energy released in the excitations of the daughter molecules, it is necessary to understand the molecular final-state distribution for all three tritiated molecules T_2, DT, HT and their corresponding daughter molecules $^3HeT^+$, $^3HeD^+$ and $^3HeH^+$. Due to the molecular appearance, additional rotational and vibrational degrees of freedom are added to the electronic excitations of the daughter molecule. Precise calculations of the individual energy levels and the population probability are therefore. Going back to the 1980s, several publications [Koł85; Fac85; Jez85; Sza87] dealt with the calculation of the final-state distribution of molecular tritium. Due to an increasing sensitivity, Saenz et al. [Fro96; Sae97b; Sae97a; Jon98; Jon99; Sae00] repeated the

Table 3.1: The systematic uncertainty budget of the KATRIN experiment. The table lists all the systematic effects in the KATRIN system and is the starting point for this work. The second column shows the neutrino mass shift Δm_ν^2 for each effect. The * symbol indicates effects related to the source of KATRIN. Data taken from [Sei19].

systematic effect	Δm_ν^2 $(10^{-3}\,\mathrm{eV}^2/\mathrm{c}^4)$
Theoretical corrections of the β-spectrum	0.0
Relativistic correction of transmission function	0.0
Synchrotron radiation	-0.2
Doppler effect*	±0.2
Modified angular distribution	0.0
Analysing plane: potential and magnetic field	
- absolute magnetic field	±2.5
- radial inhomogeneities	-0.3
HV stability	-0.6
Detector-related effects	in progress
Ions	in progress
Backscattering at rear wall	< 0.1
Source magnetic field*	±1.9
Trapped electrons in WGTS*	< 0.1
Potential variations in WGTS*	-0.7
Gas dynamics in WGTS*	±3.0
Monitoring of column density*	±0.2
Energy loss function	in progress
Final-state distribution*	in progress
Slope of the background rate	in progress

calculations. In 2006, Doss and Saenz [Dos06] published their latest results on the calculation of the six lowest electronic states of $^3HeT^+$, $^3HeD^+$ and $^3HeH^+$ resulting from the β-decay of the three tritiated isotopologues T_2, DT, HT. Following the work of Bodine [Bod15a; Bod15b][1] and combining it with the work of Doss et al. [Dos06] and the work of Seitz-Moskaliuk [Sei19], there are three main effects that influence the final-state distribution:

1. The calculation of the final-state distribution itself is subject to uncertainties arising from the underlying theory.
2. Besides the theory, there are experimental parameters that serve as input variables for the calculations:

[1] especially her theoretical based dissertation [Bod15a] with the title "Assessment of molecular effects on neutrino mass measurements from tritium β decay".

a) the composition of the gas mixture (chemical and op[2]) and

b) the temperature of the tritium gas inside the WGTS.

In the molecular context, the latter two are of interest. For each molecule and for each rotational state, the final-state distribution is calculated taking the molecular recoil into account. The final-state distribution depends primarily on the occupation of the rotational states of the molecules, which depends on the temperature according to the Boltzmann law. Since the op states couple to the rotational states, they directly influence the excitations of these rotations, as assigned by Bodine [Bod15b]. Therefore, the op and the temperature effects are discussed below.

Chemical and ortho-para gas composition As the three final-state distributions of the individual tritiated molecules T_2, DT, HT are different, the gas composition has to be monitored. This is done by the KATRIN LARA system which measures only the chemical composition at room temperature by inelastic light scattering. The trueness and the accuracy of this measurement are the resulting contributions to the systematic uncertainty budget. Two values are defined for the measurement:

- Isotopic purity ϵ_T: The isotopic purity represents the relative amount of tritium isotopes in the gas mixture. The trueness requirement is $\Delta\epsilon_T/\epsilon_T \leq 0.03$. Aker et al. [Ake20b] demonstrated that with the LARA system the measured trueness is achieved with $\Delta\epsilon_T/\epsilon_T = 0.001$.
- HT to DT ratio κ: The ratio of HT to DT indicates the amount of DT in the gas. The requirement for trueness is $\Delta\kappa/\kappa \leq 0.1$. According to [Ake20b], the requirement was also met with $\Delta\kappa/\kappa = 0.05$.

The input values are therefore known and quantified by the LARA system. However, since the tritium source cycle is a dynamic and thermal cycle, see figure 3.1, the values measured with LARA are only a snapshot for this time, pressure and temperature. In order to be able to make statements about how the gas composition changes on its way to the source, the equilibrium states are important in a first step. For the chemical and the op conversion, the temperature dependent equilibria are known, see the figures 3.4 and 3.2. From these, the state in the source at the known temperature of 30 K could thus be calculated. This is based on the assumption that the mixture in the WGTS is in equilibrium. Such equilibrium states are reached by internal conversion processes (isotope exchange) and exchange reactions with other particles. Time constants τ and reaction constants k describing these complex processes are pressure, temperature and concentration dependent. In this context, values for tritium are only partially or incompletely available in the literature. Therefore, the open question remains whether the gas mixture is already equilibrated when it arrives in the WGTS. If this is not the case, the question remains as to the actual state of the gas composition. This uncertainty remains until an experimental verification is carried out. The more detailed discussion on the topic of equilibria, exchange reactions and other effects that have an influence on the composition can be found in the sections 3.4, 3.5, 3.6.

[2] A detailed explanation of the ortho-para mechanism can be found in section 3.4.2. For now, it is sufficient to know that op leads to an additional freedom for the homonuclear isotopologues T_2, D_2, H_2.

In addition to the molecular gas composition, there is also the possibility that two molecules combine to form a dimer $(Q_2)_2$[3] via Van-der-Waals forces. Such dimers again have a direct effect on the final-state distribution, since the recoil of the dimer is different from that of the single molecule, and the electron requires more energy to leave the potential of the dimer. This has a direct impact on the energy released and therefore on the shape of the spectrum. There is currently no experimental way to determine the dimer concentration in the source. Furthermore, the KATRIN design report [Ang05] states that dimers only appear below 30 K and are therefore not relevant for the measurement uncertainty budget. However, Mirz [Mir20], in his studies of H_2 and D_2 under conditions similar to KATRIN, showed that dimers are formed. It can therefore be assumed that dimers also form in a tritium atmosphere. A detailed discussion is given in section 3.5.3.

Gas temperature The temperature of the tritium gas affects the calculation of the final-state distribution in three ways: through the trueness of the absolute temperature, through the stability of the WGTS temperature over time and through the excitation of higher rotational states [Sei19]. The temperature trueness introduces a smearing of the initial and final states is introduced by . It also affects the resulting Doppler broadening of the distribution. Both the final-state distribution and the Doppler broadening are also affected by the temperature stability, as small fluctuations lead to an additional smearing. Regarding the presence of higher rotational excitations, Seitz-Moskaliuk [Sei19] states that due to the op prevention of rotational transitions with $\Delta J = \pm 1$ and the fact that the gas is equilibrated at room temperature, higher rotational excitations are possible. Therefore, Seitz-Moskaliuk suggests further (experimental) investigations [Sei19].

Uncertainty calculations for DT concentration and fot ortho-para To date, there have been two calculations of the uncertainty for the DT concentration and the op concentration in the WGTS in relation to the final-state distribution.

- Explicit calculations of the final-state distributions of the daughter molecules for the β-decay of T_2 for the rotational states $J = 0$, 1, 2 and 3 and of DT and HT for $J = 0$ and 1 by Saenz and Doss were performed to investigate the effect of rotational excitations of the parent molecules. An estimate of the uncertainty in the neutrino mass was obtained by fitting theoretical curves with uncertainties for the temperature, the op ratio and the concentration of DT molecules. The results show that both the op ratio and the temperature have less influence compared to the number of DT molecules at the source [Dos06]. For the DT concentration, a 10 % change in the amount of DT leads to an uncertainty of $\approx$ 22 % in the derived neutrino mass, assuming a neutrino mass of 0.2 eV. Conclusion: For this reason, an additional experiment to measure the DT concentration in the cold phase is proposed by Saenz and Doss [Dos06].
- Since the op ratio cannot be measured in the beam tube at cryogenic temperatures, thus simulations and calculations were carried out. Assuming a transit time of the tritium molecules inside the WGTS of 1.5 s at 30 K, the op ratio in the cold region remain the same as the ratio at room temperature, with an uncertainty of 3 %, according to investigations

[3] A detailed explanation of the dimer formation process is given in section 3.5.3.

by Krochin[4]. Furthermore, a calculation done by Schlösser and Urena[5] states that the rotational temperature is thermalised at 30 K. This would be in agreement with the determination of the rotational temperature with 10 % trueness as required by Bodine [Bod15a]. However, all these theoretical calculations and studies are based on various assumptions and preconditions that have never been verified. More importantly, the self-equilibration time for this is based on H_2 and D_2 data. No data are available for samples containing tritium. Therefore, Seitz-Moskaliuk [Sei19] proposes a detailed look at these calculations.

Conclusion In summary, it can be said that the molecular gas composition and its spatial and temporal stability are of utmost importance for the determination of source-related systematic effects, as shown by the example of the final-state distribution. Furthermore, the detailed study of molecular effects in the context of the final-state distribution ha shown that instead of experimentally investigating such molecular effects in order to quantify their contribution to the uncertainty budget, only simulation studies and theoretical calculations have been performed. Moreover, these calculations often raise new questions or suggest further investigations. In particular, the question of the time constants for exchange and self-equilibrium reactions is an important open issue. In addition, the lack of knowledge about the presence of tritium dimers in the WGTS represents an uncertainty for the calculation of the final-state distribution. Thus, the assumptions can be verified and quantified by targeted measurements, allowing the contribution to the measurement uncertainty budget and thus the influence on the neutrino mass shift to be determined. In particular, this statement is supported by the inclusion of the status "in progress" for neutrino mass shifts in the table 3.1 for the final-state distribution.

In the next section, the variations of temperature, pressure and gas composition along the source loop are presented.

3.3 Thermal cycle in the KATRIN tritium source loop

In the previous section it was shown that the op composition and the temperature influence the rotational population of the molecules and thus the final-state distribution. To investigate the systematic effects influenced by molecular effects, it is necessary to consider the entire KATRIN tritium source, which is a common system of WGTS and the tritium inner loop, as explained in figure 2.5. Inside this "closed" loop system, the molecular gas composition can change due to internal or external reactions or due to a change in the system boundary conditions, e.g. temperature, pressure, flow, geometry. However, to gain a better understanding of the complexity of the interplay between the various system parameters, e.g. temperature, the DT concentration and the op ratio, an imaginary run on the back of a T_2 molecule through the tritium source is performed while explaining the changes. Figure 3.1 shows the variation of the pressure and temperature parameters and the corresponding temperature equilibrium constant and the population number of odd rotational states after this run through the tritium source.

[4] Krochin, A. 2014. Untersuchungen zum Einfluss des Verhältnisses von Ortho-Paratritium auf die Neutrinomassensensitivität bei KATRIN. Bachelor thesis. Karlsruhe Institute of Technology. Karlsruhe.

[5] Schlösser, M. and Urena, A. G. 2015. Rotational temperature of tritium in the WGTS gas feed. KATRIN internal report.

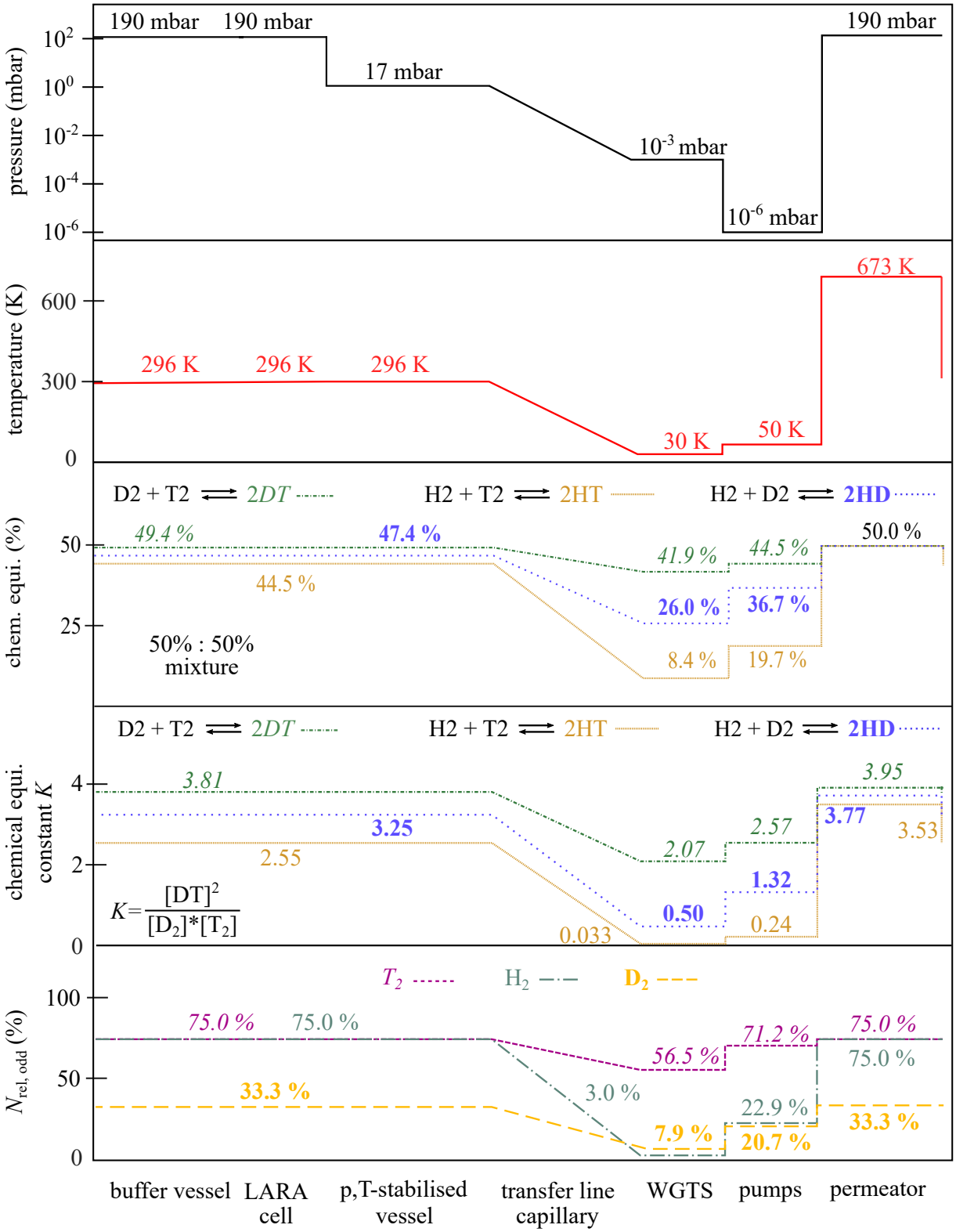

Figure 3.1: Thermal cycle in the KATRIN tritium source loop. The five subplots show pressure, temperature, chemical equilibrium, chemical equilibrium constant K and op equilibrium along the tritium source loop, where the left side (buffer vessel) and the right side (permeator) are connected in a closed loop, see figure 2.5. For process control, the pressure regimes are of primary interest, but with respect to the equilibria (see figures 3.2 and 3.4), the direction of the chemical exchange and the op conversion processes is important. Temperature is the dominant contributor to these conversion processes. However, the time constants of these processes are dependent on temperature, pressure, geometry and surface properties of the material and therefore need to be considered carefully. Hence, the true composition in the cold cannot be assumed to be in equilibrium.

- Buffer vessel: Tritium of at least $\epsilon_T \geq 95\,\%$ purity is stored in the buffer vessel at 190 mbar and room temperature. The gas leaves the buffer towards the
- Laser Raman cell: Here the gas composition is measured at room temperature by inelastic light scattering. This is the only point in the whole tritium source loop where gas composition data is monitored.
- Stabilised buffer vessel: After the gas composition measurement, the gas enters the 15 l big vessel, which ensures a well defined gas flow into the transfer line and thus into the WGTS.
- Transfer line and capillary: The transfer line connects the buffer vessel to the WGTS cryostat tube. In this line, the pressure drops from 17 mbar down to 10^{-3} mbar and the temperature decreases down to 30 K. Before the gas enters the WGTS beam tube in the next step, it has to flow through the nozzles to obtain a uniform distribution. These nozzles could force an exchange reaction between the molecules due to their geometry, see section 3.6.4.
- WGTS: The gas is injected through the nozzles of the capillary in the centre of the beam tube and pumped out at both ends, giving a column density of $5 \cdot 10^{12}$ molecules $/\mathrm{cm}^2$ is reached. As can be seen, the chemical equilibrium changes accordingly during cooling. Up to now, it has been assumed that the op ratio does not change as the gas is only in the WGTS for 1.5 s at 30 K. The state shown is the equilibrated state for the temperature.
- Pumps: Various cascades of turbomolecular pumps pump the injected gas and returned it to the buffer vessel.
- Permeator: But before the gas enters the buffer vessel, it must pass through the permeator. The permeator is heated to 673 K. Its function is to block impurities and allow only hydrogen isotopologues to pass. Its working principle is to split the hydrogen molecules into their atomic states H, D, T and allow them them to pass through a membrane to recombine. The recombination to the equilibrium takes place according to the ambient temperature. As a result, any information about the gas composition inside the WGTS that might have been carried with the molecules is destroyed and lost. It is not possible to obtain any information, see section 3.6.1
- Surfaces: In addition, the hydrogen isotopologues can interact with the stainless steel walls at any time. Exchange reactions are possible, see section 3.6.2.

This single run through the source loop illustrates how much the chemical and op gas composition changes and how much the temperature influences the changes. With regard to the actual chemical equilibrium and the actual equilibrated op ratio inside the WGTS, it has only been assumed that the changes are too small to have an effect on the neutrino mass measurement. Nevertheless, figure 3.1 displays the calculated equilibrium states. However, the crucial question is what are the time constants to reach these states and how do the system parameters (e.g. temperature, pressure, flow, material surface properties) influence these time constants to reach the equilibrated state. Thus, the real composition in the cold parts cannot be assumed to be in equilibrium.

Therefore, a theoretical description of the underlying (internal) conversion reactions is given in the next three sections. Section 3.4 presents the temperature dependence of the op and the chemical equilibrium. The following two sections show the different reactions schemes to

change the gas composition. Section 3.5 gives an overview of the interactions and exchange reactions within the gas itself. The change in the gas composition due to interactions with external partners is presented in section 3.6.

3.4 Gas composition and thermal equilibria

In the previous section, the thermal cycle within the KATRIN source loop, with its different temperature regimes and the resulting chemical and op gas composition were presented in detail. This section focuses on the chemical and op equilibria and their temperature dependence for the six hydrogen isotopologues H_2, HD, D_2, HT, DT, T_2.

3.4.1 Chemical composition and its equilibrium

There are three hydrogen isotopes T, D, H, which form the six hydrogen isotopologues T_2, DT, D_2, HT, HD, H_2 by covalent bounding. If the gas sample consists of only one type of isotopologue, the atomic concentration remains constant over time. For a binary mixture of hydrogen and deuterium, the following equilibrium reaction takes place

$$H_2 + D_2 \rightleftharpoons 2\,HD. \tag{3.7}$$

The equilibrated state can be calculated according to [Sou86] to

$$\frac{c_{HD}}{c_{H_2} + c_{D_2}} = \exp\left(-\frac{\Delta E}{k_B T}\right), \tag{3.8}$$

using the concentration c of the isotopologues, the energy difference $\Delta E = E(H_2 + D_2) - 2E(HD)$ between the two states, the temperature T and k_B as the Boltzmann constant. The equilibrium state is therefore temperature dependent. Figure 3.2, shows the equilibrated concentrations for HD, HT and DT for an initial 50:50 mixture. For temperatures $T \to \infty$, the equilibrium state foresees 50 % for the heteronuclear isotopologues. This is close to a stable static system. By lowering the temperature to 0 K, the concentration of the heteronuclear isotopologues decreases and disappears completely at 0 K. In order to be independent of the (initial) concentration, the chemical equilibrium constant K for the heteronuclear hydrogen isotopologues is shown in figure 3.3.

Besides the chemical equilibrium of the hydrogen isotopologues, the op ratio and its temperature dependent equilibrium are important for the thermal cycle and for the population of rotational states, as discussed in section 3.2. The op mechanism, including the theory and its equilibrium, are discussed in the next section.

3.4.2 Ortho-para ratio and its equilibrium

As already mentioned in various places above, the homonuclear isotopologues H_2, D_2, T_2 have an additional degree of freedom, the so-called op modification, which was discovered for H_2 by Arnold Eucken in 1912 [Sch02].

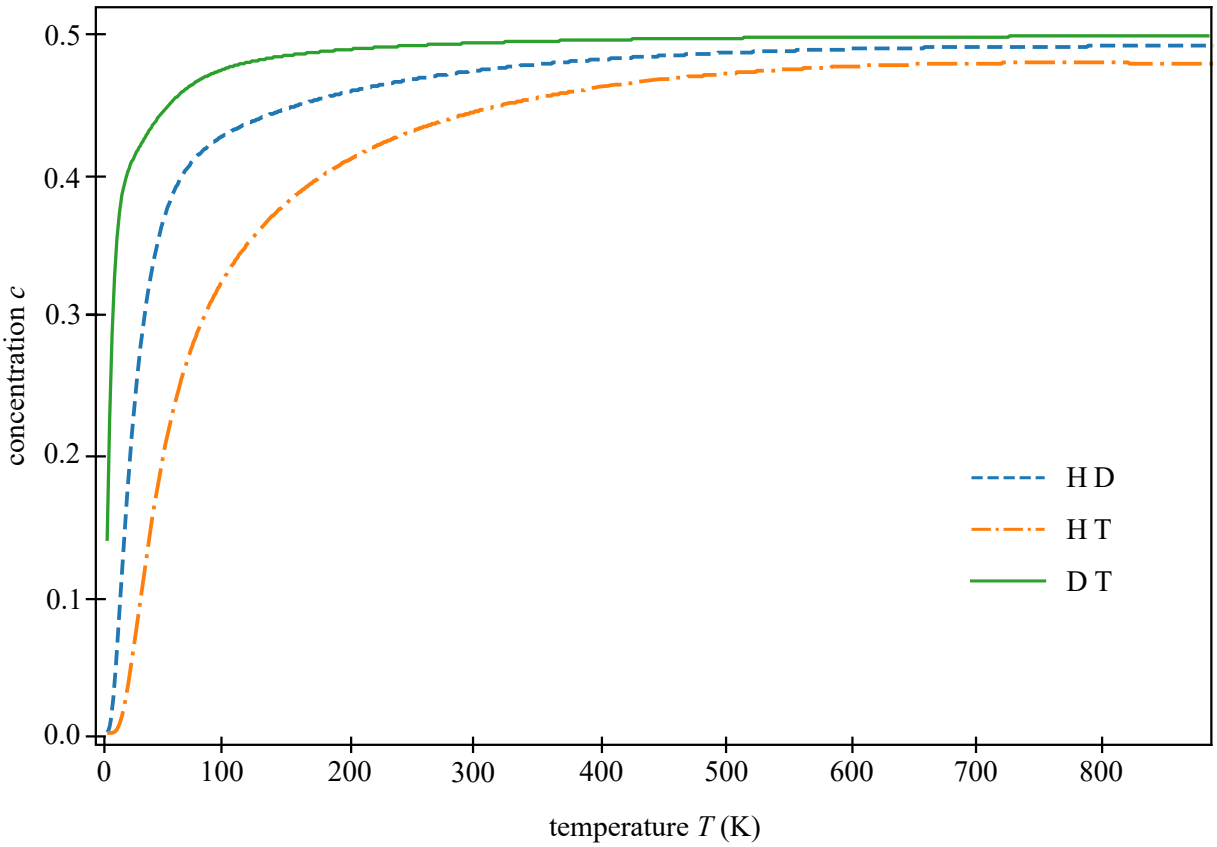

Figure 3.2: Chemical equilibrium of the heteronuclear hydrogen isotopologues. For initial 50:50 mixtures, the equilibrated HD, HT and DT concentrations are plotted as a function of the temperature. Data according to [Grö15b].

The underlying theoretical explanations are kept as short as possible, so a more detailed description can be found in [Her66; Sou86; Dem05; Her10]. The total wave function of a hydrogen molecule Ψ_{tot} is given by

$$\Psi_{\text{tot}} = \Psi_{\text{vib}} \cdot \Psi_{\text{rot}} \cdot \Psi_{\text{nuc}}, \tag{3.9}$$

with the three individual wave functions for the vibrational, rotational and nuclear spin contributions [Her10]. On the one hand, the nuclear spin of H and T is 1/2, so they are fermionic, and therefore, H_2 and T_2 require an anti-symmetric total wave function under the application of the particle exchange operator. On the other hand, D has a spin of 1, so it is bosonic, and therefore, D_2 requires a symmetric total wave function under the application of the particle exchange operator.

At room temperature and below, Ψ_{vib} is in a very good approximation to almost 100 % in the ground state. The vibrational wave function Ψ_{vib} is always symmetric [Her66] and therefore, Ψ_{rot} and Ψ_{nuc} are directly coupled to fulfil the symmetry constraint of fermions (H_2, T_2) or bosons (D_2) with respect to the total wave function Ψ_{tot}.

The rotational wave function Ψ_{rot} is under the particle exchange $(-1)^J$, with J as the rotational quantum number. This means, that the wave function Ψ_{rot} is anti-symmetric for odd J and symmetric for even J. This condition, together with the overall coupling of Ψ_{rot} and Ψ_{nuc} to the total wave function Ψ_{tot}, leads to two different cases:

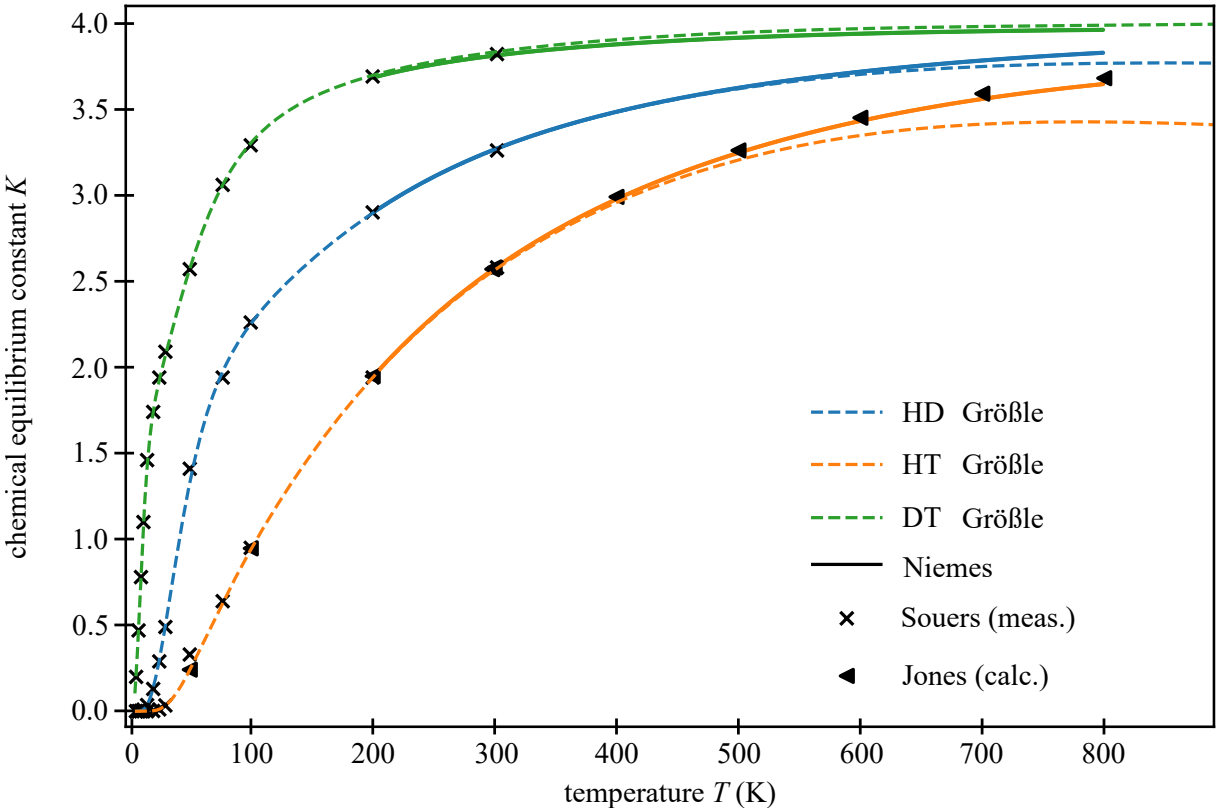

Figure 3.3: Temperature dependence of the chemical equilibrium constant K. The equilibrium constant is shown as a function of the temperature for HD, HT and DT. Data taken from [Sou86; Jon00; Grö15b; Nie21a] and calculations made by R. Größle (personal communication). The calculations differ depending on the reference. In particular, the number of used rotational and vibrational states uased has a greater effect at higher temperatures. Down to low temperatures, the op ratio influences the calculations. The calculations of S. Niemes are optimised for high temperatures and the calculations of R. Größle are optimised for low temperatures. The latter two calculations were used for the input for the thermal cycle in figure 3.1.

- For the fermionic H_2, T_2: For Ψ_{tot} to remain anti-symmetric, a symmetric Ψ_{rot} requires an anti-symmetric Ψ_{nuc}, or Ψ_{rot} is anti-symmetric and Ψ_{nuc} is symmetric.
- For the bosonic D_2: For Ψ_{tot} to remain symmetric, a symmetric Ψ_{rot} also requires a symmetric Ψ_{nuc}, or Ψ_{rot} and Ψ_{nuc} are both anti-symmetric.

The nuclear spin wave function Ψ_{nuc} itself is a combination of the wave functions of the two nuclei in the molecule. For the fermionic H_2 (single proton) and T_2 (one proton, two neutrons) the nuclear spin of each nucleus is $\frac{1}{2}$. The total nuclear spin I can be $I = 0$ (anti-symmetric state) or $I = 1$ (symmetric state). It can be shown, that there are three symmetric spin states for $I = 1$ and one anti-symmetric spin state for $I = 0$, given by the non-vanishing Clebsch-Gordon coefficients [Dem06]. The nuclear spin multiplicities are 3 for odd J states and 1 for even J states. For the bosonic D_2 (one proton and one neutron), three nuclear spin states are possible $I = 0$, $I = 1$ and $I = 2$. There is one state with $I = 0$, three states for $I = 1$ and five states for $I = 2$. This time, the spin multiplicities are 3 for odd J states and 6 for even J states. The symmetric spin state is called ortho and the anti-symmetric is called para for all three homonuclear isotopologues. For the heteronuclear isotopologues HD, HT, DT there are no ortho and para states because the nuclei are distinguishable. This leads to a spin multiplicity of 1 for all three.

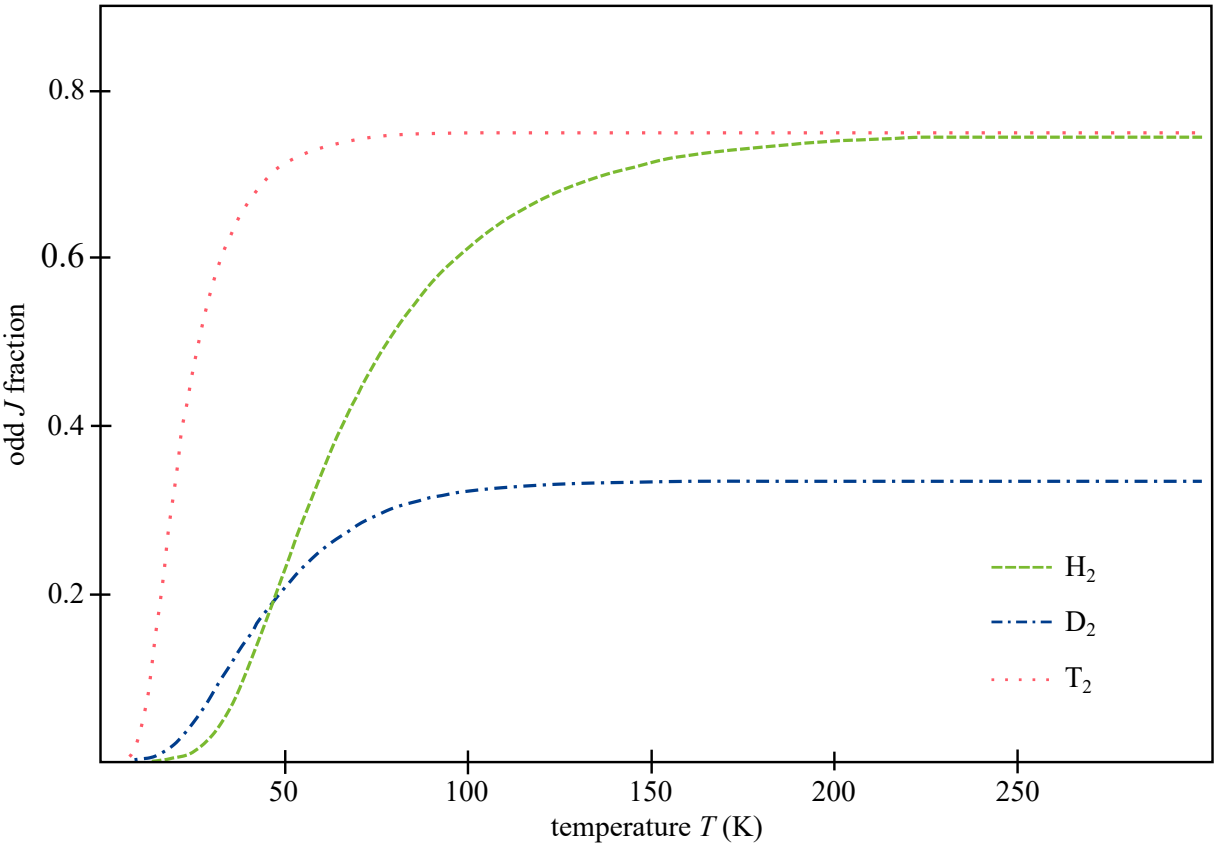

Figure 3.4: Odd J fractions of H_2, D_2 and T_2 in thermodynamic equilibrium. The odd J fractions for the homonuclear hydrogen isotopologues are shown as a function of the temperature T. The odd J fractions tend to 0 for $T \rightarrow 0\,\mathrm{K}$ and tend to the ratio of the nuclear spin multiplicities for $T \rightarrow \infty$. Figure adapted from [Mir19].

In summary, the rotational and the nuclear spin wave functions of homonuclear isotopologues cannot change separately. The rotational states are populated according to the Boltzmann distribution, which is temperature dependent. When the temperature changes, the so-called op transition interdiction does not allow transitions with $\Delta J = \pm 1$ and therefore influences the occupation of the energy levels. The even and odd J states act as independent species and remain in even or odd states. If now a change from an even to an odd J state is desired, this is only possible if there is a transition of the nuclear spin function from symmetric to anti-symmetric or vice versa. The result is a meta-stable non-equilibrated ratio of odd and even J states, which slowly converges to its equilibrium. The op equilibrium is therefore also temperature dependent. Figure 3.4 shows the temperature behaviour for the odd rotational states J for the homonuclear isotopologues. For tritium, at room temperature and above, the ortho fraction is 75 % and the para fraction is 25 %. At lower temperatures, the ortho fraction decreases slowly. For hydrogen, the ortho fraction decreases more rapidly as the temperature is lowered.

There are two ways to break this strict op interdiction, : natural conversion and catalytically enhanced conversion processes. Therefore, in the next two sections the conversion processes in terms of internal exchange reactions and external reactions with surfaces are presented for the chemical composition and the op ratio.

3.5 Change in gas composition due to internal interactions

In section 3.3, it was shown that along the tritium source loop the gas composition changes mainly due to temperature variations. The equilibrated chemical and op states and their temperature dependence for the hydrogen isotopologues were presented in the previous section 3.4. Therefore, this section focuses on how he equilibria can be achieved by the internal exchange reactions. Internal reaction means that the atomic composition (H, D, T) cannot change. There are three reaction chains of interest: the natural exchange reaction within the gas, the ortho to para exchange within the gas and the formation of hydrogen clusters.

3.5.1 Natural exchange reaction

The equilibrium state of HD is given by

$$\mathrm{H_2 + D_2 \rightleftharpoons 2\,HD.} \tag{3.10}$$

Isotope exchange is a first order process and has been well studied in the literature for the stable hydrogen isotopologues in the gas phase. According to [Sou86], the time constants for equilibration are in the order of months for the natural conversion. The use of catalysts is therefore necessary. [Uda92b; McC81] state that the natural conversion is negligible compared to the exchange reaction with (metal) surfaces. The above reaction is slow, in contrast to reactions involving tritium. For the KATRIN experiment, mainly the reaction of

$$\mathrm{D_2 + T_2 \underset{k_{-1}}{\overset{k_1}{\rightleftharpoons}} 2DT,} \tag{3.11}$$

is of interest, with k_1, k_{-1} as rate coefficients of the formation reaction in ($\mathrm{h^{-1}}$). The equilibrium constant K is

$$K = \frac{[\mathrm{DT}]^2}{[\mathrm{D_2}][\mathrm{T_2}]} = \frac{k_1}{k_{-1}}, \tag{3.12}$$

where $[X]$ is the mole or partial pressure of the hydrogen isotopologue X. In general, in the first-order hydrogen isotope exchange reaction $\mathrm{A + B \rightleftharpoons C}$ [Uda92b], the decay rate of A is expressed as

$$\frac{dx}{dt} = k_1(a - x) - k_{-1}(c + x), \tag{3.13}$$

where a is the initial concentration of molecular gas A, c is the initial concentration of molecular gas C and x is the varied concentration of molecular gas A. The elapsed time t is in h. Integrating this equation leads to

$$-\ln Q = (k_1 + k_{-1}) \cdot t, \tag{3.14}$$

with Q

$$Q = \frac{m - x}{x}, \tag{3.15}$$

whereas m is the varied concentration of molecular gas A at the equilibrium rate state or after a very long time [Uda92b]. Replacing A by $\mathrm{T_2}$, Q becomes

$$Q = \frac{[\mathrm{T_2}]_t - [\mathrm{T_2}]_m}{[\mathrm{T_2}]_0 - [\mathrm{T_2}]_m}, \tag{3.16}$$

where $[T_2]_t$ is the concentration of T_2 at the elapsed time t, $[T_2]_m$ is the concentration of T_2 at the equilibrium and $[T_2]_0$ is the initial concentration of T_2. The DT formation rate is then

$$Q = 1 - \frac{[DT]_t}{[DT]_m}. \tag{3.17}$$

If the relation between elapsed time t and $\ln Q$ is linear, its slope is the first order hydrogen isotope exchange reaction rate k. This is a brief introduction to the reaction rates. In the following the reaction kinetics of the above hydrogen isotope reaction will be investigated.

The molecular tritium decay follows

$$T_2 \rightarrow {}^3HeT^+ + \bar{\nu}_e + e^- + 18.6\,\text{keV}, \tag{3.18}$$

by emission of the well known β-electron e^-. According to [Uda92b], two major processes are induced by the tritium β-decay.

- Formation of ions and radicals by tritium β-decay:

$$\begin{aligned} T_2 &\xrightarrow{\beta^-} HeT^+, \\ D_2 + HeT^+ &\rightarrow D_2T^+ + He, \\ D_2T^+ &\rightarrow DT + D^+, \\ D^+ + e^- &\rightarrow D^\bullet, \\ T_2 + D^\bullet &\rightarrow DT + T^\bullet \end{aligned} \tag{3.19}$$

- Formation of ions and radicals by ionisation effects of tritium β-decay:

$$\begin{aligned} T_2 &\xrightarrow{\beta^-} HeT^+ + e^-, \\ T_2{}^+ + D_2 &\rightarrow T_2D^+ + D \rightarrow DT^+ + DT, \\ T_2 + e^- &\rightarrow T_2^* \rightarrow 2\,T^\bullet, \\ D_2 + T^\bullet &\rightarrow DT + D^\bullet \end{aligned} \tag{3.20}$$

T_2^* stands for the excited state and $D^\bullet$ and $T^\bullet$ are free radicals. In terms of the reaction chains shown above, the isotopic exchange reaction is caused by the formation of ions and radicals[6]. In total, there are radicals, ions and the β-electrons which accelerate the natural conversion when tritium is involved. As tritium decays continuously, new β-electrons, ions and radicals are produced to further accelerate the conversion process even faster. Compared to the studies of the stable hydrogen isotopologue, only a small number of experimental results have been published in the literature [Jon48; Mat52; Ter69; McC83b; McC85; Sou86]. Souers [Sou86] tabulates time constants for the $D_2 - T_2$ reaction with different molar fractions of tritium for different temperatures. The time constants are in the range of several minutes up to an hour. The data show that as the amount of tritium increases, the time constants become much shorter, as expected due to the increased amount of free electrons. McConville et al. [McC83b] investigated the formation of DT at temperatures of (295, 273, 195, 77) K and determined the reaction time τ to be between 1.5 min (90 % T_2 at 295 K) and 280 min (90 % T_2 at 77 K). McConville et al. [McC83a;

[6] Radicals are atoms or molecules with an unpaired valence electron.

McC85] investigated reaction rates for deuterium and tritium at 295 K by varying the initial tritium concentration and the pressure. In [Uda92b] Uda et al. investigated time constants for the formation of HT and DT. Their statements are:

- The first order rates of hydrogen isotope exchange reactions are $5.54 \cdot 10^{-2}\,\mathrm{h}^{-1}$ for $H_2 + T_2$ and $4.76 \cdot 10^{-2}\,\mathrm{h}^{-1}$ for $D_2 + T_2$.
- The actual HT and DT production rates are almost equal, but the reverse reaction of HT is about 55 % greater than that of DT.
- The hydrogen isotope exchange reaction takes place via ions and radicals due to the tritium β-decay.
- The actual exchange rate is about twenty times greater than the ion production rates for hydrogen isotope mixed gases. It is assumed that the hydrogen isotope radicals continue to undergo chain reactions.

Their results also show reaction time constants between a few minutes and several hours.

Summary: Natural exchange reactions without tritium have time constants of two orders of magnitude higher than those reactions with tritium. The reason is that molecular β-decay produces radicals, ions and free electrons through various chain reactions. These three types of particles dramatically accelerate the exchange reaction within the gas.

At this point, a short note on this investigation by [Sou86]. He carried out the $D_2 - T_2$ reaction under two new conditions. For the first measurement, he filled deuterium into a stainless steel vessel and waited for 24 h. After filling tritium into the vessel, the expected time constant was obtained. The second time, tritium was added first, followed 24 h later by deuterium. Investigation of the reaction time showed a significantly slower constant. The reason is that the tritium interacted with the surface material of the stainless steel vessel and most of the decay electrons were lost due to the interactions. But more details on the reaction with external partners in the next section.

3.5.2 Internal ortho-para conversion

As explained earlier, due to the coupling of the rotational wave function Ψ_{rot} to the nuclear wave function Ψ_{nuc}, a transition from an even to an odd J state is only possible if the nuclear wave function changes from symmetric to anti-symmetric or vice-versa. This means that both wave functions must change simultaneously. There are two ways to break the strict interdiction on the op transition: natural conversion and catalytically enhanced conversion processes. In this section, only the first process is of interest.

- Spontaneous conversion: The underlying process of a natural conversion of an isolated molecule is the interaction of the electron spin with the nuclear spin. There are theoretical calculations for this spontaneous flipping of nuclei with $1.85 \cdot 10^{-13}$ /a and $6.20 \cdot 10^{-14}$ /a [Rai63; Pac08]. Quantum mechanically speaking, this flip is forbidden. This conversion is a first order process following the differential equation

$$-\frac{\mathrm{d}N}{\mathrm{d}t} = N \cdot k, \tag{3.21}$$

where N is the number of particles (in this case equal to the concentration), t is the time and k is the reaction rate. In the case of a first order process, the simple relation between the time constant τ and the reaction rate is given by

$$\tau = \frac{1}{k}. \tag{3.22}$$

- Self conversion in the gas phase: Conversion is based on the interaction of the fields of a molecule with the fields of the neighbouring molecules [Mot62], e.g. the magnetic moment with the core moment. In the literature [Mil97] the process of the self conversion is a second order process. The neighbouring molecules are regarded as a catalyst. For hydrogen, the ortho molecules have stronger dipole fields than the para hydrogen molecules. Therefore, the conversion is mainly a process at the magnetic moment of the ortho molecule. Furthermore, the catalytic performance decreases with time as the molecules convert from ortho to para. The differential equation for the second order process is

$$-\frac{\mathrm{d}N}{\mathrm{dt}} = N^2 \cdot k. \tag{3.23}$$

  The relation is $k = 1/\tau$. According to [Ess13], an additional factor a as the mean lifetime, must be considered for a more accurate calculation. Another conversion possibility is the interaction due to collision [Sou86]. In the literature, time constants of $0.0114\,\mathrm{h}^{-1}$ to $0.0127\,\mathrm{h}^{-1}$ are given for the gaseous and liquid phases according to [Lar48; Mil97]. The latest results for hydrogen are published by R. Größle [Grö15b] with a time constant of $0.01\,\mathrm{h}^{-1}$.

- Conversion by radiolysis: As mentioned for the natural chemical conversion, the molecular tritium decay allows radicals, ions and the emitted β-electron to interact with atoms of the molecule and replace one of the atoms by breaking the nuclear spin coupling. An advantage of the reaction chain is that a new radical or ion is formed after the reaction. This makes further conversions possible. For further information see [Sch64].

Summary: The op modification is an additional degree of freedom for the three homonuclear isotopologues. Due to the coupling of the rotational and the nuclear spin wave functions, a transition with $\Delta J = \pm 1$ is forbidden. Only an interaction that breaks the coupling of the nuclear spin allows a transition from an even to an odd J state or vice versa.

3.5.3 Formation of tritium dimers inside the WGTS

As already known from the previous explanations, there are three covalently bound hydrogen isotopologues $H_2, HD, HT, D_2, DT, T_2$. These six hydrogen isotopologues interact via Van-der-Waals forces [Van73] and form weakly bound Van-der-Waals clusters. Weak here means relative to the binding of a molecule. In [McK90], the dissociation energy for a $(H_2)_2$ is given as 0.36 meV and for an H_2 molecule as 4.477 eV according to [Her61]. The London dispersion force is one of the Van-der-Walls forces and the binding force of the clusters [Van73]. The simplest and smallest cluster is the $(Q_2)_2$ dimer. The dispersion interaction energy is given by the London equation [Lon30]

$$w(r) = -\frac{3}{2} \cdot \frac{\alpha_1 \alpha_2}{(4\pi\epsilon_0)^2 r^6} \cdot \frac{I_1 I_2}{I_1 + I_2}, \tag{3.24}$$

with the polarizabilities α_1, α_2 of the interacting molecules, the intermolecular distance r and I_1, I_2 as the ionisation potentials. Hydrogen dimers $(Q_2)_2$ can be described with the model of a vibrational an-harmonic oscillator. For a detailed analysis of the theoretical background of clusters and dimers, [Isr11] is recommended. A review of the literature shows that polarizabilities values can be found for the three inactive hydrogen isotopologues. Experimental results are given in [Ste64; You68; Kog71; Mil72; Con75] and computed values are in [Koł67]. Data are missing for three tritiated hydrogen isotopologues HT, DT, T_2. The first experimental evidence of dimers was provided by [Wel51] using infrared absorption spectroscopy.

In the context of the KATRIN experiment, the final-state distribution determines the shape of the energy spectrum. Since the whole spectrum is the weighted sum of all possible initial and final states, Van-der-Waals clusters, formed by molecules in the WGTS, influence the shape of the spectrum and hence the neutrino mass measurement. The number, size, excitation and possible final states of such clusters should be taken into account in the analysis as an additional systematic effect. The design report [Ang05] states that only temperatures below 30 K cause the formation of $(T_2)_2$ dimers. However, Mirz [Mir19] studied Van-der-Waals dimers over a wide range of temperatures and pressures, similar to the conditions in the WGTS. He observed Van-der-Waals clusters of the non-tritiated hydrogen isotopologues in the liquid phase for H_2 and D_2 and in the gaseous phase for D_2 in the temperature range of (27 – 38) K. The results show an explicit dependence on the absorbance. This is the reason why Mirz favours the existence of $(T_2)_2$ dimers in the WGTS, since their bindings are expected to be stronger compared to deuterium due to their higher mass.

Summary: This explanation shows the importance of studying tritiated clusters under KATRIN-like conditions by experimental studies, simulations and calculations to identify the influence on the final-state distribution and thus the contribution to the neutrino mass shift.

Conclusion: In the context of the KATRIN experiment, natural chemical and op conversions are processes that internally change the gas composition (chemical and op) of the hydrogen isotopologues. Ions, radicals and emitted β-electrons are produced by the molecular decay of tritium and dominate the exchange reactions for the chemical and op conversion. There is a complete lack of tritium data for the dimer formation process, so experimental studies are strongly recommended.

In the next section, the field of exchange reactions is opened to external partners, e.g. surfaces.

3.6 Gas composition change due to external interactions

The previous section described various phenomena of how the gas composition itself changes due to internal conversions and exchange reactions. In this part, the field is opened to external reactions, which means that molecules and atoms from the outside can interact with the tritium gas. External reactions mean that the atomic composition can change due to exchange reactions with surfaces. Therefore, monitoring the atomic composition besides the molecular composition reveals exchange reaction chains and properties. As the focus is still on the KATRIN experiment, only KATRIN-related effects are mentioned and briefly discussed.

3.6.1 Forcing an equilibrium within a permeator

As KATRIN requires a high luminosity and a pure tritium source, the tritium purity must be above $\epsilon_T \geq 95\,\%$. In addition to filling with fresh tritium gas, the removal of impurities is a necessary step. As mentioned in section 2.2.2, there is a palladium membrane permeator inside the tritium source loop which acts as a barrier blocking all non-hydrogen isotopologues. The working principle of the permeator is that it breaks the bindings of all the molecules on the surface with a combination of heat (working temperature is 673 K) and a catalytic reaction with the atoms. Only the hydrogen atoms (H, D, T) can pass through the palladium membrane, everything else (as carbon C or oxygen O) recombines at the front side of the permeator. The hydrogen atoms passing through the permeator recombine to molecules in the thermal equilibrium with the respect to the chemical composition and the op ratio of the permeator temperature, see figures 3.2 and 3.4 for the evolution of the equilibria as a function of the temperature. Therefore, all information about chemical composition, op ratio and chemical impurities like methane are lost at this point in the source loop and reset to the high temperature.

3.6.2 Metal surfaces and methane production

As mentioned in the previous section, Souers [Sou86] was able to show that there is a strong interaction of tritium with stainless steel surfaces. Since all vessels, pipes and most parts of the pumps in the KATRIN tritium source loop are made of stainless steel, many interactions are possible. In this case, the carbon is a new external partner of the tritium with which the other isotopologues can interact. For a detailed experimental study of hydrogen isotope exchange reactions in a methane atmosphere with tritium, [McC83a; McC85] and especially [Uda92a] are highly recommended. The main results are summarised here. As for the natural and the op reaction kinetics, radicals, ions and the β-electron from the tritium decay

$$\begin{aligned} T_2 &\rightarrow 3\,HeT^+ + e^- + \bar{\nu}_e + 18.6\,\mathrm{keV}, \\ 3\,HeT^+ &\rightarrow T^+ + He \end{aligned} \tag{3.25}$$

form a huge scheme of reaction chains. The binding energy of CH_4 is 13.3 eV and that of CT_4 is 13.1 eV, showing that the emitted β-electron has enough energy to break the bindings. But compared to the formation rates without methane, this time the reaction rates are 1/20 to 1/10 slower than the rates of just $H_2 + T_2$ mixed gases. Although the formation of radicals and ions is thought to trigger the hydrogen isotope exchange reaction, the radicals in the methane mixed gas tend to disappear quickly. This suggests that methane would act as a scavenger. In summary, the presence of methane leads to much longer isotope reaction rates until the equilibrium state is reached.

Since the β-decay of tritium, with its emitted electron, radicals and ions, initiates the isotope exchange reactions, the entire setup was filled with tritium before starting a tritium measurement campaign. The tritium was kept inside until a chemical equilibrium was reached and the surfaces were saturated with tritium. This is the reason why once a system has been contaminated with tritium, it will always contain small amounts of tritium, even after purging.

The following statements are based on the publication by Sturm et al. [Stu21]. Full operation of tritium started in the first quarter of 2019. After a few days of normal operation mode, the throughput over the WGTS decreased drastically. The reason for this decrease in throughput can be explained by the geometry of the injection capillary. The injection capillary is almost

6 m long. A part of the injection capillary inside the WGTS cryostat is connected to the liquid nitrogen temperature and the rear part is thermally coupled to the 30 K shield. In addition, the diameter of the line is reduced from 6 mm to 2.1 mm. In principle, any gas other than hydrogen, neon or helium, could have been frozen out in the line and formed an orifice. Since no such reduction in throughput was observed during the commissioning with deuterium, and since all impurities were blocked by the permeator, the impurities must occur after the permeator and before the WGTS beam tube. After the injection was stopped, the beam tube was heated up to 80 K and a mass spectrometer measured mainly the mass 28 equivalent to CO and the mass 24 equivalent to CT_4. Since the release occurred only after the beam tube had reached the 80 K, it was concluded that the CO and CT_4 were frozen in between the two parts of the injection capillary. It was shown that tritiated methane was formed due to the radiochemical reactions, caused by the β-electrons from tritium decay, tritiated methane were formed. This is a known effect when tritium comes into contact with stainless steel surfaces such as buffer vessels, pumps, etc.

Methane generation is strongly dependent on the quality of the surface [Mor77; Gil80]. The results show that the highest production rates occur immediately after the tritium exposure and decrease with time. A comparison of the amount of ^{3}He produced with the maximum amount of methane produced shows that the methane rate was lower than the helium production rate. This means that on average less than one molecule of methane is created per decay [Cof79]. The formation of CO has not yet been reported in the literature. Sturm et al. suggest the following possible mechanisms

- electron and ion stimulated desorption of CH_4 and CO, according to [Mal13],
- radiolysis of impurity surface films [Föl80] and
- subsequent isotope exchange reactions within the gas phase [Pra61], or
- directly induced reactions by radical ions such as T^+ and $T_3{}^+$.

3.6.3 Catalytic ortho-para conversion

In the previous section, the op mechanism was explained. It also introduced the interdiction of the op transition and explained that only a decoupling of the two nuclear spins due to interactions with other molecules can break this interdiction. One way of improving the process of the op equilibrium conversion is to use catalysts. There are two processes by which the conversion is feasible: physisorption and chemisorption. Regarding the physisorption, the molecule is bound to the surface of the catalyst material by the Van-der-Waals force. The molecule is not split but interacts with the fields of the catalyst material. op catalyst are therefore mainly para-magnetic materials whose high magnetic field decouples the nuclear spins. This process is appropriate for cold temperatures. Regarding the chemisorption, the molecule is chemically bound to the surface of the catalyst material as it splits into its atoms. This process is enhanced at higher temperatures as energy is needed to split the molecules. Besides this, a chemical conversion is possible at the same time. Unlike natural conversion (see section 3.5.2, catalytic op conversion is a first-order process [Cha57]. First-order kinetics is widely used in the literature, although sometimes in a more complex form [Cun58; Wei58b; Ess13]. Since op conversion plays an important role in hydrogen liquefaction, physisorbed catalysts have mainly been studied at low temperatures. As a result, in most publications use either ferromagnetic or paramagnetic

catalyst materials. Hutchinson et al. [Hut67; Hut70] used an iron oxide catalyst, Cunningham and Johnston [Cun58] used an iron oxide and chromium-oxide based catalyst, Essler [Ess13] and Weitzel [Wei56; Wil57; Wei58a; Wei60] used iron oxide and Chapin and Johnston [Cha57] used chromium-oxide. Gold particles are also a candidate for the op conversion [Boe17].

Summery: op catalysts increase the conversion process by several orders of magnitude, depending on the material and its properties, such as grain size, and on the parameters, such as temperature, pressure and flow. For a deeper insight, it is recommended to read the following publications: [Tay33; Emm35; Wei55; Wil57; Cha57; Wei58b; Sou86; Ili92; Fuk13].

3.6.4 Separation in the injection chamber by the capillary

The last point in this section deals with the possible separation of the gas constituents by the injection capillary with its 415 orifices. According to some of the assumptions made by Bodin, Seitz-Moskaliuk, Kronich and Schlösser, the op ratio inside the WGTS should be the same as at room temperature when the gas is equilibrated. The freezing of the injection capillary with methane and CO showed that a narrow geometry can, in this case, affect larger molecules. Following this idea, it could also be possible that the gas mixture of the six isotopologues is separated by floating through the injection capillary. It could be assumed that the lighter molecules can pass through the capillary more easily than the heavier molecules, especially tritium T_2. Due to this separation, the tritiated molecules would spend more time in the 30 K regime, leading to a higher probability of reaching the op equilibrium state. Given the surface and the interactions with it, a longer time in the transfer line would enhance the exchange reactions. The present work is aware of the fact that these considerations are based on assumptions, but assumptions that are partly confirmed by already discovered phenomena. Therefore, experimental studies that allow the investigation of such possible separation effects would be beneficial for the KATRIN experiment.

Conclusion of this section: It is shown that external partners offer a wide field of new interaction possibilities for the hydrogen isotopologues. Especially with catalyst materials to accelerate the chemical or op equilibrium state are interesting and promising candidates. Interactions with surface walls of vessels, pumps and pipes are always present and cannot be neglected. Since effects such as capillary separation cannot be investigated directly in KATRIN, experimental studies are necessary to gain access to these phenomena.

3.7 Scientific objectives of this work

The KATRIN experiment aims to determine the electron antineutrino mass $m_{\bar{\nu}_e}$ with a projected sensitivity of $0.2\,\mathrm{eV/c^2}$ (90 % C. L.). This ambitious goal can only be achieved if all contributions to the total systematic uncertainty budget are identified, determined and updated. As shown in the previous sections, there are a large number of different systematic effects distributed throughout the KATRIN setup. Most of them have been investigated and determined in recent years by simulation studies, during the commissioning phase or by additional experiments. Some of these systematic effects are source-related, e.g. the final-state distribution. The gas composition (chemical, op, dimers) and the temperature influence the rotational population and thus the final-state distribution. So far the varying gas composition along the thermal cycle is either measured, e.g. with the LARA system in the warm, or it is calculated from the equilibrium

states for the cold. Although the equilibrium states for the op conversion and the chemical composition are known for a given temperature, the associated time constants are largely unknown. This means that it is unclear how quickly the gas composition changes from warm to cold (WGTS) and back from cold to warm, and therefore there is no experimental evidence that equilibrated states are reached. Experimental investigations are therefore necessary. Simarly, Saenz and Doss [Dos06], Bodin et al. [Bod15a; Bod15b] and Seitz-Moskaliuk [Sei19] claim in their papers that experimental studies of molecular effects are important, because the effects are either known but not treated (e.g. thermalisation of rotational states or DT concentration in the WGTS), or they are simply neglected for unexplained reasons (e.g. tritium clusters only occur below 30 K). Concerning this last effect of tritium clusters, recent results by Größle [Grö15a; Grö15b; Grö17] and Mirz [Mir19], showing the formation of non-tritiated dimers under KATRIN-like conditions, indicate the presence of $(T_2)_2$ in the WGTS at 30 K. Data on tritium clusters are completely missing in the literature.

Since it is not possible to spectroscopically investigate molecular effects or to spectroscopically observe the change in gas composition inside the KATRIN tritium source, and since some assumptions and simulations rely on experimental data as input parameters, experimental studies outside of KATRIN are the only remaining option to gain access to this information. TO date, no design or experimental setup is available to study the molecular effects of all six hydrogen isotopologues under the conditions of the thermal cycle in the KATRIN tritium source loop. This leads to the following requirements for a new experiment:

- A fully tritium compatible system capable of handling all six hydrogen isotoplogues and large quantities of tritium (up to 10^{15} Bq, equivalent to 13.5 g or 50 standard l of pure T_2).
- Provide cryogenic temperatures down to 10 K for the study of all three hydrogen aggregate states and the corresponding phase transitions.
- Provide thermal cycle studies associated with the KATRIN tritium source loop.
  - Provide converters with appropriate catalyst materials to force specific chemical and op mixtures to induce exchange reactions.
  - Investigate the conversion kinetics and underlying physical processes for the natural and, in particular, op conversion depending on the system parameters, such as temperature, flow, pressure and catalyst material properties, such as grain size, porosity, activation.
  - Determination of the time constants τ of the hydrogen isotope exchange reactions for pure hydrogen mixtures as well as with impurities (CH_4, O_2) and of the op conversion online and in real-time. Raman spectroscopy is the method of choice according to [Sha59; Uda92b; Uda92a].
  - Experimental investigations of hydrogen intermolecular effects under KATRIN-like source conditions, e.g. to determine the amount of dimers and their formation process. Based on the experience of the previous experiments by Kosmider and Größle [Kos09; Kos11; Grö15a; Grö17; Mir19], infrared absorption spectroscopy is the method of choice.

- Finally, a combination of Raman and IR spectroscopy is required to spectroscopically investigate all these diverse molecular effects (exchange reactions, conversion rate, time constants, dimers) between 10 K and 300 K.

Based on these key messages and requirements, the objective of this work is as follows:

> **Design, construction and set-up of a new, fully tritium-compatible experiment that fulfils the above requirements and thus allows the systematic investigation of hydrogen molecular effects in the temperature range of (10 – 300) K.**

Dedicated measurements must be carried out beforehand, as their results (both measurement results and measurement concept) directly influence the design of the new experiment. Therefore, the following results of these pre-investigations are presented in chapter 4:

- Two spectroscopic cells are required to investigate how quickly the gas composition changes as it passes from the warm region to the cold region and vice versa. First investigations in the warm region on the expected slow natural exchange of H_2 and D_2 are presented in section 4.2.2. Due to the β-decay, the isotope exchange reaction of H_2 and T_2 is faster. This phenomenon is discussed in section 4.2.3.
- In order to accelerate the natural isotope exchange and the natural op conversion process, a catalyst is used to selectively force the gases into different compositions, thereby triggering exchange reactions. The demonstration of the feasibility of a suitable measurement principle for experimental studies of the op and chemical conversion kinetics with the newly designed RaCoon setup is presented in section 4.3.2.
- With the RaCoon setup, experimental studies of the op and the chemical conversion between room temperature and 77 K can be performed simultaneously, allowing spectroscopic systems (such as LARA4) to be calibrated. An important parameter is the gas purity in the conversion process. Therefore, measurements with gas admixtures to poison the catalyst material are carried out in section 4.3.4. Based on this, a proper calibration procedure will be developed and tested.
- The thermal cycle of KATRIN requires the use of both Raman spectroscopy (conversion rates, gas composition, rotational states) and infrared absorption spectroscopy (intermolecular effects such as dimers). This results in a common measurement setup, the core of which is a measurement cell suitable for both IR and Raman and compatible with that for cryogenic temperatures. The use of movable optics to switch between spectroscopic methods seems reasonable. Since KATRIN requires a precession of 5 % for Raman and 1 % for IR, studies on the reproducibility during switching are carried out in advance. The results are presented in section 4.4.2. The influence of gold and silver coated mirrors for IR and Raman measurements is also investigated in the following section 4.4.3.

The present work is structured as follows: Chapter 4 deals with the results of the pre-investigations. An overview of the measurements carried out is given in section 4.1. In section 4.2 the natural isotope exchange reactions of $H_2 + D_2$ and $H_2 + T_2$ are discussed. This is followed by the introduction of the RaCoon experiment in section 4.3, which allows the investigation of the time constants for the op conversion. 4.4 presents the results for a combined IR and LARA spectroscopic setup and the resulting requirements for the optical components. The T_2ApIR experiment is presented in chapter 5. The experimental and scientific objectives are discussed in section 5.1, the different design requirements (e.g. cryogenic, fully tritium

compatible) are part of section 5.2. The final process design is presented in section 5.3, followed by the technical implementation in section 5.4. Finally, the conclusion and outlook are part of section 5.5. The summary and the final outlook are presented in the concluding chapter 6.

4 Pre-investigations for the design of T_2ApIR

As described in section 3.1, the study of molecular effects, such as exchange reactions, conversion rates, dimer formation, in the KATRIN source is of essential importance for the systematic effects and their measurement uncertainty budget. Since there is no direct spectroscopic study of the molecular effects in the KATRIN source loop, and since data in the literature related to tritium studies are sporadic, a new tritium-compatible experiment is needed. The newly developed T_2ApIR experiment enables the study of molecular effects under conditions similar to the thermal cycle of the KATRIN source loop , see section 3.3. The resulting requirements (tritium compatible, cryogenic measurement range, combined Raman and IR measurement system) for the design of T_2ApIR are complex and diverse. Therefore, specific pre-investigations will be carried out to develop new and to improve existing measurement technologies.

To improve the parallel measurement of op and chemical composition in the warm region, the RaCoon facility using LARA spectroscopy will be developed during this thesis. With the addition of catalysts, gas mixtures can be forced into specific compositions in order to trigger exchange reactions. Studies of the temperature dependence of catalysts for op and chemical conversion performed with RaCoon allow a deeper understanding of the underlying kinetics. IR spectroscopy investigations of inactive hydrogen isotopologue dimers were performed by Mirz [Mir19]. In order to be able to detect both conversion or exchange rates (LARA) and dimers (IR) in the cold, both techniques (LARA and IR) need to be combined. The development of a suitable measurement technique is part the present work. The results obtained will play an important role in shaping the design of T_2ApIR.

In this chapter, an overview of the measurements carried out and the results obtained is given in section 4.1. The results of the investigation of the time constants of the natural exchange reaction of H_2 and D_2 and, for comparison, of H_2 and T_2 are presented in section 4.2. Since the op ratio directly influences the final-state distribution (see section 3.2), the study of the op conversion is of particular interest. The investigation of the conversion properties is multifaceted and technically complex, which is why a new experimental setup, RaCoon, is being built for this purpose. The design, the proof of principle of the measurement technique and the results of the catalyst studies are explained in section 4.3. Section 4.4 presents the spectroscopic pre-investigations on reproducibility and on the use of gold- or silver-coated mirrors for a combined LARA and IR spectroscopy system. In the last section of the chapter 4.5, the results of the investigations are summarised and classified in relation to the design of T_2ApIR.

4.1 Overview and objectives of the measurements performed

A total of three pre-investigations will be carried out to ensure that the knowledge gained and the measurement technologies are incorporated into the design of T_2ApIR.

Natural isotope exchange With respect to the thermal cycle of KATRIN, it is important to know how fast the gas composition changes when passing from the warm region (e.g. buffer vessel, LARA cell) to the cold region (capillary, WGTS) and vice versa. Therefore, spectroscopic studies with one cell in the warm region and one cell in the cold region should be performed beforehand. Regarding the natural isotope exchange, according to the literature an exchange between pure hydrogen H_2 and pure deuterium D_2 is hardly to be expected [Sou86]. However, the presence of tritium T_2 accelerates the exchange reaction due to β-decay [Uda92b]. In order to investigate this influence of β-decay, measurements of the isotopic exchange between $H_2 + D_2 \rightleftharpoons 2\,HD$ and of $H_2 + T_2 \rightleftharpoons 2\,HT$ in the warm are performed in this work. In addition to different initial concentrations, the influence of the laser beam and the stainless steel surfaces on the exchange reactions will be investigated. Based on the results from the measurement in the warm region, corresponding investigations can be carried out in the cold region with T_2ApIR. The results of the HD measurement campaign are described in section 4.2.2 and the results of the HT measurement campaign are described in section 4.2.3.

Parallel op and chemical conversion as well as catalyst studies Since natural isotope exchange and natural op conversion are slow, catalysts are needed to selectively force the gases into different compositions and trigger exchange reactions. With the RaCoon facility, it is possible to conduct catalyst and op and chemical conversion studies in parallel. This has the advantage that the instrumentation can be calibrated to measure the op and chemical composition simultaneously. On the one hand, a proof of principle of the measurement concept is provided, where a conversion takes place in the cold, but the online and real-time measurement by LARA spectroscopy takes place in the warm, see section 4.3.2. On the other hand, conversion studies with RaCoon are possible depending on the system parameters pressure, flow, temperature as well as the catalyst material grain size, porosity. The results of the proof of principle and the determination of the conversion time constant are presented in section 4.3.4.1 and are directly transferred to T_2ApIR. Furthermore, the influence of a contamination of the catalyst material on the catalysis process is investigated in section 4.3.4.2. Since the catalyst material always comes into contact with air when it is fed into the RaCoon system and is thus poisoned, the material must be activated accordingly. The activation procedure developed and its dependence on temperature are summarised in section 4.3.4.3. These converter results determine the design of the cold T_2ApIR converter in terms of geometry, heaters and amount of catalyst material.

Spectroscopic pre-investigations for reproducibility and coated mirrors In the RaCoon system, LARA spectroscopy is used to measure the gas composition and thus the conversion time constant. As molecular effects such as dimer formation and exchange effects are also to be investigated in the thermal cycle of the KATRIN source loop, IR spectroscopy is required. As a consequence, the design of T_2ApIR requires a common system for IR and LARA investigations over a temperature range of (10 – 300) K. For the core of this common setup, a measuring cell is needed that is compatible for both types and can be used in the cryogenic and overpressure range. To minimise the heat input in the cryogenic range, the number of windows is reduced to the minimum, two for transmission spectroscopy. Such a measurement cell is being developed specifically for T_2ApIR. The use of a combination of these two techniques (IR and LARA) means that either the same optics can be used or the optics can be changed in an automated way. Automated because the entire setup is in a glove box and the handling of small, delicate screws is not always possible. Therefore, there are two pre-investigations of the spectroscopic setup, the

results of which directly influence the spectroscopic design of T_2ApIR. By moving the optical components in and out, it must be ensured that the reproducibility is sufficient to meet the precision required by KATRIN, see section 4.4.2. The second experiment will test which mirrors, silver- or gold-coated, are more suitable for LARA and IR spectroscopy.

Conclusion: These different pre-investigations show the complexity of the design of T_2ApIR is and why this information is needed for the final design.

The next section begins with the investigation of the natural isotope exchange of the hydrogen isotopologues.

4.2 Natural isotopic exchange

The natural isotopic exchange between the six hydrogen isotopologues is a fundamental process. The conversion process proceeds at different rates depending on temperature, pressure and initial concentration. The special feature of the hydrogen isotopologues is the presence of tritium. As a radioactive element, tritium decays into a positively charged ion and emits an electron. Both particles decisively shape the exchange reaction through new reaction channels. The theoretical basis for natural conversion (isotope exchange) is presented in section 3.5.1.

In this section, 4.2.1 presents the objectives of the measurement campaigns. The results of the $H_2 + D_2 \rightleftharpoons 2\,HD$ study are presented in 4.2.2 and those of the $H_2 + T_2 \rightleftharpoons 2\,HT$ study in 4.2.3. The final classification of the results of the investigations in relation to the design of T_2ApIR is given in 4.2.4.

4.2.1 Objectives of the measurement campaign

In this section the isotopic exchange of the reaction $H_2 + D_2 \rightleftharpoons 2\,HD$ and the reaction $H_2 + T_2 \rightleftharpoons 2\,HT$ will be investigated. Three objectives are pursued:

1. To determine the time constant for the isotope exchange reaction of $H_2 + D_2 \rightleftharpoons 2\,HD$ and $H_2 + D_2 \rightleftharpoons 2\,HT$ and to compare the time constants in order to understand the influence of tritium.
2. Determine the influence of the laser and the surface of the stainless steel container on the reaction. For this purpose, a sample is continuously irradiated with the laser beam in the form of a continuous measurement, and the other sample only at the end of the measurement time. In addition, the same gas mixture is stored in two stainless steel vessels of different sizes during the measurement period.
3. To gain experience in the experimental handling of tritium for the design of T_2ApIR. As tritium is more reactive than the other isotopes due to its decay, the preparation and execution of the measurements must be carefully planned. The measurement results will be used to gain a better understanding of the influence of accurate and precise determination of the time constants on the design of T_2ApIR.

In the following sections, the results of the investigations are explained and compared.

4.2.2 Investigations of $H_2 + D_2 \rightleftharpoons 2\,HD$

The basic description of isotope exchange is explained in the previous chapter in the section 3.5.1. The reaction

$$H_2 + D_2 \rightleftharpoons 2\,HD \tag{4.1}$$

is a first order process, i.e. the time evolution of the concentration can be described by a simple single exponential function.

A LARA measurement system is used to measure the chemical concentration. There are currently four LARA measurement systems, all of which have been developed and built at the TLK. The measuring principle is the same for all systems and is based on the effect of inelastic light scattering (Raman effect). Only the resolution and the parameter space to be investigated are different due to the use of different components, such as filters and spectrometers. At this point, a brief explanation of the Raman effect is given. Raman spectroscopy is sensitive to rotational and vibrational excitations. The Raman effect is a second order process where light is inelastically scattered on the molecule. There are two types of LARA cell: a static cell with a defined gas mixture or a cell through which a gas stream flows. The Lara cell consists of a stainless steel cuboid with viewports in CF-16 flanges on four sides in the horizontal plane. The laser beam passes through the cell in the longitudinal direction and the light is isotropically scattered. The light scattered at 90° to the incident laser beam is directed by lenses and an optical fibre to a grating spectrometer for analysis and then to a CCD for detection. The in-house developed analysis software LARASoft [Jam13b] can determine the corresponding concentrations on the basis of the measured absolute intensities by means of a pre-calibration. The grating spectrometer is equipped with three different gratings. Since the scattered Raman light interferes differently at the gratings, the rotation lines can be resolved separately or together for all three isotopologues H_2, D_2 and HD. For more information on the theory of the Raman effect and Raman spectroscopy see [Lon02]. A detailed description of the Raman system developed at the TLK regarding its components, the experimental setup and the calibration procedure can be found in [Jam13b; Sch13c; Zel17; Nie21a].

The LARA2 system was used to study the reaction $H_2 + D_2 \rightleftharpoons 2\,HD$. A total of two measurement campaigns were carried out, with a 50:50 and a 75:25 mixture of H_2 and D_2.

Experimental preparation and procedure Two steps are of central importance in the preparation of the experiment. The first is to prepare the LARA cell and the three containers (one additional LARA cell and two stainless-steel vessels) with the desired mixture and the second is to make the LARA measurement system ready for use.

- **Filling process** The filling of the LARA cell and the containers takes place at the HYdrogen DEuterium (HYDE) loop. This is a facility for the production of equilibrated mixtures of the inactive hydrogen isotopologues at the TLK. For this purpose, two equal-sized buffer vessels are filled to 950 mbar each, one with H_2 and the other with D_2[1]. The gas mixture is then circulated for 10 min to achieve the best possible mixing. It is important to ensure that the gas mixture is well mixed, but also that the circulation pump does not have a catalytic effect on the exchange reaction. After circulation, the LARA cell and the three containers are filled with the gas mixture. A pressure of approximately 900 mbar is reached.

[1] This is only the case for a 50 % : 50 % mixture. For mixing ratios, the vessels are filled to the appropriate pressures.

- **Calibration of LARA2** In this case the LARA2 system is used for the reaction $H_2 + D_2 \rightleftharpoons 2\,HD$. The measurement system has to be calibrated before starting, as the components, such as filters and mirrors depend on the spectral sensitivity. This is done by measuring a LARA reference cell with a known concentration. The calibration factor k_{calib} for each isotopologue is given by

$$k_{\text{calib},\,Q_2} = \frac{c_{\text{reference},\,Q_2}}{I_{\text{meas.,rel.},\,Q_2}}, \tag{4.2}$$

  where c is the known concentration of the reference cell and I is the relative intensity of the isotopologue measured with the Raman system. The absolute intensity $I_{\text{abs},\,Q_2}$ is obtained by fitting so-called peak shapes to the measured peaks. Therefore, 60 spectra were recorded and analysed using the LARASoft analysis software. With the calibration factors determined in this way, the intensity of the subsequent measurement can be converted into concentration. After successful calibration, the filled LARA cell is inserted into the LARA2 setup and the continuous measurement is started.

- **LARA measurement** The LARA system measures the intensity over a period of 60 s. The LARASoft analysis software performs various steps, such as cosmic ray removal, baseline substraction, dead pixel removal. A detailed description of the analysis software can be found in [Jam13b]. After completion of the continuous measurement, the concentration is measured in the second LARA cell for 60 spectra. The LARA cell is then evacuated and filled with gas from the large vessel for a concentration determination. After evacuation, the gas composition of the smaller vessel is measured. The two containers and the additional LARA cell are connected by a corrugated tube and corresponding manual valves.

Experimental results The HD measurement campaign consists of two runs to study the exchange reaction. The first run lasted almost 45 days, with 63381 spectra recorded, with a 50:50 mixture and the second run lasted just under 35 days with 50036 spectra recorded with a 75:25 H_2 and D_2 mixture.

A Raman spectrum for the first run is shown in the figure 4.1. It can be seen that after each week the absolute intensities of the H_2 and D_2 peaks decrease and at the same time the HD peaks increase. By fitting the peak shapes, the intensity per peak is determined and multiplied by the calibration factor. For each isotopologue, one ortho and one para state were selected: HD: $J = 0, 1$; H_2: $J = 0, 1$; D_2: $J = 1, 2$. These peaks were chosen because their shape and intensity of the peaks were the most appropriate. The concentrations determined in this way are shown for the entire time profile in figure 4.2 for the first run and in the figure 4.3 for the second run. The decreasing concentration of H_2 and D_2 and the increasing concentration of HD can be observed. To determine the time constant τ, as explained in section 3.5.1, an exponential function of the form

$$c_{Q_2}(t) = C_{Q_2} + a \cdot \exp\left(-t/\tau\right), \tag{4.3}$$

is used, where $c_{Q_2}(t)$ is the concentration of the isotopologue at time t and C_{Q_2} is the equilibrium concentration. The results are listed in table 4.1.

In addition to the measuring cell that was permanently exposed to the laser beam, another LARA cell and two vessels with different volumes were used for the second run. The large stainless steel vessel has a volume of 1 l and the small vessel has a volume of 250 ml. Both the additional LARA cell and the two vessels were filled at the same time with the same mixture as

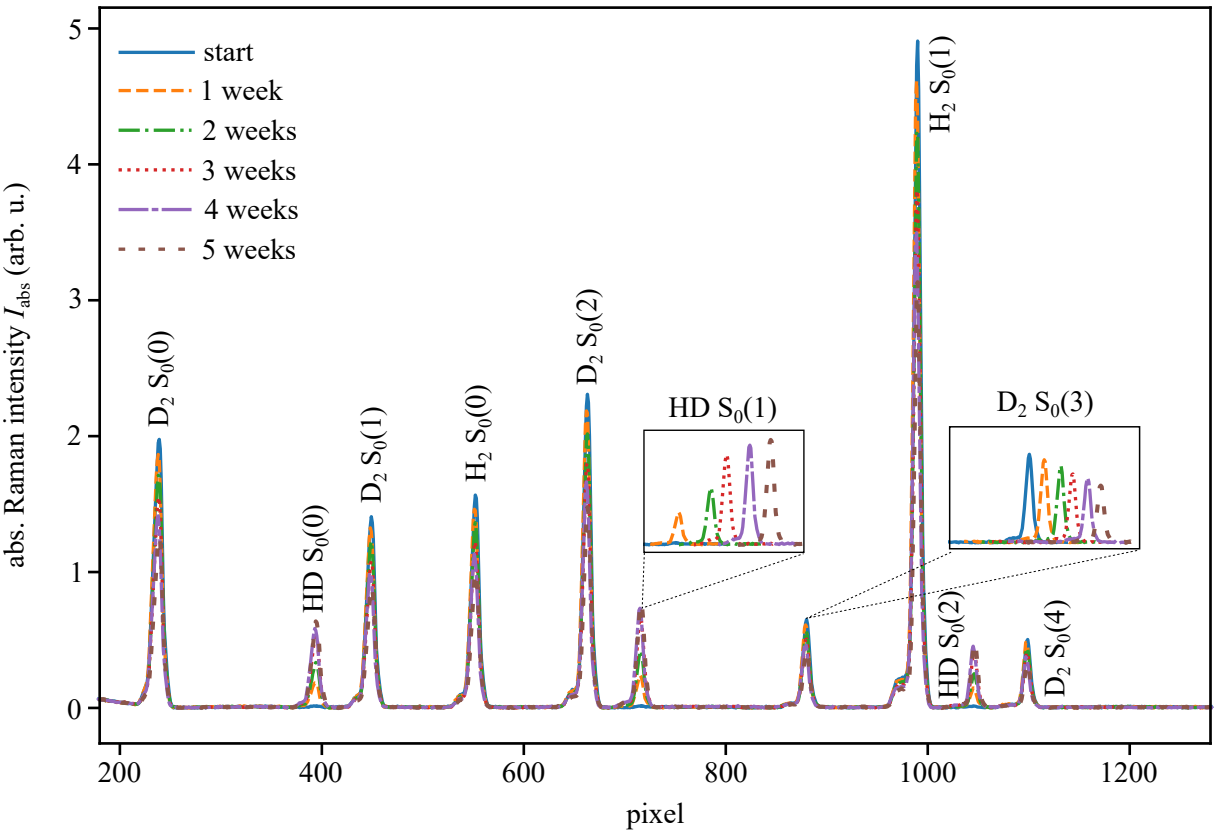

Figure 4.1: Raman spectra of the S_0 branch of the inactive hydrogen isotopologues. The absolute intensities are plotted as a function of the pixel channel of the charge coupled device (CCD). There is one spectrum at the beginning, followed by a new spectrum after each week. The two extracts show the increase of the HD peak and the decrease of the D_2 peak. The individual spectra are pixel shifted by a few pixels for a better visualisation. $S_0(0)$ represents $\Delta J_{\Delta\nu}(J')$ with $\Delta J = 2$, $\Delta\nu = 0$ and J' is the initial J state. The typical LARA signal is integrated over 60 s.

Table 4.1: HD measurement campaign: fit parameters. Shown are the time constants τ and the equilibrium concentration C for the three isotopologues.

run	ratio H_2:D_2	Δt (days)	p (mbar)	τ_{H_2} (days)	τ_{HD} (days)	τ_{D_2} (days)	C_{H_2} (%)	C_{HD} (%)	C_{D_2} (%)
1	50:50	45	950	45.33	48.54	52.25	36.1	29.8	0.34
2	75:25	35	950	33.91	44.17	68.01	66.1	18.6	13.6

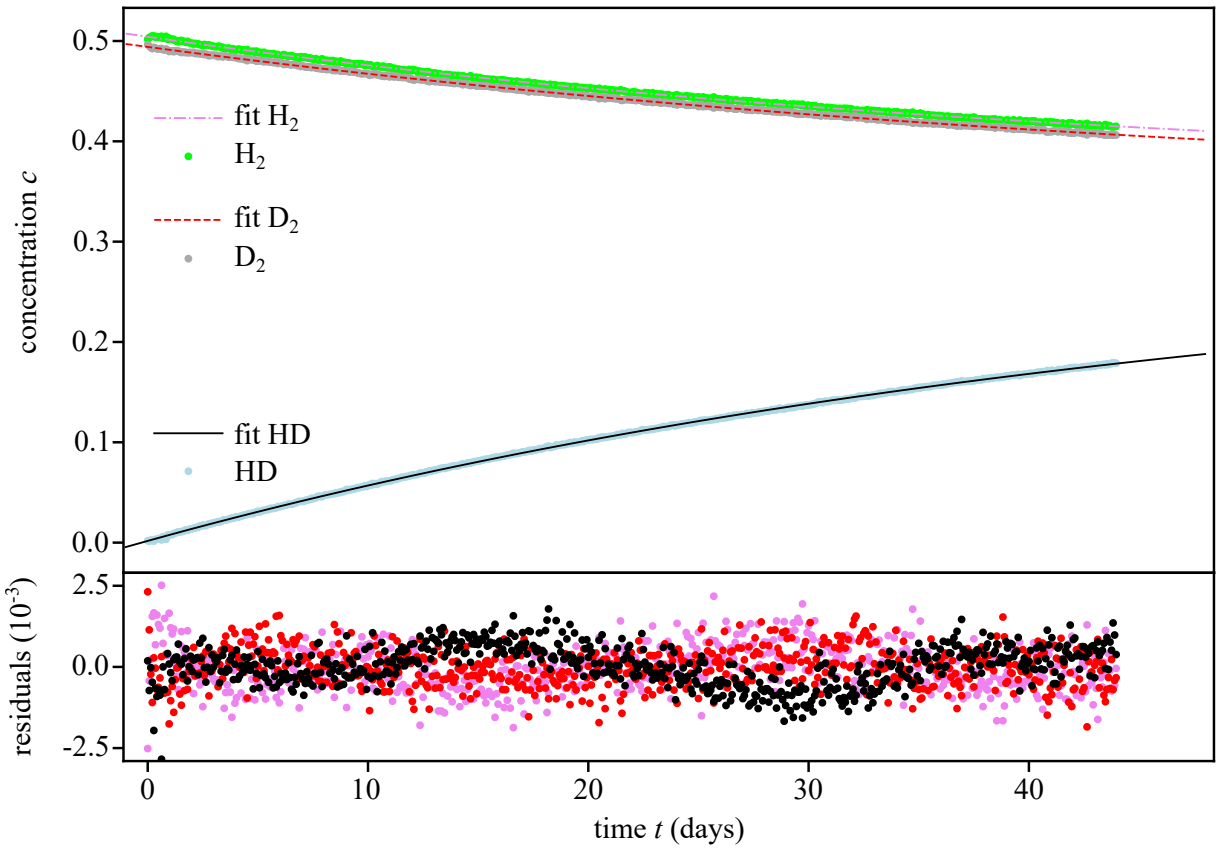

Figure 4.2: HD measurement campaign run 1: concentration profile. The upper graph shows the concentrations plotted against time for the three isotopologues H_2, HD and D_2. The solid curves represent fits with a single exponential function. The lower plot shows the residuals. For the visualisation, only every hundredth measurement point is shown.

Table 4.2: Comparison of HD concentrations. The table contains the last measured concentration value of the long-term measurement cell, which was under continuous laser irradiation and the concentration for the LARA cell and the two vessels.

	permanent	cell	big vessel	small vessel
c_{HD} (%)	10.22	1.70	0.33	0.49
$c_{\mathrm{perm.}} - c_{\mathrm{container}}$ (% points)	0	8.32	9.89	9.74

the permanent measuring LARA cell. This virtually eliminates the possibility of a difference in concentration at the start.

In order to compare whether the laser has an influence on the conversion and whether the stainless steel vessels have an influence, the measured concentrations were compared with the last concentration value of the continuous measurement. The results are shown in the table 4.2.

A note on measurement uncertainty. The main contribution is due to the calibration of the LARA2 system, so the uncertainties from the pressure sensors during the filling process or the uncertainty due to the exponential fit are negligible. The total uncertainty is in the range of 3 %.

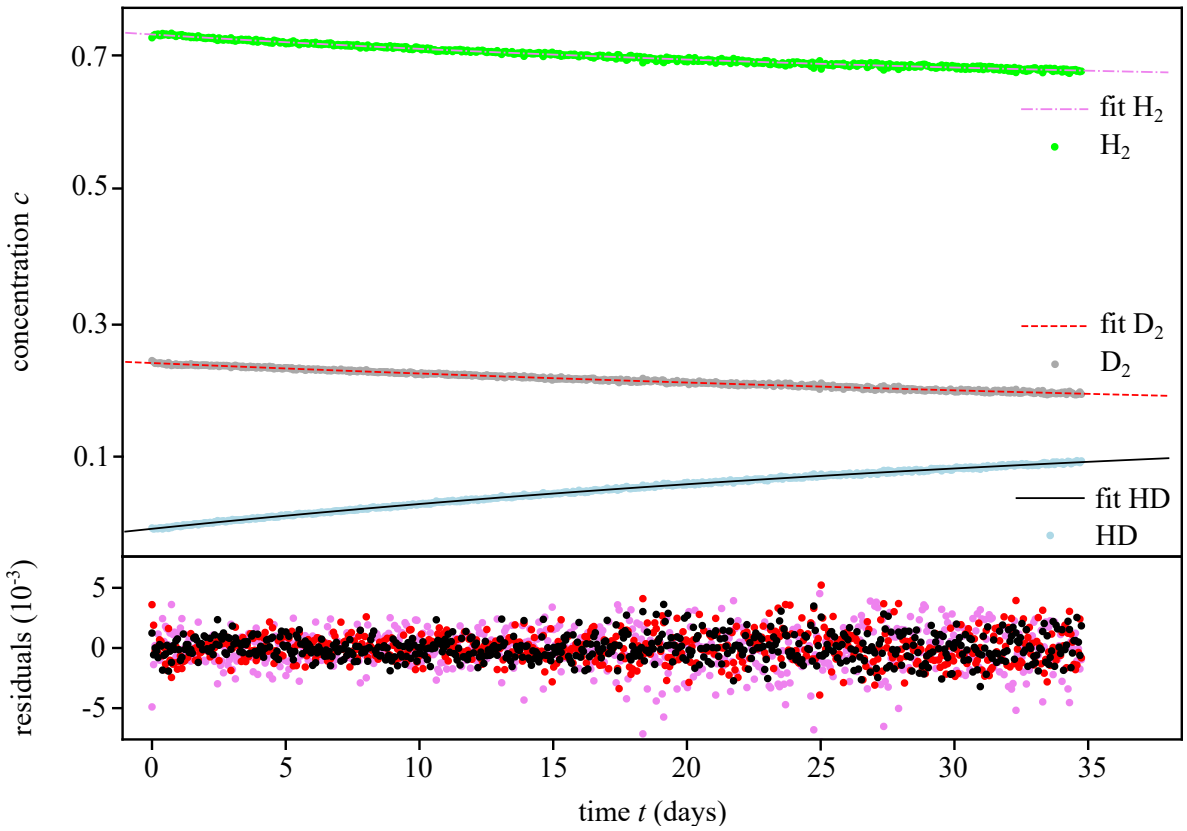

Figure 4.3: HD measurement campaign run 2: concentration profile. The upper plot shows the concentrations over time for the three isotopologues H_2, HD and D_2. The solid curves represent fits with a single exponential function. The lower plot shows the residuals. For the visualisation, only every hundredth measurement point is shown.

Data analysis and discussion The results of the first measurement run show that only 18 % of the HD was formed after more than 40 days of continuous measurement. The fitted time constants from the 50:50 mixture fit the general statements of Souers [Sou86] who gives values between weeks and months for the time constants. In a 50:50 mixture, the time constants for the products and reactants should be the same. In the present case the values obtained do not agree even within the uncertainty of 3 %. Furthermore, the value for the equilibrium concentration of HD is 29.8 %, whereas it should be close to 49 percent, see Figure 3.2. These results suggest that the conversion process does not follow a first order process. For this reason, the influence of the laser was investigated in the second run.

The measurement results of the second LARA cell and the two containers show that significantly less HD was formed than in the continuous measurement with 10 % of HD, see table 4.2. After almost 35 days, the stainless steel containers contain less that 1 % HD. This is probably due to the energy introduced by the laser [2]. The conversion was also accelerated by this continuous energy input (heat input). The reason why more HD was formed in the second LARA cell than in the stainless steel containers may be due to the optical windows made of fused silica. Due to the interaction with the windows and the incident daylight from outside, it is possible that the conversion was also accelerated in this case, albeit to a lesser extent. Comparison of the concentrations in the two vessels suggests that, due to the larger volume and hence larger

[2] The laser used was a 2 W continuous wave laser with a wavelength of 532 nm.

surface area, H_2 and D_2 interacted with the atoms on the surface of the walls and were therefore absent from the HD reaction.

Conclusion: As expected from the literature, the time constants for the natural conversion of the inactive isotopologues are in the range of weeks and days. The permanent use of the laser for continuous measurement of the concentration shows an accelerating effect on the isotope exchange, as energy is continuously introduced into the gas mixture. In order to prove this correlation unambiguously, further measurements with different laser power and the same gas composition have to be made. In the present case, several parameters were changed simultaneously, such as the initial gas composition and the measurement time. In this context, further investigations are needed to verify whether the laser beam actually influences the reaction order. Therefore, when using the T_2ApIR experiment, it should be considered to record the measuring points not every minute but every hour and to switch off the laser with a shutter between the measurements. It is not possible to make an assured statement about the interaction with the walls on the basis of the data available. There is only the hint that due to the large surface H_2 and D_2 interact with the surface's atoms For the KATRIN experiment, the natural conversion in this form will not be important, since the presence of tritium would catalyse this reaction.

4.2.3 Investigations of $H_2 + T_2 \rightleftharpoons 2\,HT$

In contrast to the previous section, the natural chemical conversion of tritium with hydrogen is now examined. Due to the radioactive decay and the resulting molecule and electron, new reaction channels open up which accelerate the conversion, see the explanations in section 3.5.1. The reaction for the isotope exchange is

$$H_2 + T_2 \rightleftharpoons 2\,HT \tag{4.4}$$

and is again a first-order process, so the concentration development is again described by an exponential function. The LARA1 system is used to investigate the exchange reaction.

Experimental preparation and procedure As tritium can only be handled in closed glove boxes, the preparation is more complex and time-consuming. The tritium transfer system (TTS) of the TLK is used to provide the samples. Since almost all tritium transfers go through this system, a permanently installed LARA system called LARA1 is located there. Again, two LARA cells and two stainless steel vessels are filled.

- **Filling process** In order to fill the containers, hydrogen is first stored in one of the storage buffer vessels of the TTS. The tritium is transferred from the ISS to the TTS via a connecting line and stored in another buffer vessel. Both buffer vessels are then opened simultaneously so that the gas volumes mix. After a circulation time of 5 min, the gas mixture is filled into the four containers. The pressure for each run is 900 mbar.
- **Calibration of LARA1** The calibration of the LARA1 system is not carried out by measuring the concentration of a well-defined cell, as is the case with LARA2, but with the aid of a standard reference material (SRM) 2242, which is manufactured, distributed and certified by the American National Institute of Standards & Technology (NIST). The calibration procedure developed is described in detail in the work of Zeller [Zel17]. Further information

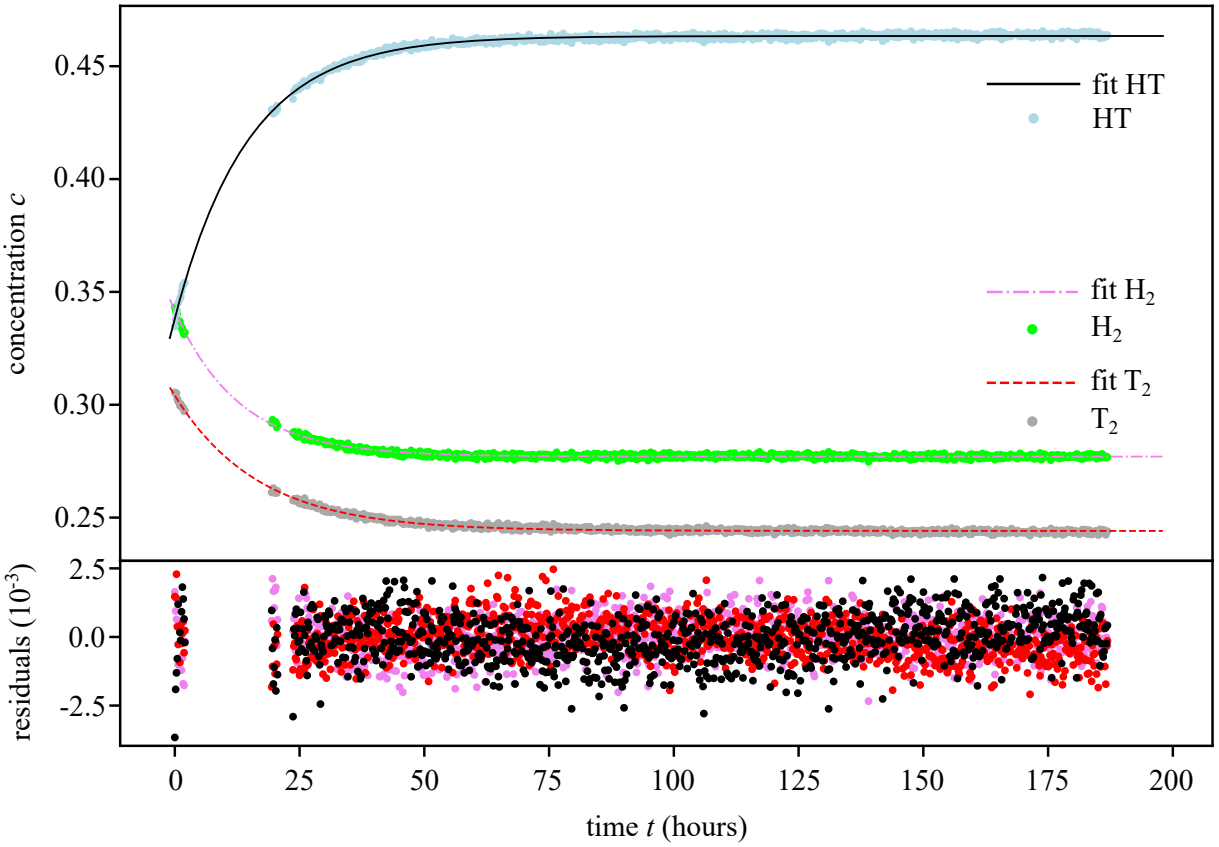

Figure 4.4: HT measurement campaign run 1: concentration profile. The concentration of the three isotopologues is plotted as a function of time. The solid curves represent the exponential curve fit. The missing data points within the first 25 h are due to an error in the water cooling of the laser power unit. The subplot shows the residuals of the fit. For visualisation only every tenth measurement point is shown.

on spectral sensitivity can be found in [Sch15c]. The corresponding concentration values are given by LARASoft after completion of the analysis steps.

- **LARA measurement** The measurement time per spectrum is again 60 s. Each spectrum passes through the typical steps of the LARASoft analysis chain. As the HT conversion reached equilibrium in a few days compared to the HD conversion, the HT runs are significantly shorter. After completion of the continuous measurement, the gas composition from the second LARA cell and the two stainless steel vessels was pumped into the LARA measuring cell one after the other. In between, the connecting lines were evacuated. Here, a first problem already became apparent: Since the LARA cell cannot be flowed through, the gas had to be partially forced into the cell with the circulation pump. This requires reusing the pump. The original idea was to fill the cell directly with hydrogen and then with tritium. This did not work because there was no mixing inside the LARA cell.

Experimental results A total of 5 measurement runs were performed to investigate the isotope exchange. The first three runs were carried out with a 50:50 mixture, the fourth with a 25:75 mixture and the fifth with a 75:25 mixture of tritium and hydrogen.

The results for the concentration curve of the first run are shown in the figure 4.4. As can be seen, the initial concentrations of H_2 and T_2 are not 50:50. This is mainly due to the fact that

Table 4.3: HT measurement campaign: parameter overview. For the five HT runs performed, the total measurement time Δt, the initial concentrations c_i, the filling pressure p, the time constants τ and the equilibrium concentration C for the three isotopologues are shown.

#	ratio H_2:T_2	Δt (h)	p (mbar)	$c_{H_2,i}$ (%)	$c_{T_2,i}$ (%)	$c_{HT,i}$ (%)	τ_{H_2} (h)	τ_{HT} (h)	τ_{T_2} (h)	C_{H_2} (%)	C_{HT} (%)	C_{T_2} (%)
1	50:50	182	950	34.31	30.55	33.47	12.92	14.72	16.81	27.70	46.34	24.41
2	50:50	16.5	950	46.82	42.97	8.64	15.20	12.37	10.27	29.00	42.89	26.08
3	50:50	23	950	43.14	49.70	9.47	14.43	14.01	13.59	22.38	46.56	29.37
4	75:25	163	950	70.00	23.80	5.10	34.33	36.16	36.34	52.54	38.19	8.22
5	25:75	139	950	21.57	69.43	7.86	6.15	6.46	6.81	7.49	36.54	55.19

Table 4.4: HT measurement campaign: comparison of long-term measurement results. The table displays the final HT concentration for the LARA cell under continuous laser irradiation c_{perm} and the HT concentration value for the second LARA cell c_{cell}, the big c_{cell} and small c_{small} vessel after the long-term measurement. The last three columns show the difference in HT concentration between the last measurement point of the continuous measurement c_{perm} and the three containers.

run	$c_{perm,end}$ (%)	$c_{cell,end}$ (%)	$c_{big,end}$ (%)	$c_{small,end}$ (%)	$c_{perm} - c_{cell}$ (% points)	$c_{perm} - c_{big}$ (% points)	$c_{perm} - c_{small}$ (% points)
2	35.59	41.40	40.03	42.81	-5.81	-4.44	-7.22
3	39.46	42.58	45.52	45.29	-3.12	-6.07	-5.84
4	37.33	35.57	37.23	37.07	1.76	0.10	0.26

during the preparation the gas was circulated for 10 min to ensure good mixing. This time is already too long. Therefore, the time was reduced to 5 min. The concentration development for the next four runs is shown in figure 4.5 for the second and third runs and in figure 4.6 for the fourth and fifth runs.

The results of the experimental fit and additional run information are summarised in table 4.3.

The investigations of the laser influence and the exchange with molecules from the surface of the stainless steel vessels were carried out during the second, third and fourth measurement runs. The results are summarised in the table 4.4.

Data analysis and discussion The first thing to note is that the time constants of HT conversion are two orders of magnitude smaller than those of HD conversion. It is therefore possible to measure the conversion process up to thermodynamic equilibrium. The comparison of the time constants of the first three runs with each other is difficult, because also in the following two runs there was always an initial concentration between 8 % and 9 % of HT and also the initial concentration of H_2 and T_2 were not identical. In the second measurement run the initial concentration of H_2 was 46 % and in the third campaign 42 %. Nevertheless, the deviation under the time constants of the HT conversion is much less pronounced than that of the HD conversion, which is due to the fact that a possible influence of the laser is weaker here. The change in the initial ratio can be seen directly from the time constants. From the fifth run it is clear that a

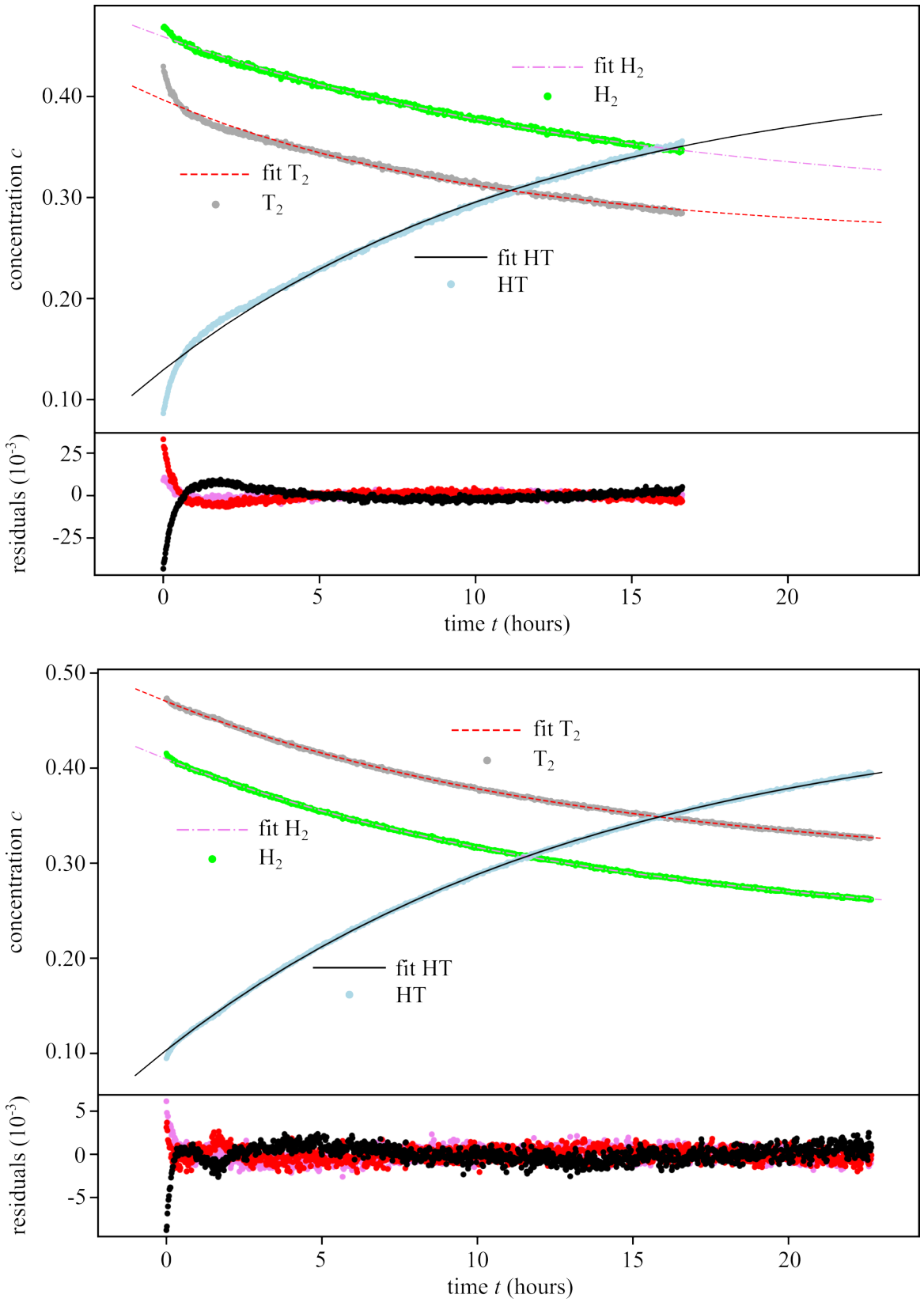

Figure 4.5: HT measurement campaign run 2 and 3: concentration profile. The concentration is plotted as a function of time. The curves represent the exponential curve fit. The subplots show the residuals of the fit. As can be seen, although a 50:50 mixture was aimed for in, there is always an initial concentration of HT and also the same initial ratio of H_2 to T_2 is technically difficult to reproduce.

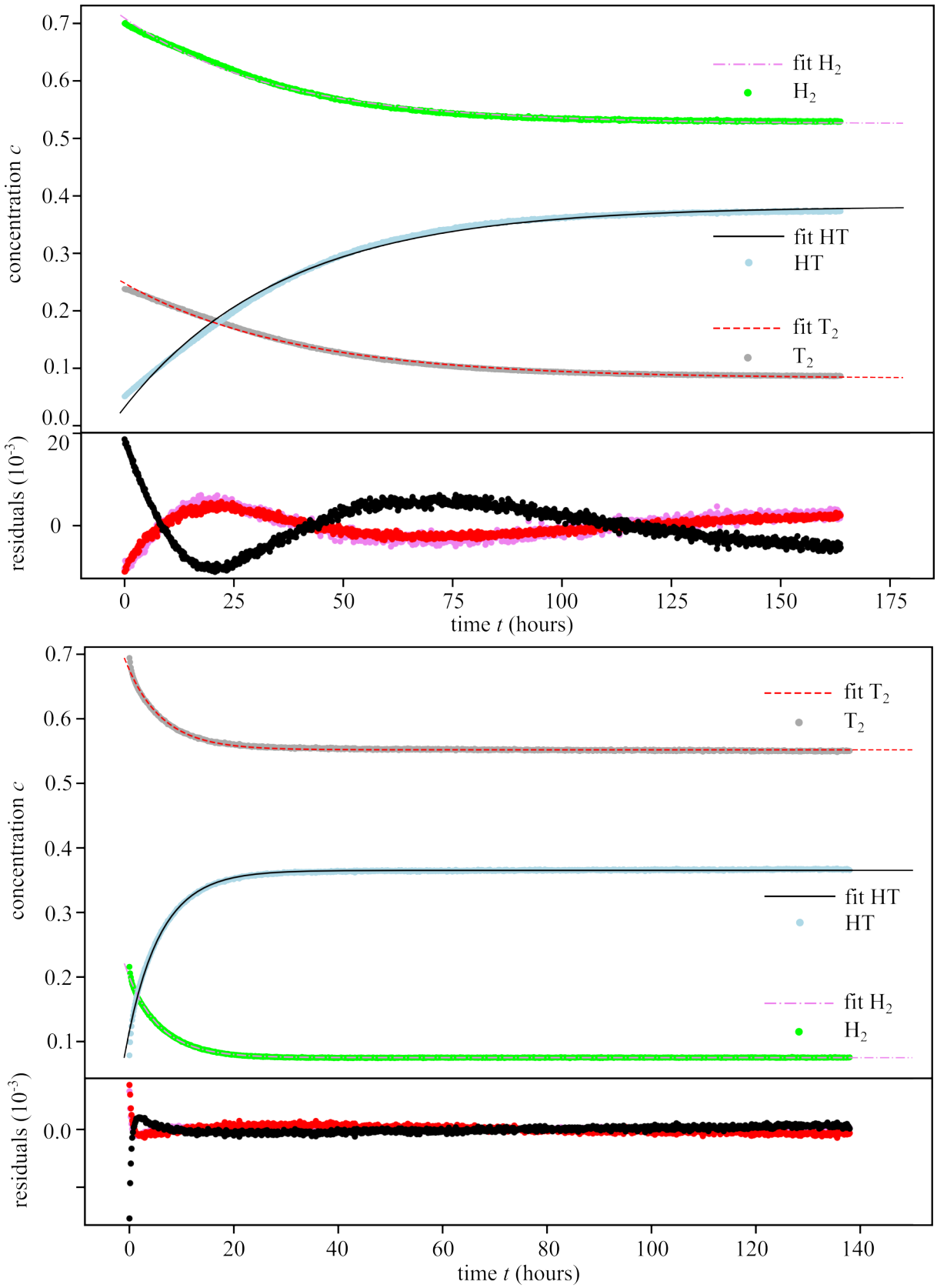

Figure 4.6: HT measurement campaign run 4 and 5: concentration profile. The concentration is plotted as a function of time. The curves represent the exponential curve fit. The subplots show the residuals of the fit. For visualisation only every eighth measurement point is shown. Run 4 has an initial concentration of 75:25 H_2:T_2 and run 5 of 25:75 H_2:T_2.

higher amount of tritium leads to a faster conversion to equilibrium. There, the time constants are between 6.15 hour and 6.81 h. In contrast, the fourth run with 75 % H_2 has a slower time constant of 34.33 h to 36.34 h. Compared to the literature, the obtained time constants are two orders of magnitude larger. Uda et al. [Uda92a] measured time constants of $5.54 \cdot 10^{-2}\,h^{-1}$. Further investigations are therefore needed to determine the time constants more accurately and precisely.

At the beginning of each measurement, there is more fluctuation in the measurement points. This can also be seen in the fit and the residuals. The slope is stronger at the beginning. This is particularly evident in the second run. There seems to be a second process underlying this. According to Fischer et al. [Fis11] there is a second slope due to second-order wall-gas interactions with the hydrogen reservoir given by the stainless steel walls. However, this process is described by a longer time constant and therefore does not explain the present phenomenon. There was also a small deviation in the HD conversion for the very first measurement points. The graphs show that the gradients are larger at the beginning, i.e. more HT is formed. It is not clear what effects are at work here.

In the case of the investigations into the influence of the laser and the surfaces of the stainless steel containers, the measured values of the second and third runs show that more HT was formed than during the actual measurement. The fourth run showed less HT. At first glance, these results appear to be contradictory. However, it should be noted that the second and third runs were significantly shorter. McConcille et al. [McC83b; McC83a] showed in their studies that low levels of CT_4 contamination slow down the reaction rate by a factor of 10. This means that as time goes on, the proportion of CT_4 increases and tritium no longer participates in the isotopic search. This would be visible in the fourth run with less HT.

Conclusion: Studies of the isotope exchange reaction with tritium and hydrogen have shown that the presence of tritium speeds up the reaction by two orders of magnitude. This is due to the ions and electrons produced during the decay, which in turn trigger further reaction channels. The influence of the laser or the surfaces of the stainless steel containers could not be clearly demonstrated, so further research is needed in this area. With regard to practical handling, it has been shown that the mixing of the gas and the filling of the LARA measuring cell must be carried out much more quickly. Too long circulation times lead to incipient conversion. It is also difficult to obtain the purest possible mixtures of HT or, later, DT at the beginning in the current setup because the tritium gas from the ISS consists of only 98 % pure tritium, the remaining percentages being admixtures of deuterium or hydrogen.

4.2.4 Conclusion and impact on the T_2ApIR design

Based on the results of the previous studies of the isotope exchange reaction of hydrogen with deuterium and of hydrogen with tritium, the following conclusions can be drawn for the design of T_2ApIR.

Sample preparation must be carried out carefully, especially in the presence of tritium. The circulation times for mixing the gas volumes must be kept as short as possible in order to avoid premature conversion processes. Conversion processes with tritium are significantly faster (two orders of magnitude) than those for the HD formation, which is consistent with the assumption that the radioactive decay opens up new reaction channels for the ion and the β-electron. Raman spectroscopy was found to be a suitable measurement method. When

investigating HD conversion, the sample should not be permanently exposed to light. But also for HT or DT investigations it can be useful not to measure permanently. With the new T_2ApIR setup it is then possible to investigate conversion processes as a function of pressure and temperature. Further investigations into the influence of the laser beam and the metal surfaces can be performed with T_2ApIR in both the warm and cold regions. Systematic parameter studies in the warm and cold region will allow a deeper and better understanding of the underlying physical processes.

In the next section, the RaCoon setup and the catalytically accelerated conversion studies are presented.

4.3 The Raman catalytic ortho-para normalizer (RaCoon) experiment

Within the framework of this thesis, both the RaCoon experiment and the LARA4 system were designed and set up for accurate and real-time op and chemical conversion studies of the inactive hydrogen isotopologues H_2, HD and D_2. With regard to the design of the T_2ApIR experiment, RaCoon was built to perform pre-investigations

1. on the op conversion,
2. on the calibration of the LARA4 system for the simultaneous measurement of op and chemical composition,
3. for the verification of the thermal cycle measuring principle,
4. on catalysts for chemical and/or op conversion as a function of system parameters, such as temperature, pressure and flow, as well as catalyst material properties, such as grain size and porosity,
5. on the influence of gas admixtures on conversion processes, and
6. on the detection of very short circulation times with LARA4.

The measuring principle is a combination of two technologies: a thermally adjustable conversion cycle, through which only a part of the gas volume is converted at a time, and an online and real-time determination of the op composition of the gas by LARA spectroscopy.

To study how quickly the gas composition changes within the thermal KATRIN cycle (warm to cold and vice versa), catalysts are required to force the gas mixture into different compositions. RaCoon allows the experimental study of catalysts for both the op and chemical conversion at the same time.

The scientific requirements of RaCoon are explained in section 4.3.1. The measuring principle of a thermal cycle as well as the technical realisation are discussed in section 4.3.2. Section 4.3.3 gives a brief overview of the measurements and their objectives with respect to T_2ApIR. The results of the measurements are discussed in detail in section 4.3.4. The summary and implications for the T_2ApIR design are the subject of the final section 4.3.5.

4.3.1 Scientific requirements of the RaCoon experiment

As described above, the RaCoon system, in combination with the LARA4 high performance measurement system, will allow a wide variety of pre-investigations for the op and the chemical

conversion studies in relation to the design of T_2ApIR. The scientific requirements for the RaCoon facility resulting from the overall objectives are as follows:

- advanced LARA4 system
  - parallel measurement of H_2, HD, and D_2 concentrations,
  - measurement of both op ratios of H_2 and D_2 and
  - inline and high detection frequency better than 1 min
- converter
  - adjustable temperature range of (77 – 500) K for cooling and activation
  - modular design for quick the catalyst material replacement
  - homogeneous heating during catalyst material activation
  - temperature process control within the converter
- control of impurities
  - leak tightness of 10^{-9} mbar l,
  - vacuum pumping to evacuate to a pressure of 10^{-6} mbar,
  - purging with noble gas
- operating modes
  - closed-loop operation: Contrary to experiments or technical arrangements, where the aim is to convert the gas volume quickly to thermodynamic equilibrium, a closed-loop mode (also called multi-pass mode) must be implemented in order to catalyse only a small part of the gas volume at a time. This increases the sensitivity for the detection of the various influences.
  - single-pass mode: For other investigations, e.g. to activate the catalyst material, the gas only passes through the converter once. Therefore, a single pass mode is also important, but plays a subordinate role.
- technical and other specifications
  - supply of different gases (H_2, D_2, He),
  - general guidelines for the safe handling of hydrogen at the TLK [Wel15].

The knowledge on which these requirements are based comes partly from the literature, but mainly from previous measurements and technical experience in dealing with hydrogen isotopologues at the TLK. In this context, the following works should be mentioned in particular: [Ric14; Mir14; Sch15d; Grö15b]. In his work, Richler [Ric14] investigated the difference between palladium and iron oxide as catalysts for the op conversion of hydrogen. Schmidt [Sch15d] in turn compared the chemical and op conversion of hydrogen for iron oxide. The dependence of the nuclear spin on the infrared absorption of liquid hydrogen isotopologues is simulated as well as experimentally investigated by Mirz [Mir14]. The study of the op conversion as a systematic influence on the calibration of the IR spectra of the inactive hydrogen isotopologues was part

of the work of Größle [Grö15b] with the Tritium Absorption Infrared Spectroscopy (TApIR) experiment, which is an important cornerstone for the follow-up experiment T_2ApIR.

In the following section, the experimental setup and the measuring principle of the RaCoon experiment are explained. The main focus is on the closed thermal cycle and the partial conversion.

4.3.2 Measuring principle and experimental setup

In order to achieve the objective described in the previous section, i.e. to systematically investigate the kinetics of the op conversion as a function of the system parameters and the material properties of the catalyst used, the RaCoon experiment uses a small amount of catalyst material and circulates the gas through the converter several times (circular approach). This makes it possible to determine the influence of changing variables (system parameters and catalyst properties) on the ortho and para concentrations.

Measuring principle Initially, the gas is circulated in the warm state at room temperature and the rotational states are occupied accordingly, see the first row in figure 4.7. The process of catalysis is initiated by ooling the converter. The gas is circulated in the closed system until it is completely in thermodynamic equilibrium according to the set temperature in the converter. The measurement of the op concentration is carried out again in the warm state using LARA spectroscopy. This is possible because the catalytic conversion is much faster than the natural conversion, see [Lar48; Rai63; Mil97; Pac08; Grö15b]. Due to the prohibition of op transitions (see section 3.5.2), no transitions can take place between the even and odd transitions. This means that the sum s_{odd} and the sum s_{even} are conservation variables during heating and cooling respectively, see row 2 and f in figure 4.7. This means that the op ratio with which the gas leaves the cold catalyst can be measured in the warm gas, although the occupation numbers of the individual J states change. Therefore, a measurement directly in the cold gas is required later. Figure 4.7 further illustrates this thought process.

The technical realisation of this measuring principle, taking into account the requirements of section 4.3.1, is presented in the next paragraph.

Experimental setup As explained in the previous two sections, the core of the RaCoon system is a closed-loop system that allows the op conversion from warm to cold and vice versa to be studied by LARA spectroscopy. Figure 4.8 shows a simplified sketch of the experimental setup. Hydrogen, deuterium and helium enter the system via the gas supply. The cycle looks like this: a buffer vessel, the converter with the catalyst material, the laser Raman measuring cell and a circulation pump. The detailed P& ID diagram of RaCoon can be found in the appendix A.

The individual components in detail:

- **Buffer vessel** The buffer vessel is made of stainless steel and has a volume of $\approx 1\,\mathrm{l}$. It can be shut off and bypassed via two manual valves. The RP001 pressure sensor measures the pressure in the vessel.
- **Converter** The converter consists of three individual U-shaped stainless steel pipes with an outer diameter of 10 mm and an inner diameter of 8 mm. These three pipes are connected

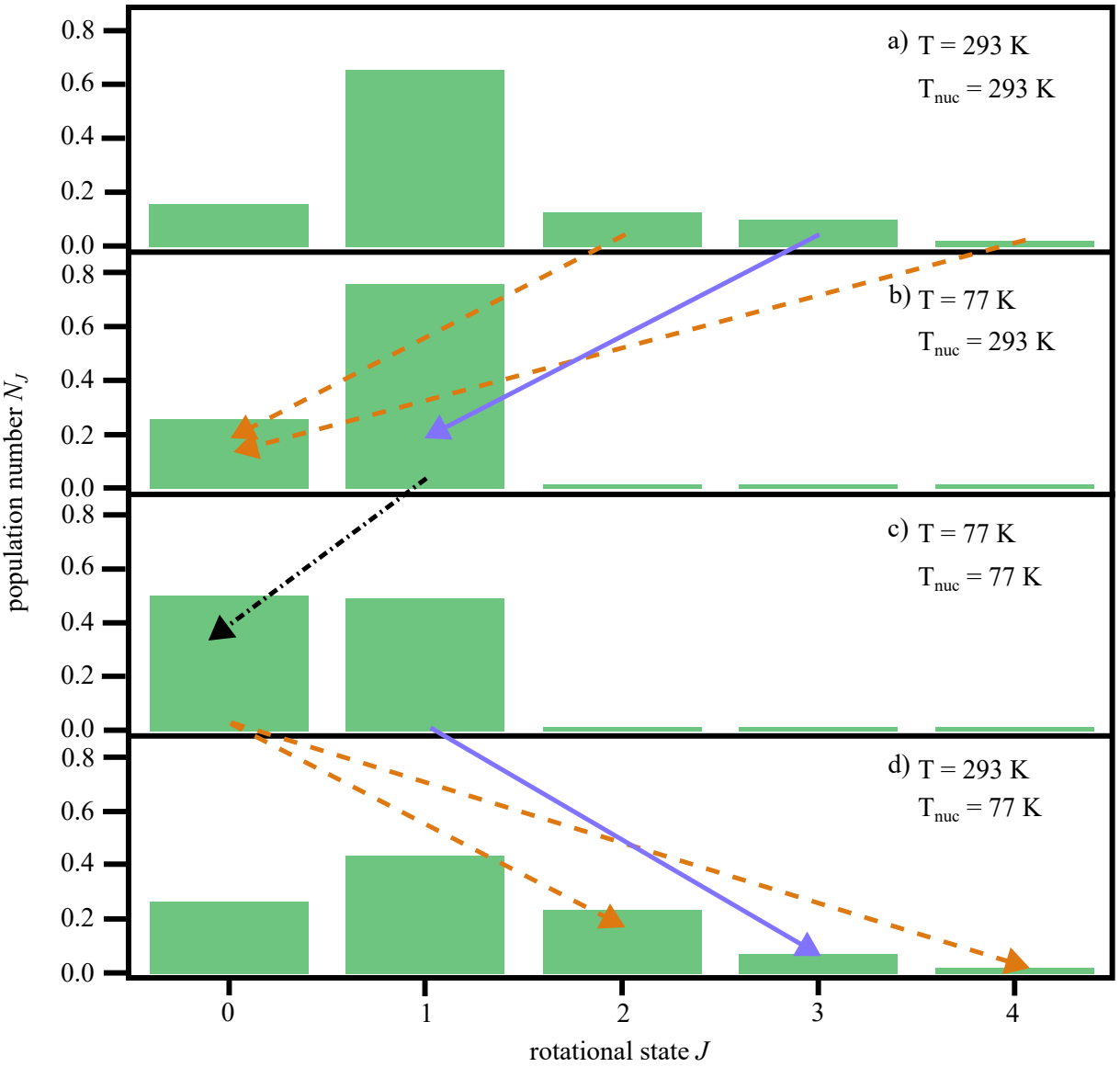

Figure 4.7: Population of rotational states in the thermal cycle of RaCoon. As a function of the first five rotational states, the respective population for the rotational temperature T and the nuclear spin temperature T_{nuc} is given. The first subplot shows the distribution of the rotational states in equilibrium when both temperatures are equal to room temperature. In the second subplot it can be seen that the molecules cool rapidly, but due to the prohibition of the op transition, the molecules can only change from an odd or even rotational state to an odd or even rotational state. Here illustrated by the dashed arrows. As soon as the transition prohibition is lifted by the onset of catalysis, the 50 % : 50 % ratio is established, see the third subplot and additionally also the figure 3.4. In the fourth subplot, the op ratio remains for 77 K, but the room temperature changes, which again allows the molecules to change only within an odd or even rotational state. This graph illustrates the measuring principle that a conversion occurring in the cold can be measured in the warm, since the natural conversion can be neglected with respect to the catalytic conversion, see section 3.6.3.

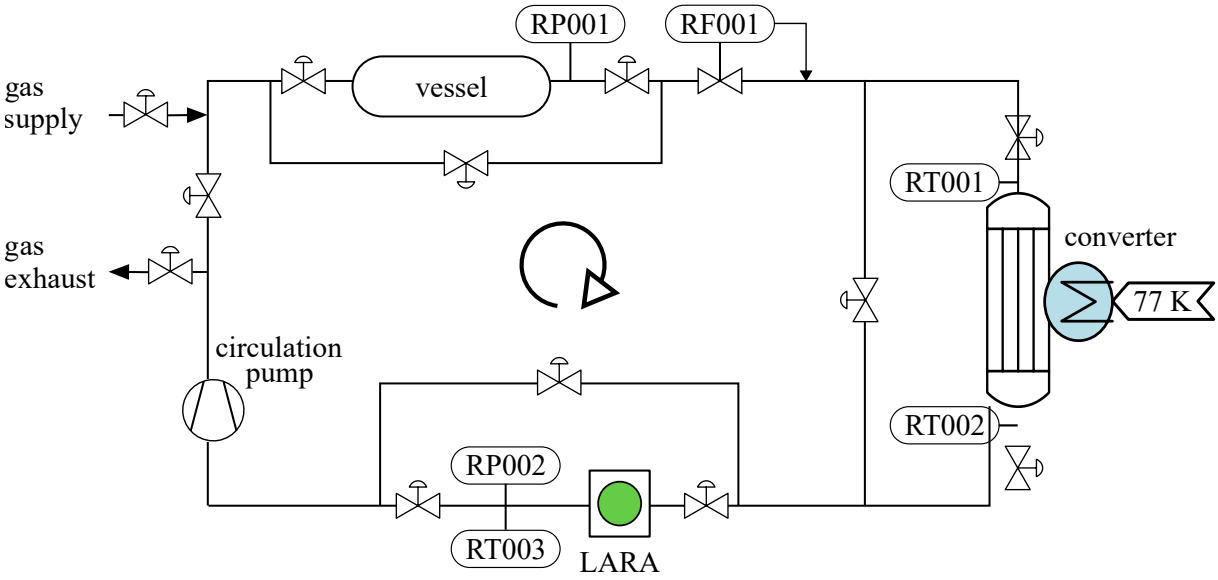

Figure 4.8: Flow chart of the RaCoon experiment. The simplified flow diagram shows that the gas enters the system at the top left, through a buffer vessel, then through the converter, to be measured in the LARA system. A circulation pump circulates the gas. All three main components (vessel, converter, laser Raman cell) can also be bypassed. With the pressure sensors RP001 and RP003, temperature sensors RT001 to RT003 and flow controller RF001. The gas leaves the system via the exhaust arrow. Not shown is a two stage pumping strain for evacuation and an additional connection for filling gas cylinders for external analysis.

in series. The middle tube contains the catalyst material, see figure 4.9, which can be immersed in a dewar filled with liquid nitrogen. The two additional u-tubes are used to ensure that the gas has already reached the cold temperature before it hits the catalyst material. At the inlet and outlet of the middle tube there is a Pt 100 sensor 1 cm above the material to measure the temperature. There is also a second path so that the gas can be bypassed at the converter if necessary.

- **Catalyst material** The catalyst material used is iron oxide Fe_2O_3 from Sigma Aldrich. Initially there was 25 g and later 18 g in the converter. The grain size is between 0.7 and 1.1 mm. To activate the material, a heating jacket is used that can be heated up to 200 °C and wrapped around the converter.

- **Laser Raman system and LARA cell** RaCoon uses a LARA system developed at TLK, namely LARA4. The measuring principle and the experimental setup of a LARA system are explained in the previous section 4.2.2. The LARA4 system uses a LARA cell with 3 fused silica viewports. The LARA cell can also be flowed through. A green laser of 2 W and 532 nm is used.

- **Pumps** The circulation pump is a Normetex scroll pump. The pumping unit for evacuating the system consists of a Roots pump (Adixen ACP 15) as a pre-vacuum pump and a turbo molecular pump for the vacuum (Pfeiffer HiPace 300). This allows the system to be evacuated to a pressure of 10^{-6} mbar.

- **Sensors** Three Pt 100 sensors, two on the converter and one on the LARA cell, are used to monitor the temperature. Pressure is measured by a Honeywell sensor (SPTmA0015PA9B) on the buffer vessel and an MKS Baratron (750C51PCD4RA) on the LARA cell. A third

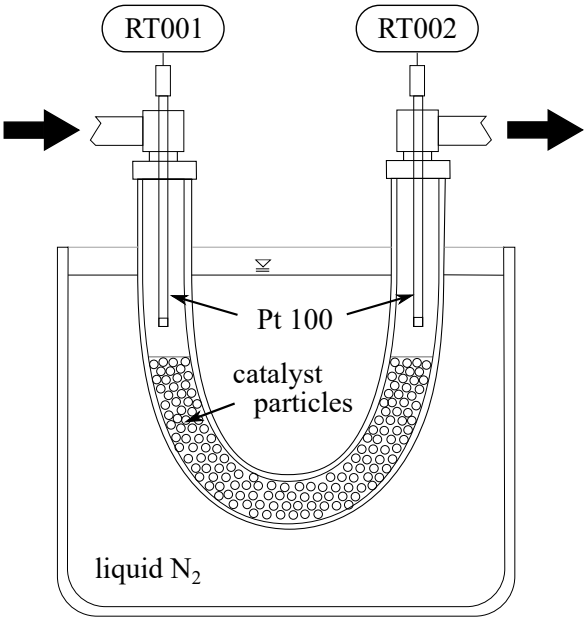

Figure 4.9: Technical scheme of the op converter. A cross-section of the converter is shown. The converter consists of three U-shaped pipes, the middle one is shown here. The catalyst material is filled into the centre of this pipe. A Pt100 sensor for measuring the gas temperature is located at the inlet and outlet, just 1 cm above the filling. The Pt100 sensors are welded directly into the VCR connection. In addition, there is a sealing frit in the VCR connection at the inlet and outlet to prevent any catalyst material from being carried into the system by the gas stream. The converter is then cooled by a dewar filled with liquid nitrogen.

pressure sensor is installed at the pumping station. This is a Pfeiffer PKR361. A Bronkhorst El-Flow series sensor (F-201CV 20K) is used for measurement and also for setting the desired flow. The measuring principle of the flow sensor is based on the measurement of the heat capacity. For this purpose, part of the gas flow is passed through a bypass. The temperature of the gas is measured with a thermal resistor. The gas is then heated by an electric heater at a constant power. The temperature is then measured again and the diverted mass flow is returned to the main flow. The temperature difference is proportional to the mass flow and proportional to the heat capacity. At room temperature, there is a 5 % difference in heat capacity between pure ortho and pure para hydrogen. The sensor is calibrated to a room temperature hydrogen mixture. The conversion changes the para and ortho fractions and thus also the total heat capacity. The sensor adjusts accordingly, which is undesirable for constant flow experiments. Therefore, the aperture at the output of the sensor is set to a fixed value so that it is not controlled but only measured. The measured flow can then be corrected using a correction term of the company[3].

The whole system is designed to withstand a total pressure of 1 bar absolute.

Mode of operation There are generally two ways of operating the RaCoon system. In most cases, closed-loop operation (also known as multi-pass operation or circular approach) is used, where the gas is circulated through the converter several times. In single-pass operation, the manual valve between the pumping station and the inlet is closed. As a result, the gas flows

[3] Subsequent measurements have shown that the systematic uncertainty is always less than 0.5 %. This is smaller than the combined measurement uncertainty from the systematic and stochastic contribution of 1 %.

continuously through the converter, through the LARA cell and is then pumped out directly. The following is an overview of a measurement procedure in the multi-pass mode:

- The system is filled with hydrogen and deuterium up to the desired partial pressures.
- The gas is then circulated through the system, through the converter, several times at room temperature. The LARA system measures the concentration during this process.
- The nozzle inside the flow meter is adjusted to the desired opening position.
- The next step is to cool the converter to 77 K in a dewar.
- The gas circulates until equilibrium is reached in the cold. Meanwhile, the LARA system continuously monitors and records the gas composition.
- At the end of the cold measurement phase, the converter is reheated and the op conversion from cold to warm can be observed.

Summary In conclusion, this experimental setup allows the study of the conversion characteristics of the op conversion depending on the system parameters and the material properties of the catalyst. It is also possible to investigate the conversion from room temperature to 77 K and from 77 K to room temperature. The LARA system allows a direct determination of the concentration independent of temperature or flow. This is a significant advantage over methods based on heat capacity, heat conduction or ortho-para conversion, as these methods use the energy released and rely on the overall heat transport to the measuring cell not being disturbed and on stable temperature conditions. In addition, such methods cannot detect near equilibrium because the energy released is too small. The LARA system can also detect contamination by other molecules such as oxygen, water or methane, which means that the effect of poisoning[4] of the converter on the conversion can also be investigated. As the LARA system can also measure the HD concentration, it is possible to determine the chemical contribution to the conversion. Thus, the above mentioned conditions for the system are met by the chosen methods and by the chosen components, so that conversion studies are possible.

A more detailed description of this section can be found in our publication [Kra22].

In the next section, the individual measurements and their results are discussed, as well as the implications for the design of the T_2ApIR experiment.

4.3.3 Objectives of the measurements carried out

Since the commissioning of the RaCoon system, up to 80 measurement campaigns have been carried out. The following overview presents the objectives of the measurements performed in relation to T_2ApIR.

- Does the measuring principle work? The proof of principle is to verify that the concept (closed loop and partial conversion in the multi-pass mode) works and that the time constants of the op conversion can be calculated from it and thus transferred to measurements on tritiated samples with T_2ApIR.

[4] Impurities such as water can be deposited on the surface of the catalyst and reduce its activity. This phenomenon is called poisoning.

- Simultaneous measurement of the op and chemical composition with LARA4.
- How must the gases be prepared in T_2ApIR? Examinations are carried out to determine the influence of gas admixtures on the op conversion.
- What is the geometry of the converter and what temperature must be reached for activation? It will be shown that the design of three U-shaped stainless steel pipes connected in series is a practical and sufficient converter design. Systematic investigation of the temperature dependence for the activation of the catalyst material will answer this question.
- Further investigations include:
  - Influence of the mass flow on the conversion using the RF001 flow controller.
  - Theoretical modelling of the RaCoon system to predict the temperature dependence of the rate constant k.
  - Contribution of chemisorption to the temperature dependence of the rate constant k by measuring the HD concentration.

In the next section, the individual measurements, their results and the implications for T_2ApIR are explained.

4.3.4 Ortho-para conversion studies

The results of this work were largely derived from supervised bachelor's, master's and diploma theses according to [Alt17; Smo18; Süß18; Pod19].

4.3.4.1 Proof of principle and determination of conversion time constants

The aim of this measurement campaign is to demonstrate the feasibility of the measuring principle and the extraction of time constants. The data shown here are from the experimental run36 and are presented in figure 4.10 for the time window between 1124 min and 1404 min. A detailed description of this measurement campaign can be found in [Kra22].

Preparation The system was purged of impurities by flushing with fresh hydrogen gas for several times. The catalyst material was activated at 120 °C for three days with continuous evacuation. Finally, the system was filled with 700 mbar, as shown in figure 4.10, subplot b).

Measurement After the system was filled, the gas was circulated for some time. The converter was then alternately cooled down and heated up for 10 cycles to measure several half-life times constants. Figure 4.10 shows the results for a cooling down and heating up cycle between 1124 min and 1404 min.

Analysis A measured Raman spectrum of the first five rotational excitations is shown in figure 4.11. The ortho-para ratio was extracted by adding up the occupation number N for even and odd states respectively, see figure 4.10 subplot d). The relative ortho fraction is given by

$$x_\mathrm{o} = \frac{\sum N_{J=\mathrm{odd}}}{\sum N_{J=\mathrm{odd}} + \sum N_{J=\mathrm{even}}}, \tag{4.5}$$

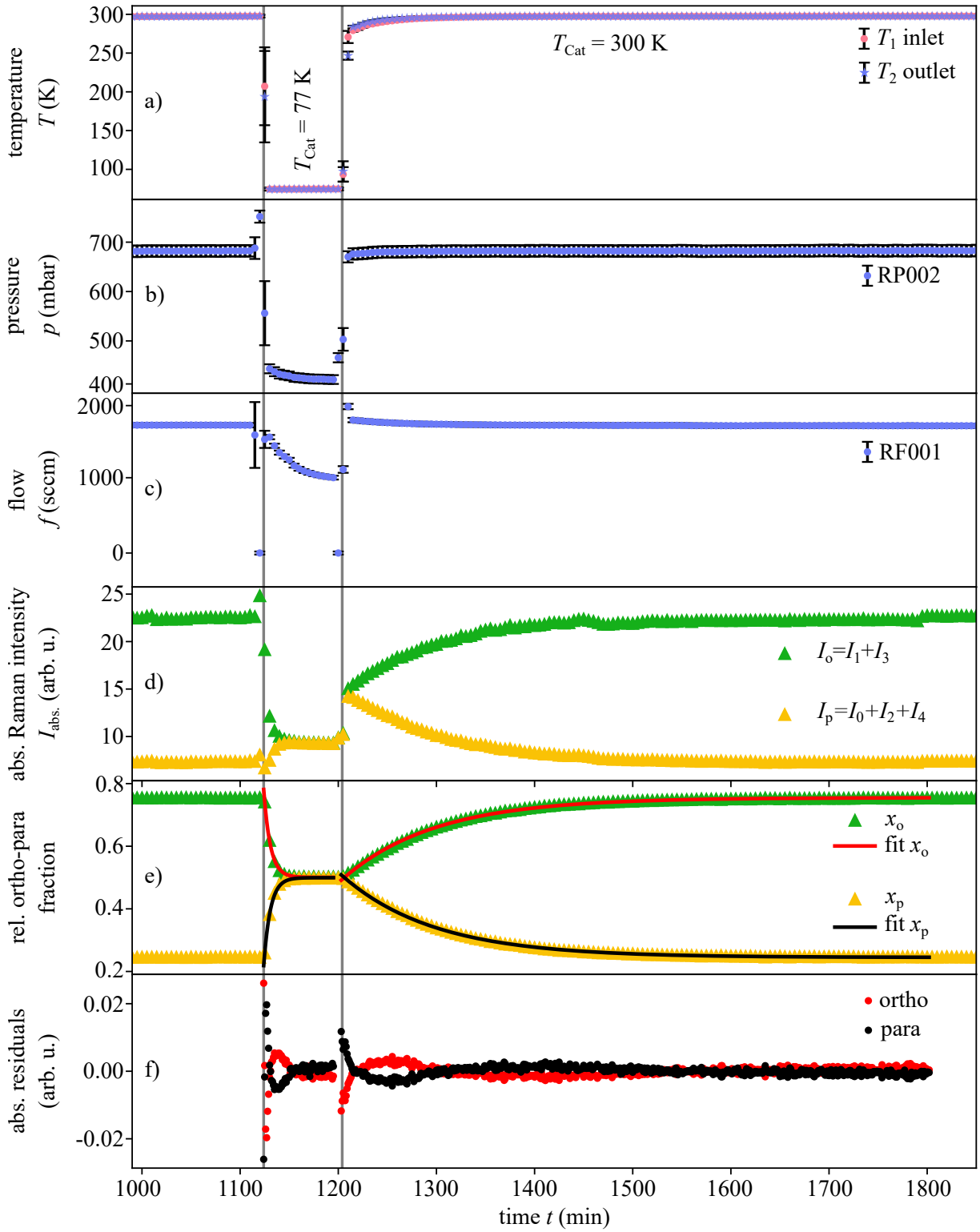

Figure 4.10: Ortho-para conversion for a thermal cycle. The corresponding curves are shown for a conversion from warm to cold and from cold to warm. The first subplot a) shows the temperature at the inlet and outlet of the converter. It can be seen that the cooling process is faster than the heating process. The pressure curve at the LARA cell is shown in the second subplot b). The flow is measured with RF001 and is shown in the third subplot c). The measured absolute Raman intensities I correspond to the ortho I_o and para Ip states added together. The resulting relative proportions x_o and x_p are shown in the next subplot e). In addition, the fit functions are plotted in e). The final subplot f) shows the residuals of the fits.

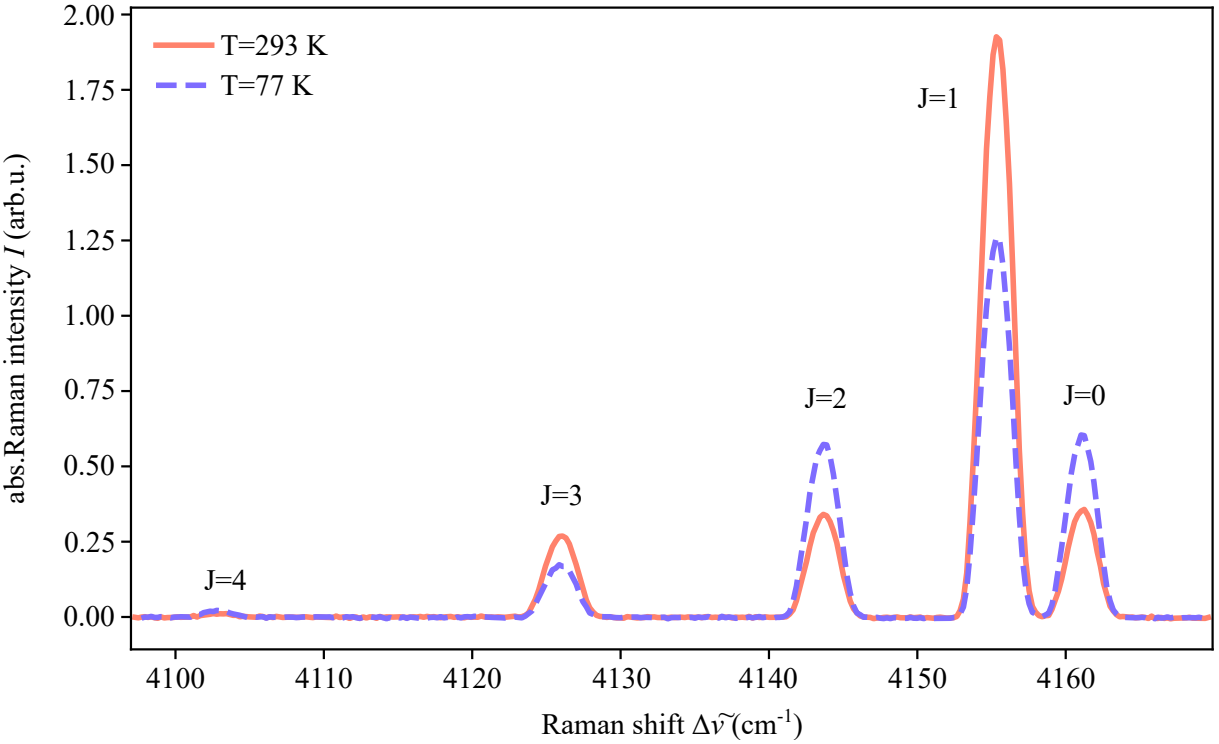

Figure 4.11: Raman spectrum of the Q_1 branch of hydrogen at room temperature. The two Raman spectra were each recorded at room temperature, but for the equilibrated op compositions at room temperature and 77 K, i.e. after conversion. The measured intensities of the first 5 rotational levels of the Q_1 branch are plotted as a function of the Raman shift. The Raman shift is proportional to the energy difference between the laser light and the scattered molecule. The Q_1 indicates with Q no rotational change and the 1 indicates one vibrational excitation. It can be seen that all even J states increase and all odd states decrease, so the op ratio decreases.

see subplot e). To extract the time constant τ, an exponential function f

$$f = a + \cdot b \exp -\frac{t}{\tau}, \tag{4.6}$$

with t as time and a, b as constants is fitted. See 3.6.3 for the theoretical background.

Results for one selected cycle The extracted time constants for the cycle shown in figure 4.10 are

$$\begin{aligned} \tau_{\text{cold}} &= 6.8\,\text{min}, \\ \tau_{\text{warm}} &= 94.4\,\text{min}. \end{aligned} \tag{4.7}$$

The relative ortho concentrations for the warm and the cold equilibrium are

$$\begin{aligned} c_{\text{o,cold}} &= 0.501, \\ c_{\text{o,warm}} &= 0.755. \end{aligned} \tag{4.8}$$

These values are within the accuracy of the uncertainty budget of the whole setup, which is mainly dominated by the trueness of the calibration process, see [Kra22]. In this very first run, the repeatability of the extracted time constants τ is better than 10 %. One reason for this is that

the catalyst material was best activated at the end, as even the purging with hydrogen at room temperature helped to clean the catalyst's surface. However, further investigations are needed to determine the influence of temperature and purging on the activation process.

Conclusion and discussion The time evolution of the system parameters and of the measured op ratios shown in figure 4.10 enable the feasibility of the measuring principle and the resulting experimental setup to be demonstrated. The circular approach allows systematic conversion studies of the op conversion for the transition from cold to warm and vice versa. The extraction of the time constant τ is a quantification of the activity of the catalyst material. By changing other parameters (catalyst material or pressure and flow) further investigations are possible.

For the experiment, this means that small amounts of catalyst material and partial conversion allow studies to be carried out on tritiated mixtures. The conversion is further accelerated by the β-decay of tritium, which means that a smaller amount of catalyst material is required. The design of a U-shaped converter with temperature sensors and frits is transferable, see figure 4.8, and allows the catalyst material to be changed.

4.3.4.2 Influence of impurities on the ortho-para catalytic process

Impurities such as water can be deposited on the surface of the catalyst material, reducing its efficiency. This phenomenon is known as catalyst poisoning and is investigated in this section. Water is typically present as a residual moisture of 0.5 ppm in a gas bottle filled with hydrogen as used at the TLK.

Apart from water, other impurities will also occupy the surface of the catalyst and thus inhibit its activity and, crucially, the conversion rate. The following measurement was carried out with a mixture of 66.0 mol % hydrogen and 33.9 mol % humid air. The system was pressurised to 750 mbar. The measurement lasted one week. The results are shown in figure 4.12. The following observations can be made from the time evolution of each parameter. Firstly, the temperature T is not affected by the water contamination. It is noticeable that the pressure p and the absolute intensities $I_{\text{abs.}}$ decrease by about 15 %. The mass flow f increases by 25 %. The op ratio obtained in the cold is 61 %:39 %, which is greater than the 50 %:50 % expected for hydrogen at 77 K. The characteristic changes can be described by the following equation

$$2H_2 + O_2 \rightleftharpoons 2H_2O\,. \tag{4.9}$$

The pressure decrease can be explained by the fact that, according to the ideal gas equation [Atk06]

$$p \cdot V = n \cdot R \cdot T \tag{4.10}$$

with p as pressure, V as volume, n as number of particles, R as gas constant and T as temperature, the pressure p in a closed system decreases as the number of particles n decreases. According to the above reaction, there are three particles on the left and only two particles on the right. The total number of particles n has therefore decreased. The absolute Raman intensities $I_{\text{abs.}}$ decrease as does the pressure. Due to the above reaction, hydrogen is "lost"and since the Raman intensity is proportional to the number of particles, it also decreases. The mass flow f is proportional to the specific heat capacity. This is about three times greater for water than for hydrogen. Due to the limited solubility of water in the gas mixture, the increase in mass flow is

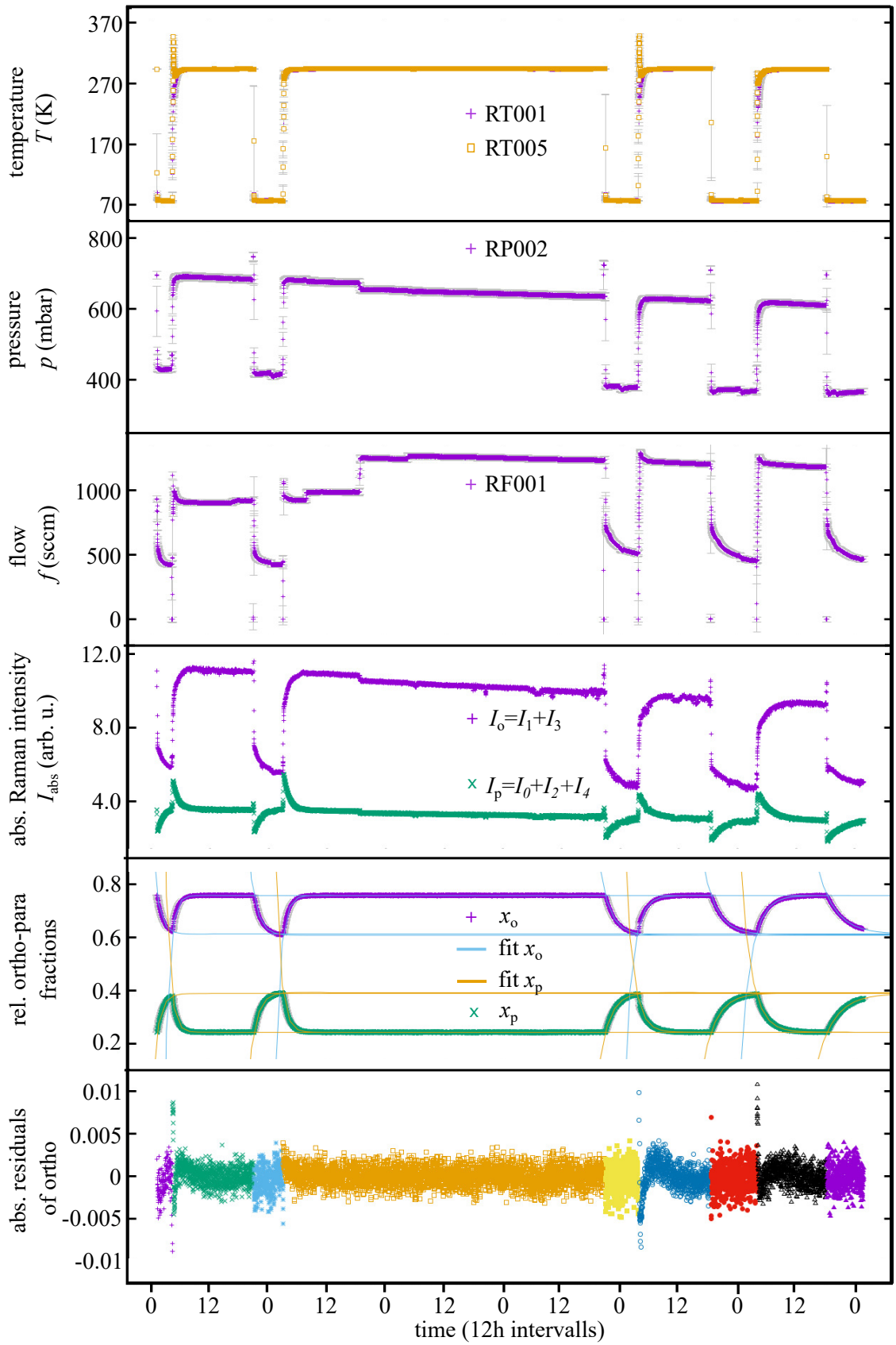

Figure 4.12: Influence of water on the op conversion of hydrogen gas. As a function of the time (12 h intervals), the temperature T, the pressure p, the flow f, the absolute Raman intensities for ortho and para and their fractions are shown for 5 cooling downs and heating cycles. In addition, the fit curves and their residuals are shown at the bottom. The data were acquired during RUN033.

limited. The op ratio measured in the cold is 61 %:39 %. This means that there is less para than normal at 77 K, see figure 3.4. The reason for this is that oxygen gas is paramagnetic and thus catalytically accelerates the reaction [Nie67]. As oxygen is also present in the warm part of the system, the op mixture there is driven towards the thermal equilibrium of room temperature, working against the cold equilibrium. This is why the equilibrium is reached. The reaction rate decreases by 2/3 during the measurement and is a factor of 10 lower than in measurements with pure hydrogen. The reason for this is that the air components occupy the surface of the catalyst and reduce the active surface area [Wei60].

Conclusion and discussion This measurement campaign showed that water H_2O or oxygen O_2 have a negative effect on the op conversion. On the one hand, foreign particles occupy the active surface of the catalyst and thus reduce its activity. In the case of oxygen, it is also the fact that it is paramagnetic and therefore has an additional catalytic influence on the conversion. As a result, the equilibrium shifts to an average value of room temperature and 77 K equilibrium value. For the T_2ApIR experiment, it follows that a system must of course be closed and there must be no leaks through which air and thus oxygen can enter the system. Since commercial gas bottles for hydrogen and deuterium always contain a residual moisture content of 0.5 ppm, the gas must be purified accordingly before entering the system. This requires the use of molecular sieves or gas filter cartridges, otherwise measurement results will be distorted. In the case chosen here, a larger amount of air was deliberately fed into the system to illustrate the effect. However, for high accuracy analysis and calibrations, even small amounts are critical. This also has implications for the catalyst material. The material inevitably comes into contact with air when it is filled into the converter. Simply pumping it out will not completely remove the air molecules on the surface. Therefore, the catalyst material must also be activated by heating it to at least 100 °C.

An activation strategy is developed in the next section. In a first step, the temperature dependence is investigated.

4.3.4.3 Activation strategy of the catalyst material iron oxide Fe_2O_3

The investigations in this section were mainly performed as part of the bachelor thesis by Gerold Podbielski [Pod19] under my supervision. An important systematic contribution is made by the activation of the catalyst material. As shown in the previous section by means of the poisoning of the catalyst material, the activity of the catalyst is reduced by foreign atoms on its surface. In particular, the exchange with oxygen leads to a reduction of the active surface. In order to reactivate the surface of the catalyst, it must be activated accordingly. The activation temperature plays a crucial role [Wei58b]. The duration of the purging process and the recovery are therefore of secondary importance. Therefore, in a first step, the temperature dependence of iron oxide activation was investigated. The air molecules physisorb onto the surface and reduce it. In the case of α-iron(III) oxide, this reacts with water to form α-iron(III) oxide hydroxide. This substance is capable of absorbing additional water as water of crystallisation. To prevent this process, the sorption behaviour must be shifted in the direction of desorption. This is done by reducing the partial pressure of the gas in the system and increasing the temperature of the catalyst material. There are several proposals in the literature for the activation of iron oxide, some of which are contradictory and do not take all parameters into account. Weitzel et al. [Wei58b] activated the material at 1 mmHg ($\approx$ 1.32 mbar) for 16 hours. According to

the results, the best activation is obtained between 110 °C and 120 °C. Above 140 °C there is, according to Weitzel, the catalyst is destroyed. In the work of Essler [Ess13] nitrogen is used as a carrier gas. The investigations showed that 120 °C gives the best activation. Essler found no destruction at temperatures above 140 °C. The manufacturer Molecular Products, on the other hand, recommends heating the catalyst to 160 °C for more than 16 hours. This is done by purging with a constant hydrogen gas flow at 1200 volume units per volume unit of catalyst material. The hydrogen gas flow is not circulated, but is passed over the material once.

Due to the contradictory and sometimes also very complex activation strategies in the literature, and because reproducibility is more important for T_2ApIR and, in addition, mainly hydrogen and occasionally noble gases are studied due to the reactions resulting from radiolysis, the following activation strategy is adopted.

- The RaCoon system is filled with hydrogen to 500 mbar.
- Apply the heating jacket and close the valves on the converter.
- Heat the converter to the desired temperature.
- Open the valves on the converter, switch on the circulation pump and fully open the internal valve of the flow sensor.
- Allow the gas to circulate for 2 hours.
- After two hours, evacuate the system and remove the heating jacket.
- Fill with fresh gas and start measuring the op conversion. Firstly, the single-pass mode measurement and secondly the multi-pass mode measurement.

This procedure was repeated three times for each temperature. This sequence was increased from 80 °C (non-activated catalyst as reference), in 20 °C steps up to 200 °C.

As explained in the previous two sections, the time constant τ is obtained by fitting it to the op fractions. This was done a total of three times for all temperatures. In all runs, there were three measurements each in the single-pass and multi-pass mode. Only the single-pass mode measurements are relevant for the study of activation. The ortho-para ratios of the individual measurements are shown as a function of temperature in figure 4.13. 4.13 It can be seen that the activation of the catalyst material improves with increasing temperature. In the single-pass mode, the op ratio approaches the equilibrium of 77 K with increasing temperature. This is true up to a temperature of 180 °C. Thereafter the activation seems to deteriorate. As the heating element can only be controlled up to 200 °C, tests at higher temperatures were not possible. It is also noticeable that the catalyst contributes to the conversion even without activation. The largest change occurs after the first activation and amounts to 3 percentage points. The outlier in the temperature range of 180 °C (run056) is due to the fact that the gas only partially flowed over the converter because the bypass valve was open. No material degradation could not be detected.

Conclusion This measurement campaign has shown that the activation is temperature dependent and that the best performance of the catalyst is achieved at 180 °C. Since temperature is only one effect, further investigations are needed. In particular, other measurement parameters and their influences need to be investigated with regard to the purging processes and their frequency,

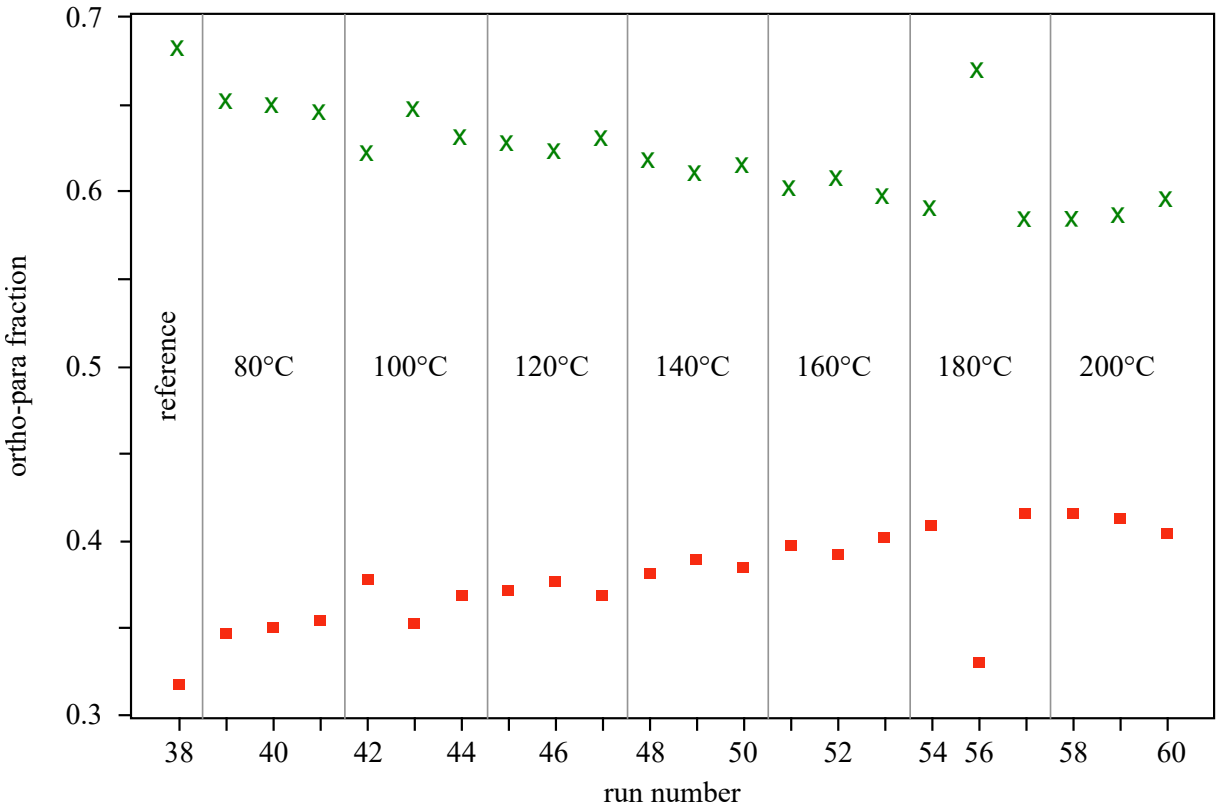

Figure 4.13: Temperature dependence of catalyst activation. The mean value of the op ratio is plotted as a function of each run. For each run, 10 min were measured in the equilibrium. These are the measurement point from the single-pass mode. RUN055 is missing due to an error in the data acquisition.

pressure and flow. For the design of the T_2ApIR experiment, it follows that the converter must be heatable to at least 200 °C. A homogeneous heating phase is just as important, as a previous version with heating wires along the U-tube did not achieve uniform heating of the catalyst.

4.3.4.4 Further Results

Further results from the numerous studies on conversion kinetics at the RaCoon facility are presented here. More detailed descriptions can be found in the corresponding theses.

- Oliver Süß [Süß18] found out that the converter should first be cooled down completely before the gas flows through it and the conversion starts. This means that measurements taken during the cooling process need not to be excluded from the subsequent analysis.
- In the course of the investigations by Arne Smolinski [Smo18], it was shown that the mass flow in the RaCoon system has no influence on the conversion rate.
- For a theoretical description of the system, the model of a PFR (plug flow reactor) fits well [Süß18]. Based on this theoretical model, the temperature dependence of the reaction constant K was simulated for the RaCoon setup. For the temperature dependence, all processes involved in the conversion such as adsorption, desorption, number of collisions with the surface must be taken into account. With this model it is then possible to predict the temperature dependence of the conversion process.

- Through the targeted addition of deuterium bunches in a hydrogen-filled cycle, circulation times and backmixing were studied, which had a direct influence on the theoretical model of the setup. The time constant of the backmixing is smaller than the time constant of the op conversion. Due to the exchange of D_2 with H_2, the formation of HD could be detected with LARA4. Thus, both conversions can be detected simultaneously.

4.3.5 Conclusion and impact on the T_2ApIR design

The previous explanations and results show that the developed measuring principle of partial conversion in combination with real-time and online measurement using laser Raman spectroscopy is an ideal solution for the closed-loop determination of the conversion rate as a function of various different parameters. The experimental setup allows both single-pass and multi-pass measurements depending on the experimental requirements. First measurement results confirmed the measuring principle and provided results for the time constant. Considering the uncertainties of the measurement setup, further systematic investigations are necessary.

For T_2ApIR this means that

- The measuring principle can be adopted and is also applicable to investigations of the kinetics of gas mixtures with tritiated molecules.
- The LARA4 system allows a simulated measurement of the op and chemical composition and can thus also be calibrated for different gas compositions.
- The U-shaped design with appropriate temperature sensors and sealing frits, proved to be useful. Exchange of catalyst material must be ensured.
- Activation of the catalyst material is necessary in any case. The results so far favour a temperature of around 180 °C, which means that appropriate heaters must be installed.
- Studies on reducing the activity of the catalyst material have shown that the gases to be used must be purified beforehand. Oxygen in particular has a negative effect on the conversion in two ways. Firstly, it blocks the surface and secondly, due to its paramagnetic properties, it converts the conversion to the warm equilibrium in the warm state.
- The measurement of backmixing shows that, in addition to op conversion, the chemical conversion can be measured and investigated simultaneously.
- Furthermore, based on the previous experiments and their results, it can be shown that physisorption processes occur more strongly at low temperatures than chemisorption processes. The latter increases with increasing temperature. The iron oxide used is a paramagnetic material and therefore mainly suitable as a physisorbed and thus op catalysing material at low temperatures. Palladium, on the other hand, is a suitable as a chemical converter at high temperatures.

Ortho-para conversion is not only important in relation for the KATRIN experiment, but also for fusion research (cryogenic destillation) [Grö15a] and for the liquefaction and storage of hydrogen as an energy carrier in industry, [Ber09; Car17; Yin19].

4.4 A combined IR and Raman system: reproducibility and coated mirrors

The diverse molecular effects in the thermal cycle of KATRIN require the use of both Raman spectroscopy and IR spectroscopy. Raman spectroscopy can be used to study conversion rates as well as equilibrium states, whereas IR spectroscopy is used to study molecular effects such as the dimer formation. This requirement necessitates the use of a common spectroscopic measurement setup for investigations in the cryogenic temperature range (10 – 300) K. As mentioned as the beginning of this section 4.1, the requirement to minimise thermal input means that the number of viewports of the cryogenic measuring cell must be reduced to a minimum, i.e. 2 windows, since transmission spectroscopy is used. All these requirements mean that the optical components used must either be suitable for both Raman and IR or that they must be movable.

This section is structured as follows: Section 4.4.1 outlines the objectives of the two measurement campaigns carried out with regard to the design of T_2ApIR. The results of the investigation into the reproducibility of the movement of the optical components are presented in section 4.4.2. Section 4.4.3 presents the results of the investigation into the suitability of silver- and gold-coated mirrors for use in Raman and IR spectroscopy. The lessons learned from this for the design of T_2ApIR are part of the final section in 4.4.4.

4.4.1 Objectives of the measurement campaigns

Most of the pre-investigations for the spectroscopic design of T_2ApIR was carried out during Svenja Müller's bachelor thesis [Mül19b]. In addition to the initial test setup of the individual spectroscopic components in the TLK's optics laboratory, her investigations include measurements of the reproducibility of the movement of optical components as well as the suitability of coated parabolic mirrors. Two objectives are being pursued:

1. **Reproducibility** Due to the wavelength optimisation of individual optical components such as mirrors or filters and the different beam paths of the two optical spectroscopy methods, optical components must be forcibly moved out of and back into the beam path. The aim of the study of the reproducibility of such movements is to check whether the precision requirements of KATRIN of 5 % for Raman and of 1 % for IR are still met. For this purpose, a mirror and a lens are mounted on a movable linear z-stage, which moves the components out of and back into the beam path. A spectrum is recorded after each movement.
2. **Coated parabolic mirrors** Other optical components, on the other hand, cannot be easily moved out of the beam path, such as two parabolic mirrors. The company Thorlabs offers silver- and gold-coated parabolic mirrors with the corresponding focal length requirements. To decide which coating is equally suitable for Raman and IR, the respective Raman and IT spectra of silver and gold are compared.

4.4.2 Reproducibility test of the moving linear z-stage

In order to determine the measurement uncertainty of the linear z-stage in relation to its precision during moviement, Raman spectra are recorded after each movement. The reason why only Raman spectra are recorded is that the optical components for IR spectroscopy are not moved.

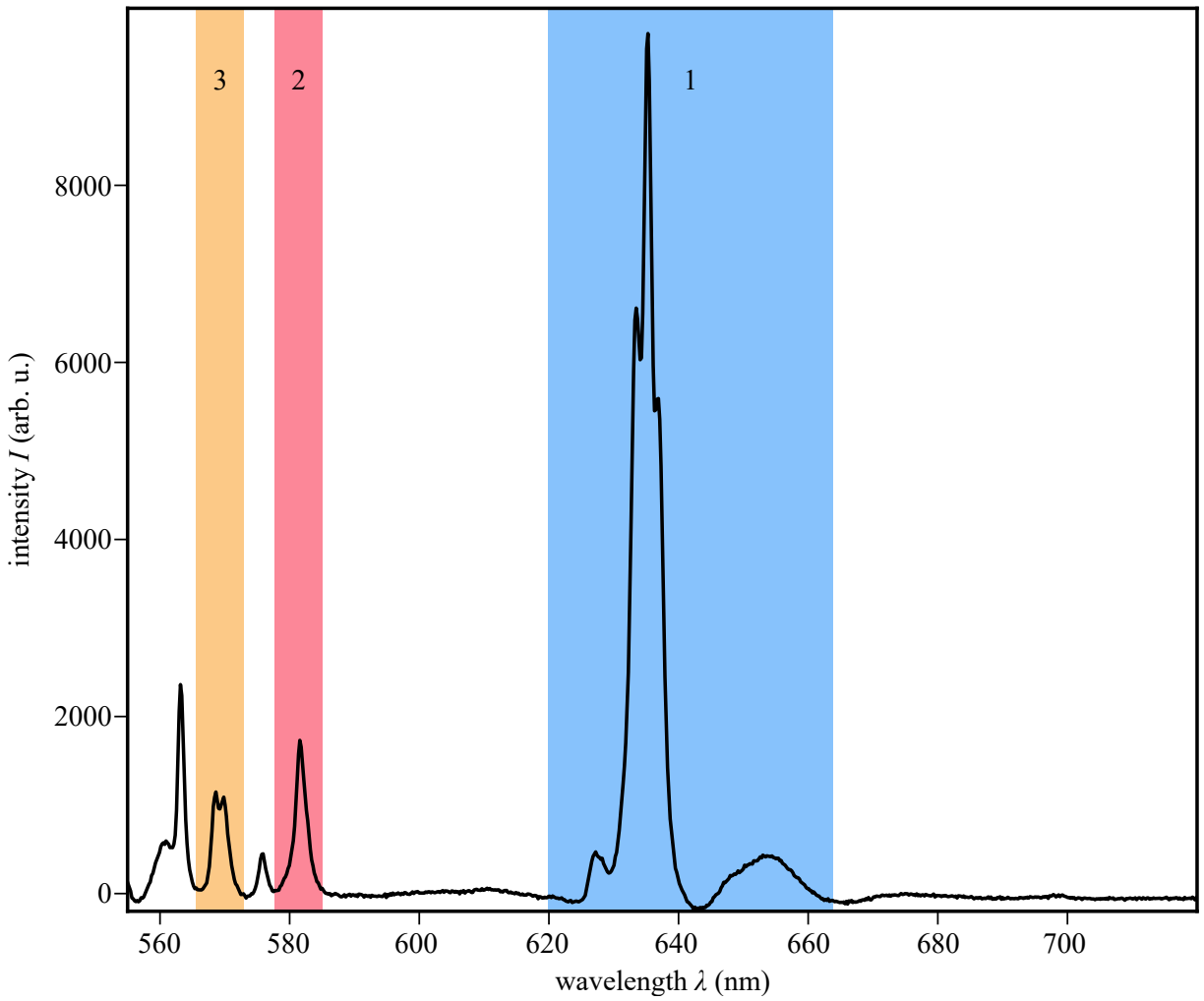

Figure 4.14: Raman spectrum of ethanol. The measured intensity I of the ethanol Raman spectrum is shown as a function of wavelength λ. The three peaks for analysis are highlighted in orange (3), red (2) and blue (1).

Experimental preparation and procedure A 2 W continuous wave (cw) 532 nm laser from Quantum Laser (type gem532) is used for the investigation. The optical LARA cell is filled with liquid methanol. The optical components for adjusting the laser beam path are mounted firmly on an optical plate (breadboard). The same applies to the LARA cell. In contrast, the components for guiding the scattered Raman light are mounted on a motorised linear z-stage. These components include a mirror (Thorlabs, BB1-E02) and a lens (Thorlabs, LA1951-A-ML) that focus the scattered light onto an optical fibre to guide the light to the spectrometer and CCD. The motorised z-stage is a Standa linear stage (8MT167-100) with a travel distance of 100 mm and a resolution of 125 nm.

For the measurement, the linear z-stage, and thus the optical components were moved out of and back into the Raman beam path. 15 spectra per 10 s are then recorded. The 10 s measurement time is sufficient compared to gas phase measurements with hydrogen isotopologues, as the density in the liquid phase is significantly higher. For each Raman spectrum, three peaks are identified and examined, see figure 4.14. For each of these three peaks, the intensity I, the intensity centre of mass I_{CM} as well as the peak position are determined for each spectrum, and then a respective mean value is averaged for each measurement. A total of 10 measurements

Table 4.5: Measurement results of the reproducibility test. The results for the measured intensity I, the intensity centre of mass I_{CM} and the peak position are tabulated for the a movable and a static z-stage.

		movable z-stage			static z-stage		
	peak	mean	σ	σ (%)	mean	σ	σ (%)
	1	207300	6319	3	164899	2055	1.2
I (arb. u.)	2	18894	484	2.5	14698	230	1.6
	3	15609	359	2.3	15609	174	1.3
	1	636	0.038	<0.01	635.9	0.04	<0.01
I_{CM} (nm)	2	581.7	0.014	<0.01	581.7	0.013	<0.01
	3	569.2	0.01	<0.01	569.3	0.013	<0.01
	1	635.3	0	<0.01	635.3	0	<0.01
peak pos. (nm)	2	581.6	0.014	<0.01	581.8	0	<0.01
	3	569.2	0	<0.01	568.6	0.09	<0.01

of 15 spectra each are recorded. Then 10 measurements of 15 spectra each are taken without moving the linear z-stage. This ensures that any fluctuation is actually caused by the traversing process.

Experimental results and analysis A total of 10 measurements of 15 spectra each are recorded twice. The mean values of the 10 measurements for the intensity I, the intensity centre of mass I_{CM} as well as the peak position are summarised in the following table 4.5 below. Firstly, it can be seen that even without moving the z-stage, the intensity I fluctuates with an uncertainty of 1.4 %, which is due to fluctuations in the laser power. A comparison of the two measurement campaigns shows that it is intensity fluctuation which is the most significant difference. This is approximately 2.6 % for the moving z-stage measurements. This is 1 %-point more than for the measurement without moving z-stage. The standard deviation at the intensity centre of mass as well as at the peak position is below 0.01 % for both measurement campaigns. Thus, the traversing process mainly affects the intensity, which can be explained by the fact that the optical components are not reattached to the originally adjusted position. Due to the new position, the beam path is not as well focused on the optical fibre as well as before. The measurement results do not show a continuous increase in standard deviation after repeated movements.

Conclusion The reproducibility test was carried out for components that are only required for LARA spectroscopic investigations. Of the three quantities examined, intensity I, intensity centre of mass I_{CM} and peak position, intensity has the largest contribution with a measurement uncertainty of 2.6 %. The KATRIN precision requirements are 5 % for Raman and 1 % for IR. Thus, the measurement uncertainty due to the method of optical components with a linear z-stage is within the KATRIN requirements.

4.4.3 Suitability of silver- and gold-coated mirrors for laser Raman and IR spectroscopy

The second measurement campaign will investigate the suitability of silver- and gold-coated parabolic mirrors for use in LARA and IR spectroscopy. Measurements will only be performed with respect to IR spectroscopy. For Raman measurements and the corresponding wavelength range, please refer to the manufacturer's specifications.

Experimental preparation and procedure The Vertex 70 spectrometer from Bruker is used to investigate the gold- and silver-coated parabolic mirrors for infrared spectroscopy. It already contains an integrated IR source for the near infrared range (780 – 2500) nm. The light coming from the IR source is guided to the IR detector by a total of three mirrors. The first mirror is a broadband plane mirror. The other two mirrors are parabolic mirrors, with the first mirror focusing the IR light onto the common focal point of the two parabolic mirrors. The second parabolic mirror directs the IR light parallel to the detector. In total, there are three measurements where the second mirror (first parabolic mirror) is replaced by a silver-coated parabolic mirror (Thorlabs, MPD508508H2-90-P01), a gold-coated parabolic mirror (Thorlabs, MPD508762-90-M01) and a broadband plane mirror as a reference. To make a qualitative statement, the shape of the spectra is compared.

Experimental results and analysis Spectra are recorded for all three configurations. For better comparability, all spectra are normalised to 1 and the reference spectrum is superimposed on the gold and silver spectrum, see figure 4.15. The clearest difference with a maximum deviation of 5 % can be seen between the reference spectrum and the spectrum with the gold-coated mirror. The deviation is much smaller for the measurement with the silver-coated mirror. The observation of the water bands is not important for the overall interpretation of the shape of the spectrum and is therefore neglected. For a qualitative comparison, the intensity spectra of the two measurements are divided into

$$I_\mathrm{R} = \frac{I_\mathrm{gold}}{I_\mathrm{silver}}. \tag{4.11}$$

The corresponding values for IR are plotted in figure 4.16. If the two spectra have approximately the same shape, the values for I_R would lie on a straight line. In this case the values are around $I_\mathrm{R} = 0.5$. This means that the intensity of the measurement of the gold-coated mirror is only about half that of the measurement with the silver-coated mirror. The water bands are also not taken into account.

For statements on the suitability for LARA measurements, the manufacturer's data on reflectivity are used, see figure 4.17. Since a laser with a wavelength of 532 nm is used for Raman measurements, the scattered Raman light is in the range of (533 – 735) nm, depending on which transitions of the hydrogen isotopologues are being studied. The reflectivity curves show that the silver-coated mirrors have a higher reflectivity than the gold-coated mirror for the range of scattered Raman light. Based on the manufacturer's data, parabolic mirrors with a silver coating are more suitable than parabolic mirrors with a gold coating for the desired wavelength range.

Conclusion Measurements of the reflectivity of gold and silver-coated parabolic mirrors for IR light have shown that the influence on the shape of the measured spectrum is negligible. This means that both silver and gold mirrors are suitable for IR measurements. Reflectivity data

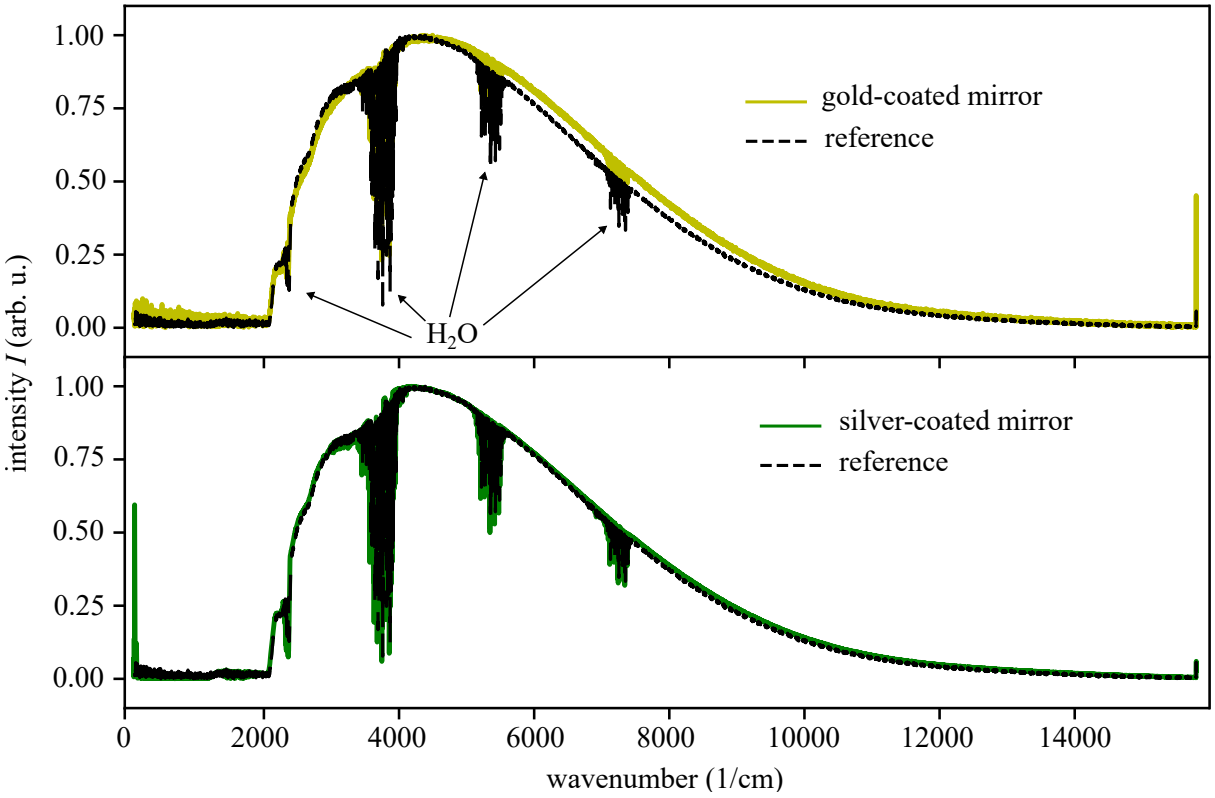

Figure 4.15: Normalised IR intensity spectra. The normalised intensity spectra are plotted as a function of the wavenumber. The upper figure shows the spectrum of the gold-coated mirror next to the reference spectrum and the lower figure shows the spectrum of the silver-coated mirror. The visible bands are due to water in the air and are not important for the present investigations.

from Thorlabs for the Raman wavelength range (533 – 735) nm show that silver-coated mirrors in particular reflect better. Therefore, silver-coated parabolic mirrors are recommended for the spectroscopic design of T_2ApIR.

4.4.4 Conclusion and implications for the T_2ApIR design

For the joint IR and Raman setup in the glove box, it is essential that there is only one beam path through the cryogenic measuring cell to minimise heat input. This means that individual optical components can be used for both types of spectroscopy (IR and LARA) or that components can be automatically moved out of and back into the beam path. Studies have been carried out for both scenarios.

With respect to the process of moving optical components out and back, it was shown that the intensity varies with a standard deviation of 2.6 %. This value is within the required precision of KATRIN. Nevertheless, further research is useful to reduce the uncertainty, for example by moving the stage more slowly or using shorter travel distances.

From the investigations into the suitability of silver-coated and gold-coated parabolic mirrors, it can be concluded from the results for the design of T_2ApIR that silver mirrors are more suitable as they have a higher reflectivity for the Raman light over the entire wavelength range. The IR investigations have shown that the difference is negligible.

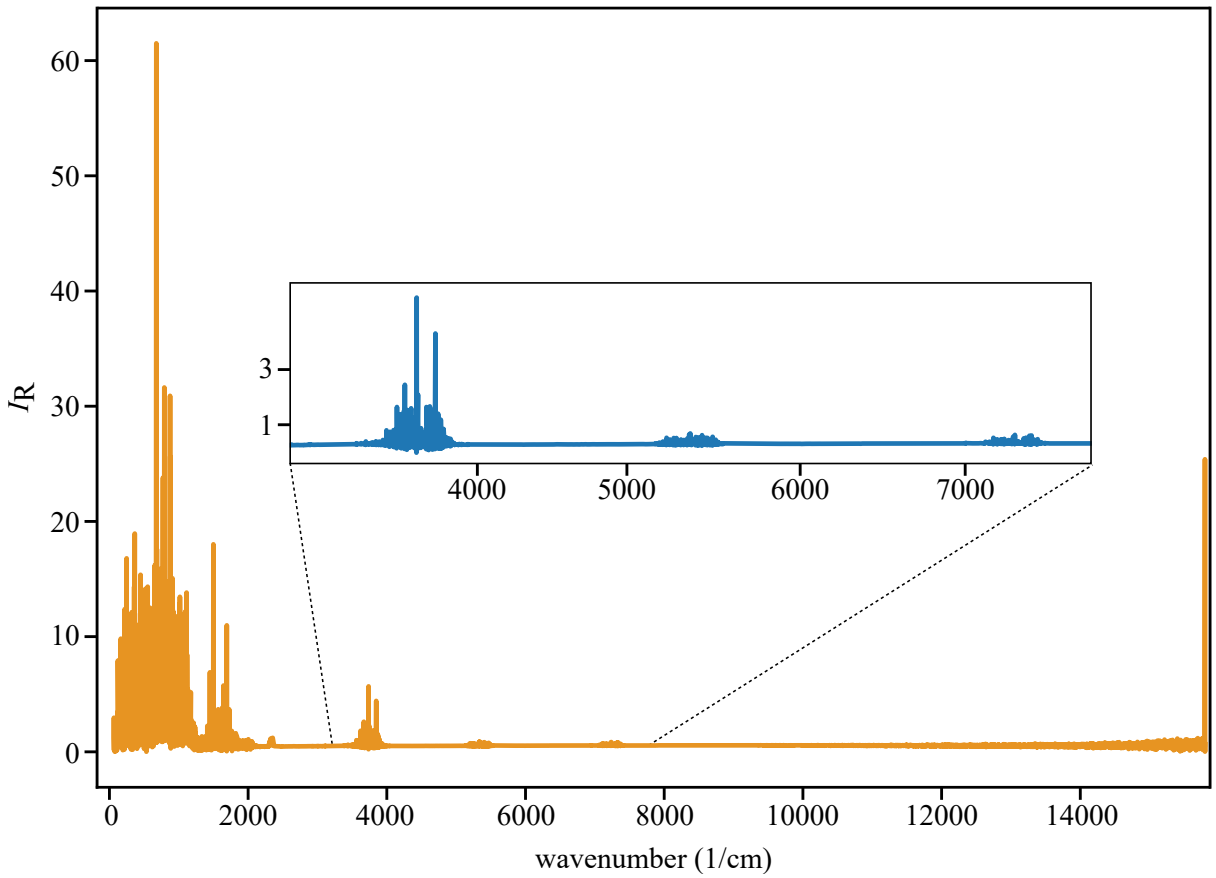

Figure 4.16: Ratio of the intensity of silver- and gold-coated mirrors. The ratio I_R is plotted as a function of the wavenumber. The ratio is close to 0.5 without considering the water bands.

4.5 Summary and discussion

To meet KATRIN's design sensitivity of $0.2\,\mathrm{eV/c^2}$, the individual systematic contributions must be quantified. A large part of these systematic contributions is related to the source loop of KATRIN, in particular the WGTS. This source loop is a thermal cycle in which temperatures and pressures in particular change by orders of magnitude. This has a direct influence on the molecular gas composition, which in turn is an important parameter for the determination of the systematic contributions. Molecular effects such as op conversion, isotope exchange reactions, dimer formation significantly determine the gas composition in the source loop of KATRIN and thus the systematic contributions. In order to be able to investigate these molecular effects quantitatively and qualitatively, a new experiment suitable for tritium, T_2ApIR, will be designed and constructed, since neither direct spectroscopic investigations on KATRIN are possible, nor do experiments already exist which allow such investigations. The requirements for the design of T_2ApIR are complex and diverse. For example, it must be tritium-capable, allow cryogenic investigations in the temperature range of (10 – 300) K, and combine IR and Raman spectroscopy. Especially for tritium, important preliminary information is lacking and the literature contains only sporadic information. For this reason, specific pre-investigations are required, the results of which will have a significant influence on the design of T_2ApIR. In this chapter, the natural isotope exchange of $H_2 + D_2 \rightleftharpoons 2\,HD$ as well as $H_2 + T_2 \rightleftharpoons 2\,HT$, the ortho-para conversion at RaCoon and a combined IR and Raman spectroscopy setup were investigated. The results of these investigations and the significance for the design of T_2ApIR are summarised below.

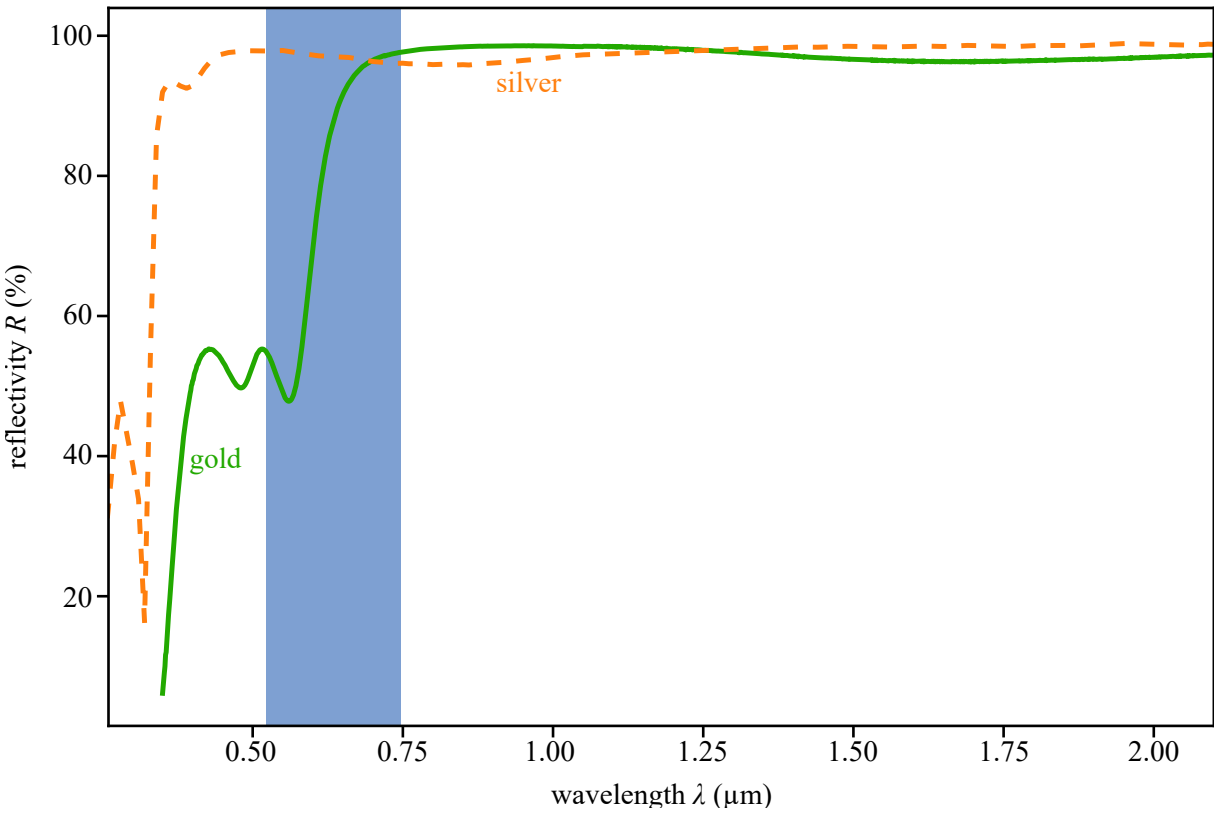

Figure 4.17: Reflectivity of silver- and gold-coated parabolic mirrors. The reflectivity R is shown as a function of wavelength λ. The reflectivity of the two mirrors differs most clearly between 400 nm and 750 nm. The blue background shows the spectral range of the scattered Raman light for a laser with a wavelength of 532 nm.

The results of the natural isotope exchange studies have shown that the presence of tritium reduces the time constants by two orders of magnitude compared to the formation of HD. Both the β-electron and the ion produced during tritium decay greatly accelerate isotope exchange by opening new reaction channels. In the handling of tritium, it has been shown that too long circulation times also promote isotope exchange, so short mixing times should be chosen for mixing in T_2ApIR. LARA spectroscopy has proven to be a real-time and non-invasive method of analysis. Continuous irradiation of the gas sample under investigation with laser light should be avoided because, as has been shown for HD formation, the laser light introduces additional energy into the system which accelerates the exchange. The results of the investigations on the exchange of tritium with atoms from the stainless steel surfaces could only give a first insight. The literature suggests that tritium interacts with carbon and thus partly undergoes the isotope exchange, which slows down reaching of the equilibrium state. Further investigations with T_2ApIR on this topic are necessary.

The construction of the RaCoon system allows the systematic study of the chemical and op conversion and the underlying kinetics of the inactive hydrogen isotopologues. The proof of principle measurement has shown that the developed measurement method is suitable for investigating the conversion time as a function of system parameters (pressure, temperature, flow) and the catalyst properties (porosity, grain size, activation). In the partial conversion method, only a small amount of catalyst material is deliberately filled into the converter so that the influence of the above parameters on the conversion becomes clear and measurable. In

addition, the conversion in the catalyst takes place in the cold state, but the measurement is done in the warm state using Raman spectroscopy. This is possible because Raman spectroscopy is only sensitive to the occupation of the rotational states and these are distributed according to the room temperature and the op transition prohibition. Raman has the advantage over other methods in that it does not rely on the energy released during the op conversion or on the change in heat capacity or thermal conductivity. Therefore, real-time, non-invasive measurement is possible. In addition to this measuring principle adopted for T_2ApIR, the design of the converter is also adopted. The three stainless steel u-tubes are connected in series, with the middle U-tube filled with the catalyst. This arrangement allows easy replacement of the catalyst material. The use of temperature sensors at the inlet and outlet, together with two sealing gaps, makes it possible to determine the conversion temperature and prevent the material from entering the system. Research into the contamination of the catalyst material suggests that the gases used in T_2ApIR must be purified before use. Humid air, especially oxygen, has a detrimental effect on the conversion time and the equilibrium state. On the one hand, the active surface of the catalyst is reduced because foreign atoms settle on the surface, and on the other hand, oxygen catalyses hydrogen even in the warm part of the facility due to its paramagnetic intrinsic properties. This creates an op equilibrium state between the cold and the warm areas. Air enters the system both from residual moisture in gas bottles and when the catalyst material is filled. Therefore, in addition to pre-cleaning the gases, it is also necessary to clean the system (flushing) and activate the catalyst material. Investigation of the temperature dependence has shown that, at present, iron oxide is best activated at 180 °C and by repeated purging with hydrogen gas. Iron oxide is a physisorbing material and is suitable as an ortho-para converter at low temperatures. As the RaCoon system can also measure chemical reactions using LARA spectroscopy, it is possible to analyse chemical and physical adsorption processes simultaneously. This provides new insights into the fundamentals of conversion processes and reaction kinetics. For the T_2ApIR design, LARA spectroscopy is therefore used to investigate the conversion times of isotope exchange and ortho-para conversion. The principle of only partial catalysis per cycle has also proved successful and is also implemented in T_2ApIR.

Besides LARA spectroscopy, IR spectroscopy is also required to study molecular effects such as dimer formation. As the cryogenic measuring cell has only two viewports, only one optical beam path is available for both methods. As a consequence, the optical components must either be suitable for IR and LARA or can be moved using motorised stages. The investigation of the reproducibility of the movement of a linear z-stage has shown that the deviation of the measured intensity of 2.6 % is currently in line with the required KATRIN precision of 5 % for LARA. However, further investigations into the speed of the movement and testing of other stages with better resolution should be carried out. The fixed parabolic mirrors used for both methods have been coated with silver gold to check their suitability. For IR spectroscopy, the difference is negligible. For Raman spectroscopy, the manufacturer's data show that silver-coated surfaces have a higher reflectivity (90 % compared to 50 % for gold) for the spectral range of Raman light used (535 – 735) nm.

In conclusion, the results of the three pre-investigations are important and have a direct influence on the design (spectroscopic, ortho-para measurement). In the next chapter, the final design of T_2ApIR is presented.

5 T_2ApIR: Empirically based development of a tritium compatible experiment for Raman and IR investigations of molecular effects

The KATRIN experiment aims to determine the mass of the electron neutrino with a sensitivity of $0.2\,\mathrm{eV/c^2}$ [Ang05]. Understanding the systematic effects along the entire KATRIN beamline is the key to maintaining the design sensitivity. As mentioned in section 3.1, there are a number of different systematic effects, most of which are related to the WGTS. The WGTS is one part of the thermal cycle of the KATRIN tritium source loop, see section 3.3 for more details. Along the KATRIN source loop, the gas composition changes due to intermolecular and molecular effects, such as isotope exchange reactions, op conversion, dimer formation. This in turn has a direct influence on the systematic effects, i.e. the final-state distribution (see section 3.2). Since it is not possible to measure these molecular effects directly in the source of KATRIN, for example by laser spectroscopy, the search for alternatives is indispensable. On the one hand, simulations are always a way of approaching scientific problems, but they are no suitable in every case, especially if the underlying physical concepts require the gas composition as an input parameter. On the other hand, the development of additional experiments which allow the study of these molecular effects under KATRIN-like conditions seems to be a promising alternative. This train of thought led to the creation of the T_2ApIR experiment. The design and development of the T_2ApIR experiment has been driven mainly by the aim to investigate spectroscopically the intermolecular effects of all hydrogen isotopologues ($H_2, HD, D_2, HT, DT, T_2 = Q_2$), in particular the tritiated species HT, DT and T_2, at cold temperatures (down to 10 K) according to the conditions of the thermal cycle of KATRIN. The design of such a complex experiment requires prior expertise and experience. Two contributions were therefore crucial to the success of T_2ApIR. Firstly, the predecessor experiments AIWA [Kos11] and TApIR [Grö15b]. These two experiments were the first to measure IR absorption spectra of non-radioactive hydrogen isotopologues at low temperature ($T = 20\,\mathrm{K}$) [Kos09]. Secondly, targeted pre-investigations were conducted with the aim that their results (measurement technology, design of components, measurement results) would directly influence the design of T_2ApIR, see sections 4.2, 4.3 and 4.4. All these previous obtained results and the knowledge gained from the previous experiments paved the way for the design of T_2ApIR, still based on the premise of measuring intermolecular effects under KATRIN-like conditions.

The chapter is structured as follows: Section 5.1 presents the scientific goals that can be achieved with the new T_2ApIR experiment. From theses goals and the results of the pre-investigations, the necessary requirements for the design can be derived, such as thermal cycle studies, tritium compatibility, cryogenic temperature range and a combined LARA and IR setup. All these requirements are summarised in section 5.2. Knowing the goals and all the requirements, the next step is the conceptual and process design of the T_2ApIR experiment, which are described in section 5.3. Within section 5.4, the implementation and the manufacturing process are described. The final section 5.5 summarises the main findings.

5.1 Scientific and experimental objectives

The scientific objectives of the new, fully tritium compatible T_2ApIR experiment were primarily driven by the two main research fields of the TLK, KATRIN and the fusion fuel cycle [Bor11]. The overarching goal is to study of quantum mechanical influences in cold hydrogen isotopologues Q_2.

In the context of KATRIN, this means the investigation and quantification of the intermolecular and molecular interactions of all six hydrogen isotopologues under the conditions of the thermal cycle of the KATRIN tritium source loop. These molecular effects, such as isotope exchange reactions, dimer formation, op conversion and exchange reactions with surfaces, are described in the sections 3.3 to 3.6,

In the context of fusion technologies, this means the development of a spectroscopic system in a combined ISS and water detriation system (WDS) for process monitoring and control [Kos11]. With the predecessor experiments AIWA [Kos09] and TApIR [Grö15b] first investigations with the three inactive hydrogen isotopologues H_2, HD and D_2 were carried out.

Thereby, the main scientific goals of the T_2ApIR experiment are as follows

- IR and Raman spectroscopic studies of radiochemical molecular processes such as Van-der-Waals cluster formation and phase transitions, spectroscopic investigations of conversion rates and equilibrium states of isotope exchange reactions, of op conversion and of exchange reactions with surfaces under KATRIN-like conditions in the temperature range (10 – 300) K.
- A complete calibration of the IR absorbance of all six hydrogen isotopologues in the solid, liquid and gaseous phases depending on the concentration and on the op ratio.
- Quantification of the influence of the op ratio on the IR absorbance spectra as its main systematic effect.

In detail, these three goals have the following purpose. For the KATRIN experiment, the complete thermal cycle will be modelled with T_2ApIR (30 K WGTS, permeator, circulation pump, see section 3.3). The aim is to obtain the missing information on conversion times, equilibrium states and exchange effects as well as dimers, since intermolecular effects are ubiquitous in the KATRIN source loop but not fully quantified. For example, the KATRIN design report from 2005 [Ang05] states that hydrogen clusters only exist below 30 K. However, a recent investigation by Mirz et al. [Mir19] showed the presence of dimers, the simplest bounded Van-der-Waals cluster of two molecules, below 30 K for inactive hydrogen isotopologues under KATRIN-like conditions. Yet tritium studies are lacking, as is information in the literature. The T_2ApIR experiment will determine the dependencies of cluster formation on density, temperature and pressure, as well as their intrinsic properties such as binding and dissociation energies. The great advantage of T_2ApIR is the combination of IR and Raman to compare both methods on the one hand and on the other hand the different output information of the spectra to get a deeper physical insight into the molecules and their interaction.

Due to the full tritium compatibility of the T_2ApIR system, all six hydrogen isotopologues can be investigated. A complete calibration relation between measured IR spectra and corresponding concentrations is therefore accessible. This is the last step towards the installation of a spectroscopic system in a cryogenic distillation procedure (ISS/WDS) for process monitoring and

control. Previous experiments with inactive Q_2 have achieved a calibration with an accuracy of better than 5 % absolute [Kos11; Grö15b; Grö17].

The ortho-para effect is introduced as a main molecular effect in the KATRIN source loop. A transition from one state to the other, ortho and para, is extremely unlikely, see section 3.5.2, and the natural time constants vary between thousand hours in the gas phase and 10 h in the liquid phase [Lar48; Sou86; Mil97]. Since a change in temperature changes the ortho-para equilibrium distribution, the influence of the ortho-para states on the rotational population, measured by IR spectroscopy, must be known.

In conclusion, the new, fully tritium compatible T_2ApIR experiment enables in-depth studies of cold hydrogen isotopologues, especially the tritiated species. Thus, T_2ApIR is crucial for not only to measure but also to quantify molecular effects and their temporal evolution as they occur in the KATRIN source loop. Furthermore, this experiment allows the scientific research in the field of technologies for the fusion cycle, as an analytical system for hydrogen liquefaction processes [Ber09; Car17; Yin19], and other future projects such as DARWIN (noble gas clusters of xenon) [Aal16; Ago20].

5.2 Design requirements and criteria

Bringing together the goals from the previous section 5.1 as well as the experience of the AIWA and TapIR experiments with the results presented in the chapter 4, the following design requirements can be derived. The criteria are categorised and presented as follows: scientific and technical, tritium and safety, cryogenic, and optical.

5.2.1 Scientific and technical requirements

This section specifies the scientific and technical requirements for the entire setup. Most of the scientific and technical criteria go hand in hand with processual requirements, so no strict separation is made here.

- Studies of time constants and equilibrium states of intermolecular effects of all Q_2 under KATRIN-like conditions require:
  - The whole system allows to handle all six hydrogen isotopologues in the gaseous, liquid, and solid phases.
  - The actual operating temperature range is (10 – 300) K.
  - The implementation of a combined LARA and IR spectroscopic system without major changes to the experimental setup inside the glove box, see also section 4.4.4. LARA determines conversion rates and equilibrium states and IR allows the investigation of dimer processes.
  - Mapping of the thermal cycle of the KATRIN source loop (buffer vessel, inlet pressure, Raman cell, capillary, WGTS beam tube, permeator, circulation pump, see 2.2.2 and 3.3) from 300 K to 30 K.
- op conversion studies (see also section 4.3.5) require:

  - It is necessary to produce chemically and op equilibrated and non-equilibrated gas mixtures with an uncertainty better than 5 %.
  - The design of the op converter must allow easy exchange of catalyst material. Temperature sensors at the outlet and inlet for process control and sealing frits to prevent catalyst material to get from entering the system, see section 4.3.4.1.
  - The measurement principle of a partial conversion has to be implemented, as in the RaCoon facility, to allow op conversion and kinetic studies, see section 4.3.2 and 4.3.4.1.
  - Due to contamination, catalyst materials must be heated, see section 4.3.4.3
  - The op conversion of H_2, D_2, and T_2 at (10 – 300) K runs with a flow of 1 mol h^{-1}.
  - The chemical conversion runs with a flow of 1 mol h^{-1}.
  - Cooling and reheating of the system is fast enough to investigate the change of the ortho and para states. Liquefaction of 1 mol of hydrogen isotopologues down to 10 K within of 3 h due to a desired cooling time of 1 K min^{-1}.
  - A LARA system for simultaneous measurement of the op and chemical conversion.

- successful calibration of IR spectra requires
  - The concentration analysis of isotopologic mixtures and the op ratio must be achieved with an uncertainty better than 1 %.
- offline analysis requires
  - The implementation of sampling ports for analysis with analytical devices, such as quadrupole mass spectrometers or calorimeters.
  - The connection of an additional offline Raman system for gas concentration analysis is desired for op measurement at room temperature.
- technical aspects require
  - Gas purification is necessary to keep out impurities, see 4.3.4.2 for the effects on the op conversion or the freezing of the capillary in the KATRIN transfer line 3.6.2.
  - The operating pressure is limited to 2.5 bar absolute, but the whole system has to withstand a pressure of 5.0 bar absolute in a case of emergency or failure to ensure a safe tritium containment.
  - The addition of He, Ne, and N_2 gas is necessary for purging, among other things.
  - Due to the mechanical vibrations of the cryocooler, decoupling from the remaining system, especially the sample cell, is necessary to avoid possible influences such as losing connections.
  - The maximum tritium inventory is limited to 13.5 g $\left(5 \cdot 10^{15}\,\text{Bq} \approx 2\,\text{mol}\right)$.

In terms of cryogenic temperature down to 10 K, absolute pressure of 2.5 bar, tritium compatibility with 13.5 g of pure T_2 and integration of a combined optical analysis system (IR and Raman) show the high complexity that had to be met.

5.2.2 Tritium and safety requirements based on the general TLK guidelines

T_2ApIR is the first experiment with an amount of 13.5 g tritium, which can be handled and liquefied in a single setup in a glove box at the TLK. In comparison, the KATRIN experiment has a throughput of $40\,\mathrm{g\,d^{-1}}$ of T_2. Since its inception in the early 90s, the TLK has followed a comprehensive safety philosophy. The "Tritium-Liefer- und Abnahmebedingungen"[1] [Wel15] define guidelines for the manufacture, delivery, commissioning, and operation of tritium components and experiments at the TLK. The primary objectives behind these guidelines and the general philosophy of the TLK are, on the one hand, the safe **tritium confinement** and thus safe handling and, on the other hand, the **principle of minimisation** of the tritium inventory. The first point is realised by the multi barrier concept and the closed tritium cycle approach [Dör05]. The first barrier is the primary system, which includes all components directly exposed to tritium. The second barrier is usually the glove box surrounding the experimental setup. The pressure inside these glove boxes is (300 – 70) Pa lower than the pressure inside the laboratory, which in turn is 52 Pa lower than the ambient pressure. This ensures that, in the event of a leakage, tritium diffusion to the outside is prevented by the gas flows entering the system. This multi-barrier concept is complemented by the specification to keep the amount as low as possible. In the case of the T_2ApIR experiment, the minimum amount of tritium depends on the liquefaction process. The design activity value for T_2ApIR is $5 \cdot 10^{15}$ Bq, corresponding to 13.5 g or 2 mol of pure T_2.

The following list summarises not only the main requirements for the T_2ApIR experiment based on the TLK tritium standards and general safety aspects, but also for the TLK infrastructure.

- Its radiochemical properties, such as radioactive, reactive, toxic, easily diffuses through materials, make tritium difficult to handle.
- the first, internal barrier concept requires
  - All components of the primary system (such as pipes, vessels, pumps, and sensors) must be made of metals or ceramics. Organic materials such as Viton or elastomers for sealings are prohibited because of the interaction of tritium with fluorine to form highly toxic hydrofluoric acid.
  - All pipes must be double walled.
  - The leak rate of a single connection has to be less than $1 \cdot 10^{-10}\,\mathrm{Pa\,m^3\,s^{-1}}$ and the integral leak rate of a system is required to be lass than $1 \cdot 10^{-9}\,\mathrm{Pa\,m^3\,s^{-1}}$. For this reason, only VCR[2] and CF[3] connections are used for tritium components.
  - Regular leak tests of the system as well as tests of the safety conditions are mandatory.
  - Redundancy of safety related parts (e.g.: overpressure by sensor with automatic valve and a bursting disc as backup).
- the second outer barrier requires
  - The experiment must be compact to minimise the tritium inventory.

[1] In English: Technical terms of delivery and acceptance.

[2] Invention of the company Swagelok. A metal gasket is compressed by two cutting edges. For more information visit `https://www.swagelok.de/en`. Last visited on the 20th of October, 12:18.

[3] CF is the registered brandmark “ConFlat“ of the company Varian, Inc. The CF flanges are standardised according to ISO 3669:2017.

  - All components must be accessible and connectable with gloves from outside the glove box. This is particularly challenging with small optical components that need to be precisely aligned.

- TLK infrastructure requires
  - Connection to the TLK tritium infrastructure with a separate double wall pipeline to the CAPER C[4] glove box for fresh tritium supply and release.
  - Connection to the ZTS[5] for release of non tritiated or low activity gas mixtures.
  - Additional gas supply via a cabinet for gas bottles (Ar, Ne, D_2) and a connection to the N_2 and He ring lines.
  - A 400 V and 60 Hz power supply for the cryocooler and the corresponding helium compressor.
  - Process cooling water for the helium compressor.
  - Fast, precise and accurate data acquisition and an online monitoring system to ensure safe and optimum operation (process control engineering *PCS7*) is required.
  - A local or process control system with the ability to implement a safety circuit.
- T_2ApIR operates not only working in the cryogenic region but also under **overpressure**. In Germany, all overpressure components must be comply with specific legal directives. T_2ApIR obeys the AD 2000 regulations[6].
  - The entire experimental setup must withstand the design pressure of 5.0 bar absolute.
  - In the event of sudden and uncontrollable gas evaporation (due to a vacuum failure in the insulation vessel), the sample cell must be permanently connected to a sufficient buffer volume to collect the gas.
  - The cryostat itself must be designed as a primary system in the event of a pressure increase in the sample cell leading to bursting of the cell windows.
  - In addition to that, the cryostat design must enable an easy removal of the released tritium gas.
  - Quick and safe interlocks for vacuum pumps which cannot handle pressures above 1 bar.

This list gives an overview about the requirements and illustrates the interaction of the various TLK groups involved from the very beginning of the design phase. Moreover, a detailed risk assessment, similar to the hazard and operability study (HAZOP), was carried out beforehand. In summary, the T_2ApIR experiment shows the following hazards: explosive gases, gas under pressure, and radioactivity.

[4] CAPER is the acronym for **CA**PRICE **PER**MCAT at the TLK and is evolved from the experiment CAPRICE (**Ca**talytic **Puri**fication **E**xperiment). CAPER demonstrated the feasibility of a two-stage clean-up process for fusion reactor exhaust gases [Bor05].

[5] ZTS stands for central tritium retention system and is one of the key elements of the TLK infrastructure [Dör05].

[6] The AD 2000 set of rules meets the standard requirements of the European dierctive 2014/68/EU. For further information visit`https://www.vdtuev.de/themen/anlagensicherheit/dampf_und_drucktechnik/ad2000_regelwerk`. Last visited on the 20th of October, 12:18.

After a brief discussion of the safety requirements for tritium and overpressure in this section, the cryogenic requirements to enable liquefaction and spectroscopic studies are discussed below.

5.2.3 Cryogenic requirements of the cryostat

Cryogenic requirements are as diverse and important as those for tritium. Initially it was decided that a cryocooler would be used, as it is cheaper and easier to handle than instead of using a cooling power plant.

- The cryostat must provide sufficient space for all the relevant components, such as the optical sample cell, the op converter, the heat shield, and the cryocooler.
- The cryostat design must allow the cryocooler to cool down the entire setup, in particular the cryogenic cell, the op converter, and the isotopologue mixture in $1\,\mathrm{K\,min^{-1}}$ steps, taking into account the additional power for thermal radiation and thermal conduction.
- The following steps reduce the heat transfer:
  - Evacuation of the cryostat volume below $1 \cdot 10^{-5}\,\mathrm{mbar}$ to prevent heat transfer by convection before cooling.
  - Implementation of a thermal shield, connected to the first stage of the cryocooler to block the thermal radiation from the inner surface of the cryostat to the sample cell and the op converter.
  - Only low thermal conductivity materials are used and the geometry of critical components is optimised for minimum thermal conduction.
- Due to the heating of the op converter, the connection between the converter and the cryocooler must be flexible and easy to connect to prevent damage to the cryocooler.
- In the event of a cooling failure, a safe and quick interlock procedure is required to prevent an overpressure. Due to the cooling by evaporation enthalpy, a blockage of the connection pipes by a frozen plug will result in a pressure increase. Installation of additional (double redundant) heaters is required.
- Low temperature sensors are required and appropriate electrical feedthroughs are needed inside the cryostat, which are also tritium compatible.
- The heaters are doubled not only for safety but also for handling reasons (exchange of a broken heater).

The cryogenic and the tritium requirements set strict specifications for the design of the cryostat which must be carefully implemented.

The last section concludes with the optical requirements for the combination of IR and LARA spectroscopy.

5.2.4 Optical design requirements for a combination of laser Raman and IR spectroscopy

The above scientific, safety and cryogenic requirements are now complemented by the combined requirements of Raman and IR spectroscopy. Inside the compact cryostat, packed with cryocooler, cell connectors and op converter, the laser and IR beam must find a way to break through the

outer vessel, the radiation shield, through the sample cell itself and out in the opposite direction. Raman and IR enable non-invasive, real-time, and online analysis of hydrogen mixtures in any state of aggregation. As Raman and IR absorption spectroscopy are different methods based on different physical interactions, it is even more challenging to combine the two methods.

In short, laser Raman spectroscopy is the inelastic scattering of the laser light on the molecule. The transferred energy leads to an excited vibrational and/or rotational state of the molecule. The scattered laser light is detected and analysed. Raman is based on the change in polarisability of the molecule. Where as IR absorption spectroscopy is based on the change in the dipole moment of the molecule. A bright white light source is used, and the light is transmitted into a cell and the non-absorbed light is detected[7].

Nevertheless, the experimental, technical as well as the safety requirements can be derived.

- All optical components such as mirrors, lenses, and their mounts are located inside the glove box. They must therefore be accessible and manageable with the gloves on.
- Due to the requirement to reduce the thermal input, the number of viewports on the cryogenic measuring cell must be minimised. For IR and LARA this means two common viewports.
- The simultaneous combination of LARA and IR requires optical components that are either suitable for both techniques (see section 4.4.3) or can be automatically moved out of the beam path and back (see section 4.4.2).
- The Raman setup allows the simultaneous determination of the op ratio of the homonuclear isotopologues and the isotopologic concentration of all six hydrogen isotopologues at the S_0 branch. A resolution of $1\,\mathrm{cm}^{-1}$ over the spectral range from $(150-4200)\,\mathrm{cm}^{-1}$ is required to meet the requirement of a measurement uncertainty of less than 5 %. Besides, studies of the Q_1 branch, $4200\,\mathrm{cm}^{-1}$ of protium as the furthest, are demanded.
- Due to the single optical path, the scattered Raman light has to be collected in the forward or backward direction.
- The laser is located outside the glove box and requires special feedthroughs and fibres. In terms of safety, the high intensity laser beam must be enclosed to protect the operator's eyes.
- The IR spectrometer and the detector are installed outside the glove box and therefore need special feedthroughs. Both parts require a continuous purging with gaseous nitrogen to prevent moisture from adhering to the surface of the windows.
- The spectral resolution for the IR measurements should be $0.9\,\mathrm{cm}^{-1}$ for the spectral range of $(1500-16\,000)\,\mathrm{cm}^{-1}$.
- All optical components inside the glove box must be mounted on a breadboard to ensure optimum instrumentation. In addition, all the components must have a light-tight enclosure to prevent ambient light from entering the experimental setup and causing background light.

[7] This explanation is shortened and a more detailed explanation can be found for Raman in [Lon02] and for IR in [Gri07]. Hydrogen related Raman and IR measurements concerning techniques and results at the TLK are published here [Kos11; Grö15b; Grö17; Mir19] for IR and here [Stu10; Sch13b] for Raman.

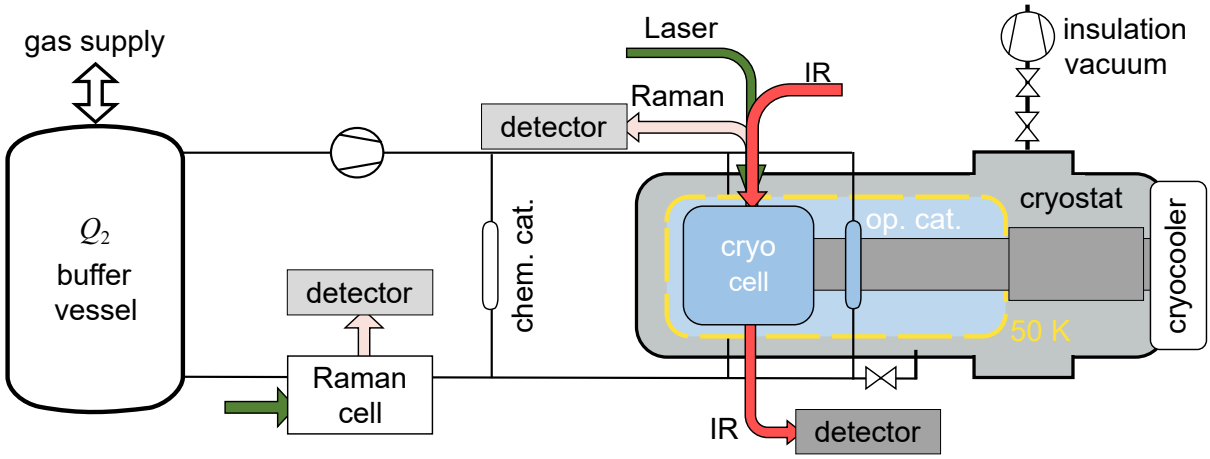

Figure 5.1: Schematic drawing of the experimental setup and process design of T_2ApIR. Starting from the right, a two-stage cryocooler is connected directly to the op converter and the sample cell via its second stage. Both the cell and the converter are surrounded by a 50 K copper shield, which is highlighted in light blue. All these components are inside the cryostat. The thin lines represent the pipes for filling the gas mixtures in the cryogenic cell and the op converter. As indicated by the coloured arrows, the laser beam (green), the back scattered Raman light (beige) and the infrared beam (red) pass through the cryostat and the cell through two sapphire viewports. Outside the cryostat is an additional converter for chemical equilibration and a second inline Raman system for gas analysis. Not shown are additional sampling ports for external gas analysis such as gas chromatography or calorimetry. The buffer vessel, for filling, mixing and buffering and the circulation pump are responsible for processing the gas. The complete and more detailed P&ID flow chart of the experiment can be found in the appendix B.

The main challenge will be to find appropriate components for both spectroscopic methods.

5.2.5 Conclusion

The previous four sections outlined the different requirements for the T_2ApIR experiment. It is not only the cryogenics or optics that make the experiment complex, but also the interaction of cold temperatures in combination with the radioactive material tritium and the requirement for spectroscopic investigations.

The next section describes how these preceding requirements have been carefully considered and implemented step by step. The main focus is on the cryogenic design of the cryostat.

5.3 Experimental concept and process design

In 2015, the first ideas of the T_2ApIR project became more concrete and were brought together in an experimental concept. Based on the three main objectives discussed in section 5.1, the focus was on the tritium compatibility, mapping the thermal cycle of KATRIN and the simultaneous application of both spectroscopic methods, Raman and IR, in the temperature range of (10 – 300) K. For the first time in 2017, Sebastian et al. [Mir17] published the general concept and the basic process design. A simplified drawing of the T_2ApIR concept is shown in figure 5.1.

Concept At the heart of the experimental concept is the cryostat, where all the requirements come together. The cross-shaped cryostat contains the two-stage RDK-415D Gifford-McMahon refrigerator with 1.5 W cooling power at 4.2 K. Directly connected to its second stage is the

coolable op converter which is filled with iron(III) oxide Fe_2O_3 for catalytic equilibration of the gas samples at low temperatures, see section 4.3. The second component within the insulation vacuum is the cryogenic sample cell with two sapphire viewports. Both components are capable of holding samples over a wide temperature range of (10 – 300) K and an absolute pressure of 2.5 bar absolute. IR and Raman use the same optical path through the cell. A 50 K copper cold shield surrounds the refrigerator, the converter and the sample cell from the first cooling stage. The cryostat contains all these components to enable a safe and technically feasible cryogenic environment. Although the cryostat is not exposed to tritium under normal operating conditions, it is designed as a primary system because of the release of tritium within the cryostat in the event of a viewport rupture. Outside the cryostat, the supporting infrastructure is assembled. A chemical converter filled with Pt on Al_2O_3 to chemically equilibrate the samples and to produce samples with different fractions of the heteronuclear hydrogen isotopologues HD, HT, and DT. There are three buffer vessels, two of 20 l and one of 1 l, for filling in and mixing gases, as well as buffers for the condensation process. A metal bellows circulation pump is used to process the gas mixtures. An additional Raman system is located outside the glove box and is connected via an appendix to a laser Raman cell for room temperature analysis. Not shown are the pumps for evacuating the setup and the additional sampling parts for external analysis. A more detailed description of the T_2ApIR experiment can therefore be found in appendix B, where the entire P&ID flow chart provides all components such as pumps, vessels, and sensors, and tables with additional information.

Thermal KATRIN cycle In order to best represent the thermal cycle as it occurs at KATRIN, the following components are installed. To force gas mixtures into specific compositions, T_2ApIR uses a hot and a cold converter. Here, the hot converter represents the permeator. This is a palladium-filled converter that operates at room temperature for chemical conversion. The cold converter is filled with iron oxide and can be cooled down to 10 K and is therefore responsible for the ortho-para conversion. These two catalysts make it possible to simulate specific cycles with varying gas compositions. With the circulation pump and the buffer vessels as well as the LARA cell in the warm and the cryogenic measuring cell, the thermal cycle of KATRIN is adequately reproduced.

Buffer size and condensation For the investigation of intermolecular effects at different temperatures, a distinction must be made between gas phase, liquid phase and phase transition measurements. The gas phase covers a temperature range of (26 – 300) K for the hydrogen isotopologues, for KATRIN 30 K is the operating temperature at the beam tube in the WGTS. The pressure must remain constant during a temperature change in the measurement cell. This is why a large buffer vessel is required. For liquid phase measurements it is necessary to provide a temperature range of at least 5 K to enable temperature dependent IR and Raman measurements. During the condensation process, the pressure dependent boiling point changes in a fixed volume as the cryogenic sample cell. The condensation process stops when the vapour pressure is reached in the system. Therefore, a sufficient buffer volume is used to ensure a complete filling of the cryogenic sample cell.

Due to the requirements of the condensation process and the vapour pressure of the pure fluid p_{vap} a minimum pressure is required to achieve the phase transition from gas to liquid. The initial pressure required before condensation is given by

$$p_{\mathrm{fill}}(T_{\mathrm{cell}}) = p_{\mathrm{vap}}(T_{\mathrm{cell}}) + \Delta p(T_{\mathrm{cell}}) \tag{5.1}$$

$$= p_{\mathrm{vap}}(T_{\mathrm{cell}}) + \frac{n_{\mathrm{liq}}(T_{\mathrm{cell}}) R T_{\mathrm{room}}}{V_{\mathrm{buffer}}}, \tag{5.2}$$

where

- $p_{\mathrm{vap}}(T_{\mathrm{cell}})$ is the vapour pressure at the operating temperature of the cell T_{cell},
- $T_{\mathrm{cell}} = (10 - 300)\,\mathrm{K}$ is the operating temperature within the cryogenic cell,
- $T_{\mathrm{room}} = 300\,\mathrm{K}$ is the temperature of the buffer vessel,
- $V_{\mathrm{buffer}} = 20\,\mathrm{l}$ is the volume of the buffer vessel[8],
- $R = 8.314\,\mathrm{J\,mol^{-1}\,K^{-1}}$ as the ideal gas constant and
- $n_{\mathrm{liq}}(T_{\mathrm{cell}})$ as the amount of substance inside the cryogenic cell.

The amount of substance $n_{\mathrm{liq}}(T)$ is given by

$$n_{\mathrm{liq}}(T_{\mathrm{cell}}) = V_{\mathrm{cell}} \cdot \frac{\rho(T_{\mathrm{cell}})}{M}, \tag{5.3}$$

where

- $V_{\mathrm{cell}} = 2010\,\mathrm{mm^3}$ is the volume of the cryogenic cell,
- $\rho(T_{\mathrm{cell}})$ is the density of the fluid as a function of the operating pressure and temperature T_{cell} and
- M is the molar mass, which is $2\,\mathrm{g\,mol^{-1}}$ for H_2, $4\,\mathrm{g\,mol^{-1}}$ for D_2 and $6\,\mathrm{g\,mol^{-1}}$ for T_2.

The results are given in table 5.1.

As long as the pressure inside the cell is higher than the vapour pressure, the liquid will continue to fill the tubes and the sampling cell. The table shows that an adjustable temperature range of 9 K is achievable for protium H_2, 8 K for deuterium D_2 and 7 K for tritium T_2 for the temperature dependent studies. This makes it possible to liquefy tritium directly with the tritium supply pressure of the TLK infrastructure of 0.9 bar is possible.

Determination of maximum pressure for worth case scenario In addition to the liquefaction process analysis, a second was carried out on the maximum pressure inside the buffer vessel was carried out. It was assumed that the op converter and the cell were completely filled with liquid hydrogen and that the inlet and outlet gas pipes as well as the 3 buffer vessels were completely filled with gaseous T_2 at the maximum operating pressure of 2.5 bar. In the event of a cooling failure, it was expected that the liwuid would evaporate completely in an instant. The question was whether the maximum design pressure of 5 bar would be exceeded. Calculations showed

[8] The volume of the pipes connecting the buffer vessel to the cryogenic cell and other dead ends is negligible compared to the buffer volume V_{buffer}.

Table 5.1: Temperature and pressure parameters for the condensation process. For the three homonuclear isotopologues, the required filling pressure p_{fill}, the vapour pressure p_{boil} and the pressure difference Δp are given for the corresponding cell temperature T_{cell}. The three letters ^{a,b,c} indicate the triple points of the isotopologues. The asterisk * indicates the maximum temperature at which the maximum pressure of 2.5 bar is reached for each isotopologue.

	H_2			D_2			T_2		
T_{cell} (K)	p_{vap} (bar)	Δp (bar)	p_{fill} (bar)	p_{vap} (bar)	Δp (bar)	p_{fill} (bar)	p_{vap} (bar)	Δp (bar)	p_{fill} (bar)
13.957^a	0.074	0.097	0.170						
14	0.075	0.096	0.172						
15	0.129	0.095	0.224						
16	0.208	0.094	0.302						
17	0.318	0.093	0.411						
18	0.466	0.092	0.558						
18.724^b	0.602	0.091	0.693	0.172	0.109	0.281			
19	0.660	0.091	0.751	0.194	0.109	0.303			
20	0.907	0.089	0.996	0.294	0.108	0.402			
20.623^c	1.091	0.088	1.180	0.374	0.107	0.481	0.216	0.114	0.330
21	1.215	0.088	1.303	0.429	0.106	0.535			
22	1.591	0.086	1.678	0.606	0.105	0.711	0.374	0.112	0.486
23	2.044	0.085	2.129	0.833	0.103	0.936			
23.711*	2.416	0.083	2.500	0.878	0.103	0.981			
24	2.581	0.083	2.664	1.116	0.101	1.217	0.741	0.109	0.850
25	3.210	0.081	3.291	1.464	0.100	1.564			
26	3.940	0.079	4.019	1.885	0.098	1.982	1.330	0.105	1.435
27	4.779	0.077	4.856	2.386	0.096	2.482			
27.033*	4.809	0.077	4.885	2.404	0.096	2.500			
28 *	5.736	0.074	5.810	2.976	0.094	3.070	2.200	0.102	2.302
30	8.043	0.068	8.112	4.458	0.090	4.547	3.410	0.097	3.507
31	9.416	0.064	9.481	5.367	0.087	5.454			
32				6.401	0.085	6.486	5.060	0.093	5.153

that the pressure would rise to 2.6 bar, still below the maximum design pressure of 5 bar. In a second step, it was assumed that all viewports would burst. As a consequence, the pressure inside the cryostat would rise up to 1.9 bar, also within the specifications.

In summary, the cell volume and the buffer volume allow temperature dependent IR and Raman studies with an adjustable temperature range of at least 6 K, and in case of a cooling failure the pressure of 5 bar is not exceeded.

5.4 Technical implementation and manufacturing

The conceptual and process design were discussed in the previous section 5.3, where a basic understanding of the T_2ApIR experiment and the main liquefaction process could already be gained. This section focuses on the realisation of the cryogenic part, especially the sample cell, the op converter and their connections to the cryocooler inside the cryostat. Finally, the optical realisation for a combined IR and LARA spectroscopic setup is presented.

5.4.1 Design and construction of the cryogenic part

The most complex parts of T_2ApIR are the cryogenic cell and the cryostat. These are the functional parts where liquid isotopologues Q_2, the IR and the laser beam, the op reactions in the catalyst intersect, while being tritium compatible, overpressure and temperature compatible. In this section, the realisation from the design to the manufacturing process is presented and explained in detail. These parts, already published in [Kra20], are also covered in this section, but in a shorter form.

Figure 5.1 shows a simplified sketch of the T_2ApIR experiment. The cross-shaped cryostat is divided into two components: the cooling/vacuum interface and the cube. Both elements are made of stainless steel (type X6CrNiMoTi17-12-2). They were then polished. Figure 5.2 shows the cryostat from the outside, with the cooling/vacuum interface and the cube clearly visible. The total volume of the cryostat is 15.6 dm^3 and with instrumentation 14.3 dm^3.

Cooling/vacuum interface

Overview Figure 5.3 shows a longitudinal cut through the cryostat. The interface is 0.5 m long and 0.3 m wide and has four CF-160 flanges in the plane. Along the longitudinal axis, the motor head of the cryocooler and, on the opposite side, the cube are connected to the flanges. Along the transverse axis, the pumping station for the insulation vacuum is connected via a flexible corrugated tube. On the other side is a blind flange with feedthroughs for sensors and cables. Inside the cross is the cryocooler with its two cooling stages and the main part of the 50 K copper shielding.

Cryocooler A Gifford-McMahon (GM) cryocooler is used to provide a variable temperature range down to 10 K. This is an RDK-415D 4 K cold head with a cooling power of 1.5 W at 4 K in the second stage and 45 W at 50 K in the first stage. The 45 W are only possible if the cryocooler is used in the 60 Hz mode, as intended in the experiment[9]. A detailed cold head capacity map for 60 Hz and 50 Hz can be found in appendix C. Each cold stage is equipped with a heater

[9] In the 50 Hz mode, the maximum cooling power of the first stage is 35 W. The second stage remains the same.

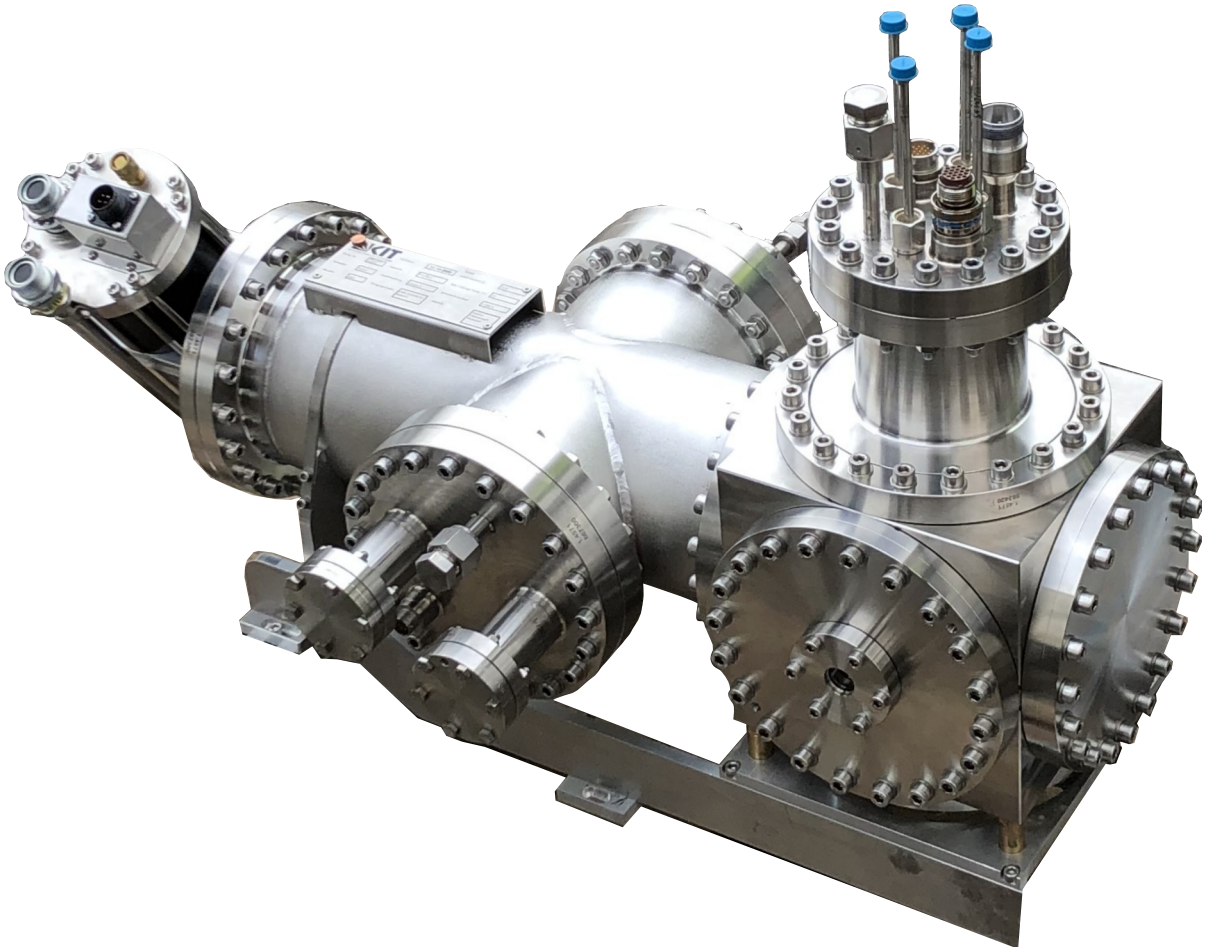

Figure 5.2: External view of the cross-shaped cryostat. The cross-shaped cryostat consists of the cube (on the right side) and the cooling/vacuum interface to the cryocooler motor head.

block, containing heater cartridges and silicon temperature sensors. Specific information on size, type of sensors, and heaters can be found in the RDK-415D supplementary material in appendix C. The RDK-415D has a total length of 558.5 mm and a total weight of 18.5 kg. During normal operation the cryocooler vibrates due to the helium being pushed back and forth internally. As the cryostat is connected to the rest of the experimental setup by braces, continuous vibration would loosen the connections. Therefore, the cross-shaped cryostat is connected to four rubber feet to dampen vibrations. A helium compressor of type CSA-71A is connected via 20 m of flexible lines. The helium is pressurised to 20 bar in these lines. The working principle of this type of cryocooler is published in [Tim66].

Insulation vacuum Sufficient vacuum is required to suppress heat transfer by convection. Therefore, the pressure inside the interface must be $p < 1 \cdot 10^{-6}$ mbar and on the other hand the whole setup must have a leak rate of $l < 10 \cdot 10^{-8}$ mbar l. To meet these two requirements, a two-stage pumping system is connected via one of the CF-160 flanges (not shown in figure 5.3): a Pfeiffer HiPace300 turbomolecular pump and an ACP15. The ACP15 evacuates the cryostat to the 10^{-2} mbar range and the HiPace300 generates the high vacuum in the order of 10^{-6} mbar. Between the HiPace300 and the CF-160 side flange there are two VAT gate valves connected in series. In the event of a tritium release, the pressure inside the cryostat rises and then these two

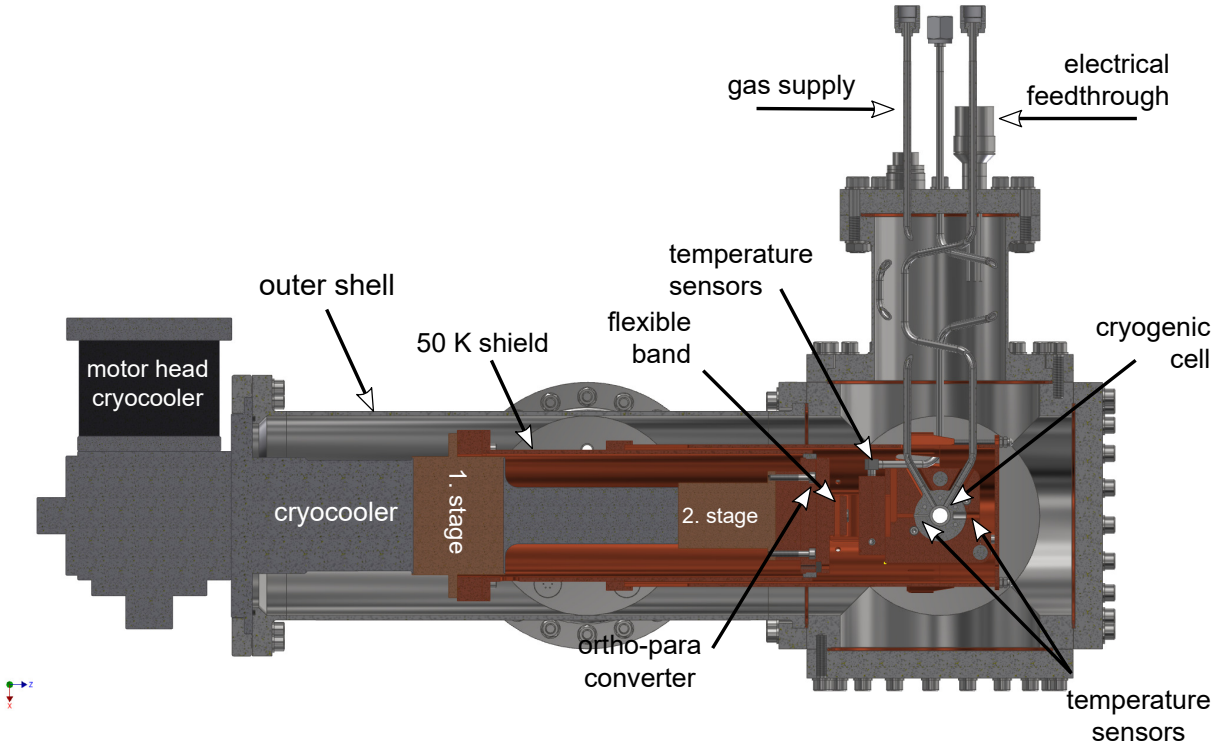

Figure 5.3: Longitudinal cut through the T_2ApIR cryostat. Starting on the left with the motor head of the cryocooler, followed by the CF-160 flange, the first and second stages are part of the so-called cooling/vacuum interface. Connected by flexible copper bands are the mountings for the op converter and the cryogenic sample cell. The copper shield is coloured in brown and surrounds everything from the first stage of the cryocooler to the sample cell. Two holes in the shield allow the IR, laser and Raman light to pass through. The copper shield and mountings are all gold-plated but not coloured.

gate valves immediately close (signal reading of 0.5 s) so that no tritium is pumped out. For the removal of the released tritium T_2, an additional pipe, as shown in figure 5.1, must be connected to the setup. Through this pipe the tritiated gases can be pumped away and fresh gas can be inserted to purge the cryostat.

Another major challenge is to find tritium compatible pumps to transfer the exhaust gases to the central tritium retention system (ZTS). The HiPace300 is an all-metal pump with CF connections, sealed with copper sealings. The KF connections of the ACP15 normally use polymer sealings. As these sealings are not tritium compatible, the T_2ApIR experiment uses a special type: helico flex from Technetics. There is an aluminium o-ring and clamps around it.

The two monitoring pressure sensors that control the gate valves are mounted on the opposite side flange via a CF-63 connection. These are two Pirani cold cathode sensors, type Pfeiffer PKR 261, for the low vacuum pressure range. Two are installed for redundancy. In addition to these two pressure sensors, there are two feedthroughs for the cryocooler heaters. More information on the Ceramaseal connections follows in the following sections.

Cube of the cryocooler

Overview A longitudinal cut through the cryostat is shown in figure 5.3. The cube has a total of six CF-160 flanges on all its sides and it is made out of stainless steel (X6CrNiMoTi17-12-2). The cryogenic sample cell is located in the centre of the cube. Next to it is the op converter. Both

components receive and return the gas via two pipes connected by a tube to the upper flange. Two CF-160 flanges, parallel to the longitudinal axis, each have a CF-40 viewport with sapphire windows for the light transmission.

Cryogenic sample cell The cryogenic sample cell is located in the centre of the cube. It is made of stainless steel (X6CrNiMoTi17-12-2) and has two CF-16 sapphire viewports through which the light can enter, see figure 5.4 A). The cell has a total volume of 2010 mm^3. The cell is also equipped with two temperature sensors, a platinum resistor based Pt1000, and a low temperature TVO sensor. The cell is mounted inside two copper half shells which are directly connected to the op converter mounting shells. It is necessary to keep the cryogenic cell in the same position at all times as the laser beam is focused on the centre of the cell. This is achieved by two zirconium oxide ceramic rods that hold the cell in position. Zirconium oxide was chosen because it has a low thermal conductivity of $(1.5-3)\,W\,m^{-1}\,K^{-1}$ and a sufficient shape and position tolerance of 0.01 mm over a total length of 200 mm.

Cold converter The op converter specifically adjusts the desired op equilibrium to determine the op influence on the IR spectra or on the thermal cycle of the KATRIN loop. Therefore, an additional experiment, called RaCoon, was used to investigate the op process extensively. The full section 4.3 deals with these investigations and the obtained results, section 4.3.5. Therefore, the whole design and the choice of catalyst material and quantity are based on the RaCoon section in chapter 4. The T_2ApIR converter is a U-shaped stainless steel tube of 6 mm diameter (X6CrNiMoTi17-12-2) with a total volume of 1.5 cm^3, see also figure 5.4 A) and B) on the right side. At the bottom of U-shaped tube, there are 2.3 g of iron(III) oxide Fe_2O_3 as catalyst material with a grain size of (700 – 1200) µm, see figure 4.8. There is a 90° Micro-Fit® elbow union at both the inlet and outlet to connect the U-shaped tube to the gas inlet and outlet pipes leading to the top flange (figure 5.4). A Pt1000 temperature sensor has been inserted through an additional bore in each elbow so that the sensor is just above the catalyst material (see figure 4.8). Two copper half-shells surround the op converter, see figure 5.4 C), and are connected on the one side to the half-shells holding the cell. On the opposite side, two flexible copper bands connect the converter-cell-unit to the second stage of the cryocooler. This ensures reliable heat transfer from the cooling stage to the cell-converter-unit is guaranteed. On the other hand, the flexible bands can be easily removed, allowing the op converter to be heated up to 200 °C to activate the iron(III) oxide. Permanent connection to the cooling stage during the activation procedure could cause damage to the cryocooler. Two Thermocoax heating wires were provided for heating the op converter, see section 4.3.4.3. As it is not possible to place the heating wire directly around the U-shaped tube, a groove was milled on the outside of each half-shell, see figure 5.4 C) left part. To activate the catalyst material, not only the material itself but also the entire copper unit is heated. Calculations show that it takes approximately 1.2 h to reach a temperature of 420 K for a 40 W heating wire. More information on the calculations is given in appendix D.

50 K copper shield T_2ApIR is designed to cool down the cryogenic measurement cell to 10 K for the desired low temperature spectroscopic studies. Therefore, not only must sufficient cooling power be available, but all thermal contributions must be minimised. There are three ways in which heat can be transported [Lie20]

1. Thermal conduction: Thermal energy is transferred through the direction of the materials.

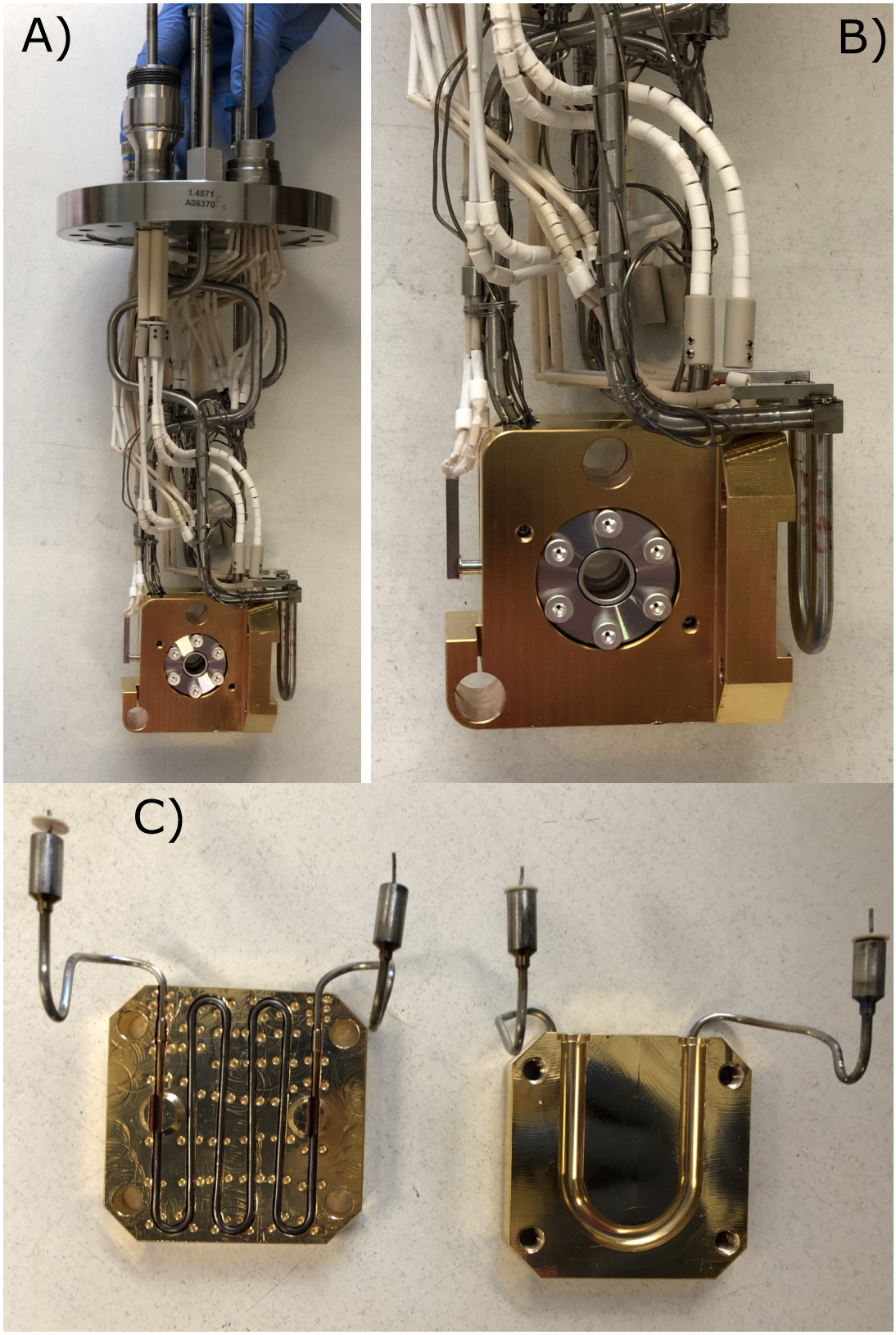

Figure 5.4: Cryogenic sample cell and ortho-para converter. The two top figures A) and B) show the cryogenic sample cell with the CF-16 sapphire viewport. To the right is the U-shaped op converter. Heating elements are wrapped around the gas supply lines. The small white pellets are made of ceramic and are used to insulate the wires for the temperature sensors. Below, figure C) shows the two half-shells that surround the U-shaped op converter. Both half-shells have the milling groove for the converter on one side and a Thermocoax wire on the back to heat the converter for activation purposes.

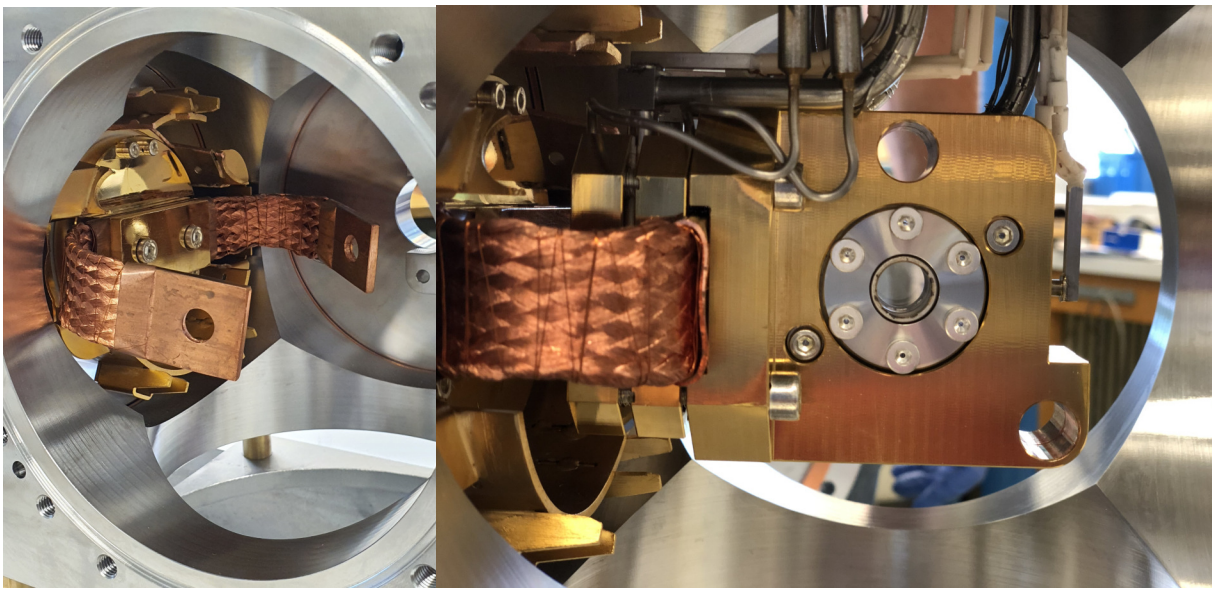

Figure 5.5: Copper band connection: second stage and converter-cell-unit. The left part shows the two copper bands connected to the second cold stage of the cryocooler by a gold-coated plate. On the right, the cryogenic cell and the op converter form a single unit. The two lugs of the copper bands are inserted between the converter and the cell.

2. Convection: Thermal energy is carried along in a flowing medium, such as air.
3. Thermal radiation: Thermal energy is transferred by electromagnetic waves.

Thermal conduction is described by the equation

$$\dot{Q}_{\text{con}} = \lambda \cdot A \cdot \frac{T_{\text{warm}} - T_{\text{cold}}}{d}, \tag{5.4}$$

with λ is the thermal conductivity (value dependent on temperature), A is the area through which the heat flows, T_{warm} is the temperature of the warm surface and T_{cold} is that of the cold surface, and d is the distance between the warm and the cold parts. A small area A and a low heat conductivity λ combined with a large distance reduce the heat input by the thermal conduction.

By creating a vacuum with a pressure of less than $10 \cdot 10^{-6}$ mbar, **thermal convection** is negligible.

Thermal radiation is given by the equation

$$\dot{Q}_{\text{rad}} = \epsilon \cdot \sigma \cdot A \cdot T^4, \tag{5.5}$$

with ϵ is the emissivity factor, σ is the Stefan-Boltzmann constant σ, A is the area and T is the temperature of the emitting body. Because of the T^4 dependence, the surface's temperature must be kept as low as possible, and low emissivity materials are preferred. This is the reason for the implementation of an additional cold shield. This additional cold shield reduces the heat input from the cryostat surface (T300 K) to the cryogenic cell ($T = 15$ K) by a factor of 1296 compared to a copper shield at $T = 50$ K[10]. The cold shield consists of three separate elements

[10] $\frac{T^4_{\text{cryo}}}{T^4_{\text{shield}}} = \frac{300^4}{50^4} = 6^4 = 1296.$

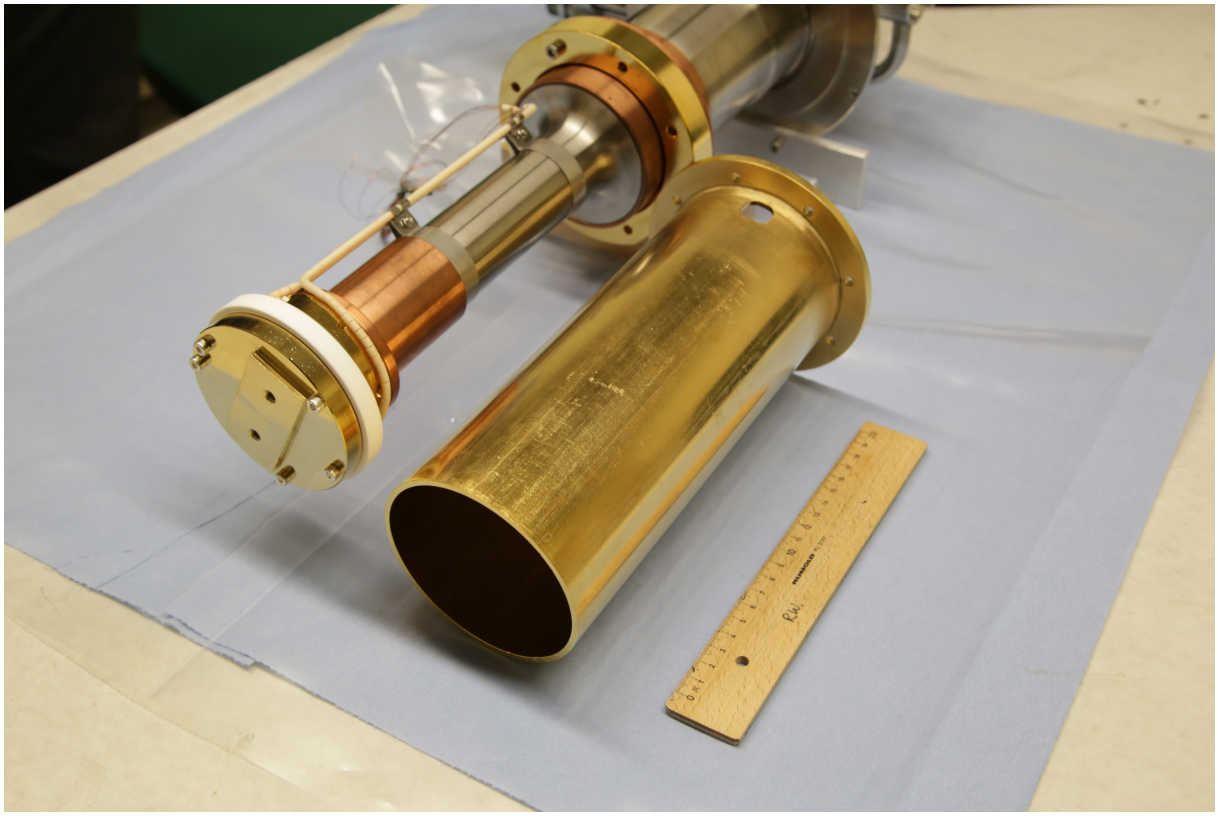

Figure 5.6: Gold-plated cold shield. The main part of the cold shield is 26 cm long and is flanged to the first cold stage of the cryocooler. It is made of copper and gold-plated. The two additional parts of the cold shield, which cover the converter and the cell, are not shown here but are shown in figure 5.3.

surrounding the cryogenic sample cell, the converter and most of the cryocooler. It is made of copper, which has a good thermal conductivity of $384\,\mathrm{W\,m^{-1}\,K}$ to transfer the cooling power to its surface. It also has a gold-plated surface, as gold ($\epsilon = 0,02$) has an emissivity 2.5 lower than polished copper ($\epsilon = 0.05$), to reduce the thermal radiation. The three parts are arranged in such a way that the back part is mounted directly on the first stage of the cryocooler, see also figure 5.6 and the sketch in figure 5.3. The centre and front sections can be separated from each other, allowing the front section to be removed and the centre section to be moved over the rear section. This flexibility and mobility of the cold shield, together with the two flexible copper bands, is essential for removing the cryogenic cell and the converter by lifting the tube on the top flange. Besides, the copper shield has two holes for the incoming and outgoing IR and laser beam and the Raman light.

Additional information on thermal calculations from thermal conduction and radiation is given in appendix E. As a result, the total heat input to the cold shield is 6.89 W (first cold stage) and to the cell is 2.28 W (second cold stage). The performance of the selected cryocooler is sufficient.

Heaters and temperature sensors Temperature sensors are essential for monitoring and measurements purposes. A total of total four temperature sensors are installed inside the cube. Two platinum sensors PT1000, industrially manufactured in accordance with EN 60751, for the op converter, installed at the inlet and outlet of the U-shaped tube via the union elbow. During the activation process, one PT1000 sensor is used as a controller and the other as a safety feature

to shut down the heater when the threshold is exceeded. The other PT1000 sensor is installed in the cryogenic cell next to a TVO, negative temperature coefficient (NTC) thermistor with a compound of coal and aluminium oxide. The measuring range of the TVO is (1.6 – 420) K. A copper sleeve encapsulates the TVO sensor for an easier installation in the bore. Figure 5.3 shows the position of the sample cell sensors, with the TVO on the right and the PT1000 opposite. Calibration of the temperature sensors prior to installation is not required but is helpful.

The Thermocoax heating wire for activating the catalyst material has already been mentioned. In addition to this, there are eight other Thermocoax heating wires implemented on the surface of the pipes for the gas supply of the cryogenic sample and the op converter, see also figure 5.4. These wire are provided for safety reasons. In the event of a sudden loss of cooling power, the liquid inside the cell and the converter would immediately begin to evaporate. The heat of evaporation can cause the connecting pipes to freeze, which would lead to an increase in pressure inside the cell, followed by a possible bursting of the window. In order to prevent such a window bursting, the Thermocoax wire heater starts to heat the pipes directly, preventing them from freezing. There are four gas supply pipes in total, two for the cryogenic cell and two for the converter. Each pipe is wired with the Thermocoax cable, even so only one is for active use and the other for compensation (for redundancy reasons).

The instrumentation of sensors and heaters inside the cryostat is so compact, that opening the cryostat and replacing components inside the glove box would be a major undertaking. All electrical cables are insulated with small white ceramic pellets to each other.

5.4.2 Combined optical system for laser Raman and IR spectroscopy

The T_2ApIR experiments enables the investigation of molecular and intermolecular effects of all six hydrogen isotopologues at cold temperature, see section 5.1. The TLK offers different analytical methods, such as calorimetry, gas chromatography, Raman spectroscopy, to meet the diverse requirements. Based on the experience and the expertise gained from previous experiments at the TLK [Lew07; Lew08; Stu10; Fis11; Sch13b; Sch13a; Sch13d; Sch13c; Jam13a; Jam13b; Kra13; Fis15; Grö15a; Grö15b; Rup15b; Rup15a; Sch15b; Sch15a; Sch15c; Jam15; Grö17; Sch17; Rei19; Mül19a; Grö20; Mir20; Ake20b; Lai20; Nie21b; Pri22], IR absorption spectroscopy and LARA spectroscopy were chosen as the methods of choice.

This section presents the optical design of the combined spectroscopic system based on the requirements and the results of the pre-investigations (reproducibility of the movable x-stage, section 4.4.2, and silver- and gold-coated parabolic mirrors, section 4.4.3).

Optical design The requirements for the combined setup have been detailed in section 5.2.4. The main limitations are: IR and Raman have to use the same optical path through the cell; the use of both techniques, Raman and IR, requires an easy switching between them and suitable optical components for both; most of the optical components are located inside the glove box, so an automated adjustment of components, such as lenses, mirrors, is desired. All these considerations, demands and requirements have led to the optical design shown in figure 5.7.

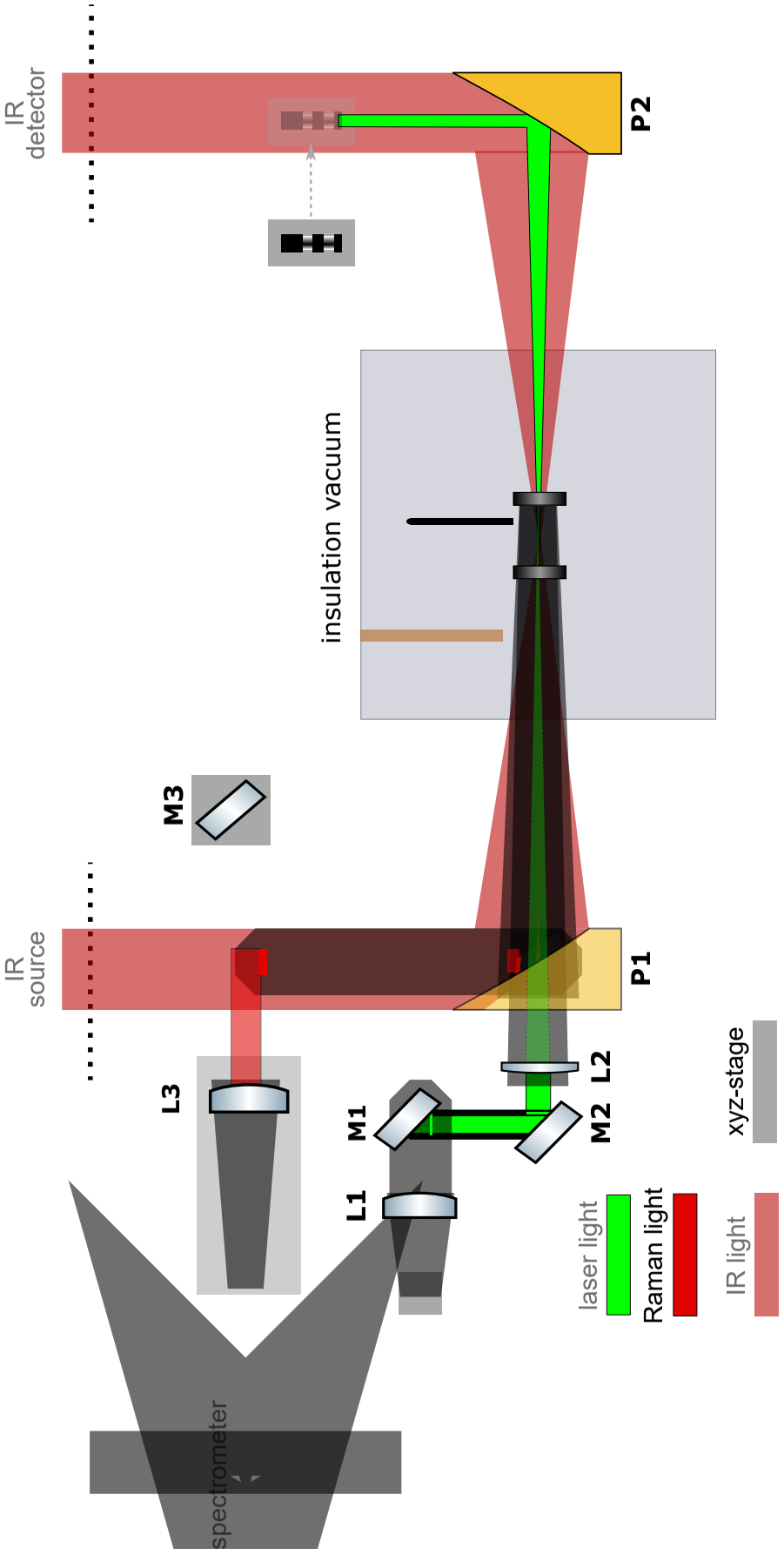
IR detector
P2
insulation vacuum
M3
IR source
P1
L3
L2
M1
M2
L1
xyz-stage
laser light
Raman light
IR light
spectrometer

In the case of LARA spectroscopy, the laser beam is transmitted from the outside of the glove box to the inside via a glass fibre. Using two lenses (L1, L2) and two mirrors (M1, M2), the laser beam is focused through the mirror with hole (P1) into the centre of the sample cell and guided via the mirror (P2) to the beam dump, where it is safely stored. The interaction between the laser beam and the molecules inside the sample cell generates the Raman light, which is emitted isotropically. The Raman light in the direction of the incoming laser beam is collected by the mirrors (P1, M3) and the lens (L3) and sent to a second glass fibre which is connected to the spectrometer outside of the glove box.

To enable IR absorption spectroscopy, the beam dump and the mirror (M3) must be moved to the side. The IR source and the IR detector are located outside the glove box. The incoming IR light is focused by the mirror (P1) into the centre of the sample cell. The unabsorbed light is collected on the other side and directed to the detector by the mirror (P2).

The two mirrors (P1, P2) are critical to the optical success of the investigation. They are parabolic mirrors and must be suitable for Raman and IR. With regard to the results of section 4.4.3, the mirrors have a silver coating, since it has a higher reflectivity in the wavelength range of the scattered Raman light. The mirror (P1) needs a hole on the inside for the laser beam.

One of the biggest challenges with viewports is the overpressure. There are almost no companies left that provide viewports for an overpressure use. Hositrad is the only company that offers the required viewports. The viewports (W1, W2) are made of sapphire. They are mounted directly in the cube. The viewports (W3, W4) are made of borosilicate glass, specially selected for good IR light transmission. The viewports (W5, W6) are CF-16 sapphire viewports that are part of the cryogenic sample cell.

Linear z-stages are used to move the optical components in and out of the beam path. As discussed in section 4.4.2, the resolution of the linear stage must be high enough to meet KATRIN's precision requirements.

In summary, the optical design developed for the combined use of LARA and IR spectroscopy is suitable for the investigation of intermolecular effects.

5.4.3 Connection to the TLK infrastructure

Like any tritium leading experiment, T_2ApIR is housed in a typical glove box of the TLK infrastructure. The main purpose of the glove box is to provide a second containment and therefore safe tritium confinement in the event of a tritium release from the primary system. One half of the BETTINA glove box houses T_2ApIR. As the BETTINA glove box has never been used for tritium experiments before, connections to the various interfaces of the TLK infrastructure had to be designed and manufactured. The main interfaces are

- the connection to the ZTS,
- the connection to the CAPER C glove box for tritium support,
- the connection to the He and N_2 ring circuits for gas supply,
- the installation of a cabinet for gas bottle for inactive gas supply,
- the connection to the UDH (negative pressure system) for the pressure inside the glove box,

Table 5.2: Overview of optical components and their properties. The table below lists all the optical components used in the glove box to guide and focus the different beam paths.

comp.	properties	company, product number
L1	lens, $f = 10\,\text{mm}, \oslash = 6\,\text{mm}$	Thorlabs, LA4280-YAG
L2	lens, $f = 300\,\text{mm}, \oslash = 1''$	Thorlabs, LA1484-A-ML
L3	lens, $f = 40\,\text{mm}, \oslash = 1''$	Thorlabs, LA1951-A-ML
M1	Nd: YAG mirror, (524 – 532) nm, $\oslash = 1''$	Thorlabs, NB1-K12
M2	Nd: YAG mirror, (524 – 532) nm, $\oslash = 1''$	Thorlabs, NB1-K12
M3	broadband dielectric mirror, (400 – 750) nm	Thorlabs, BB1-E02
P1	off-axis parabolic mirror, silver coated	Thorlabs, MPD299H2-P01-SP
	$f = 268.6\,\text{mm}, \oslash = 2'', \oslash_{\text{hole}} = 2\,\text{mm}$	
P2	off-axis parabolic mirror, silver coated,	Thorlabs, MPD299-P01-SP
	$f = 268.6\,\text{mm}, \oslash = 2''$	
W1	borsilicate glass	Hositrad, customized
W2	borsilicate glass	Hositrad
W3	CF-40 sapphire viewports, $\oslash_{\text{view}} = 2.06\,\text{cm}$	Hositrad, 18617-02-CF
W4	CF-40 sapphire viewports, $\oslash_{\text{view}} = 2.06\,\text{cm}$	Hositrad, 18617-02-CF
W5	CF-16 sapphire viewports, $\oslash_{\text{view}} = 1.016\,\text{cm}$	Hositrad, 95747-04-CF
W6	CF-16 sapphire viewports, $\oslash_{\text{view}} = 1.016\,\text{cm}$	Hositrad, 95747-04-CF
	Nexus breadboard, 300 mm × 450 mm × 60 mm, M6	Thorlabs, B3045A

- the connection to an ionisation chamber for monitoring the gas inside the glove box and
- the design, manufacture, installation and wiring of the electrical cabinet for all electrical equipment and sensors inside the glove box.

Functional testing of all these connections is therefore part of the commissioning of the second containment.

5.5 Conclusion and outlook

As mentioned at the beginning, the development of a new experiment suitable for tritium is necessary to study the molecular and intermolecular effects in the thermal cycle of KATRIN. The main focus will be on the time constants of the chemical and op conversion, as well as exchange reactions and dimer formation. In addition, a complete calibration of the IR absorbance of all six hydrogen isotopologues in all three states of aggregation should be possible in order to be able to use the calibrated system in a combined ISS and WDS for process control. The T_2ApIR experiment allows such investigations and calibrations are possible. T_2ApIR is an experiment designed to handle 13.5 g of pure tritium T_2 and an overpressure of 2.5 bar absolute.

The cryogenic measuring cell covers a temperature range between (10 – 300) K and enables both LARA spectroscopic and IR investigations.

Through the various pre-investigations, the final design of T_2ApIR was as follows. The optical design allows LARA and IR studies to be performed in a common setup, so that all molecular effects can be examined. The use of silver-coated mirrors, movable linear z-stages and special components such as mirrors with holes allows automated switching between LARA and T_2ApIR is possible. The LARA4 system provides an additional measuring cell located in the warm region at room temperature, enabling the underlying physical effects to be investigated in parallel. In addition, the cryogenic measuring cell offers the possibility to investigate impurities such as methane or oxygen in combination with tritium, which was not possible in this way before.

By using an op converter that can be cooled down to 10 K and a chemical converter at room temperature, specific mixtures can be produced to analyse the desired exchange reactions and conversion rates under different conditions. The U-shaped design of the converter is based on the studies of the RaCoon system and also enables the exchange of catalyst material in the T_2ApIR experiment, even if other components have to be removed first. The use of Thermocoax cables allows activation of the catalyst material at 180 °C. The cryogenic design, especially the copper thermal shield with a gold plating, gives the ability to cool the cryogenic cell down to 10 K and liquefy hydrogen isotopologues. Calculations of the heat input have shown that the cell and the converter can be sufficiently cooled by the cooling power available from the cryocooler.

In fact, due to the design and construction of T_2ApIR makes it possible to reproduce the complete thermal cycle of the KATRIN source loop: the cryogenic measurement cell represents the WGTS, the warm cell corresponds to the Lara measurement cell and, with the chemical converter at room temperature, the permeator can also be reproduced, the circulation pump enables the gas to be circulated.

Based on the RaCoon experiment purity studies, T_2ApIR is equipped with different gas filter cartridges for the gases used to keep out even the smallest amounts of impurities.

The design of the buffer vessels allows temperature dependent investigations in the liquid phase over a temperature range of 10 K for H_2, 8 K for D_2 and 7 K for T_2 in order to understand the formation of tritium dimers.

Calculations for possible worst-case scenarios, such as a sudden loss of cooling power when the cell is completely filled with liquid, have also shown that the buffer vessels are designed to be sufficiently large enough and that the tolerances are maintained. The design also takes into account the possibility of the cryogenic cell's viewports bursting, preventing tritium from leaving the primary system.

T_2ApIR meets the requirements for temperature (10 – 300) K, overpressure (up to 2.5 bar absolute), tritium capability, LARA and IR measurements, allowing the investigations to meet their scientific objectives. The next step is the careful commissioning of the facility. This includes checking the safety conditions, the flowability of the facility and the response of all sensors and valves. In a second step, first measurements on inactive hydrogen isotopologues can be performed. This will give a first feel for the handling of T_2ApIR. In addition, it makes sense not to contaminate the system with tritium right at the beginning, as this would make pure H_2 and D_2 studies impossible.

6 Summary and outlook

According to current knowledge, neutrinos are the most abundant massive elementary particles in the universe [Dep19]. In popular science, neutrinos are often also referred to as ghost particles because they have no electric charge and interact only weakly, making their experimental detection difficult for a long time [Cow56] and only possible with the development of new detector technologies. Nevertheless, it is precisely these properties that make neutrinos ideal messenger particles, as they carry information from distant galactic objects through the universe to us without any loss of information [Spu15; Bra16; Aar18; Reu22]. The observation of neutrino oscillation [Ahm01; Ahm02] provides unambiguous evidence that neutrinos have a finite, non-zero mass. This discovery, which directly contradicts the SM [Oer06], gave impetus to a new field of neutrino physics [Shu11; Ere17]. Research collaborations around the world have been trying to determine the absolute neutrino mass scale in various ways, but without success so far. There are two types of mass detection: model-dependent, indirect methods and model-independent, direct methods. In the model-dependent approach, the neutrino mass is obtained from calculations of cosmological and astrophysical phenomena (e.g. supernova explosion). Direct methods, on the other hand, the energy spectrum of electrons e^- produced during radioactive β-decay is investigated spectroscopically. The world's leading limit is currently held by the KATRIN experiment with an upper limit of $0.8\,eV/c^2$ (90 % C.L). KATRIN studies the kinematic endpoint of the energy spectrum of the electrons e^- released during the decay of molecular tritium T_2 with a design sensitivity of $0.2\,eV/c^2$ (90 % C.L.). Tritium has the dual advantage of a low endpoint energy E_0 of 18.6 keV and a comparatively high activity. In the 70 m long KATRIN beamline, the tritium molecules decay in the 30 K cold source, the WGTS. The emitted electrons are adiabatically guided to the spectrometer, which is based on the MAC-E filter principle, to be analysed there according to their energy. A non-zero neutrino mass has its most obvious effect on the shape at the end of the spectrum. In order to unambiguously assign these small deviations in the shape to a neutrino mass, all systematic effects must be known and taken into account. As shown in the work of Seitz-Moskaliuk [Sei19], there are a large number of systematic effects associated with the WGTS. A central systematic effect is the calculation of the FSD. This in turn requires, among other things, the gas composition in the WGTS as an input parameter. Since only the chemical composition of the gas far out in the warm is determined using LARA spectroscopy, there is no explicit measurement of the source composition inside the WGTS. Instead, simulations and calculations are used to describe the gas evolution from the measurement to the source [Dos06; Bod15b]. Exchange reactions and conversion processes play an important role here. The crucial question is: how fast does the gas composition change and what is it actually like in the source? Since there is no direct way to measure the gas composition inside the KATRIN source, and simulations and calculations are only of limited value, a new experiment is needed. Therefore, the aim of this work was:

T_2ApIR: Design, construction and set-up of a tritium-compatible experiment to systematically investigate the molecular and intermolecular effects of all six hydrogen isotopologues under KATRIN-like conditions.

The composition of the gas at KATRIN is significantly determined by three contributions: chemical (H_2, HD, HT, D_2, DT, T_2), ortho-para (o-H_2, p-H_2, o-D_2, p-D_2, o-T_2, p-T_2) and dimers, as the simplest form of two bound molecules $(T_2)_2$. Studies in the literature on conversion rates and exchange reactions or dimer formation are only partially available for tritium or, as in the case of dimer studies, not available at all. In order to be able to investigate all these different effects with the T_2ApIR experiment, the appropriate measurement technology must first be developed and tested in corresponding pre-investigations.

1. To investigate the influence of tritium decay on the exchange reactions, the natural isotope exchange of H_2 and D_2 as well as H_2 and T_2 was studied at room temperature.
2. Chemical and op catalysts are required to force mixtures into specific compositions to trigger exchange reactions. With the RaCoon facility, both chemical and ortho conversion studies of the inactive isotopologues can be investigated in parallel and measured simultaneously by LARA spectroscopy.
3. In the case of dimers, the measurement method of choice is IR spectroscopy, which has already been used in studies by Mirz [Mir19] on inactive hydrogen isotopologues. On the contrary, to study conversion rates and equilibrium states, LARA is the method of choice. For T_2ApIR this means a common optical experimental setup, since only a cryogenic optical cell is available.

The studies on isotope exchange have shown that the time constant for the formation of HT is in the order of hours, which is two orders of magnitude smaller than the time constant for the formation of HD. This supports the observations in the literature that new reaction channels are opened by the radioactive decay, in particular by the β-electron and the ion that is formed. Further experiments are needed to investigate the influence of the laser beam on the conversion, as well as the exchange reactions of atoms on metal surfaces. Regarding the production of a certain mixing ratio of only H_2 and T_2, it should be noted that circulation times longer than 5 min in the presence of tritium already initiate the conversion process.

The RaCoon system designed and constructed for this work, as well as the associated and also constructed LARA4 system, showed that the developed measurement method of partial catalysis is possible and well suited for conversion studies, depending on the parameters pressure, temperature, flow and catalyst material (grain size, activation temperature), for both chemical and op. Both the measurement principle and the design of the converter could thus be adopted for T_2ApIR.

The pre-investigations into the spectroscopic setup of a combined IR and LARA setup were necessary because either the optical components used are either suitable for both types of spectroscopy or can be automatically moved out of the beam path. For example, silver-coated mirrors are more suited to LARA and IR than gold-coated mirrors, as the former have on average a 20 % better reflectivity. The use of movable linear stages to move optical components for Raman spectroscopy shows a measurement uncertainty of 2.6 % in the intensity. This is within the KATRIN requirement. Nevertheless, further investigations to reduce the uncertainty are useful. This includes, for instance, varying the traverse speed.

All these findings have been directly incorporated into the design of T_2ApIR. The heart of the system is the cryogenic measurement cell, which together with the op converter can be cooled down to 10 K using a cryocooler (type RDK-415). The cell has two transmission viewports made

of fused silica and the associated optical setup enables IR and LARA investigations. The op converter is filled with 18 g of Fe_2O_3 iron oxide and can be heated up to 200 °C to activate the catalyst material, which is necessary as shown by measurements with RaCoon on the poisoning of catalysts with humid air. The developed activation procedure is based on the complex and partly contradictory statements in the literature and focuses on the reproducibility. 180 °C was found to be the optimum activation temperature for iron oxide. Two Pt100 sensors are used to monitor the gas temperature at the inlet and outlet. Both components are surrounded by a copper thermal shield with a gold-plated surface to minimise thermal input. Thermal calculations show that the power provided by the cryocooler is sufficient. Studies of the temperature dependence of liquid physics require a temperature range of at least $\Delta T = 5\,\mathrm{K}$. The buffer vessels were designed accordingly to provide the minimum pressure for the condensation process in the cryogenic cell. This allows IR and Raman studies over a range of 7 K for T_2, 8 K for D_2 and 9 K for H_2.

By using an additional LARA system in the warm state, changes in gas composition from warm to cold and vice versa can be investigated. By using a chemical converter at room temperature, the entire thermal cycle of KATRIN can also be mapped with T_2ApIR. The cryogenic measuring cell represents the WGTS, the additional LARA measuring cell corresponds to the measuring cell at KATRIN, the chemical converter takes over the task of the permeator and the circulation pump circulates the gas. Thus, the conditions at KATRIN can be simulated in a similar way. The T_2ApIR experiment is a complex system that has to combine different requirements such as tritium compatibility, overpressure and cryogenic measurement range. In addition, the combined LARA and IR measurement setup is housed in a glove box with all its components, which means that the handling of small optical components in particular has to be automated. However, the design developed in this thesis meets all these requirements from a scientific and technical point of view.

The next step will be the commissioning of the facility, followed by measurements with inactive isotopologue mixtures to get a first feel for the facility and to compare the results with previous experiments. In a third step, further studies with tritium will be possible. The investigations on tritium dimers should be the first step, because according to the KATRIN design report [Ang05] they only exist below 30 K, whereas Mirz [Mir19] showed that dimers of H_2 and D_2 exist under KATRIN-like conditions. The 6 K temperature range in the liquid allows the necessary pressure and density dependence studies to be carried out. Especially the combination of IR and LARA allows new insights into the underlying physical effects.

A P&ID diagram of the RaCoon experiment

The RaCoon experiment enables kinetic studies of the op and chemical conversion of the hydrogen isotopologues. In Section 4.3.2, the figure 4.8 shows a simplified flow chart of the experiment to explain the basic measurement principle and measurement procedure. As the full experimental setup is much more complex, figure A.1 displays the P&ID diagram of the RaCoon facility. Highlighted in different colours are the converter (blue) KT001 on the top right, the LARA measurement cell (green) MZ001 on the top left, the vacuum pumping strain (violet) VA001 and KP002 in the middle as well as the gas supply system (orange) at the bottom. Not shown in the simplified flow chart is the binary gas analyser (BGA). This device measures the concentration via the speed of sound. The BGA was used for the first test to get in contact with this device and for cross-checking with the LARA4 system. The BGA data were not used in any of the measurement campaigns.

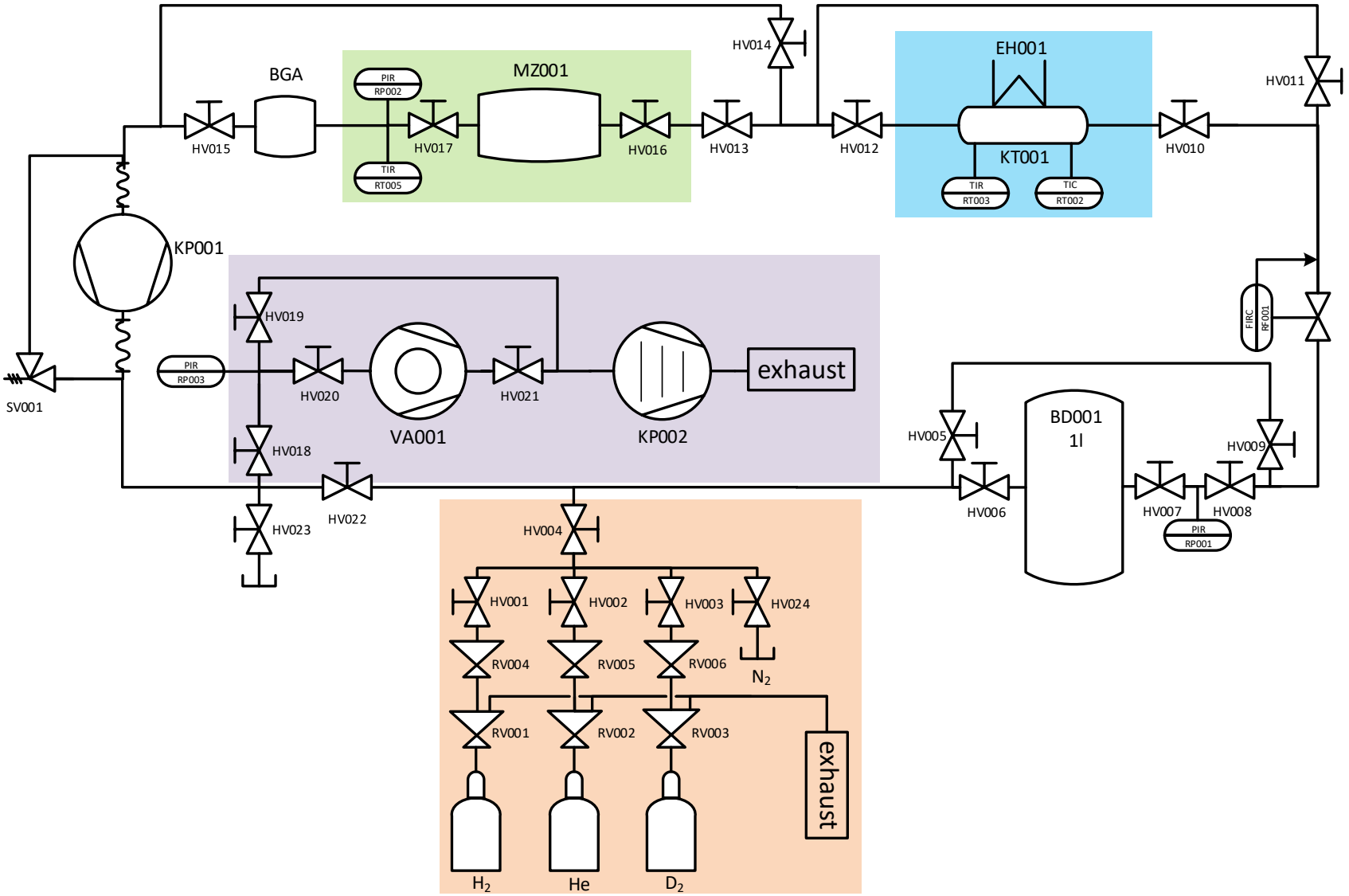

Figure A.1: P&ID diagram of the RaCoon experiment. This diagram shows all the components of the RaCoon system. HV stands for hand valve, RV for regulation valve, SV for safety valve, RP for pressure sensor, RT for temperature sensor and RF for flow sensor.

B P&ID diagram of the T_2ApIR experiment

The whole T_2ApIR experiment consists of many different components, each with a specific functionality and purpose. For a better understanding of the mode of operation, especially the processing mode, the complete P&ID diagram is shown in figure B.1. The T_2ApIR experiment can be divided into six different subgroups according to their purpose, each highlighted in a different colour:

- The two light blue areas represent the gas supply.
- The green area in the middle is called the loop and contains all the components for processing and mixing the gases.
- The purple area is the cryogenic part.
- The two sampling ports as well as the additional Raman system are underlaid in orange.
- The red part contains the vacuum pumping station.
- The last subgroup is shaded grey and shows the exhaust for the gases.

It would be beyond the scope of this work to explain each and every aspect of each component, so instead each subgroup is briefly described in terms of its purpose and operating principle. In addition to the colours and symbols for the sensors, valves etc., several dashed lines are shown. A dashed line connects a sensor to an automatic valve or pump and indicates that when the actual values are above or below a certain threshold, the valve closes or opens, the pump turns on or off respectively. All these interlocks and the safety states are explained in appendix F.

Gas supply

Two light blue areas, one at the bottom and one on the right side, mark the gas supply. The following non-radioactive gases can be used with T_2ApIR: protium (H_2), deuterium (D_2), neon (Ne), nitrogen (N_2), and helium (He). Protium, deuterium and neon are stored in carpet for gas bottles. For nitrogen and helium, the TLK has its own supply through a central ring circuit. Each of these gases passes through a gas filter cartridge (FI) to remove any impurities. Although the purity of the gas inside the bottle is quite high (10^{-6} ppm for protium), it is possible that small amounts of moisture and water vapour may be stored in the wall of the pipes. After the gas has passed the pressure controller (RV), the inlet flow is controlled by the flow controller RF001. Check valves (SV) are used to ensure that there is no back diffusion from the system to the gas bottles.

The light blue part in the middle right side shows the connection to the CAPER[1] glove box, from where T_2ApIR gets its tritium. A double implementation of automatic valves (AV) and pressure

[1] CAPER is the acronym for **Ca**talytic **PER**MCAT [Bor05].

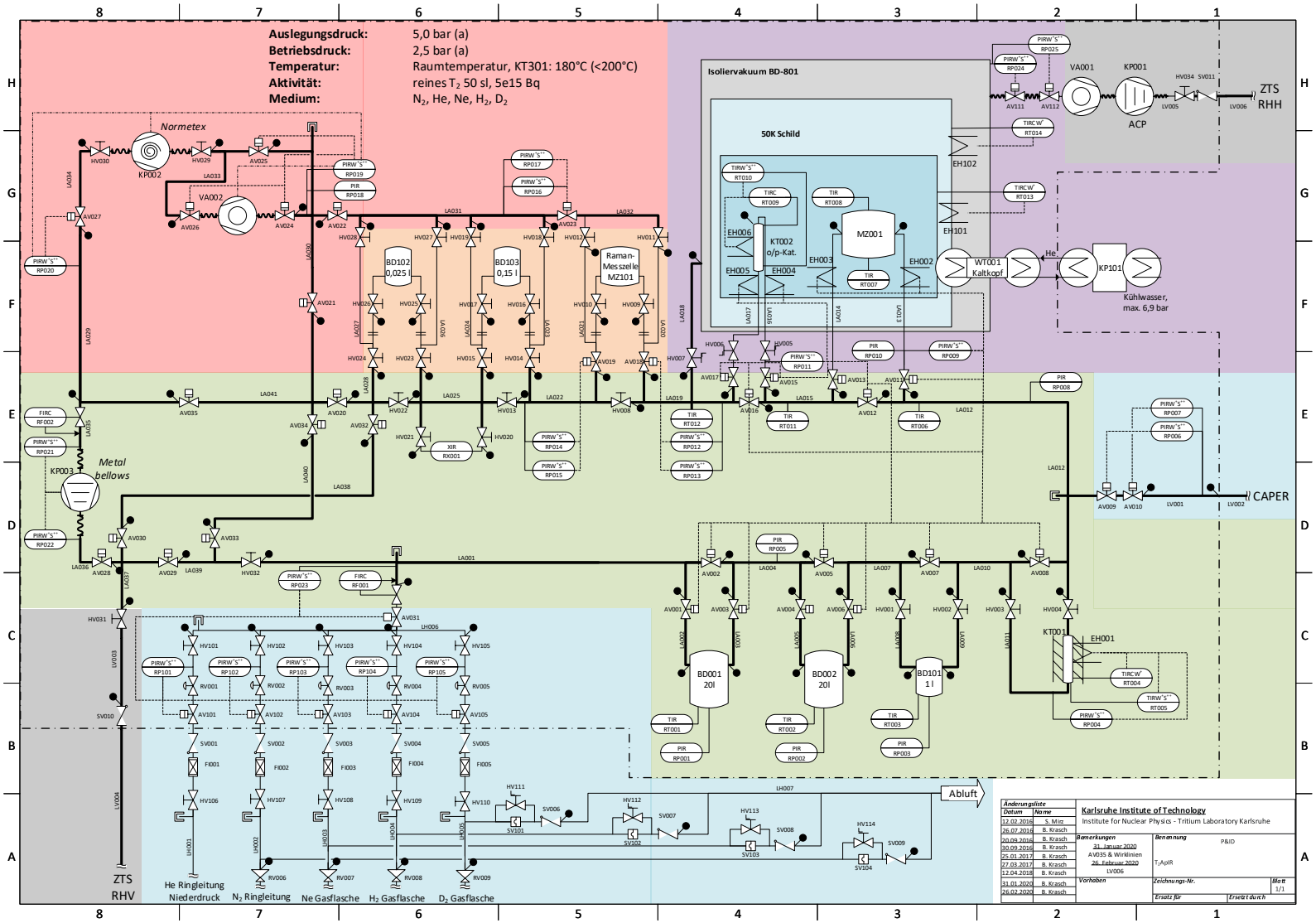

Figure B.1: P&ID diagram of the T_2ApIR experiment. The colours represent the six subgroups of the experiment; each with a specific function.

sensors (RP) is installed due to safety reasons. The TLK follows the pick-up principle for tritium transfer.

Process loop

The central green subgroup identifies most of the components and instrumentation. It consists of the three buffer vessels BD001 and BD002 with 20 l and BD101 with 1 l, the metal bellows circulation pump KP003, and the chemical converter KT001. The electric heater EH001 (heating sleeve) is used to activate the 14.8 g of 0.5 % of Pt on Al_2O_3 material inside KT001. In normal operation mode the flow direction is counterclockwise, i.e. automatic valves AV030, AV032, AV033, and AV034 are closed. By opening all four of them and closing AV020 and AV029 instead, the flow direction is changed to clockwise.

Cryogenic

The heart for the spectroscopic investigations is the cryogenic subgroup, highlighted in purple. The insulation vacuum chamber (cryostat) BD801 contains the cryogenic sample cell MZ001 and the coolable op converter. The sample cell is equipped with one PT1000 (RT007) and one TVO (RT008) temperature sensor, the converter with two PT1000 (RT009 and RT010) sensors. There are four heaters EH002 to EH005 (Thermocoax), each wired around a pipe. In the case of a sudden evaporation of the liquefied gas inside MZ001, the evaporation cooling may cause the sample cell connections to freeze. Heater EH006 (Thermocoacx) is used to activate the iron-oxide filled op converter. The two heaters EH101 and EH102 (heating cartidges with 50 Ω each) represent the two cold stages with the heating elements of the cryocooler. EH102 belongs to the first and EH101 to the second cooling stage.

Sampling ports and Raman analysis

As the T_2ApIR experiment only has one additional LARA system (MZ101) for room temperature concentration and op analysis, two further sampling ports with smaller volumes (BD102 with 25 ml and BD103 with 150 ml) are installed for offline analysis with other analytical tools. The size is determined by the TLK rules for handling of gas cylinders without a second containment. The maximum activity is limited to $<10^{-9}$ Bq.

Evacuation subgroup

It is necessary to evacuate the entire system. Therefore, three pumps are used in the following order: firstly, the metal bellows pump KP003 as a primary pre-pump, to generate a pressure of (40 – 50) mbar, then the scroll pump KP002 to go down to 10^{-2} mbar and finally the turbo molecular pump VA002 to reach a pressure regime of 10^{-6} mbar.

Cleaning and exhaust

After a successful measurement campaign, the waste gases must be returned to the central TLK infrastructure, as the TLK uses a closed tritium cycle and therefore, the gas cannot simply be blown up the chimney. The waste gases have to been separated into low and high radioactive

contaminated waste. Low contaminated waste is transferred to the RHV of the ZTS[2], bottom left corner. Highly contaminated waste is returned to CAPER where the hydrogen isotopologues are separated from the other gases. The grey area in the upper right corner contains a two-stage pump system, a scroll pump KP001 and a turbo molecular pump VA001. These two pumps create the insulation vacuum inside BD801. During normal operation there is no tritium inside BD801, so the exhaust gas is transferred directly to the RHH of the ZTS. In case that the sample cell's windows break, tritium is released into the cryostat and the two automatic valves AV111 and AV112 close immediately. The hand valve HV007 can be used to pump the contaminated gas from the cryostat into the T_2ApIR process loop.

Overview about the main components

The following tables summarise the main components and their specific characteristics in the following order: sensors, pumps, vessels, and valves.

Table B.1: Sensors installed in the T_2ApIR experiment. The table shows the number, type and model of sensors installed.

mode	#	type	model	label
temperature	8	platinum resistor	PT100	RT001-RT006, RT011, RT012
	3	platinum resistor	PT1000	RT007, RT009, RT010
	1	low temperature	TVO	RT008
	2	silicon diode	LAKE shore	RT013, RT014
pressure	3	capacitive	MKS Baratron 627F	RP001-RP003
	2	capacitive	MKS Baratron 750C	RP009, RP011
	20	solid pressure transducer	Brooks GFD01	RP004, RP006-RP008, RP012-RP017, RP019-RP023, RP101-RP105
	5	cold cathode transmitter	Pfeiffer PKR 261	RP005, RP010, RP018, RP024, RP025
flow	2	heat capacity	Brooks GF080	RF001, RF002
activity	1	Cross-I-chamber		RX001

[2] The abbreviation ZTS stands for central tritium retention system.

Table B.2: Pumps installed in the T_2ApIR experiment. The table presents some characteristics of the five pumps installed.

label	pump type	model	pressure regime (mbar)	function
KP001	dry primary	Adixen ACP15	$1013 - 3 \cdot 10^{-2}$	pre vacuum
KP002	scroll vacuum	Normetex model 15 m h^{-1}	$100 - 10^{-3}$	pre vacuum
KP003	metal bellows	Aero Space MB601-DC	5800 – 40	circulate & transfer gas mixtures
VA001	turbo	Pfeiffer HiPace300	$1 - 10^{-9}$	evacuate insulation chamber BD801
VA002	turbo	Pfeiffer HiPace300	$1 - 10^{-9}$	evacuate setup

Table B.3: Installed (buffer) vessels in the T_2ApIR experiment. The different vessels are shown with their volume, the maximum pressure they can withstand, the sensors connected to them and their function.

label	volume (l)	abs. pressure (bar)	equipped sensors	function
BD001	20	2.5	PT100, Baratron 627F	buffer, mixing
BD002	20	2.5	PT100, Baratron 627F	buffer, mixing
BD101	1	2.5	PT100, Baratron 627F	buffer, mixing
BD102	0.025	1.0		sampling port
BD103	0.150	1.0		sampling port
BD801	14.3	2.5	Baratron 750C	insulation vacuum
KT001	0.0157	2.5	2×PT100, Brooks GFD01	chemical converter
KT002	0.0015	2.5	2×PT1000	op converter
MZ001	0.002 01	2.5	PT1000 and TVO	ir and Raman
MZ101	0.0035	1.0		Raman analysis

C Supplementary material for the RDK-415D cold head

This chapter provides supplementary information on the Sumitomo RDK-415D cold head used. Figure C.1 shows the capacity map for the 50 Hz and 60 Hz mode. To enable the 60 Hz mode, a transformer was installed in the electrical cabinet. Figure C.2 is a technical drawing of the dimensions of the cryocooler. The third figure C.3 displays the two heater blocks for the two cold stages. The dimensions and the position of the temperature sensors (DT-670 diode) and the heating cartridges (50 Ω) are shown.

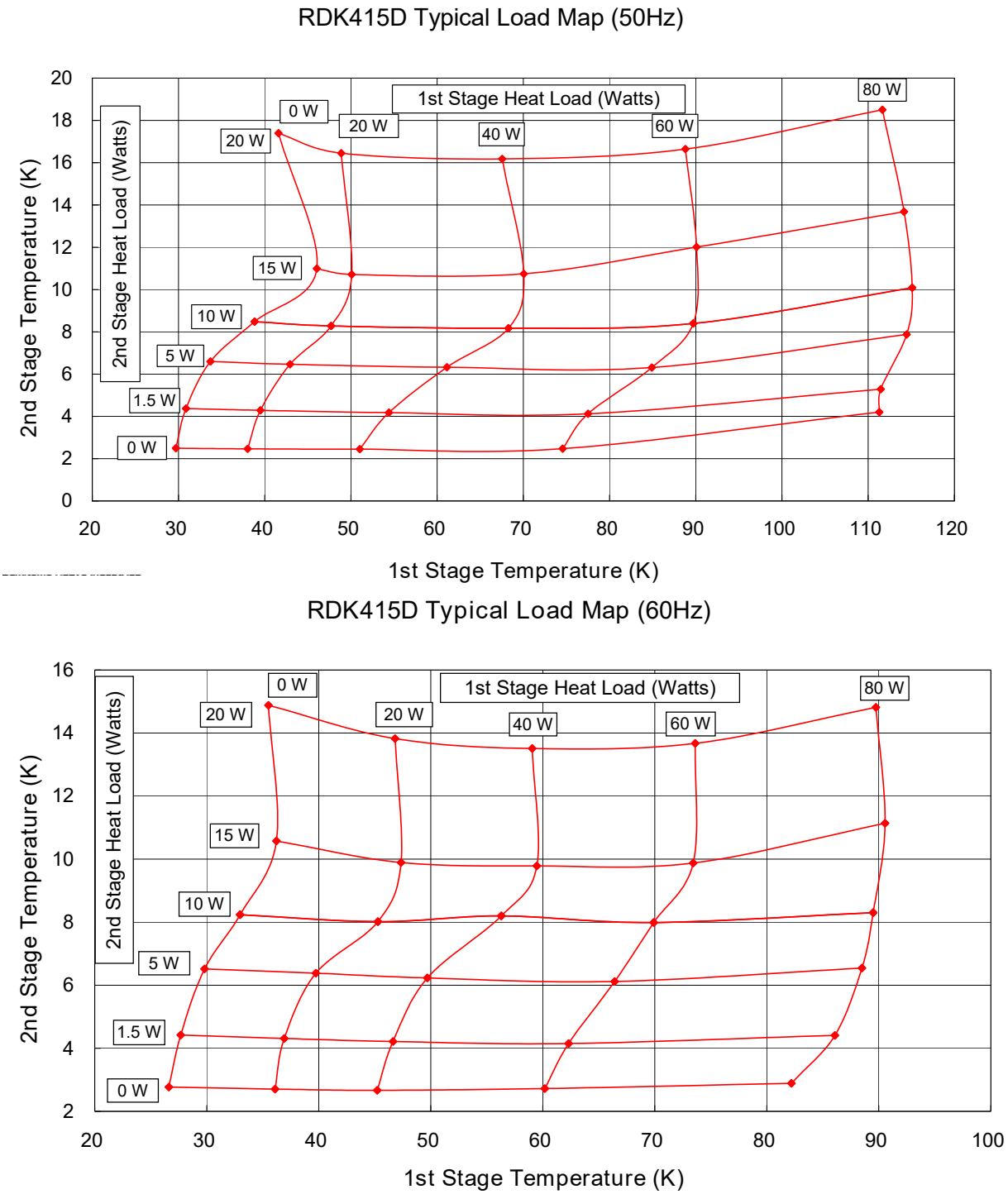

Figure C.1: RDK-415D capacity map for 50 Hz and 60 Hz. The graph displays the maximum heat load for the first and second stage as a function of the temperature at each stage.

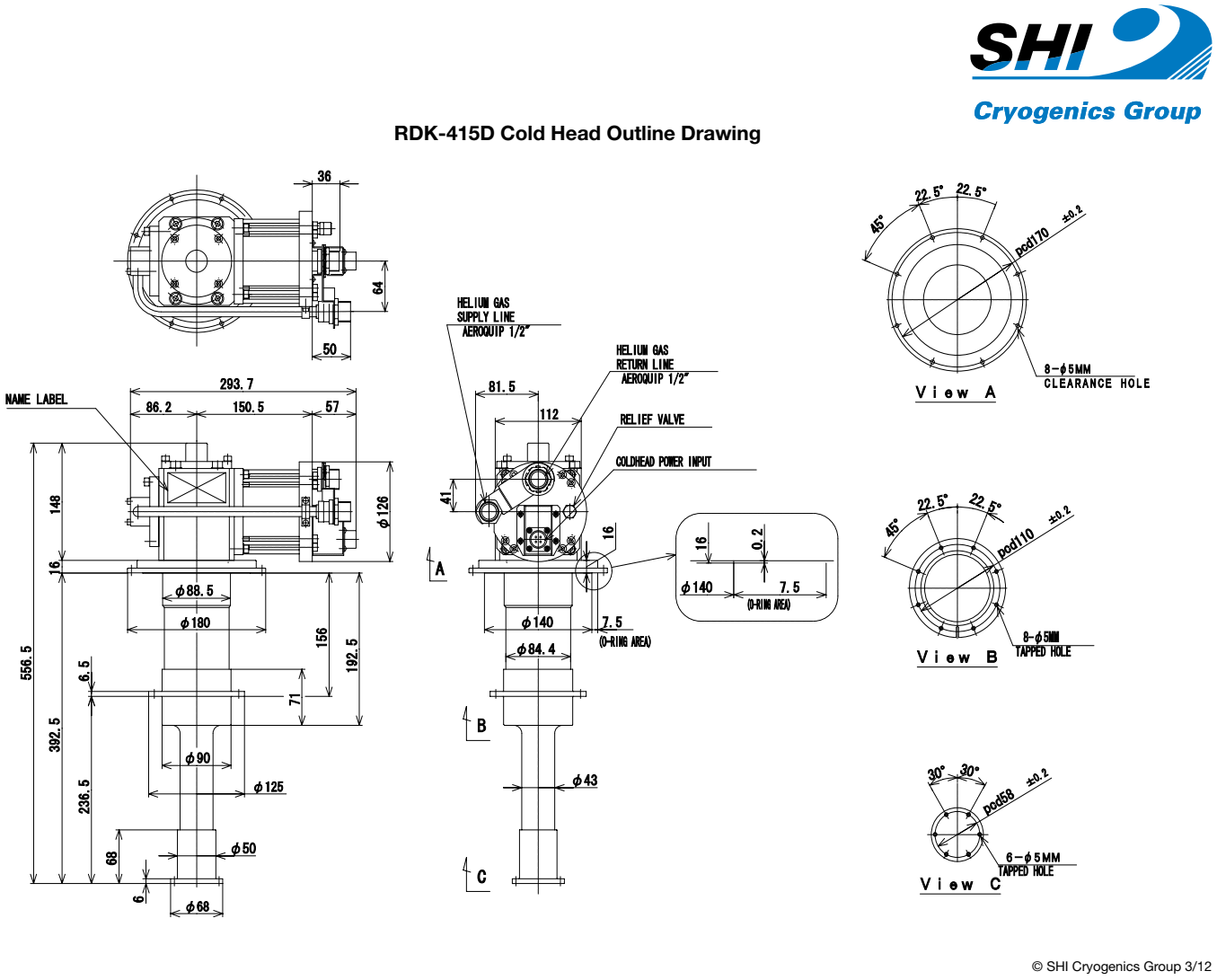

Figure C.2: Technical drawing of the RDK-415D cold head. The dimensions of the cryocooler are shown in mm.

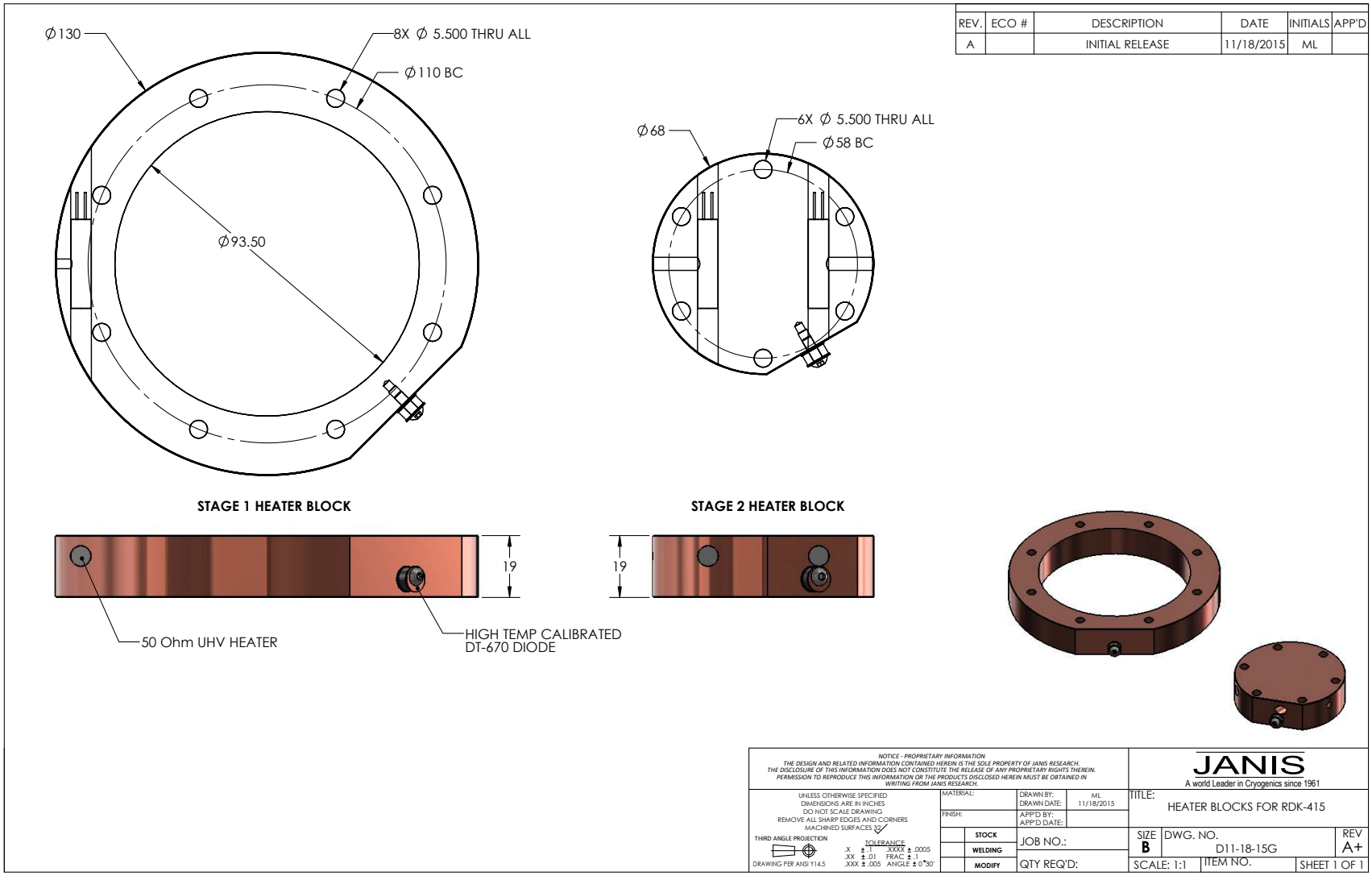

Figure C.3: Heater stages of the RDK-415D cryocooler. Each of the two cold stages is equipped with a specific heateing module. The first stage module has two holes, one for a 50 Ω UHV heater and a temperature sensor, a DT-670 diode. The second stage has three holes, two 50 Ω UHV heaters and a DT-670 temperature diode. These two heater blocks, together with the cooling power, allow the required temperature for each stage to be set.

D Thermal calculations for the design and the activation of the ortho-para converter of the T_2ApIR experiment

The op converter is filled with iron(III) oxide Fe_2O_3 as catalyst material to produce equilibrated op gas mixtures. Before Fe_2O_3 is used for the first time, the materials must be activated to remove impurities, such as moisture, water vapour, and nitrogen, see section 4.3. These impurities reduce the catalyst performance because they cover the surface of the material, preventing the hydrogen molecules from interacting with the surface atoms of the iron(III) oxide. That is why a purge gas is used to flush the impurities during the activation process.

The activation process of the catalyst material relies on various parameters, such as activation temperature, purge gas, gas flow, purging time, cycles of fresh purge gas, etc. There are few publications in the literature and these are often contradictory. A first measurement campaign was therefore carried out to find the optimum activation temperature. It was found that 180 °C is the desired value, see section 4.3.4.3. Other parameters have not yet been studied.

Based on this value, calculations were made to design the Thermocoax heating wire. Table D.1 lists all the required parameters and their values.

Firstly, the energy E_{steel} to heat up the U-shaped pipe is calculated by

$$E_{\text{steel}} = m_{\text{steel}} \cdot c_{p,\,\text{steel}} \cdot \Delta T \approx 1000\,\text{J}. \tag{D.1}$$

Secondly, the E_{Cu} to heat up the environment is calculated by

$$E_{\text{Cu}} = m_{\text{Cu}} \cdot c_{p,\,\text{Cu}} \cdot \Delta T \approx 196\,\text{kJ}. \tag{D.2}$$

Table D.1: Parameters for the design of the Thermocoax heating wire for the activation process of the ortho-para converter. The parameters required for the calculations are given as mass m, specific heat capacity c_p, and temperature T for the calculations. The intrinsic properties of the Thermocoax heating wire are its specific power P_{spec}, its specific resistance R_{spec} and its diameter d_{Therm}. The length of the wire is limited by the length of the groove l_{groove} in the copper shell, see figure 5.5.

m_{steel}	m_{Cu}	$c_{p,\text{steel}}$	$c_{p,\text{Cu}}$	T_{in}	T_{out}	P_{spec}	R_{spec}	d_{Therm}	l_{groove}
kg	kg	$\text{J kg}^{-1}\,\text{K}^{-1}$	$\text{J kg}^{-1}\,\text{K}^{-1}$	K	K	W m^{-1}	$\Omega\,\text{m}^{-1}$	mm	m
0.016	3.777	460	385	420	465	300	3.1	2	0.33

It can be seen that the energy needed to heat up the pipe is negligible compared to the total copper environment. Assuming a Thermocoax wire with a power P of 100 W, the time t needed to heat up the converter, including the environment, is

$$t = \frac{P}{E_{\text{steel}} + E_{\text{Cu}}} = 0.55\,\text{h}. \tag{D.3}$$

When selecting the appropriate Thermocoax wire, the power required as well as the length of the groove limited the choice. As the length of the groove is 0.33 m, a wire with a specific power of 300 W m^{-1} was chosen to achieve the required 100 W. This gives a total resistance of 1.02 Ω, a voltage of 10.1 V, and a current of 9.89 A. The last two parameters are used to select the appropriate electrical feedthrough.

In order to activate the catalyst material, Thermocoax wires were implemented on the gas supply pipes for the cryogenic sample cell.

E Thermal calculations for the heat input of the T_2ApIR experiment

The cryogenic design is presented in section 5.2.3. In addition to sufficient cooling power, a two-stage RDK-415D Gifford-McMahon refrigerator with 1.5 W cooling power at 4.2 K is used, the various heat entries must be minimised. Therefore, an additional copper cold shield with a gold layer on top is implemented. For the T_2ApIR experiment, only thermal conduction and thermal radiation are considered, since convection can be neglected due to the pressure of $< 1 \cdot 10^{-6}$ mbar.

The following list gives an overview of the main contributions to the heat budget.

Heat conduction Heat conduction is described by [Lie20]

$$\dot{Q}_{con} = \lambda \cdot A \cdot \frac{T_{\text{warm}} - T_{\text{cold}}}{d}, \tag{E.1}$$

where λ is the thermal conductivity (temperature dependent value), A is the area through which the heat flows, T_{warm} is the temperature of the warm surface, T_{cold} is the temperature of the cold surface, and d is the distance between the warm and cold surfaces. There are two entries in the experiment relating to heat conduction:

- by the gas lines to the converter and the cell and
- by the ceramic rods to the cryogenic cell.

Thermal radiation Thermal radiation is described by [Lie20]

$$\dot{Q}_{\text{rad}} = \epsilon \cdot \sigma \cdot A \cdot T^4, \tag{E.2}$$

with ϵ as emissivity factor, σ as the Stefan-Boltzmann constant, A as area and T as the temperature of the emitting body. There are four ways in which thermal radiation affects the cryo design by

- emission from the surface of the cryostat on the cold shield,
- emission from the viewports of the cube on the cold shield,
- emission from the cold shield onto the cryogenic sample cell and
- emission from the viewports of the cube on the sample cell.

The needed constants, parameters and material properties are listed in table E.1.

The results are given in table E.2. In terms of individual contributions, the highest one are the 6.87 W from the surface of the 300 K cryostat. Without the cold shield, the direct input on the

Table E.1: Parameters, coefficients, and settings for thermal calculations. Listed are the needed parameters required for the calculation of thermal conduction and radiation.

parameter	value
room temperature	300 K
temperature first stage, cold shield	50 K
temperature second stage, cell	15 K
Boltzmann constant	$11.38 \cdot 10^{-23}\,\mathrm{J\,K^{-1}}$
Stefan-Boltzmann constant	$5.67 \cdot 10^{-8}\,\mathrm{W/m^2/K^4}$
emission coefficient stainless steel	0.4
emission coefficient polished stainless steel	0.05
emission coefficient gold	0.02
thermal conductivity of stainless steel	$15\,\mathrm{W\,m^{-1}\,K^{-1}}$
thermal conductivity of ceramic	$1.5\,\mathrm{W\,m^{-1}\,K^{-1}}$
length of gas pipe	0.35 m
cross-sectional area gas pipe	$1.57 \cdot 10^{-5}\,\mathrm{m^2}$
length of ceramic rods	0.1 m
cross-sectional area ceramic rods	$1.13 \cdot 10^{-4}\,\mathrm{m^2}$
area cryostat	$2\,\mathrm{m^2}$
area shield	$0.3\,\mathrm{m^2}$

Table E.2: Results for thermal conduction and thermal radiation. Listed are the six contribution used in the calculations. The last column indicates which cooling stage is affected.

heating transfer	contribution	effect on cold stage one or two
4 gas pipes to cell and converter	0.76 W	cold stage 2
4 ceramic rods to cell	1.93 W	cold stage 1
emission cryostat on shield	6.87 W	cold stage 1
emission window on shield	0.02 W	cold stage 1
emission shield on cell	0.000 57 W	cold stage 2
emission window on cell	0.06 W	cold stage 2

cryogenic cell would be much higher and not coolable. Summing up the effects for each cold stage of the cryocooler:

- stage 1: 6.89 W, where the thermal radiation from the surface of the cryostat has the highest effect and
- stage 2: 2.275 W, where the thermal conduction from the four ceramic rods has the highest impact.

The proposed cryocooler is capable to handle these additional contributions.

F Safety states and interlocks of the T_2ApIR experiment

A crucial part during the early design phase was the safety discussions and analyses, similar to the HAZOP. The aim was to identify the possible failure in the first place and to implement appropriate safety and interlock features in the second step. The safety analysis is one part of the overall STB[1] document that required for each tritium experiment. This chapter gives an overview of all safety states, including what is the initial event causing a failure, what would be the possible consequence, and how it can be prevented. Firstly, there are five safety states, A1 - A5, for the T_2ApIR experiment. The definition for a safety state versus an interlock state is the potential damage to the system and subsystems. It was decided that an exceeding pressure leading to a possible tritium release was the worthwhile case scenario. For T_2ApIR, the safety states are defined as follows:

A1 At the gas supply (light blue area, without tritium supply) the pressure is $p > 2.5$ bar a.

A2 The connections to the Raman cell MZ101 remain closed as long as a pressure $p > 1$ bar a.

A3 In the cryogenic sample cell MZ001, the pressure exceeds the threshold of 2.5 bar a.

A4 In the op converter KT002, the pressure exceeds the 2.5 bar a threshold.

A5 Inside the insulation vacuum chamber BD801 the pressure is greater than 10^{-3} mbar.

Derived from these safety states, table F.1 lists all the additional information. In the appendix B, the dashed lines, also known as action lines, show the dependencies between a sensor and the effecting component. Some of the pressure and temperature sensors have a W^+ or S^{++}. The W stands for warning and the S for safety. Besides these five safety states, there are nine other interlocks presented in table F.

[1] STB stands for sicherheitstechnische Beschreibung and means in English safety technical description.

Table F.1: Safety states of the T_2ApIR experiment. For each safety state, the sensor(s) presented are listed with their threshold, the triggering event and the resulting shutdown.

safety state	sensor	threshold	shutdown
A1	RP023, RP101, RP102, RP103, RP104, RP105	2.5 bar a	close AV031, AV101, AV102, AV103, AV104, AV105
A2	RP012, RP013	1.0 bar a	close AV018
	RP014, RP015		close AV019
	RP016, RP017		close AV023
A3	RP009	2.5 bar a	open AV003, AV005, AV006, AV007, AV008, AV011
			close AV001, AV002, AV016
			turn on EH002, EH003
A4	RP0011	2.5 bar a	open AV003, AV005, AV006, AV007, AV008, AV011, AV012, AV015
			close AV001, AV002, AV016, AV017
			turn on EH004, EH005
A5	RP024	10^{-3} mbar a	close AV111
	RP025		close AV112

Table F.2: Interlocks for the T_2ApIR experiment. Nine different interlocks are defined. The sensor and the threshold indicate the triggering event and the shutdown is the resulting consequence.

#	sensor	threshold	shutdown
1	RT005	> 200 ° °C	turn off EH001
2	RP004	> 2.5 bar	turn offEH001
3	RP006	> 1.0 bar	close AV009
4	RP007	> 1.0 bar	close AV010
5	RT010	> 170 ° °C	turn off EH006
6	RP019	> 1.0 bar	close AV024, AV025, AV026
		> 5 mbar	turn off VA002
		> 0.1 mbar	turn off KP002
7	RP020	> 1.0 bar	close AV027
		> 0.1 bar	turn off KP002
8	RP021	> 2.5 bar	turn off KP003
9	RP022	> 2.5 bar	turn off KP003

Publications

Peer-reviewed articles

Krasch, B., Größle, R., Mirz, S., Smolinski, A., Süß, O. 2022. Raman Spectroscopy for Ortho-para Hydrogen Catalyst Studies. *International Journal of Hydrogen Energy.*. Accepted and must be published.

Krasch, B., Größle, R., Kuntz, D., Mirz, S. 2020. Design of a Cryostat for Spectroscopic Investigation of All Hydrogen Isotopologues in the Solid, Liquid, and Gaseous Phases. *Fusion Science and Technology*. 76(4): 481-487.

Antunes, R., Böhmländer, A., Cruz, M. M., Frances, L., Hillesheimer, D., Krasch, B., Welte, S. 2020. Isotopic effects on the permeation of all hydrogen isotopologues through MFI-ZSM-5 zeolite membranes. *International Journal of Hydrogen Energy*. 45(3): 2009-2016.

Mirz, S., Brunst, T., Größle, R., Krasch, B. 2020. Concentrated Nonequilibrium HD for the Cross Calibration of Hydrogen Isotopologue Analytics. *Fusion Science and Technology*. 76(3): 284–290.

Antunes, R., Böhmländer, A., Bükki-Deme, A., Krasch, B., Cruz, M. M., Frances, L. 2019. Experimental investigation of the ideal selectivity of MFI-ZSM-5 zeolite-type membranes for a first evaluation of the separation of hydrogen isotopologues from helium. *Separation and Purification Technology*. 212: 767-773.

Mirz, S., Besserer, U., Bornschein, B., Größle, R., Krasch, B., Welte, S. 2017. Design of a Spectroscopy Experiment for All Hydrogen Isotopologues in the Gaseous, Liquid, and Solid Phase. *Fusion Science and Technology*. 71(3): 375–380.

KATRIN-all

Aker, M. et al. 2022. Direct neutrino-mass measurement with sub-electronvolt sensitivity. *Nature Physics*. 18(2): 160–166.

Aker, M. et al. 2022. New Constraint on the Local Relic Neutrino Background Overdensity with the First KATRIN Data Runs. *Physical Review Letters*. 129(1): 011806.

Aker, M. et al. 2022. KATRIN: status and prospects for the neutrino mass and beyond. *Journal of Physics G. Nuclear and Particle Physics*. 49(10): 100501.

Aker, M. et al. 2022. Improved eV-scale sterile-neutrino constraints from the second KATRIN measurement campaign. *Physical Review D*. 105(7): 072004.

Aker, M. et al. 2021. Analysis methods for the first KATRIN neutrino-mass measurement. *Physical Review D*. 104(1): 012005.

Aker, M. et al. 2021. Precision measurement of the electron energy-loss function in tritium and deuterium gas for the KATRIN experiment. *The European Physical Journal C*. 81(7): 579.

Aker, M. et al. 2021. Bound on 3+1 Active-Sterile Neutrino Mixing from the First Four-Week Science Run of KATRIN. *Physical Review Letters*. 126(9): 091803.

Aker, M. et al. 2021. The design, construction, and commissioning of the KATRIN experiment. *Journal of Instrumentation*. 16(08): T08015.

Altenmüller, K. et al. 2020. High-resolution spectroscopy of gaseous 83mKr conversion electrons with the KATRIN experiment. *Journal of Physics G: Nuclear and Particle Physics*. 47(6): 065002.

Aker, M. et al. 2020. Quantitative Long-Term Monitoring of the Circulating Gases in the KATRIN Experiment Using Raman Spectroscopy. *Sensors*. 20(17): 4827.

Aker, M. et al. 2020. First operation of the KATRIN experiment with tritium. *The European Physical Journal C*. 80(3): 1–18.

Aker, M. et al. 2020. Suppression of Penning discharges between the KATRIN spectrometers. *The European Physical Journal C*. 80(9): 821.

Aker, M. et al. 2019. Improved Upper Limit on the Neutrino Mass from a Direct Kinematic Method by KATRIN. *Physical Review Letters*. 123(22): 221802.

Altenmüller, K. et al. 2019. Gamma-induced background in the KATRIN main spectrometer. *The European Physical Journal C*. 79(9): 807.

Arenz, M. et al. 2018. First transmission of electrons and ions through the KATRIN beamline. *Journal of Instrumentation*. 13(04): P04020–P04020.

Altenmüller, K. et al. 2019. Muon-induced background in the KATRIN main spectrometer. *Astroparticle Physics*. 108: 40–49.

Arenz, M. et al. 2018. Calibration of high voltages at the ppm level by the difference of 83m-Kr conversion electron lines at the KATRIN experiment. *The European Physical Journal C*. 78(5): 368.

Arenz, M. et al. 2018. Reduction of stored-particle background by a magnetic pulse method at the KATRIN experiment. *European Physical Journal C*. 78(9): 778.

Arenz, M. et al. 2018. The KATRIN superconducting magnets: overview and first performance results. *Journal of Instrumentation*. 13(08): T08005–T08005.

Arenz, M. et al. 2016. Commissioning of the vacuum system of the KATRIN Main Spectrometer. *Journal of Instrumentation*. 11(04): P04011–P04011.

Poster contributions

Krasch, B. and Marsteller, A. 2018. Commissioning and Characterization of the Tritium Gas Circulation System of the KATRIN Experiment. *XXVIII International Conference on Neutrino Physics & Astrophysics*. Heidelberg, Germany.

Krasch, B. 2017. Design of an experiment for the experimental determination of the efficiency of converters for ortho-para conversion of hydrogen isotopologues. *International Conference on vibrational spectroscopy (ICAVS)*. Victoria, Canada. Poster award.

Krasch, B. 2017. Natural chemical conversion and catalytic ortho-para conversion of the non-radioactive hydrogen isotopologues. *DPG-Frühjahrstagung der Sektion Atome, Moleküle, Quantenoptik und Plasmen (SAMOP)*. Mainz, Germany.

Krasch, B. 2016. Raman spectroscopic determination of the molecular constants of the hydrogen isotopologues with high accuracy. *DPG-Frühjahrstagung der Sektion Materie und Kosmos (SMuK)*. Hamburg, Germany.

Bibliography

[Aal16] Aalbers, J. et al. 2016. DARWIN: towards the ultimate dark matter detector. *Journal of Cosmology and Astroparticle Physics*. 2016(11): 017–017.

[Aar18] Aartsen, M. et al. 2018. Multimessenger observations of a flaring blazar coincident with high-energy neutrino IceCube-170922A. *Science*. 361(6398): 1378.

[Abe16] Abe, Y. et al. 2016. Measurement of θ_{13} in Double Chooz using neutron captures on hydrogen with novel background rejection techniques. *Journal of High Energy Physics*. 2016(1): 1–26.

[Abe18] Abe, K. et al. 2018. Search for CP Violation in Neutrino and Antineutrino Oscillations by the T2K Experiment with $2.2 \cdot 10^{21}$ Protons on Target. *Physical Review Letters*. 121(17): 171802.

[Abi20] Abi, B. et al. 2020. Long-baseline neutrino oscillation physics potential of the DUNE experiment. *The European Physical Journal C*. 80(10): 1–34.

[Ace19] Acero, M. et al. 2019. First measurement of neutrino oscillation parameters using neutrinos and antineutrinos by NOvA. *Physical Review Letters*. 123(15): 151803.

[Ada14] Adamson, P. et al. 2014. Combined Analysis of ν_μ Disappearance and $\nu_\mu \rightarrow \nu_e$ Appearance in MINOS Using Accelerator and Atmospheric Neutrinos. *Physical Review Letters*. 112(19): 191801.

[Ade18] Adey, D. et al. 2018. Measurement of the Electron Antineutrino Oscillation with 1958 Days of Operation at Daya Bay. *Physical Review Letters*. 121(24): 241805.

[Ago19] Agostini, M. et al. 2019. Probing Majorana neutrinos with double-β decay. *Science*. 365(6460): 1445–1448.

[Ago20] Agostini, F. et al. 2020. Sensitivity of the DARWIN observatory to the neutrinoless double beta decay of ^{136}Xe. *The European Physical Journal C*. 80(9):

[Ahm01] Ahmad, Q. R. et al. 2001. Measurement of the Rate of $\nu_e + d \rightarrow p + p + e^-$ Solar Neutrinos at the Sudbury Neutrino Observatory. *Physical Review Letters*. 87(7): 071301.

[Ahm02] Ahmad, Q. R. et al. 2002. Direct Evidence for Neutrino Flavor Transformation from Neutral-Current Interactions in the Sudbury Neutrino Observatory. *Physical Review Letters*. 89(1): 011301.

[Ake19] Aker, M. et al. 2019. Improved Upper Limit on the Neutrino Mass from a Direct Kinematic Method by KATRIN. *Physical Review Letters*. 123(22): 221802.

[Ake20a] Aker, M. et al. 2020. First operation of the KATRIN experiment with tritium. *The European Physical Journal C*. 80(3): 1–18.

[Ake20b] Aker, M. et al. 2020. Quantitative Long-Term Monitoring of the Circulating Gases in the KATRIN Experiment Using Raman Spectroscopy. *Sensors*. 20(17): 4827.

[Ake21] Aker, M. et al. 2021. The design, construction, and commissioning of the KATRIN experiment. *Journal of Instrumentation*. 16(08): T08015.

[Ake22] Aker, M. et al. 2022. Direct neutrino-mass measurement with sub-electronvolt sensitivity. *Nature Physics*. 18(2): 160–166.

[Alt17] Altenbrand, F. 2017. *Messung und Modellierung der Effizienz von ortho/para-Katalysatoren für Wasserstoff und Deuterium*. Diploma thesis. Karlsruhe.

[Alt19] Altenmüller, K. et al. 2019. Muon-induced background in the KATRIN main spectrometer. *Astroparticle Physics*. 108: 40–49.

[Alv19] Alvis, S. I. et al. 2019. Search for neutrinoless double-β decay in ^{76}Ge with 26 kg yr of exposure from the Majorana Demonstrator. *Physical Review C*. 100(2): 025501.

[Ams15] Amsbaugh, J. et al. 2015. Focal-plane detector system for the KATRIN experiment. *Nuclear Instruments and Methods in Physics Research Section A: Accelerators, Spectrometers, Detectors and Associated Equipment*. 778: 40–60.

[An16] An, F. et al. 2016. Neutrino physics with JUNO. *Journal of Physics G: Nuclear and Particle Physics*. 43(3): 030401.

[Ang05] Angrik, J. et al. 2005. *KATRIN Design Report 2004. Wissenschaftliche Berichte FZKA*. vol. 7090. tech. report.

[Ant19] Anton, G. et al. 2019. Search for Neutrinoless Double-β Decay with the Complete EXO-200 Dataset. *Physical Review Letters*. 123(16): 161802.

[Aqu65] Aquilanti, V. et al. 1965. Ion—Molecule Reactions in Hydrogen—Rare-Gas Mixtures. *The Journal of Chemical Physics*. 43(6): 1969–1973.

[Are16] Arenz, M. et al. 2016. Commissioning of the vacuum system of the KATRIN Main Spectrometer. *Journal of Instrumentation*. 11(04): P04011–P04011.

[Are18a] Arenz, M. et al. 2018. Calibration of high voltages at the ppm level by the difference of 83m-Kr conversion electron lines at the KATRIN experiment. *The European Physical Journal C*. 78(5): 368.

[Are18b] Arenz, M. et al. 2018. First transmission of electrons and ions through the KATRIN beamline. *Journal of Instrumentation*. 13(04): P04020–P04020.

[Arn19] Arnold, R. et al. 2019. Detailed studies of ^{100}Mo two-neutrino double beta decay in NEMO-3. *The European Physical Journal C*. 79(5): 1–11.

[Ase11] Aseev, V. N. et al. 2011. Upper limit on the electron antineutrino mass from the Troitsk experiment. *Phys. Rev. D*. 84: 112003.

[Ash22] Ashtari Esfahani, A. et al. 2022. *The Project 8 Neutrino Mass Experiment*. tech. report.

[Ath22] Athar, M. S. et al. 2022. Status and perspectives of neutrino physics. *Progress in Particle and Nuclear Physics*. 124: 103947.

[Atk06] Atkins, P. W. and De Paula, J. 2006. *Physical Chemistry*. Oxford: Oxford University Press.

[Bab12] Babutzka, M. et al. 2012. Monitoring of the operating parameters of the KATRIN Windowless Gaseous Tritium Source. *New Journal of Physics*. 14(10): 103046.

[Bab14] Babutzka, M. 2014. *Design and development for the Rearsection of the KATRIN experiment*. PhD thesis. Karlsruhe.

[Bah01] Bahcall, J. N. et al. 2001. Solar Models: Current Epoch and Time Dependences, Neutrinos, and Helioseismological Properties. *The Astrophysical Journal*. 555(2): 990–1012.

[Bah63] Bahcall, J. N. et al. 1963. Solar Neutrino Flux. *The Astrophysical Journal*. 137: 344.

[Bah64] Bahcall, J. N. 1964. Solar Neutrinos. I. Theoretical. *Physical Review Letters*. 12(11): 300–302.

[Bah96] Bahcall, J. N. 1996. Solar neutrinos: Where we are, where we are going. *Nuclear Physics B - Proceedings Supplements*. 48(1-3): 309–316.

[Bas09] Basunia, M. 2009. Nuclear Data Sheets for A = 187. *Nuclear Data Sheets*. 110(5): 999–1238.

[Bec96] Becquerel, A. 1896. Sur les radiations invisibles émises par les corps phosphorescents. *CR Acad. Sci. Paris*. 122: 501.

[Ber09] Berstad, D. O. et al. 2009. Comparison criteria for large-scale hydrogen liquefaction processes. *International Journal of Hydrogen Energy*. 34(3): 1560–1568.

[Bil10] Bilenky, S. 2010. *Introduction to the Physics of Massive and Mixed Neutrinos*. Springer Berlin Heidelberg.

[Bod15a] Bodine, L. I. 2015. *Molecular Effects in Tritium Beta-Decay Neutrino-Mass Measurements*. PhD thesis. Washington.

[Bod15b] Bodine, L. I. et al. 2015. Assessment of molecular effects on neutrino mass measurements from tritium β decay. *Phys. Rev. C*. 91: 035505.

[Boe17] Boeva, O. A. et al. 2017. Low-temperature ortho–para hydrogen conversion catalyzed by gold nanoparticles: Particle size does not affect the rate. *International Journal of Hydrogen Energy*. 42(36): 22897–22902.

[Bor05] Bornschein, B. et al. 2005. Successful Experimental Verification of the Tokamak Exhaust Processing Concept of ITER with the CAPER Facility. *Fusion Science and Technology*. 48: 11–16.

[Bor11] Bornschein, B. 2011. Between Fusion and Cosmology – The Future of the Tritium Laboratory Karlsruhe. *Fusion Science and Technology*. 60(3): 1088–1091.

[Bra04] Bragg, W. 1904. LXXIII. On the absorption of α rays, and on the classification of the α rays from radium. *The London, Edinburgh, and Dublin Philosophical Magazine and Journal of Science*. 8(48): 719–725.

[Bra16] Branchesi, M. 2016. Multi-messenger astronomy: gravitational waves, neutrinos, photons, and cosmic rays. *Journal of Physics: Conference Series*. 718: 022004.

[Car17] Cardella, U. et al. 2017. Economically viable large-scale hydrogen liquefaction. *IOP Conference Series: Materials Science and Engineering*. 171: 012013.

[Cha14] Chadwick, J. 1914. Intensitätsverteilung im magnetischen Spectrum der β-Strahlen von radium B + C. *Verhandl. Dtsc. Phys. Ges.* 16: 383.

[Cha32] Chadwick, J. 1932. Possible Existence of a Neutron. *Nature*: 312.

[Cha57] Chapin, D. S. and Johnston, H. L. 1957. The Surface Catalysis of the Ortho- to Para- Conversion in Hydrogen under Pressure at Low Temperatures. *Journal of the American Chemical Society*. 79(10): 2406–2412.

[Cof79] Coffin, D. and Walthers, C. 1979. *Methane generated from graphite–tritium interaction. [In hydrogen isotopes separation by cryogenic distillation]*. tech. report.

[Con75] Constable, J. H. et al. 1975. The dielectric constant of H_2, D_2, and HD in the condensed phases. *Journal of Low Temperature Physics*. 21(5): 599–617.

[Cow56] Cowan, C. L. et al. 1956. Detection of the Free Neutrino: a Confirmation. *Science*. 124(3212): 103–104.

[Cun58] Cunningham, C. M. and Johnston, H. L. 1958. The Surface Catalysis of the Ortho- to Para-Conversion in Liquid Hydrogen by Paramagnetic Oxides on Alumina. *Journal of the American Chemical Society*. 80(10): 2377–2382.

[Cur10] Curie, M. 1910. Traité de radioactivité. *Gauthier-Villars*. 2: 1.

[Dan62] Danby, G. et al. 1962. Observation of High-Energy Neutrino Reactions and the Existence of Two Kinds of Neutrinos. *Physical Review Letters*. 9(1): 36–44.

[Dav94] Davis, R. 1994. A review of the homestake solar neutrino experiment. *Progress in Particle and Nuclear Physics*. 32: 13–32.

[Dem05] Demtröder, W. 2005. *Molecular Physics: Theoretical Principles and Experimental Methods*. Weinheim: Wiley VCH.

[Dem06] Demtröder, W. 2006. *Atoms, Molecules and Photons: An Introduction to Atomic-, Molecular- and Quantum-Physics*. Berlin: Springer.

[Dep19] Deppisch, F. F. 2019. *A Modern Introduction to Neutrino Physics*. IOP Concise Physics.

[Dör05] Dörr, L. et al. 2005. The Closed Tritium Cycle of the Tritium Laboratory Karlsruhe. *Fusion Science and Technology*. 48(1): 262–267.

[Dor54] Dorfman, L. M. 1954. Absorption of Tritium Beta Particles in Hydrogen and Other Gases. *Physical Review*. 95(2): 393–396.

[Dos06] Doss, N. et al. 2006. Molecular effects in investigations of tritium molecule β decay endpoint experiments. *Physical Review C*. 73(2): 025502.

[Dre13] Drexlin, G. et al. 2013. Current Direct Neutrino Mass Experiments. *Advances in High Energy Physics*. 2013: 293986.

[Dvo11] Dvornický, R. et al. 2011. Absolute mass of neutrinos and the first unique forbidden β decay ^{187}Re. *Physical Review C*. 83(4): 045502.

[Ell27] Ellis, C. D. et al. 1927. The average energy of disintegration of radium E. *Proceedings of the Royal Society of London. Series A, Containing Papers of a Mathematical and Physical Character*. 117(776): 109–123.

[Ell87] Elliott, S. R. et al. 1987. Direct evidence for two-neutrino double-beta decay in ^{82}Se. *Physical Review Letters*. 59(18): 2020–2023.

[Emm35] Emmett, P. H. and Harkness, R. W. 1935. The Catalytic Interconversion of Ortho Para Hydrogen over Iron, Platinum and Nickel Catalysts. *Journal of the American Chemical Society*. 57(9): 1624–1631.

[Ere17] Ereditato, A. 2017. *The State of the Art of Neutrino Physics*. World Scientific.

[Ess13] Essler, J. 2013. *Physikalische und technische Aspekte der Ortho-Para-Umwandlung von Wasserstoff*. PhD thesis. Dresden.

[Est20] Esteban, I. et al. 2020. The fate of hints: updated global analysis of three-flavor neutrino oscillations. *Journal of High Energy Physics*. 2020(9): 1–21.

[Fac85] Fackler, O. et al. 1985. Accurate Theoretical β-Decay Energy Spectrum of the Tritium Molecule and Its Neutrino Mass Dependence. *Physical Review Letters*. 55(13): 1388–1391.

[Fis11] Fischer, S. et al. 2011. Monitoring of Tritium Purity During Long-Term Circulation in the KATRIN Test Experiment LOOPINO Using Laser Raman Spectroscopy. *Fusion Science and Technology*. 60(3): 925–930.

[Fis15] Fischer, S. et al. 2015. Investigation of Durability of Optical Coatings in Highly Purified Tritium Gas. *Fusion Science and Technology*. 67(2): 316–319.

[Föl80] Földiák, G. 1980. Radiolysis of liquid hydrocarbons. *Radiation Physics and Chemistry (1977)*. 16(6): 451–463.

[Fro96] Froelich, P. and Saenz, A. 1996. Calculation of the T_2 Molecule beyond the Sudden Impulse Approximation. *Physical Review Letters*. 77(23): 4724–4727.

[Fuk00] Fukugita, M. et al. 2000. Limits on Neutrino Mass from Cosmic Structure Formation. *Physical Review Letters*. 84(6): 1082–1085.

[Fuk13] Fukutani, K. and Sugimoto, T. 2013. Physisorption and ortho–para conversion of molecular hydrogen on solid surfaces. *Progress in Surface Science*. 88(4): 279–348.

[Fuk98] Fukuda, Y. et al. 1998. Evidence for Oscillation of Atmospheric Neutrinos. *Physical Review Letters*. 81(8): 1562–1567.

[Gan99] Ganchuk, N. et al. 1999. Calculation of equilibrium composition and establishing time in a mixture of three hydrogen isotopes. *Hyperfine Interactions*. 119(1/4): 357–360.

[Gas17] Gastaldo, L. et al. 2017. The electron capture in ^{163}Ho experiment – ECHo. *The European Physical Journal Special Topics*. 226(8): 1623–1694.

[Gen70] Genty, C. and Schott, R. 1970. Quantitative analysis for the isotopes of hydrogen - H_2, HD, HT, D_2, DT, and T_2 - by gas chromatography. *Analytical Chemistry*. 42(1): 7–11.

[Gil10] Gil, W. et al. 2010. The Cryogenic Pumping Section of the KATRIN Experiment. *IEEE Transactions on Applied Superconductivity*. 20(3): 316–319.

[Gil17] Gil, W. et al. 2017. Commissioning the Magnet Safety System of the Cryogenic Pumping Section of KATRIN. *IEEE Transactions on Applied Superconductivity*. 27(4): 1–4.

[Gil80] Gill, J. T. 1980. Effect of container preparation on the growth of protium and methane impurities into tritium gas. *Journal of Vacuum Science and Technology*. 17(2): 645–654.

[Gri07] Griffiths, P. R. 2007. *Fourier Transform Infrared Spectrometry*. Hoboken: Wiley-Blackwell.

[Gro08] Grohmann, S. et al. 2008. Cryogenic Design of the KATRIN Source Cryostat. *AIP Conference Proceedings*. 985(1): 1277–1284.

[Gro09] Grohmann, S. 2009. Stability analyses of the beam tube cooling system in the KATRIN source cryostat. *Cryogenics*. 49(8): 413–420.

[Grö15a] Größle, R. et al. 2015. First Calibration Measurements of an FTIR Absorption Spectroscopy System for Liquid Hydrogen Isotopologues for the Isotope Separation System of Fusion Power Plants. *Fusion Science and Technology*. 67(2): 357–360.

[Grö15b] Größle, R. 2015. *Das TApIR Experiment IR-Absorptionsspektren flüssiger Wasserstoffisotopologe*. Phd thesis. Karlsruhe.

[Grö17] Größle, R. et al. 2017. First Calibration of an IR Absorption Spectroscopy System for the Measurement of H_2, D_2, and HD Concentration in the Liquid Phase. *Fusion Science and Technology*. 71(3): 369–374.

[Grö20] Grössle, R. et al. 2020. Minimal and complete set of descriptors for IR-absorption spectra of liquid H_2–D_2 mixtures. *AIP Advances*. 10(5): 055108.

[Hei17] Heizmann, F. and Seitz-Moskaliuk, H. 2017. The Windowless Gaseous Tritium Source (WGTS) of the KATRIN experiment. *Journal of Physics: Conference Series*. 888: 012071.

[Her10] Hertel, I. V. 2010. *Atome, Moleküle und optische Physik 2: Moleküle und Photonen - Spektroskopie und Streuphysik*. Berlin, Heidelberg: Springer Berlin Heidelberg.

[Her61] Herzberg, G. and Monfils, A. 1961. The dissociation energies of the H_2, HD, and D_2 molecules. *Journal of Molecular Spectroscopy*. 5(1): 482–498.

[Her66] Herzberg, G. 1966. *Molecular Spectra and Molecular Structure: III. Electronic Spectra and Electronic Structure of Polyatomic Moleculs*. Van Nostrand.

[Hig64] Higgs, P. W. 1964. Broken Symmetries and the Masses of Gauge Bosons. *Physical Review Letters*. 13(16): 508–509.

[Hir88] Hirata, K. S. et al. 1988. Observation in the Kamiokande-II detector of the neutrino burst from supernova SN1987A. *Physical Review D*. 38(2): 448–458.

[Hir91] Hirata, K. S. et al. 1991. Real-time, directional measurement of ^{8}B solar neutrinos in the Kamiokande II detector. *Physical Review D*. 44(8): 2241–2260.

[Hos06] Hosaka, J. et al. 2006. Solar neutrino measurements in Super-Kamiokande-I. *Physical Review D*. 73(11): 112001.

[Hut67] Hutchinson, H. L. et al. 1967. Langmuir-Hinschelwood Kinetics and the catalytic Para-Orthohydrogen Shift reaction. *Chemical Engineering Progress Symposium Series*. 63(72): 18–30.

[Hut70] Hutchinson, H. L. et al. 1970. Comparison of rate expressions for the low-temperature para-orthohydrogen shift. *Advances in Cryogenic Engineering Vol. 16. Proceedings of the 1970 Cryogenic Enginerring Congress*. 16: 96–103.

[Ili92] Ilisca, E. 1992. Ortho-para conversion of hydrogen molecules physisorbed on surfaces. *Progress in Surface Science*. 41(3): 217–335.

[Isr11] Israelachvili, J. N. 2011. *Intermolecular and Surface Forces*. Waltham: Elsevier Science.

[Jam13a] James, T. M. et al. 2013. Accurate depolarization ratio measurements for all diatomic hydrogen isotopologues. *Journal of Raman Spectroscopy*. 44(6): 857–865.

[Jam13b] James, T. M. et al. 2013. Automated Quantitative Spectroscopic Analysis Combining Background Subtraction, Cosmic Ray Removal, and Peak Fitting. *Applied Spectroscopy*. 67(8): 949–959.

[Jam15] James, T. M. et al. 2015. Trace gas and dynamic process monitoring by Raman spectroscopy in metal-coated hollow glass fibres. *Analytical Methods*. 7(6): 2568–2576.

[Jez85] Jeziorski, B. et al. 1985. Molecular effects in tritium β. II. Rotation-vibration excitation, dissociation, and rotational predissociation in the decay of the T_2 and TH molecules. *Physical Review A*. 32(5): 2573–2583.

[Jon00] Jones, W. J. 2000. High-resolution Raman spectroscopy of gases and the determination of molecular bond lengths. *Canadian Journal of Physics*. 78(5-6): 327–390.

[Jon48] Jones, W. M. 1948. Thermodynamic Functions for Tritium and Tritium Hydride. The Equilibrium of Tritium and Hydrogen with Tritium Hydride. The Dissociation of Tritium and Tritium Hydride. *The Journal of Chemical Physics*. 16(11): 1077–1081.

[Jon98] Jonsell, S. et al. 1998. Non-adiabatic couplings between the final states of tritium beta decay. *Pol. J. Chem.* 72: 1323–1333.

[Jon99] Jonsell, S. et al. 1999. Neutrino-mass determination from tritium β: Corrections to and prospects of experimental verification of the final-state spectrum. *Physical Review C*. 60(3): 034601.

[Kaz08] Kazachenko, O. et al. 2008. Tritium Processing Loop for KATRIN Experiment. *Fusion Science and Technology*. 54(1): 67–70.

[Kis13] Kisslinger, L. S. 2013. Review of Recent Neutrino Physics Research. *Modern Physics Letters A*. 28(29): 1330024.

[Kle17] Klein, M. and Glück, F. 2017. Tritium ion blocking and detection in the KATRIN experiment. *Journal of Physics: Conference Series*. 888: 012073.

[Kle18] Klein, M. 2018. *Tritium ions in KATRIN: blocking, removal and detection*. PhD thesis. Karlsruhe.

[Kle19] Kleesiek, M. et al. 2019. β-Decay spectrum, response function and statistical model for neutrino mass measurements with the KATRIN experiment. *The European Physical Journal C*. 79(3): 1–24.

[Kod01] Kodama, K. et al. 2001. Observation of tau neutrino interactions. *Physics Letters B*. 504(3): 218–224.

[Kog71] Kogan, V. S. et al. 1971. Dielectric constant measurement of hydrogen isotopes in the liquid phase. *Physica*. 53(1): 125–131.

[Koł67] Kołos, W. and Wolniewicz, L. 1967. Polarizability of the Hydrogen Molecule. *The Journal of Chemical Physics*. 46(4): 1426–1432.

[Koł85] Kołos, W. et al. 1985. Molecular effects in tritium β decay: Transitions to the discrete electronic states of the HeT^+ molecule. *Physical Review A*. 31(2): 551–555.

[Kon47] Konopinski, E. J. 1947. H3 and the Mass of the Neutrino. *Physical Review*. 72(6): 518–519.

[Kos09] Kosmider, A. 2009. *Planung, Aufbau und Inbetriebnahme eines Experiments zur Analyse von flüssigen Wasserstoffisotopologen durch Infrarotstrahlung*. Diploma thesis. Karlsruhe.

[Kos11] Kosmider, A. and Drexlin, G. 2011. Infrared Spectroscopy in Liquid Hydrogen Isotopologues for the ISS of ITER. *Fusion Science and Technology*. 60: 956–959.

[Kra05] Kraus, C. et al. 2005. Final results from phase II of the Mainz neutrino mass search in tritium β decay. *European Physical Journal C - EUR PHYS J C*. 40: 447–468.

[Kra13] Kraus, A. 2013. *Weiterentwicklung der Analysekette und empirische Modellierung der IR-Absorptionsspektren des TApIR-Experiments*. Bachelor thesis. Karlsruhe.

[Kra20] Krasch, B. et al. 2020. Design of a Cryostat for Spectroscopic Investigation of All Hydrogen Isotopologues in the Solid, Liquid, and Gaseous Phases. *Fusion Science and Technology*. 76(4): 481–487.

[Kra22] Krasch, B. et al. 2022. Raman spectroscopy for ortho-para hydrogen catalyst studies. *submitted to International Journal of Hydrogen Energy*:

[Kru83] Kruit, P. and Read, F. H. 1983. Magnetic field paralleliser for 2π electron-spectrometer and electron-image magnifier. *Journal of Physics E: Scientific Instruments*. 16(4): 313–324.

[Lai20] Lai, K.-F. et al. 2020. Precision measurement of the fundamental vibrational frequencies of tritium-bearing hydrogen molecules: T_2, DT, HT. *Physical Chemistry Chemical Physics*. 22(16): 8973–8987.

[Lar48] Larsen, A. H. et al. 1948. The Rate of Evaporation of Liquid Hydrogen Due to the Ortho-Para Hydrogen Conversion. *Review of Scientific Instruments*. 19(4): 266–269.

[Les12] Lesgourgues, J. and Pastor, S. 2012. Neutrino Mass from Cosmology. *Advances in High Energy Physics*. 2012: 1–34.

[Lew07] Lewis, R. J. 2007. *Development of a Raman System for in-line monitoring of Tritium at the Karlsruhe Tritium Neutrino (KATRIN) Experiment*. Phd thesis. Swansea.

[Lew08] Lewis, R. J. et al. 2008. Dynamic Raman spectroscopy of hydrogen isotopomer mixtures in-line at TILO. *Laser Physics Letters*. 5(7): 522–531.

[Lie20] Lienhard, J. 2020. *A Heat Transfer Textbook*. Dover Publications Inc.

[Lob03] Lobashev, V. 2003. The search for the neutrino mass by direct method in the tritium beta-decay and perspectives of study it in the project KATRIN. *Nuclear Physics A*. 719: C153–C160.

[Lon02] Long, D. 2002. *The Raman Effect: A Unified Treatment of the Theory of Raman Scattering by Molecules*. Wiley.

[Lon30] London, F. 1930. Zur Theorie und Systematik der Molekularkräfte. *Zeitschrift für Physik*. 63(3): 245–279.

[Lor02] Loredo, T. J. and Lamb, D. Q. 2002. Bayesian analysis of neutrinos observed from supernova SN 1987A. *Physical Review D*. 65(6): 063002.

[Luk12] Lukić, S. et al. 2012. Measurement of the gas-flow reduction factor of the KATRIN DPS2-F differential pumping section. *Vacuum*. 86(8): 1126–1133.

[Mak62] Maki, Z. et al. 1962. Remarks on the Unified Model of Elementary Particles. *Progress of Theoretical Physics*. 28(5): 870–880.

[Mal13] Malyshev, O. B. et al. 2013. Electron stimulated desorption from the 316 L stainless steel as a function of impact electron energy. *Journal of Vacuum Science & Technology A: Vacuum, Surfaces, and Films*. 31(3): 031601.

[Mar21] Marsteller, A. et al. 2021. Neutral tritium gas reduction in the KATRIN differential pumping sections. *Vacuum*. 184: 109979.

[Mat52] Mattraw, H. C. et al. 1952. Mass Spectometric Determination of the Hydrogen-Tritium Equilibrium. *The Journal of Chemical Physics*. 20(5): 926–926.

[McC81] McConville, G. T. 1981. A consistent spherical potential function for para-hydrogen. *The Journal of Chemical Physics*. 74(4): 2201–2205.

[McC83a] McConville, G. T. et al. 1983. Reaction rates of D_2 + T_2 mixtures at 295 K. *Journal of Vacuum Science & Technology A: Vacuum, Surfaces, and Films*. 1(3): 1441–1446.

[McC83b] McConville, G. T. et al. 1983. Summary abstract: Reaction rates for the formation of DT under various conditions from T_2 + D_2. *Journal of Vacuum Science & Technology A: Vacuum, Surfaces, and Films*. 1(2): 874–875.

[McC85] McConville, G. T. et al. 1985. Reaction Rates for the Formation of Deuterium Tritide from Deuterium and Tritium. *Fusion Technology*. 8(2P2): 2245–2256.

[McK74] McKellar, A. R. W. and Welsh, H. L. 1974. Spectra of $(H_2)_2$, $(D_2)_2$, and H_2–D_2 Van der Waals Complexes. *Canadian Journal of Physics*. 52(12): 1082–1089.

[McK90] McKellar, A. R. W. 1990. Infrared spectra of hydrogen dimers. *The Journal of Chemical Physics*. 92(6): 3261–3277.

[McK91] McKellar, A. R. W. and Schaefer, J. 1991. Far-infrared spectra of hydrogen dimers: Comparisons of experiment and theory for $(H_2)_2$ and $(D_2)_2$ at 20 K. *The Journal of Chemical Physics*. 95(5): 3081–3091.

[McK94] McKellar, A. R. W. and Clouter, M. J. 1994. Infrared spectra of liquid hydrogen and deuterium. *Canadian Journal of Physics*. 72(1-2): 51–56.

[Mer19] Mertens, S. et al. 2019. A novel detector system for KATRIN to search for keV-scale sterile neutrinos. *Journal of Physics G: Nuclear and Particle Physics*. 46(6): 065203.

[Mil72] Milenko, Y. Y. et al. 1972. On temperature dependence of the polarizability of H_2 and D_2 molecules. *Physica*. 60(1): 90–96.

[Mil97] Milenko, Y. Y. and Sibileva, R. M. 1997. Natural Ortho-Para Conversion Rate in Liquid and Gaseous Hydrogen. *Journal of Low Temperature Physics*. 107(12): 77–92.

[Mir14] Mirz, S. 2014. *Simulation and Experimental Investigation of the Nuclear Spin Dependence of the Infrared Absorption of Liquid Hydrogen Isotopologues*. Master Thesis. Karlsruhe.

[Mir17] Mirz, S. et al. 2017. Design of a Spectroscopy Experiment for All Hydrogen Isotopologues in the Gaseous, Liquid, and Solid Phase. *Fusion Science and Technology*. 71(3): 375–380.

[Mir19] Mirz, S. 2019. *Investigation of Van-der-Waals Clusters of Liquid and Gaseous Hydrogen Isotopologues via Infrared Absorption Spectroscopy*. PhD thesis. Karlsruhe.

[Mir20] Mirz, S. et al. 2020. Concentrated Nonequilibrium HD for the Cross Calibration of Hydrogen Isotopologue Analytics. *Fusion Science and Technology*. 76(3): 284–290.

[Mor77] Morris, G. 1977. *Methane formation in tritium gas exposed to stainless steel*. tech. report.

[Mot62] Motizuki, K. 1962. Note on Para-Ortho Conversion in Solid Deuterium. *Journal of the Physical Society of Japan*. 17(7): 1192–1192.

[Mül19a] Müller, J. et al. 2019. Custom-built light-pipe cell for high-resolution infrared absorption spectroscopy of tritiated water vapor and other hazardous gases. *Optics Express*. 27(12): 17251.

[Mül19b] Müller, S. 2019. *Erster Aufbau und Charaktrisierung des optischen Systems des TApIR2-Experiments zur parallelen Analyse mittels Raman- und IR-Spektroskopie*. Bachelor thesis. Karlsruhe.

[Nie21a] Niemes, S. 2021. *Calibration of a Laser-Raman-System using gas samples of all hydrogen isotopologues for KATRIN*. Phd thesis. Karlsruhe.

[Nie21b] Niemes, S. et al. 2021. Accurate Reference Gas Mixtures Containing Tritiated Molecules: Their Production and Raman-Based Analysis. *Sensors*. 21(18): 6170.

[Nie67] Nielsen, S. E. and Dahler, J. S. 1967. Paramagnetic Catalysis of the Ortho—Parahydrogen Conversion. *The Journal of Chemical Physics*. 46(2): 732–744.

[Nuc18] Nucciotti, A. et al. 2018. Status of the HOLMES Experiment to Directly Measure the Neutrino Mass. *Journal of Low Temperature Physics*. 193(5-6): 1137–1145.

[Oer06] Oerter, R. 2006. *The Theory of Almost Everything*. Penguin Publishing Group.

[Pac08] Pachucki, K. and Komasa, J. 2008. Ortho-para transition in molecular hydrogen. *Phys. Rev. A*. 77: 030501.

[Par12] Parkinson, D. et al. 2012. The WiggleZ Dark Energy Survey: Final data release and cosmological results. *Physical Review D*. 86(10): 103518.

[Pat01] Patzak, T. 2001. First direct observation of the tau neutrino. *Europhysics News*. 32(2): 56–57.

[Pau30] Pauli, W. 1930. *Offener Brief an die Gruppe der Radioaktiven bei der Gauvereins-Tagung zu Tübingen*.

[Pod19] Podbielski, G. 2019. *Messung der Temperaturabhängigkeit der Aktivierung von Fe_2O_3 für die ortho/para-Konversion von Wasserstoff*. Bachelor thesis. Karlsruhe.

[Pon57] Pontecorvo, B. 1957. Mesonium and anti-mesonium. *Sov. Phys. JETP*. 6: 429.

[Pon58] Pontecorvo, B. 1958. Inverse beta processes and nonconservation of leptoncharge. *Zh. Eksp. Teor. Fiz.* 34: 247.

[Pon68] Pontecorvo, B. 1968. Neutrino experiments and the problem of conservation of leptonic charge. *Sov. Phys. JETP*. 26: 984–988.

[Pov15] Povh, B. et al. 2015. *Particles and Nuclei*. Springer Berlin Heidelberg.

[Pra61] Pratt, T. H. and Wolfgang, R. 1961. The Self-induced Exchange of Tritium Gas with Methane. *Journal of the American Chemical Society*. 83(1): 10–17.

[Pri15] Priester, F. et al. 2015. Commissioning and detailed results of KATRIN inner loop tritium processing system at Tritium Laboratory Karlsruhe. *Vacuum*. 116: 42–47.

[Pri20] Priester, F. et al. 2020. Tritium Processing Systems and First Tritium Operation of the KATRIN Experiment. *Fusion Science and Technology*. 76(4): 600–604.

[Pri22] Priester, F. et al. 2022. μRA: A New Compact Easy-to-Use Raman System for All Hydrogen Isotopologues. *Sensors*. 22(10): 3952.

[Rai63] Raich, J. C. 1963. *Ortho-para transition in molecular hydrogen*. Phd thesis. Iowa.

[Raj16] Rajasekaran, G. 2016. *The Story of the Neutrino*.

[Rei19] Reinking, J. et al. 2019. First high-resolution spectrum and line-by-line analysis of the $2\nu 2$ band of HTO around 3.8 microns. *Journal of Quantitative Spectroscopy and Radiative Transfer*. 230: 61–64.

[Reu22] Reusch, S. et al. 2022. Candidate Tidal Disruption Event AT2019fdr Coincident with a High-Energy Neutrino. *Physical Review Letters*. 128(22): 221101.

[Ric14] Richler, K.-D. 2014. *Untersuchung der Ortho/Para-Konversion für Wasserstoff unter Verwendung von Palladium- und Eisenoxid-Katalysatoren*. Bachelor thesis. Karlsruhe.

[Rie11] Riess, A. G. et al. 2011. A 3% Solution: Determination of the Hubble Constant with the *Hubble Space Telescope* and Wide Field Camera 3. *The Astrophysical Journal*. 730(2): 119.

[Rie14] Riemer-Sørensen, S. et al. 2014. Combining Planck data with large scale structure information gives a strong neutrino mass constraint. *Physical Review D*. 89(10): 103505.

[Rob88] Robertson, R. G. H. and Knapp, D. A. 1988. Direct Measurements of Neutrino Mass. *Annual Review of Nuclear and Particle Science*. 38(1): 185–215.

[Rob91] Robertson, R. G. H. et al. 1991. Limit on ν_e mass from observation of the β decay of molecular tritium. *Phys. Rev. Lett.* 67: 957–960.

[Röl13] Röllig, M. et al. 2013. Activity monitoring of a gaseous tritium source by beta induced X-ray spectrometry. *Fusion Engineering and Design*. 88(6-8): 1263–1266.

[Röt17] Röttele, C. 2017. Results of the first Cool-down of the KATRIN Cryogenic Pumping Section. *Journal of Physics: Conference Series*. 888: 012228.

[Rup15a] Rupp, S. et al. 2015. Enhanced Sensitivity of Raman Spectroscopy for Tritium Gas Analysis Using a Metal-Lined Hollow Glass Fiber. *Fusion Science and Technology*. 67(3): 547–550.

[Rup15b] Rupp, S. et al. 2015. Improving the Detection Limit in a Capillary Raman System for In Situ Gas Analysis by Means of Fluorescence Reduction. *Sensors*. 15(9): 23110–23125.

[Rut99] Rutherford, E. 1899. VIII. Uranium radiation and the electrical conduction produced by it. *The London, Edinburgh, and Dublin Philosophical Magazine and Journal of Science*. 47(284): 109–163.

[Sae00] Saenz, A. et al. 2000. Improved Molecular Final-State Distribution of HeT^+ for the beta-decay process of T_2. *Physical Review Letters*. 84(2): 242–245.

[Sae97a] Saenz, A. and Froelich, P. 1997. Effect of final-state interactions in allowed β decays. I. General formalism. *Physical Review C*. 56(4): 2132–2161.

[Sae97b] Saenz, A. and Froelich, P. 1997. Effect of final-state interactions in allowed β decays. II. Reliability of the β-decay spectrum for T_2. *Physical Review C*. 56(4): 2162–2184.

[Saz11] Sazonov, A. B. and Magomedbekov, E. P. 2011. Hydrogen Isotope Equilibration Induced by Tritium Radiation - Ab Initio Approach to Reaction Kinetics. *Fusion Science and Technology*. 60(4): 1383–1386.

[Sch02] Schindewolf, U. 2002. Zur Erinnerung an Karl Friedrich Bonhoeffer (1899-1957). *Bunsen-Magazin*. 4(6): 139–146.

[Sch13a] Schlösser, M. et al. 2013. Evaluation method for Raman depolarization measurements including geometrical effects and polarization aberrations. *Journal of Raman Spectroscopy*. 44(3): 453–462.

[Sch13b] Schlösser, M. 2013. *Accurate Calibration of the Raman system for the Karlsruhe Tritium Neutrino Experiment*. Phd thesis. Karlsruhe.

[Sch13c] Schlösser, M. et al. 2013. Accurate calibration of the laser Raman system for the Karlsruhe Tritium Neutrino Experiment. *Journal of Molecular Structure*. 1044: 61–66.

[Sch13d] Schlösser, M. et al. 2013. In-Line Calibration of Raman Systems for Analysis of Gas Mixtures of Hydrogen Isotopologues with Sub-Percent Accuracy. *Analytical Chemistry*. 85(5): 2739–2745.

[Sch15a] Schlösser, M. et al. 2015. How to Make Raman-Inactive Helium Visible in Raman Spectra of Tritium-Helium Gas Mixtures. *Fusion Science and Technology*. 67(3): 559–562.

[Sch15b] Schlösser, M. et al. 2015. Raman Spectroscopy at the Tritium Laboratory Karlsruhe. *Fusion Science and Technology*. 67(3): 555–558.

[Sch15c] Schlösser, M. et al. 2015. Relative Intensity Correction of Raman Systems with National Institute of Standards and Technology Standard Reference Material 2242 in 90°-Scattering Geometry. *Applied Spectroscopy*. 69(5): 597–607.

[Sch15d] Schmidt, H. 2015. *Vergleich der Ortho/Para Konversion und der chemsichen Konversion von H_2 und D_2 unter Verwendung von Eisenoxid als Katalysator*. Bachelor thesis. Karlsruhe.

[Sch16] Schönung, K. 2016. *Development of a Rear Wall for the KATRIN Rear Section and investigation of tritium compatibility of Rear Section components*. PhD thesis. Karlsruhe.

[Sch17] Schlösser, M. et al. 2017. CARS spectroscopy of the ($v = 0 \rightarrow 1$) band in T_2. *Journal of Physics B: Atomic, Molecular and Optical Physics*. 50(21): 214004.

[Sch64] Schmauch, G. E. and Singleton, A. H. 1964. Technical Aspects of ortho-parahydrogen Conversion. *Industrial & Engineering Chemistry*. 56(5): 20–31.

[Sei19] Seitz-Moskaliuk, H. 2019. *Characterisation of the KATRIN tritium source and evaluation of systematic effects*. PhD thesis. Karlsruhe.

[Sha59] Shavitt, I. 1959. A Calculation of the Rates of the Ortho-Para Conversions and Isotope Exchanges in Hydrogen. *The Journal of Chemical Physics*. 31(5): 1359–1367.

[Shi17] Shirai for the Kam*LAND*-Zen Collaboration, J. 2017. Results and future plans for the KamLAND-Zen experiment. *Journal of Physics: Conference Series*. 888: 012031.

[Shi20] Shin, C. D. et al. 2020. Observation of reactor antineutrino disappearance using delayed neutron capture on hydrogen at RENO. *Journal of High Energy Physics*. 2020(4): 1–25.

[Shu11] Shun Zhou, Z. X. 2011. *Neutrinos in Particle Physics, Astronomy and Cosmology*. Springer-Verlag GmbH.

[Sis04] Sisti, M. et al. 2004. New limits from the Milano neutrino mass experiment with thermal microcalorimeters. *Nuclear Instruments and Methods in Physics Research Section A: Accelerators, Spectrometers, Detectors and Associated Equipment*. 520(1-3): 125–131.

[Smo18] Smolinski, A. 2018. *Experimental Characterization of the Catalytic Process of ortho/para Catalysts for Hydrogen and Deuterium*. Master thesis. Karlsruhe.

[Sou86] Souers, P. 1986. *Hydrogen properties for fusion energy*. Berkeley: University of California Press.

[Spu15] Spurio, M. 2015. *Particles and Astrophysics*. Springer International Publishing.

[Ste64] Stewart, J. W. 1964. Dielectric Polarizability of Fluid Para-Hydrogen. *The Journal of Chemical Physics*. 40(11): 3297–3306.

[Stu10] Sturm, M. et al. 2010. Monitoring of All Hydrogen Isotopologues at Tritium Laboratory Karlsruhe Using Raman Spectroscopy. *Laser Physics*. 20(2): 493–507.

[Stu21] Sturm, M. et al. 2021. Kilogram scale throughput performance of the KATRIN tritium handling system. *Fusion Engineering and Design*. 170: 112507.

[Süß18] Süß, O. 2018. *Modellierung der Aktivität und Effizienz von ortho/para-Katalysatoren für Wasserstoff und Deuterium*. Master thesis. Karlsruhe.

[Sza87] Szalewicz, K. et al. 1987. Molecular effects in tritium β decay. III. Electronic resonances of the HeT^+ ion and dependence of neutrino mass on the accuracy of the theoretical model. *Physical Review A*. 35(3): 965–979.

[Tay33] Taylor, H. S. and Diamond, H. 1933. The Para-hydrogen Conversion At Paramagnetic Surfaces. *Journal of the American Chemical Society*. 55(6): 2613–2614.

[Ter69] Terao, T. and Back, R. S. 1969. Radiation-induced isotopic exchange in gaseous hydrogen-deuterium mixtures. *The Journal of Physical Chemistry*. 73(11): 3884–3890.

[The02] The Royal Swedish Academy of Science. 2002. *Scientific Background on the Nobel Prize in Pysics 2002*.

[The15] The Royal Swedish Academy of Science. 2015. *Scientific Background on the Nobel Prize in Pysics 2015*.

[The95] The Royal Swedish Academy of Science. 1995. *Scientific Background on the Nobel Prize in Pysics 1995*.

[Tho58] Thompson, S. O. and Schaeffer, O. A. 1958. The Role of Ions in the Radiation Induced Exchange of Hydrogen and Deuterium. *Journal of the American Chemical Society*. 80(3): 553–558.

[Tim66] Timmerhaus, K. D. 1966. *Advances in Cryogenic Engineering*. Springer New York, NY.

[Tre02] Tretyak, V. I. and Zdesenko, Y. G. 2002. Tables of double beta decay data - an update. *Atomic Data and Nuclear Data Tables*. 80(1): 83–116.

[Uda92a] Uda, T. et al. 1992. Hydrogen isotope exchange reaction rate in tritium and methane mixed gas. *Journal of Radioanalytical and Nuclear Chemistry Articles*. 159(1): 145–154.

[Uda92b] Uda, T. et al. 1992. Hydrogen Isotope Exchange Reaction Rates in Tritium, Hydrogen and Deuterium Mixed Gases. *ract*. 56(4): 209–214.

[Upa19] Upadhye, A. 2019. Neutrino mass and dark energy constraints from redshift-space distortions. *Journal of Cosmology and Astroparticle Physics*. 2019(05): 041–041.

[Van73] Van-der-Waals, J. D. 1873. *Over de continuiteit van den gas- en vloeistoftoestand*. Phd thesis. Leiden.

[Wat65] Watanabe, A. and Welsh, H. L. 1965. Pressure-induced infrared absorption of gaseous hydrogen and deuterium at low temperatures: I. The integrated absorption coefficients. *Canadian Journal of Physics*. 43(5): 818–828.

[Wei55] Weitzel, D. H. and White, L. E. 1955. Continuous Analysis of Ortho-Parahydrogen Mixtures. *Review of Scientific Instruments*. 26(3): 290–292.

[Wei56] Weitzel, D. H. and Park, O. E. 1956. Iron Catalyst for Production of Liquid para-Hydrogen. *Review of Scientific Instruments*. 27(1): 57–58.

[Wei58a] Weitzel, D. H. et al. 1958. Flow Conversion Kinetics of Ortho and Parahydrogen. *Advances in Cryogenic Engineering Vol. 4. Proceedings of the 1958 Cryogenic Engineering Conference*. 4: 286–295.

[Wei58b] Weitzel, D. H. et al. 1958. Ortho-Para Catalysis in Liquid-Hydrogen Production. *Journal of Research of the National Bureau of Standards*. 60(3): 221–227.

[Wei60] Weitzel, D. H. et al., "Design Data for Ortho-Parahydrogen Converters", *Advances in Cryogenic Engineering*, ed. by Timmerhaus, K. D., Boston, MA: Springer US, 1960, 73–84.

[Wel15] Welte, S. et al. 2015. Tritium Laboratory Karlsruhe: Administrative and Technical Framework for Isotope Laboratory Operation. *Fusion Science and Technology*. 67(3): 635–638.

[Wel51] Welsh, H. L. et al. 1951. Induced Infrared Absorptions of H_2, N_2, and O_2 in the First Overtone Regions. *Physical Review*. 83: 1264–1264.

[Wil57] Wilson, W. A. and Weitzel, D. H. 1957. Vapor Phase Ortho-Para Conversion in the large CEL-NBS hydrogen Liquifier. *Advances in Cryogenic Engineering Vol. 3. Proceedings of the 1957 Cryogenic Engineering Conference*. 3: 85–91.

[Wol78] Wolfenstein, L. 1978. Neutrino oscillations in matter. *Physical Review D*. 17(9): 2369–2374.

[Wu57] Wu, C. S. et al. 1957. Experimental Test of Parity Conservation in Beta Decay. *Physical Review*. 105(4): 1413–1415.

[Yin19] Yin, L. and Ju, Y. 2019. Review on the design and optimization of hydrogen liquefaction processes. *Frontiers in Energy*. 14(3): 530–544.

[You68] Younglove, B. A. 1968. Polarizability, Dielectric Constant, Pressure, and Density of Solid Parahydrogen on the Melting Line. *The Journal of Chemical Physics*. 48(9): 4181–4186.

[Zel17] Zeller, G. 2017. *Development of a calibration procedure and calculation of the uncertainty budget for the KATRIN laser Raman system*. Master thesis. Karlsruhe.

[Zub11] Zuber, K. 2011. *Neutrino physics. 2nd ed*. CRC Press, Boca Raton, London, New York.

[Zub20] Zuber, K. 2020. *Neutrino Physics*. Taylor & Francis Ltd.

[Zyl20] Zyla, P. A. et al. 2020. Review of Particle Physics. *Progress of Theoretical and Experimental Physics*. 2020(8): 1–2093.

Acknowledgements

Ich möchte mich an dieser Stelle bei all jenen bedanken, die mich während meiner Promotionszeit auf unterschiedliche Art und Weise unterstützt haben, und so zum Gelingen beigetragen haben. Sowohl im beruflichen als auch im privaten Bereich waren helfende Hände sowie aufmunternde Worte besonders wichtig für mich.

Beginnen möchte bei meinem Doktorvater Prof. Dr. Guido Drexlin, der mir diese Arbeit erst ermöglicht hat. Alles begann im 5. Semester im Astroteilchenseminar, als ich zum Probevortrag *Gravtationswellen und ihr Nachweis* zum ersten Mal an den Campus Nord kam. Er weckte mein Interesse an diesem Bereich und so folgten zunächst die Bachelor- und dann die Masterarbeit. Und da bekanntlich aller guten Dinge drei sind, auch die Doktorarbeit bei KATRIN. Ich möchte Danke für diese aufregenden und lehrreichen Jahre sagen und dafür, dass du mich bis zum Ende unterstützt hast.

Mein herzlicher Dank geht an Herrn Prof. Dr. Ralph Engel, dass er so kurzfristig eingewilligt hat, das Korreferat zu übernehmen. Ihm und Guido Drexlin danke ich für ihre interessanten Vorlesungen und die angenehme Masterprüfung in Astroteilchenphysik.

Ein besonderes Dankeschön geht an meinen Betreuer Dr. Robin Größle. Seine stete Unterstützung während dieser Arbeit, insbesondere die zahlreichen Diskussionen über die Planungen der Experimente und anstehende Messkampagnen sowie der physikalische Austausch und vor allem seine kreativen Ideen, waren goldwert und willkommen. Danke für die gemeinsame Zeit bis zum Schluss, insbesondere für das Korrekturlesen und die vielen Anmerkungen.

Dr. Beate Bornschein möchte ich von Herzen danken, dass ich meine drei Abschlussarbeiten am Tritiumlabor Karlsruhe (TLK) durchführen durfte. Dank ihrer guten wissenschaftlichen Rahmenbedingungen konnte ich in dieser Zeit viele wertvolle Erfahrungen für mein Leben sammeln. Von ihrer Einstellung zur Ausbildung und Förderung über das physikalische Fachwissen hinaus, habe ich gerade in Bezug auf die umfangreiche und gewissenhafte Betreuung von Studierenden, stark profitiert.

Herrn Dr. Uwe Besserer danke ich für die lebhaften Diskussionen, vor allem für die verfahrenstechnischen Einblicke. Seine Tür stand immer für meine unzähligen Fragen offen.

8 Jahre mit Unterbrechungen war ich am TLK und in dieser Zeit durfte ich mit vielen außergewöhnlichen Kolleginnen und Kollegen zusammen arbeiten. Ich danke daher allen ehemaligen und aktuellen TLKlern für diese wunderschöne und einmalige Zeit, die ich nie vergessen werde. Ihr habt mich von Beginn an herzlich aufgenommen und mir ein angenehmes Arbeitsklima verschafft. Eurer Unterstützung konnte ich mir immer gewiss sein. Es war daher nicht nur in wissenschaftlicher Hinsicht ein eindrucksvolles Labor, wo man jeden Tag viel lernen konnte, sondern auch in menschlicher Hinsicht.

Ein spezieller Dank geht der Reihe nach an:

Zuerst möchte ich mich bei Stefan Welte, Nancy Tuchscherer sowie Tobias Falke bedanken. Eure Expertise und Unterstützung waren unermesslich. Vor allem der Aufbau wäre ohne

eure Hilfe und vor allem eure praktischen Fertigkeiten nicht möglich gewesen. Die zahlreichen Diskussionen und Überlegungen bezüglich der Anordnung innerhalb der BETTINA-Box werden mir in lebhafter Erinnerung bleiben. Ein Dank geht auch an Herrn Albert Braun für seinen Tatendrang immer vorankommen zu wollen.

Dem Betriebsbüro unter der Leitung von Dr. Jürgen Wendel danke ich für ihre Hilfestellungen. Mein Dank geht an Dirk Osenberg für die zahlreichen Tipps und seine akribische Kontrolle in Zusammenhang mit der Dokumentation und Betriebssicherheit. Ein weiteres Dankeschön geht an Frau Sylvia Krieger für ihre Mühen, insbesondere wenn die Bestellung sofort erfolgen musste, und die humorvollen Unterhaltungen.

Mein Dank geht auch an die Mess- und Automatisierungsgruppe am TLK, die von Peter Schäfer geleitet wird. Als direkte Nachbarn war es oft von Vorteil den kurzen Weg zu wählen, wenn ich einmal wieder eure Hilfe benötigte.

Dr. Magnus Schlösser möchte ich neben den zahlreichen wissenschaftlichen Diskussionen, für seine abwechslungsreichen und vor allem lustigen Aktivitäten danken. Es war mir eine große Freude mit dir zu rappen, zu singen und zu tanzen.

Ein besonderes Dankeschön geht an alle ehemaligen und aktuellen Mitglieder der TApIR-Gruppe. Danke, dass ihr mich in diese Gruppe aufgenommen habt und mir ein derart tolles wissenschaftliches und angenehmes Umfeld geboten habt. Ich danke zum einen Dr. Sebastian Mirz und Dr. Robin Größle für ihre Zusammenarbeit und die zahlreichen interessanten sowie auch heiteren Diskussionen. Ich möchte „meinen Studenten Florian Altenbrand, Arne Smolinski, Oliver Süß, Gerold Podbielski, Alexander Böhmländer, Daniel Kurz und Charles Ruzé sowie meiner Studentin Svenja Müller dafür danken, dass ihr zu mir gekommen seid, das Vertrauen in mich gesetzt habt, eure Abschlussarbeiten betreuen zu dürfen. Es war mir eine Freude, mit euch allen zusammen gearbeitet zu haben, denn ohne eure Hilfe und die Ergebnisse eurer Arbeiten wäre T_2ApIR nicht so weit gekommen.

In diesem Zusammenhang möchte ich danke bei Daniel Kuntz vom TEC sagen. Die zahlreichen Besuche vor Ort und Diskussionen über das Design haben mich stets vorangebracht.

Mich bedanken möchte ich auch bei Frau Eva Porter. Wann ich immer ein offenes Ohr oder einen guten Ratschlag benötigte, stand deine Tür offen.

Viele Freundschaften wurden geschlossen, die auch über das berufliche Miteinander hinausgehen. Als erstes möchte ich daher der Mittagsrunde um Dirk Osenberg, Nancy Tuchscherer, Dr. Simon Niemes sowie Dr. Sebastian Mirz danken. Die vielfältigen, lustigen und teils lautstarken Diskussionen haben den Tag oft angnehmer und heiterer gemacht.

Ein herzliches Dankeschön geht an meinen ehemaligen langjährigen Zimmergenossen Andreas Off. Vieles haben wir bisher gemeinsam erlebt. Dabei konnte ich mich stets auf dich verlassen und mich deiner Unterstützung gewiss sein. Ich bin dankbar für diese langjährige Freundschaft.

Danke möchte ich auch meinen neuen Kollegen, Dr. David Saez de Jauregui und Dr. Andreas Grau. Danke für die freundliche Aufnahme in eure Gruppe und die gute Zusammenarbeit. Dass ihr mir in den letzten Wochen den Rücken freigehalten habt, hat mir sehr geholfen und viel bedeutet.

Die zeitintensive und mühsame Arbeit des Korrekturlesen wurde Simon Reinkemeier und Hans Hahne zu teil. Ich bin euch für eure unermüdliche Hilfe und eure gewissenhafte Korrektur sehr dankbar.

Aber während so einer langen Zeit bedarf es auch der Unterstützung im familiären und Freundeskreis. Zunächst danke ich meinen Kommilitonen Christoph Heidecker, Thomas Huber, Manuel Klein, Nicolas Kurz, Matthias Schnepf, Paul Schütze und Nicolai Walter. Seit dem ersten Semester bis zum Ende des Masterstudiums haben wir einander geholfen und die Zeit gemeinsam gemeistert. Ohne euch wäre das Studium nur halb so interessant verlaufen.

Auch möchte ich meiner Familie danken, die stets hinter mir steht und zu mir hält. Ohne euch wäre ich nicht so weit gekommen. Auch wenn die Entfernung zur Heimat ein regelmäßiges Sehen erschwert hat, so waren und sind die zahlreichen Telefonate ein fester Bestandteil geworden, den ich nicht missen möchte. Ein besonderes Dankeschön geht an meine Eltern, die mich stets darin bestärkt haben, meinen eigenen Weg zu gehen und mich unterstützt haben, wann immer ich auf ihre Hilfe angewiesen war. Eure liebevolle Erziehung hat mich maßgeblich zu dem Menschen werden lassen, der ich heute bin.

Auch meinen Schwiegereltern sage ich Danke. Eure liebvolle Art und hilfreiche Unterstützung sind mir immer eine besondere Freude.

Zum Abschluss bleiben noch zwei Frauen in meinem Leben, denen mein innigster Dank gilt: meiner Frau Monika und unserer Tochter Valeria. Ohne euch beide hätte ich die letzten Schritte nicht geschafft. Ihr habt mir die notwendige Rückendeckung gegeben und mir immer wieder Mut zugesprochen. Posebno sam ti zahvalan Monika. Tvoja ljubav i toplina dale su mi snagu da ustrajem i ne odustajem. Uvijek si vjerovala u mene i davala mi hrabrost da nastavim. Uvijek ću ti biti zahvalan na tome. Ti nisi samo prekrasna žena koju volim svim srcem, već i nevjerojatna majka koja se s ljubavlju brine o našoj kćeri. Hvala ti!